

Numerical Investigation of Particle-Laden Thermally Driven Turbulent Flows in Enclosure

THÈSE N° 4600 (2010)

PRÉSENTÉE LE 12 FÉVRIER 2010

À LA SCIENCES ET TECHNIQUES DE L'INGÉNIEUR
LABORATOIRE D'INGÉNIERIE NUMÉRIQUE
PROGRAMME DOCTORAL EN MÉCANIQUE

ÉCOLE POLYTECHNIQUE FÉDÉRALE DE LAUSANNE

POUR L'OBTENTION DU GRADE DE DOCTEUR ÈS SCIENCES

PAR

Riccardo PURAGLIESI

acceptée sur proposition du jury:

Dr M. Farhat, président du jury
Prof. M. Deville, Prof. A. Soldati, directeurs de thèse
Dr A. Dehbi, rapporteur
Prof. E. Leriche, rapporteur
Prof. R. Verzicco, rapporteur



ÉCOLE POLYTECHNIQUE
FÉDÉRALE DE LAUSANNE

Suisse
2010

Abstract

Nowadays, the global increase of energy demand and the necessity to satisfy high safety standards, have led engineers and scientists to focus their efforts in order to understand and describe fundamental phenomena that are crucial for a correct design of the new generation nuclear power plants.

In this framework, the present thesis aims at providing a first insight of the mechanisms of deposition of aerosol particles inside a closed geometry where relatively strong currents are present due to turbulent natural convective flows.

Direct Numerical Simulations were conducted coupling high-order pseudo-spectral code with a Lagrangian particle tracker.

Laminar flows were computed in two and three dimensions in order to benchmark the code with published reference data.

A parametric study was performed for three different aerosol micro-size particle diameters and two super-critical Rayleigh numbers in a square cavity. An extended analysis of the turbulent flows is provided in terms of first and second order statistics, time-averaged momentum and energy budgets, and moreover, important terms appearing in the transport equations of turbulent kinetic energy and temperature variance are also briefly discussed. Furthermore, the evolution in time of particle concentration for the three different diameters is considered. The text provides information about the deposition velocity, the deposition patterns on the cavity surfaces, the influence of lift and thermophoretic forces and the fractal dimension.

The same size dependent parametric study for the three different sets of micro-size particles was carried out in a fully three-dimensional closed cubic cavity for one super-critical Rayleigh number. A detailed investigation of the turbulence was performed by means of statistical quantities, signal processing and conditional averaging, in order to get a general view of the complexity of the flow and its characteristics.

Further on, the sedimentation process is studied in the same way as for the two dimensional case.

Finally a simple theoretical deposition model is provided in order to interpret the numerical results for the aerosol phase.

Keywords: DNS, natural convection, particle tracking, turbulence, aerosol deposition, two-phase flows.

Sommario

Oggigiorno, il crescente aumento della richiesta di energia su scala globale e la necessità di soddisfare elevati standard di sicurezza, hanno indotto ingegneri e scienziati a concentrare i loro sforzi nel tentativo di comprendere e descrivere fenomeni che sono fondamentali e cruciali per una corretta progettazione di impianti nucleari di nuova generazione.

In questo contesto, la presente tesi vuole fornire una prima interpretazione dei meccanismi di deposizione di particelle d'aerosol confinate in un volume chiuso nel quale sono presenti forti correnti turbolente, quest'ultime causate da moti di convezione naturale.

Simulazioni numeriche dirette (DNS) sono state effettuate utilizzando un codice pseudo-spettrale accoppiato con un tracciatore Lagrangiano.

Il codice è stato testato comparando i risultati ottenuti per flussi laminari con dati pubblicati in letteratura specializzata.

È stato condotto uno studio parametrico, in cavità quadrata, per tre diversi diametri di particelle e due valori super-critici del numero di Rayleigh. I moti turbolenti sono stati analizzati in modo esteso dal punto di vista statistico in termini di momenti di primo e secondo ordine, bilanci delle medie temporali delle equazioni di conservazione della quantità di moto e dell'energia, e inoltre i termini più significativi presenti nell'equazioni di trasporto dell'energia cinetica turbolenta e della varianza della temperatura sono brevemente discussi. Oltre a ciò, l'evoluzione temporale della concentrazione dei tre set di particelle è stata presa in esame. Il testo fornisce informazioni riguardanti importanti quantità come la velocità di deposizione e la dimensione frattale dei *cluster* di particelle; inoltre l'influenza della forza di *lift* e della termoforesi sono discussi come anche il *pattern* mostrato dalle particelle depositate sulle superfici della cavità.

Il medesimo studio parametrico basato su tre diversi diametri di particella è stato condotto in una cavità cubica per un unico numero di Rayleigh super critico. Lo studio dettagliato e approfondito della turbolenza e' stato effettuato usando strumenti statistici, trattamento del segnale e *conditional averaging* in modo da caratterizzare la complessità del moto fluido in esame.

Il processo di deposizione dell'aerosol è stato studiato in maniera analoga al caso bidimensionale.

Infine, un semplice modello teorico di deposizione è stato proposto per l'interpretazione dei risultati numerici ottenuti.

Keywords: DNS, convezione naturale, tracciamento di particelle, turbolenza, deposizione di aerosol, flussi bifase.

Acknowledgements

First of all, I would like to thank Prof. Michel Deville, Prof. Alfredo Soldati and Dr. Salih Guntay who gave me this unique opportunity and who trusted me and supported my work throughout the whole project. I am very grateful to Prof. Michel Deville and Prof. Alfredo Soldati for having supervised my thesis, having encouraged me all along, as well as for having enriched my knowledge about spectral methods and fluid mechanics.

The author wishes to express his gratitude to Prof. Emmanuel Leriche for all the fruitful discussions, suggestions and insights which had strongly inspired my research. Special thanks to Dr. Abdel Dehbi for his fundamental help at the beginning of the project and for his patience in waiting for my monthly activity reports that never arrived. Special thanks also to all the colleagues I had the luck to meet throughout the years at the Laboratoire d'ingénierie numérique (LIN), for the coffee breaks, technical discussions and most of all their friendship. I cannot forget to thank also Dr. Mahesh T. Dhotre for the funny conversations we had during my stay at PSI (Paul Scherrer Institut) and the countless cups of green tea we drank together.

Merci beaucoup to all the people with whom I shared the most beautiful moments of the last four years here in Lausanne: Angelo (a good friend, officemate and a bowling master!), Matteo (a gentleman and a dear friend), Marco (for all the interesting scientific discussions and afternoon breaks), Michele (are you ready for the next post-rock concert?), Arianna (for her famous "salsa marrone" and the delicious "salsa all'avocado"), Laura (a very good friend with the gift of making me smile every time), Annalisa (I loved her hand made banana bread and *tarte tatin*), Raffaello (a kind officemate and an expert in data backup, data indexing and data searching).

I wish to express my gratitude to Mme. Ursula Held for her hospitality in her extraordinary house and all the guys I met there in *Rue de Bassenges 33*, in particular Tomasz, Luigi and Gennady.

Finally, I offer my deepest thanks to Carla and Giuseppe, for being the wonderful parents they are and for their precious, invaluable and constant support. Grazie.

Physical concepts are free creations of the human mind, and are not, however it may seem, uniquely determined by the external world.

Albert Einstein, *The Evolution of Physics*

Contents

Contents	ix
List of Tables	xi
List of Figures	xiii
Introduction	1
1 Theoretical backgrounds	11
1.1 Continuous phase	11
1.1.1 Governing equations	11
1.1.2 Validity of the Oberbeck-Boussinesq approximation	14
1.1.3 Dimensionless Boussinesq equations	17
1.2 Aerosol dispersed solid phase	20
1.2.1 Governing equations	21
1.2.2 Dimensionless particle equation of motion	22
1.A Thermo-physical properties of air	24
1.B Aerosol particle aerodynamic diameter	25
2 Numerical methods	27
2.1 Methodology for the continuous phase	27
2.1.1 Space discretization	27
2.1.2 Solver	34
2.2 Methodology for the aerosol dispersed phase	38
2.2.1 Interpolation	38
2.2.2 Time integration	41
3 Differentially heated cavity: Two dimensional investigations	45
3.1 Steady laminar flows	46
3.1.1 Benchmark configuration	46

3.2	Chaotic flows	56
3.2.1	Time-averaged momentum and energy budgets	72
3.2.2	Turbulent kinetic energy and temperature variance budgets	76
3.3	Particle deposition	83
3.3.1	Deposition velocity	86
3.3.2	Segregation parameter: correlation dimension	96
4	Differentially heated cavity: Three dimensional investigations	99
4.1	Steady laminar flows	99
4.2	Turbulent flow	114
4.2.1	Mean fields	115
4.2.2	Time-averaged momentum and energy budgets	128
4.2.3	Turbulence characterization	129
4.3	Particle deposition	149
4.3.1	Deposition velocity	153
4.3.2	Particle residence time	161
4.3.3	Segregation parameter: correlation dimension	163
4.3.4	Theoretical simplified deposition model	164
	Conclusions and perspectives	171
	Bibliography	175
	Curriculum Vitæ	185

List of Tables

1.1	Thermo-physical properties of air at $T_R = 293.15$ [K], $p_R = 101.325$ [kPa].	24
1.2	Dynamic shape factors χ from [Dav79, Cro05].	25
2.1	The weights (η_0, ξ_i) for the implicit BDF schemes and (ζ_i) for the explicit extrapolation schemes.	37
3.1	Max-norm, 1-norm of the error in the centro-symmetry property and spectral coefficient ratio S for each field at $Ra = 10^5, 10^6, 10^7$	49
3.2	Comparison of 2d DHC flow results with the benchmark data of [dVD83, Le 91, Le 87, TLB00] for $Ra_H = 10^5, 10^6, 10^7$	50
3.3	Computational parameters: polynomial degrees N_1, N_2 , minimum and maximum grid size Δx_i , integration timestep $\Delta\tau$, number of frames per unit of time, averaging time and ratio of spectral coefficients	61
3.4	Max-norm and 1-norm of the residuals R of the time-averaged momentum and energy conservation laws.	72
3.5	Total averaged kinetic energy scaled by $Ra_H^{1/4}$ and its repartition between mean flow \overline{K} and fluctuating part \bar{k} with percentage.	76
3.6	Maximum values and position of turbulent kinetic energy and temperature variance production and dissipation.	81
3.7	Particle tracking computational parameters: Rayleigh number Ra_H , total number of particles injected N_p , particle aerodynamic diameter d_p , particle density ρ_p , Stokes number St , integration time step Δtau , final time τ_f	86
4.1	Max-norm, 1-norm of the error in the planar and centro-symmetry properties and spectral coefficient ratio S for each field at $Ra_H = 10^4, 10^5, 10^6$	102
4.2	Comparison of 3D DHC flow results with the benchmark data of [TLB00, WS04] for $Ra_H = 10^4, 10^5$	103
4.3	Comparison of 3D DHC flow results with the benchmark data of [TLB00, WS04] for $Ra_H = 10^6$	104
4.4	Max- and one- norms of errors committed in the centro- and planar- symmetries and ratio of the smallest to the largest spectral coefficients.	115
4.5	Computational parameters: polynomial degrees N_1, N_2, N_3 , minimum and maximum grid size Δx_i , integration time-step $\Delta\tau$, number of frames per unit of time and averaging time.	119
4.6	One-norm of the residuals of the time-averaged momentum and energy transport equations.	128

4.7	Total averaged kinetic energy scaled by $Ra_H^{1/4}$ and its repartition between mean flow \overline{K} and turbulent part \overline{k} in each single component $0.5\overline{u'_i u'_i}$ for $Ra_H = 10^9$	131
4.8	Integral time scales evaluated with three different criteria: integration up to the first ACF root (\mathcal{T}_0) and integration up the first ACF minimum (\mathcal{T}_{min}).	143
4.9	Particle tracking computational parameters.	153
4.10	Model function parameters a and b (Eq.4.32) for recirculating particle concentration number and coefficient of determination R^2	163
4.11	Particle settling time, model parameters and $Errr_\tau$ for particle sizes $d_p = 15, 25, 35 [\mu\text{m}]$	166

List of Figures

1	Steam generator cut view of the actual geometry and proportions.	3
1.1	Region of validity of the OB approximation in air ($T_R = 293.15$ [K], $P_R = 101.325$ [kPa]) App.(1.A).	16
1.2	Extended region of validity of the OB approximation in air ($T_R = 293.15$ [K], $P_R = 101.325$ [kPa]) App.(1.A).	17
1.3	Temperature boundary layer along a heated vertical wall.	18
2.1	First Chebyshev polynomials $T_k(x)$ of first kind for $k = 0, \dots, 5$	29
2.2	Example of Gauss-Lobatto-Chebyshev point distribution ($N = 6$) on the unit semi-circle.	31
2.3	Two-dimensional representation of Chebyshev basis functions $N_1 = N_2 = 3$ for $n = 1, \dots, 3$ and $m = 1, \dots, 3$	33
2.4	Schematic representation of the local grid used by a sixth order Lagrangian interpolator for three different particles away and close to the boundaries.	39
2.5	Lagrangian characteristic functions l_i for $K = 6$ and $i = 1, \dots, N$	40
2.6	Two-dimensional representation of Lagrangian characteristic functions l_3l_5 (a), l_5l_4 (b) with $K_1 = K_2 = 6$ and uniformly spaced knots.	40
2.7	Stability region for ERK4 method: points in the complex plane contained inside the closed curve are stable.	43
3.1	Schematic representation of the square DHC with boundary conditions.	46
3.2	Contour plots of velocity components u_1, u_2 for $Ra_H = 10^5, 10^6, 10^7$	51
3.3	Contour plots of temperature Θ and pressure p for $Ra_H = 10^5, 10^6, 10^7$	52
3.4	Contour plots of stream-function ψ and vorticity ω_3 for $Ra_H = 10^5, 10^6, 10^7$	53
3.5	Vertical velocity component profiles at different heights $x_2 = -0.3, 0.0, +0.3$ with respect to x^-	57
3.6	Temperature profiles at different heights $x_2 = -0.3, 0.0, +0.3$ with respect to x^-	58
3.7	Temperature profiles along the vertical mid-line $x_1 = 0$	59
3.8	Temperature stratification coefficient ς along the vertical mid-line $x_1 = 0$	59
3.9	Shear stress τ_w along the half cavity perimeter l	60
3.10	Local Nusselt number profile at the hot wall.	60
3.11	Time-averaged velocity components and pressure contour plots at $Ra_H = 10^9, 10^{10}$	64
3.12	Time-averaged temperature and stream-function contour plots at $Ra_H = 10^9, 10^{10}$	66
3.13	Time-averaged vertical component velocity profiles at different heights $x_2 = -0.3, 0.0, +0.3$ with respect to x^-	67

3.14	Time-averaged temperature profiles at different heights $x_2 = -0.3, 0.0, +0.3$ with respect to x^-	68
3.15	Time-averaged temperature profile along the vertical center-line.	69
3.16	Time-averaged shear stress $\langle \tau_w \rangle$ along the half cavity perimeter l	69
3.17	Time-averaged local Nusselt number $\langle Nu_h \rangle$ profile at the hot wall.	70
3.18	Reynolds-stress components contour plots at $Ra_H = 10^9, 10^{10}$	71
3.19	Time-averaged temperature and stream-function contour plots at $Ra_H = 10^9, 10^{10}$	73
3.20	Time-averaged vertical component of Convective, Pressure gradient and Reynolds stresses terms for $Ra_H = 10^9, 10^{10}$	75
3.21	Time-averaged Navier-Stokes budgets along the horizontal centerline ($x_2 = 0$) for $Ra_H = 10^9, 10^{10}$ with respect to x^- : Convective Term (CTM), Pressure Gradient (PG), Viscous Diffusion (VD), Reynolds Stresses (RS), Buoyancy Term (BT) and Residual (R).	77
3.22	Time-averaged Navier-Stokes budgets along the vertical centerline ($x_1 = 0$) for $Ra_H = 10^9, 10^{10}$: Convective Term (CTM), Pressure Gradient (PG), Viscous Diffusion (VD), Reynolds Stresses (RS), Buoyancy Term (BT) and Residual (R).	78
3.23	Time-averaged energy budgets along the horizontal centerline ($x_2 = 0$) for $Ra_H = 10^9, 10^{10}$ with respect to x^- : Convective Term (CTT), Thermal Diffusion (TD), Turbulent Heat Flux (THF) and Residual (R).	79
3.24	Time-averaged energy budgets along the vertical centerline ($x_1 = 0$) for $Ra_H = 10^9, 10^{10}$: Convective Term (CTT), Thermal Diffusion (TD), Turbulent Heat Flux (THF) and Residual (R).	80
3.25	Total kinetic energy scaled by $Ra_H^{1/4}$ as a function of Rayleigh number Ra_H	81
3.26	Turbulent kinetic energy and temperature variance contour plots at $Ra_H = 10^9, 10^{10}$	82
3.27	Budget profiles of the turbulent kinetic energy transport equations and temperature variance transport equation for $Ra_H = 10^9, 10^{10}$ along the horizontal line $x_2 = +0.3$	84
3.28	Three instantaneous snapshots of particle distribution at time $\tau = 5, 25, 125$ for $Ra_H = 10^9, 10^{10}$ and $d_p = 15[\mu\text{m}]$	88
3.29	Three instantaneous snapshots of particle distribution at time $\tau = 5, 25, 125$ for $Ra_H = 10^9, 10^{10}$ and $d_p = 25[\mu\text{m}]$	89
3.30	Three instantaneous snapshots of particle distribution at time $\tau = 5, 25, 125$ for $Ra_H = 10^9, 10^{10}$ and $d_p = 35[\mu\text{m}]$	90
3.31	Time evolution of the suspended particle number fraction for three sets of particles at $Ra_H = 10^9, 10^{10}$	92
3.32	Time evolution of the deposition velocity coefficient for three sets of particles at $Ra_H = 10^9, 10^{10}$	93
3.33	Particle probability density function at the bottom wall for the three sets of particles at three different times for $Ra_H = 10^9$	94
3.34	Particle probability density function at the bottom wall for the three sets of particles at three different times for $Ra_H = 10^{10}$	95
3.35	Time evolution of the cumulative fraction of particle deposited at the cold wall for three sets of particles at $Ra_H = 10^9, 10^{10}$	97
3.36	Schematic representation of the deposition mechanism due to lift. \mathbf{F}_l lift force, Θ_H hot wall, Θ_C cold wall, $\mathbf{u} - \mathbf{v}_p$ particle relative velocity, $\omega = \omega_3$ fluid vorticity.	98
3.37	Correlation dimension for three sets of particles at time $\tau = 125$ for $Ra_H = 10^9, 10^{10}$	98
4.1	Schematic representation of the cubical DHC with boundary conditions.	101

4.2	Horizontal and vertical velocity component iso-surfaces at $Ra_H = 10^4, 10^5, 10^6$	105
4.3	Iso-surface plots of spanwise velocity component $u_3 = -0.07, 0.1$ and temperature Θ for $Ra_H = 10^4, 10^5, 10^6$	106
4.4	Iso-surface plots of pressure p for $Ra_H = 10^4, 10^5, 10^6$	107
4.5	Vertical velocity component profiles at the mid-plane ($x_3 = 0$) for different heights $x_2 = -0.3, 0.0, +0.3$ with respect to the distance from the hot wall x^-	110
4.6	Temperature profiles at the mid-plane ($x_3 = 0$) for different heights $x_2 = -0.3, 0.0, +0.3$ with respect to the distance from the hot wall x^-	111
4.7	Temperature profiles along the vertical center-line.	112
4.8	Temperature stratification coefficient ς along the vertical center-line.	112
4.9	Iso-contours of the shear stress components along x_1 and x_2 , on the top and hot walls respectively, for $Ra_H = 10^4, 10^5, 10^6$	113
4.10	Local Nusselt number contours at the hot wall for $Ra_H = 10^4, 10^5, 10^6$	116
4.11	Instantaneous contour plots of the temperature field Θ at the midplane $x_3 = 0$ for $Ra_H = 10^9$ at each $\Delta\tau = 5$	117
4.12	Instantaneous contour plots of the temperature field Θ at the midplane $x_3 = 0$ for $Ra_H = 10^9$ at each $\Delta\tau = 5$	118
4.13	Time-averaged vertical component velocity profiles at different heights $x_2 = -0.3, 0.0, +0.3$ on the mid-plane $x_3 = 0$ with respect to x^-	120
4.14	Time-averaged temperature profiles at different heights $x_2 = -0.3, 0.0, +0.3$ on the mid-plane $x_3 = 0$ with respect to x^-	120
4.15	Time-averaged temperature profile along the vertical center-line.	121
4.16	Time-averaged temperature stratification coefficient along the vertical center-line.	121
4.17	Time-averaged Nusselt number distribution at the hot wall ($x_1 = -0.5$) for $Ra_H = 10^9$	122
4.18	Comparison of time-averaged Nusselt profile along the hot wall centerline $\langle Nu \rangle$, the 3D spanwise mean $\langle \overline{Nu} \rangle$ and the two dimensional distribution $\langle Nu \rangle^{2D}$ at $Ra_H = 10^9$	122
4.19	Time-averaged shear stress vertical and horizontal components (τ_{12} and τ_{21}) at the hot and top wall respectively at $Ra_H = 10^9$	123
4.20	Time-averaged velocity (limited to $x_3 \leq 0$), pressure and temperature fields at $Ra_H = 10^9$. Iso-surfaces levels in Fig.4.20(c) are $-0.01, 0.007$	124
4.21	Reynolds-stresses distribution limited to $x_3 \leq 0$. Levels for $\langle u'_1 u'_3 \rangle = \langle u'_2 u'_3 \rangle = \pm 2 \times 10^{-5}$	126
4.22	Turbulent heat flux in the half domain $x_3 < 0$. Levels for $\langle \Theta' u_3 \rangle = \pm 2 \times 10^{-5}$	127
4.23	Budget profiles of the second component of the time-averaged Navier-Stokes equations along the horizontal (top) and vertical centerline (bottom): Convective Term (CTM), Pressure Gradient (PG), Viscous Diffusion (VD), Reynolds Stresses (RS), Buoyancy Term (BT) and Residual (R).	130
4.24	Budget profiles of the first component of the time-averaged Navier-Stokes equations along the vertical centerline: Convective Term (CTM), Pressure Gradient (PG), Viscous Diffusion (VD), Reynolds Stresses (RS) and Residual (R).	131
4.25	Budget profiles of the time-averaged energy equation along the horizontal and vertical centerline: Convective Term (CTT), Thermal Diffusion (TD), Turbulent Heat Flux (THF) and Residual (R).	132
4.26	Iso-surfaces of turbulent kinetic energy and temperature variance for $x_3 < 0.0$ with respect to x^-	133

4.27	Turbulent kinetic energy k and temperature variance $\langle\Theta'\Theta'\rangle$ profiles in the midplane at $x_2 = +0.3$	134
4.28	Budget profiles of the turbulent kinetic energy and temperature variance production and dissipation terms for $Ra_H = 10^9$ along the horizontal line $x_2 = +0.3$ in the midplane $x_3 = 0$: P turbulent kinetic energy production due to mean shear stress, G production due to buoyancy effect, D turbulent kinetic energy dissipation rate; P_Θ temperature variance production due to mean temperature gradient, D_Θ temperature variance dissipation rate.	135
4.29	On the left: iso-contours of the instantaneous vertical component of the shear stress at the wall ($-0.5 \leq x_3 \leq 0$) and instantaneous local Nusselt number iso-contours ($0 \leq x_2 \leq 0.5$). On the right: instantaneous coherent structures identified by $\lambda_2 = -0.5$	138
4.30	Probability density function of the second and third invariants of the anisotropy tensor \mathbf{B} in regions characterized by three different levels of turbulent kinetic energy k	139
4.31	Time-history of the fluctuating part of the three velocity components sampled at the point of maximum turbulent kinetic energy $p^{k_{max}} == (-0.3469, 0.3601, -0.1113)$	140
4.32	Time-history of the temperature fluctuations sampled at the point of maximum turbulent kinetic energy $p^{k_{max}} == (-0.3469, 0.3601, -0.1113)$	141
4.33	Probability Density Functions (PDF) of velocity component fluctuation time-histories.	142
4.34	Probability Density Functions (PDF) of temperature fluctuation time-histories.	143
4.35	Auto-correlation functions of the fluctuations of the three components of velocity at $p^{k_{max}} == (-0.3469, 0.3601, -0.1113)$	144
4.36	Auto-correlation function of temperature fluctuations at $p^{k_{max}} == (-0.3469, 0.3601, -0.1113)$	145
4.37	Normalized Power Spectral Densities of the three components of velocity.	146
4.38	Normalized Power Spectral Densities of the temperature.	147
4.39	Time-series of the instantaneous production of turbulent kinetic energy Π_{22} and mean P_{22} and threshold values $\hat{\Pi}$ measured at the maximum of the turbulent kinetic energy production.	149
4.40	Probability Density Function (PDF) and Cumulative Distribution Function (CDF) of the time signal Π_{22} . Vertical lines refer to the mean value P_{22} and the threshold $\hat{\Pi}$	150
4.41	Top-left corner: Iso-surfaces of P_{22} . Bottom: Iso-contour map of P_{22} on the cross-plane containing P_K^{max} . In light-red two coherent structures identified by imposing $\lambda_2 = -0.5$	151
4.42	Time-history of horizontal and vertical velocity fluctuations measured at the maximum of the turbulent kinetic energy production.	152
4.43	Three instantaneous snapshots (side view) of particle distribution at time $\tau = 5, 25, 125$ for $Ra_H = 10^9$ and $d_p = 15, 25 [\mu\text{m}]$	155
4.44	Three instantaneous snapshots (side view) of particle distribution at time $\tau = 5, 25, 125$ for $Ra_H = 10^9$ and $d_p = 35 [\mu\text{m}]$	156
4.45	Comparison of two and three dimensional time histories of the airborne fraction of particles in the enclosure for $d_p = 15, 25, 35 [\mu\text{m}]$ at $Ra_H = 10^9$	157
4.46	PDF \mathcal{P} of particle distribution on the bottom wall surface at time $\tau = 5, 25, 125$ for $d_p = 15, 25 [\mu\text{m}]$ at $Ra_H = 10^9$	158
4.47	PDF \mathcal{P} of particle distribution on the bottom wall surface at time $\tau = 5, 25, 125$ for $d_p = 35 [\mu\text{m}]$ at $Ra_H = 10^9$	159
4.48	Time evolution of deposited particles at the cold wall for the three different particle sizes.	160
4.49	Time evolution of the recirculating particle fraction inside the control volume and correspondent fitting curves.	162

4.50	Correlation dimension of particle swarm as function of particle diameter at time $\tau = 200$ for $Ra_H = 10^9$	164
4.51	Schematic representation of the cavity partitions.	165
4.52	Time evolution of particle airborne fraction inside the cavity for $d_p = 15, 25, 35$ [μm]. Three-dimensional data and theoretical model.	167
4.53	Time evolution of mass flow rate \dot{n} for $d_p = 15, 25, 35$ [μm]. Three-dimensional data and theoretical model.	168
4.54	Time evolution of deposition velocity \mathcal{C}_d for $d_p = 15, 25, 35$ [μm]. Three-dimensional data and theoretical model.	169

Nomenclature

Roman symbols

A	matrix of coefficients	[–]
<i>a</i>	speed of sound	[ms^{-1}]
B	anisotropy tensor	[–]
b	vector of coefficients	[–]
<i>B</i>	linear boundary operator	[–]
c	vector of coefficients	[–]
<i>c</i>	specific heat capacity	[$J(kgK)^{-1}$]
<i>C_d</i>	deposition velocity	[ms^{-1}]
<i>C_p</i>	aerosol concentration	[$kg\ m^{-3}$]
<i>c_p</i>	specific heat capacity at constant pressure	[$J(kgK)^{-1}$]
<i>c_v</i>	specific heat capacity at constant volume	[$J(kgK)^{-1}$]
D	fractal dimension	[–]
<i>d</i>	dimensionless distance from the wall	[–]
<i>e</i>	dimensionless mean kinetic energy	[–]
<i>e_i</i>	internal energy per unit of mass [Jkg^{-1}], eigenvalues	[–]
f	force per unit of mass	[ms^{-2}]
<i>f</i>	forcing term, generic function	[–]
g	gravity acceleration	[ms^{-2}]

$\mathcal{H}_{\mathcal{B}}$	Hilbert subspace with embedded boundary conditions	[–]
\mathbf{h}_c	conductive heat flux	$[Wm^{-2}]$
H	height	$[m]$
\mathbf{I}	unit tensor	[–]
I	interpolating polynomial operator	[–]
II	second invariant	[–]
III	third invariant	[–]
j_p	aerosol density flux	$[kg\ s^{-1}m^{-2}]$
K	dimensionless kinetic energy of the mean flow	[–]
k	dimensionless turbulent kinetic energy	[–]
\hat{l}	molecule mean free path	$[m]$
L	length	$[m]$
l	Lagrangian characteristic polynomial, linear coordinate along half cavity perimeter	[–]
M	time-dependent second-order linear differential operator	[–]
m_p	particle mass	$[kg]$
Ma	Mach number	[–]
\mathcal{N}	number of particles contained in a sphere of radius r	[–]
N_a	number of particles entrained in the flow	[–]
N_d	number of particles	[–]
n_d	number of particles deposited at the bottom wall	[–]
N_l	order of local interpolation	[–]
n_t	number of particles deposited at the cold wall	[–]
n_v	number of particles in a control volume	[–]
Nu	local Nusselt number	[–]

\overline{Nu}	spatial averaged Nusselt number	[–]
\mathcal{P}	probability density function of deposited particles	[–]
p	pressure	[Pa]
p_R	reference pressure	[K]
Pr	Prandtl number	[–]
\dot{Q}	internal energy production/dissipation per unit of volume	[Wm ⁻³]
q	convergence rate	[–]
\overline{R}_t	dimensionless mean residence time	[–]
R	specific gas constant	[J(kgK) ⁻¹]
r	order of Runge-Kutta method	[–]
Ra	Rayleigh number	[–]
\mathbf{S}	symmetric part of velocity gradient tensor	[s ⁻¹]
S_0	Sutherland' s law constant	[K]
\mathcal{T}	dimensionless integral time scale	[–]
T	temperature [K], first order Chebyshev polynomial	[–]
T_0	Sutherland' s law reference temperature	[K]
T_R	reference temperature	[K]
t	time	[s]
\mathbf{u}	dimensionless fluid velocity	[–]
\mathbf{u}	fluid velocity vector	[ms ⁻¹]
\mathbf{V}	particle velocity	[ms ⁻¹]
\mathbf{v}	dimensionless particle velocity	[–]
V	aerosol phase volume	[m ³]
V_p	particle volume	[m ³]

v_t	dimensionless terminal velocity	[–]
$\tilde{\mathbf{x}}$	numerical solution	[–]
\mathbf{Y}_d	particle position	[m]
\mathbf{y}_d	dimensionless particle position	[–]

Greek symbols

α	isothermal compressibility	[Pa^{-1}]
β	isobaric thermal expansion coefficient	[K^{-1}]
χ_E	particle fraction which deposits following an exponential decay law	[–]
χ_G	particle fraction which deposits by gravity	[–]
χ_P	particle fraction with vertical linear distribution	[–]
δ_T	thermal boundary layer thickness	[m]
γ	ratio of specific heats	[–]
κ	thermal diffusivity coefficient	[m^2s^{-1}]
λ	fluid thermal conductivity	[$W(mK)^{-1}$]
μ	dynamic viscosity	[$kg(ms)^{-1}$]
μ_0	Sutherland' s law reference dynamic viscosity	[$kg(ms)^{-1}$]
ν	kinematic viscosity	[m^2s^{-2}]
$\boldsymbol{\omega}$	dimensionless fluid vorticity vector	[–]
Φ	energy dissipation per unit of volume due to internal friction	[Wm^{-3}]
ϕ	volume fraction	[–]
ψ	stream-function	[–]
$\hat{\Pi}$	dimensionless turbulent kinetic energy threshold	[–]
Π	dimensionless instantaneous turbulent kinetic energy production	[–]
ρ	fluid density	[kgm^{-3}]

σ	stress tensor	[Pa]
ς	dimensionless temperature stratification coefficient	[−]
τ	shear stress tensor	[Pa]
τ	dimensionless time	[−]
τ_s	dimensionless settling time	[−]
τ_w	shear stress at the wall	[−]
Θ	dimensionless fluid temperature	[−]

Subscripts

C	quantity referred to the cold wall
H	quantity referred to the hot wall
i	index
j	index
k	index
R	reference quantities, thermo-physical quantity measured at reference temperature and pressure)

Superscripts

★	scaling quantities
---	--------------------

Introduction

In present years the upcoming problem concerning energy production and environmental pollution have convinced engineers, physicists and researchers to focus their efforts on different aspects of nuclear energy production processes and nuclear power plant safety. In particular, the increased safety requirements of the new generation nuclear power plants have led to investigate the mechanisms of deposition of radioactive aerosol inside closed containment like the heat exchanger of the steam generator or inside larger containment buildings. In fact, in the case of a severe nuclear accident the high temperature and pressure in the primary side can induce the rupture of one or more pipes of the heat exchanger in the steam generator. The pressure drop between the water in the primary and the secondary sides causes the cooling water to be released in form of micro-size droplets inside the secondary loop that under normal conditions drives the steam at the turbines for the production of electric energy. The released aerosol water drops contain a small amount of metallic contaminants coming from the fuel rods of the radioactive core [GSDK04]. Moreover, in the steam generator, due to the presence of cold surfaces, where water steam condenses, and hot surfaces (the heat exchanger tube bundle for example), it has been shown that there is formation of recirculating natural turbulent convective currents that affect particle deposition. The resulting multiphysics two-phase flow presents an intrinsic complexity due to the thermal coupling between the carrier phase energy and the momentum, through the buoyancy force, that leads to different dynamics concerning the turbulence generation and dissipation with respect to the isothermal flows. Moreover, since the geometry is closed, there is always coexistence and interaction of laminar, transitional and turbulent structures that together with the bounding walls produce a highly inhomogeneous and anisotropic turbulent structures. On the other hand, the particle deposition and segregation phenomena besides gravitational deposition may be affected by other aspects, like turbophoresis (i.e. settling due to turbulence) and/or thermophoresis (i.e. settling induced by local temperature gradients in the carrier phase), that are difficult to be addressed by experimental measurements and deserve to be studied in detail.

For these reasons the tools of choice for studying thoroughly these complex dynamics are Direct Numerical Simulation (DNS) using pseudo-spectral collocation methods coupled

INTRODUCTION

with a Lagrangian Particle Tracking (LPT) code. The first numerical technique allows to avoid any type of turbulent modeling because it involves the direct solution of the transient, non-linear Navier-Stokes equations, providing very accurate results for all the flow scales avoiding numerical diffusion problems. The second methodology allows to include the most important forces acting on the particle surface and to describe each single particle trajectory in order to distinguish the phenomenology that links flow patterns with the different mechanisms of deposition, both in a qualitative and quantitative ways. The main outcome of this investigation is to provide a more rigorous understanding of particle settling in a turbulent flow cavity. The study underlines the most important factors that affect the particle sedimentation as well as the influence of particle inertia and turbulence. Furthermore it addresses the importance of each single force in the transport of particles towards and away from the walls. The present research will also provide an insight of the turbulence production mechanisms and will help in understanding the relation between coherent structures and turbulent heat transfer at the walls, and it will characterize the turbulence anisotropy inside the cavity. Last but not least it provides a numerical database useful in further possible works for modeling turbulence closure relations of LES or RANS models [JH96].

The actual problem involves very complex geometries (see Fig.1 for instance), turbulent natural convective flows that may reach high Rayleigh numbers (i.e. $Ra_H \approx 10^{12} \div 10^{15}$) and the range of particle diameters spans from 1 to 5 micro-meters. It is a matter of fact that the real problem cannot be studied without making drastic simplifications due to the undersized capabilities of high performance computing centers. Anyway, in order to be able to simulate some of the most important mechanisms of aerosol depletion in natural convective flows, in the present work the geometry has been modeled as a cube ($\approx 1[m]$ high), the maximum Rayleigh number presented in the three dimensional case is 10^9 ($Ra_H = 10^{10}$ in 2-D simulations) and the aerosol particles were characterized by a minimum diameter of $d_p = 15[\mu m]$ and a maximum one of $35[\mu m]$. Finally, the presented results might be of interest for other disciplines, besides nuclear engineering, such as electronic engineering concerning electronic device cooling process, or civil engineering concerning the transport of micro-size dust (the so called PM_{10}) inside buildings with natural convective flows generated by wall heaters or simply heat transfer due to solar irradiation or even in solar heating technologies.

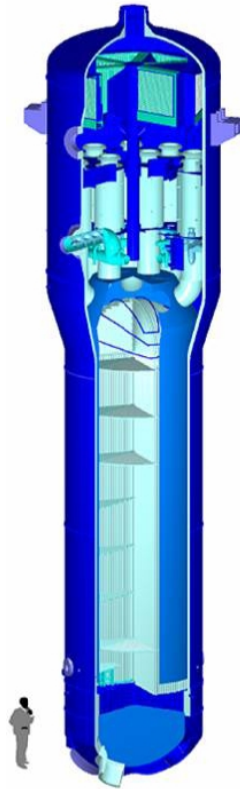


Fig. 1: *Steam generator cut view of the actual geometry and proportions.*

Literature review

Continuous phase

In thermal convective flows it is common to distinguish between forced and natural convective flows depending on the relative strength of the inertial forces against the buoyancy ones: if the inertia is larger than the buoyancy, the temperature can be approximated as a passive scalar which is convected by the unaffected fluid flow (which is treated as isothermal) and governed by the temperature transport equation. On the contrary, if the buoyant force is much larger than the inertial term, the temperature is strongly coupled with the momentum equation through the buoyancy term leading to a completely different flow with respect to the isothermal one. Furthermore, in heat transfer flows, depending on the driving temperature difference, the physical properties can be considered constant or variable with the temperature: in the first case the Navier-Stokes equations are simplified using the Boussinesq approximation; otherwise, for a non-Boussinesq flow, a set of equations that describe the variations of the physical properties, like the Sutherland's laws, and the equation of state have to be included. If inertia and buoyancy are of the same order of magnitude

then it is possible to speak about mixed convection. Typical examples of forced convective flows are those occurring inside liquid-liquid heat exchangers, or liquid cooling systems of electronic devices or also of internal combustion engines and atmospheric wind among the others. Typically forced flows do assume external devices or energy source that drive the motion like fans, pumps, etc. Examples of natural convective flows are those occurring in room heating, melting processes, reacting flows, cooling towers where the distribution of temperature causes the fluid motion. In the present work the attention will be focused on natural convective flows inside a cavity heated from aside. Unlike the cavities heated from below (also referred as Rayleigh-Bénard cavities) that have received great attentions in the last century, there is a lack of knowledge in the literature regarding the Differentially Heated Cavity (DHC) in the turbulent regime. Basically this is due to the fact that in the latter case the flow turns unstable for Rayleigh numbers that are four orders of magnitude larger than those that characterize the first bifurcation of Rayleigh-Bénard problems in three dimensional geometry requiring more powerful computational resources and longer computing time.

The 2-D benchmark configuration stated in [dVD83, dVDJ83] received many contributions in the years. Since the pioneering work conducted by de Vahl Davis [dVD83, dVDJ83], who provided the reference solutions for Prandtl number $Pr = 0.7$ (air) and values of Rayleigh number ranging from 10^3 up to 10^6 in the laminar case, using a second order central difference method with extrapolation to the limit and a streamfunction-vorticity formulation for the momentum equation, Le Quéré [Le 91] presented very accurate solutions for $10^6 \leq Ra \leq 10^8$ in the laminar regime employing pseudo-spectral Chebyshev collocation method in order to solve the Navier-Stokes and energy transport equations written in primitive variables under the Boussinesq approximation. Noteworthy findings are the detachment region at the horizontal adiabatic walls and the large zone of linear thermal stratification of the core. For increasingly higher Rayleigh numbers the flow eventually turns to unsteadiness. The onset of the first transition to periodicity and the physical description of the instability mechanism are still an open question. Paolucci and Chenoweth [PC89] supposed an internal wave breaking mechanism due to hydraulic jump instability of the impinging vertical jets. Their simulations were based on a low-Mach-number approximation of the governing equations and weakly non-linear analysis. On the other hand Ravi *et al.* [RHH94] showed that the theory of hydraulic jump does not explain the presence of the detachment region and moreover, in clear contrast, the low rate of viscous dissipation at the adiabatic horizontal walls. In [JH96], Kelvin-Helmholtz instability is addressed as the first mechanism which yields to periodicity. Moreover, Le Quéré and Benhia [LQB98] conducted DNS calculations around the transitional regime up to $Ra = 10^{10}$. Their main findings are the identification of the critical Rayleigh number Ra_c for the 2-D square cavity, $Ra_c^{2D} = 1.82 \times 10^8$ and the fact that the linear stratified core region becomes smaller

because of the enhanced turbulent mixing. Furthermore they provided first and second order time averaged statistics for velocity, temperature and *turbulent* kinetic energy and temperature variance and the respective dissipation fields. Large eddy simulation (LES) is presented in [PD01] for $Ra = 1.58 \times 10^9$. The filtered governing equations are discretized employing a second order central differencing finite-volume technique and second order Crank-Nicolson time integration. Two different subgrid scale models (SGSs) are compared with experimental results provided in [TK00a, TK00b] where the adiabatic horizontal walls are replaced with high conductive walls, on the other hand in the numerical simulations the experimental temperature profile has been imposed. Both the SGSs capture the global feature of the mean flow with improvements if the dynamic model is used, whereas the second order statistics show discrepancies with the experimental measurements. Several other works have investigated different aspect ratios ($A_r = 4$ in [RSH06, PQ01] and $A_r = 8$ in [XLQ02, Gel04]) and non-Boussinesq fluids [LMP92, SP95, SP97, MTN97]. It has been found that for aspect ratios larger than five the critical Rayleigh number (Ra_c) decreases. The same behavior for Ra_c appears to be valid for non-Boussinesq solutions in comparison with the Boussinesq ones, furthermore the typical center-symmetry property of the flow does not hold any longer. The treatment of heat transport in fluids with variable physical properties can be tackled basically with two approaches: the so-called Low-Mach number approximation and the fully compressible formulation of the governing equations. The first approach, used in [SP97, SP95, LMP92], discards the presence of acoustic phenomena that characterize the solution of compressible flows, with the net advantage of yielding less limitations on the mesh resolution and the integration time-step. This technique in fact makes use of a derived pressure in the momentum equations which is equal to the deviation from the average thermodynamic pressure and the hydrostatic component in the isothermal cavity (see [LMP92]). In addition the equation of state and the Sutherland's laws has to be included in the model.

From the experimental point of view only a few works have been published so far [TK00a, TK00b, MLHJ03], mainly for the three following reasons: first difficulties arising in the matching of perfectly adiabatic horizontal walls, secondly, the three-dimensional nature of the flow in the experimental facilities which also leads to earlier transition to unsteadiness, and last the effect of second order effects like variable physical properties and radiation, the latter reduces the core temperature stratification and enhances the flow at the horizontal walls diminishing the Ra_c [WXL06].

The problem of natural convection in a 3-D differentially heated cavity has been studied by only a few research groups. A first study of the three dimensional laminar flow structures has been published in [MdVD77]: the vector-potential formulation of the governing equations were discretized by means of a second-order finite difference method on a 15^3 grid. Subsequent studies concerning the laminar cubical benchmark case, ranging

from Rayleigh number 10^3 up to 10^7 and Prandtl number 0.71, include [FHKF91, TLB00, PSC03, WS04, BH06]. In Fusegi *et al.* [FHKF91] and Tric *et al.* [TLB00] the governing equations have been written in primitive variables, whereas a thermal lattice Boltzmann formulation has been used in [PSC03], vorticity-vector potential in [WS04] and finally vorticity-velocity in [BH06]. Moreover, it is worth to say that only Peng *et al.* have not expressed the energy equation into its temperature form but they have considered the internal energy as an unknown variable. The discretization techniques employed include finite differences [FHKF91, WS04, BH06] and pseudo-spectral method [TLB00] among the others. The largest grids contain 111^3 points [TLB00] and 120^3 [WS04]. The main result to be pinpointed is that the flow at the mid-plane presents a strong similarity with the two dimensional calculations and the 3-D effects are more influent at low Rayleigh number. Due to prohibitive computational costs for DNS only few studies have dealt with three-dimensional computations introducing spanwise homogeneous direction, reducing the overall cost of the computation but at the same time neglecting the influence of the spanwise walls. For instance, an extensive study of 2-D and 3-D turbulent quantities obtained by DNS, using spectro-consistent spatial discretization and adaptive central difference time splitting scheme, in a cavity with aspect ratio 4 and spanwise periodic boundary conditions, for $6.4 \times 10^8 \leq Ra \leq 10^{10}$ has been presented in [TSOPS07]. They concluded that the 2-D and 3-D mean fields are similar but the turbulent intensity and eddy ejection process are rather stronger in the two-dimensional case leading to turbulent activity also in the core region and higher levels of turbulent kinetic energy and dissipation rate. To the author's knowledge only [JH96, TLB00, ?, dXD03] reported accurate results of direct numerical simulations in a fully enclosed cubical domain at slightly sub-critical and critical Rayleigh numbers ($Ra_c \approx 3.3 \times 10^7$), in order to address the identification of the mechanism which yields the first transition to unsteadiness (due to Kelvin-Helmholtz instability of the turning and detaching impinging jets at the horizontal walls away from the lateral walls), and supercritical Rayleigh number for characterizing the time averaged flows and turbulence intensity ($Ra = 1.5 \times 10^9$). The time-averaged results reported in [?] are in good agreement with the experimental profiles of vertical velocity component and temperature along the horizontal line at half-height of the midplane, but on the other hand discrepancies occur for the temperature vertical profile, as well as temperature variance profiles probably due to the fact that in the experimental set up the lateral walls were not perfectly adiabatic and also radiative effects between the walls might influence the vertical thermal stratification leading also to a different temperature variance distribution.

From the experimental viewpoint there exist very few published works [MP96, MP97, LHB98, LHB99, MLHJ03, MJHL08, ?], with the Rayleigh number going from 10^4 up to 1.69×10^9 . Most of these works do not present adiabatic horizontal walls because of practical difficulties encountered in the realization of four contiguous perfectly insulated walls.

The group of Leong [LHB98, LHB99, MLHJ03, MJHL08] has then stated that the experimental setup should have perfect conducting horizontal walls, imposing in such a way a linear temperature profile between the two vertical active walls. Hence, any comparison between experimental data and numerical results obtained with adiabatic conditions are just qualitatively useful. Anyway, attempts to resolve numerically the same DHC using experimental temperature profiles did not yield much improvements particularly for turbulent flows [?], but good agreement was registered for laminar case [MJHL08]. Furthermore, another cause of discrepancies may be the change in the physical properties (in the experimental setup when increasing the Rayleigh number) and Leong *et al.* [LHB98] have suggested that simulations involving variable fluid properties would be more accurate. At the author's knowledge there are no publications of three dimensional computations of turbulent flows with physical variable properties in a differential heated cavity. Last but not least, as already mentioned above the heat transfer due to radiation could also affect the global energy balance.

Dispersed phase

In the last decades multiphase flows have attracted the attention of the scientific community because of their importance, their intrinsic complexity and the variety of the transportation mechanisms that characterizes every sort of fluid motion from the atmospheric wind transport of smog and pollutants, transport of sediment produced by rivers, to industrial applications like boilers, electrostatic precipitators, direct injection of fuel in combustion engines, or even medical and biological flows as aerosol in the pharynx or vascular blood flows for instance.

There exist two important approaches for describing the dynamics of multiphase flows, namely Eulerian and Lagrangian. The first one implies the solution of a set of partial differential equations that describe the conservation of mass, momentum and energy of the different phases thought as a continuum, i.e. a unique mixture. One advantage is that the numerical methods used for solving a single-phase fluid flow are directly applicable. On the other hand the source terms that govern the exchange of mass, momentum and energy between the different phases need to be modeled from experiments or theoretical investigations and could lead to complicated models in the case of turbulent reacting flows. This approach is very useful when the fraction of volume or mass between the phases is very large. The Lagrangian approach, on the other hand, implies the integration of a system of ordinary differential equations that describes the equation of motion and energy conservation for each particle. This technique is appropriate for dispersed flows with low volume fraction and implies the use of experimental or theoretical formulas for the forces that act on the particle surface if the pointwise approximation is used. Re-

cently, simulations that involve the use of moving mesh that fully resolve the dynamics of the fluid flow around the particle surface without any modeling have been performed but due to the high computational costs the number of particles is not sufficient to be statistically meaningful for capturing the mechanisms of deposition, segregation and other issues. Depending on the volume fraction, and the tendency of particles to form clusters, the most simple Lagrangian formulation that consider only the effect of the fluid forces on the particle surfaces (one-way coupling) may not be sufficient and the two-way coupling or the four-way coupling are needed. The first one, in fact, considers also the influence of the particle motion on the fluid, whereas the last one introduces also particle-particle collisions. Over the last decade, research on particle-laden turbulent flows has shown that particle concentration may be highly non-uniform. This behavior is commonly indicated by the term *preferred segregation* and more widely it indicates the mechanisms of particles to organize themselves into clusters located in particular regions under the action of the carrier turbulent flow [SE91, FKE94, RE01, PMRS05]. It has been found [EF94] that preferential segregation in homogeneous turbulence occurs in regions of low vorticity and high strain. Moreover, there is experimental evidence and numerical studies have confirmed [PMB92, UO96, MA02] that particle-laden turbulent flows bounded by solid walls are characterized by net fluxes of particles directed toward the walls with peaks of extremely high concentration regions close to the surfaces. All these effects may have critical consequences in industrial applications and it is the result of the interaction of particle inertia with turbulent coherent structures. If the transport of heavy particles has been object of numerous experimental and numerical studies (for a review [Elg94, GB98, Sol05]), there is a deep lack of knowledge in segregation and sedimentation processes inside closed cavities. In [TCLY06, TCL⁺08] stereo imaging and signal processing techniques are used to reconstruct and visualize the pathlines of macroscopic neutrally buoyant particles in three-dimensional lid driven cavity flow at low Reynolds number ($Re = 470$). Spiral motions from the mid plane to the sidewalls and back are depicted and particle fluid structure selectivity is also encountered. In [ABH08] proper orthogonal decomposition (POD) of the relevant fluid flow modes based on LES computation is coupled with a Lagrangian particle tracker that uses standard Runge-Kutta method for the integration of the particle equation of motion (PEM). The main advantage of the proposed method is to decrease drastically the computational costs in comparison with LES and DNS but no quantitative information is provided. Oresta et al. [OLVS06] have conducted three-dimensional DNS in the Rayleigh-Bénard configuration at $Ra = 2 \times 10^8$ in a slender cylinder coupled with Lagrangian particle tracking. The set of governing equations for the continuous phase written in cylindrical coordinates are discretized using a finite difference approach in space and a third-order Runge-Kutta (RK) time integration technique; the PEM is integrated as well using third-order RK method. The advection-diffusion model proposed for the dis-

persed phase describing the time evolution of particle concentration along the vertical axis for three different particle diameters is in excellent agreement with the DNS data. At the author knowledge the only published study on numerical and experimental visualization of neutrally buoyant particles inside a differential heated cavity is [YKHK96] using high Prandtl number fluid. One of their finding is that particles in both cases remain suspended in closed recirculating spiraling loops at the hot wall. They state that the effect of the spanwise velocity is important for the particle trapping. Finally, concerning the nuclear engineering and safety, experimental campaigns have depicted aerosol particles settling rate greater than expected under quiescent conditions, settling rate weakly dependent on particle inertia and finally particles preferred deposition on horizontal surfaces when the carrier fluid velocity is increased (see [CHGR⁺03, GSDK04]).

Thesis outline

The present work is structured into four chapters that are the core of the work accomplished by the author and follow the present introductive pages:

Chapter 1 is devoted to the description of the physical and mathematical models of the governing equations for natural convective flows and dispersed aerosol particles of a two-phase flow problem.

Chapter 2 describes the numerical methods employed for the discretization in space and time of the partial differential equations (PDEs) that govern the motion of a homogeneous, Newtonian, incompressible fluid under the Boussinesq assumptions, as well as space interpolation and time integration needed to solve the ordinary differential equations (ODEs) of the particle equation of motion.

Chapter 3 presents several topics concerning the two dimensional calculations. First of all different solutions of the benchmark configurations are compared with published data. First and second order statistics are shown at very high Rayleigh numbers for unsteady and chaotic regimes. Furthermore mean momentum and energy budgets are presented and discussed. Finally the deposition mechanisms of three different size of particle swarms are investigated in detail.

Chapter 4 addresses the three dimensional problem of the benchmark configuration at three different Rayleigh numbers. The discussion of first and second order moments is carried out for a regime that is weakly chaotic. The same analysis performed for the two dimensional cavity is also reported for the three dimensional case. The mechanisms of production and dissipation are described both for the turbulent kinetic

INTRODUCTION

energy and temperature variance. Moreover a first incursion into the coherent turbulent structures and the anisotropy map are included. In the last part the settling of micro-size particles is studied as for the two dimensional case and a theoretical model is proposed.

In the last and conclusive chapter a summary of the work performed is provided together with the most important findings and the possible future developments and the improvements.

Chapter 1

Theoretical backgrounds

The present chapter is devoted to the description of the physical and mathematical models of the governing equations for natural convective flows and dispersed aerosol particles of a two-phase flow problem.

The first part deals with the equations which govern the motion of continuous, incompressible, viscous Newtonian, homogeneous fluid. The Oberbeck-Boussinesq approximation is employed in order to simplify the problem and its validity range is discussed in detail. The identification of dimensional groups which allows a more general approach to the problem is also discussed and the resulting system of dimensionless equations is given.

The second part concerns the description of the motion of heavy solid aerosol particles in a Lagrangian fashion. On the base of the relative importance of the forcing terms a simplified equation of motion is derived which takes into account the influence of local quantities and temperature gradients. Finally, the corresponding version of dimensionless equations is also provided.

1.1 Continuous phase

1.1.1 Governing equations

In continuum mechanics the motion of fluids is described by the conservation laws of mass, momentum and energy. Together with the constitutive laws for the stress tensor and the conductive heat flux they describe entirely the behavior of any kind of fluid which undergoes motion. In the present case the fluid is considered Newtonian, i.e. the stress tensor $\boldsymbol{\sigma}$ is a linear function of the rate of strain tensor $\mathbf{S} := 1/2[\nabla\mathbf{u} + (\nabla\mathbf{u})^T]$ (the superscript T indicates the transpose) as expressed by Eq.(1.1)

$$\boldsymbol{\sigma} = -p\mathbf{I} + \boldsymbol{\tau} = -p\mathbf{I} + 2\mu \left(\mathbf{S} - \frac{1}{3}\text{tr}(\mathbf{S})\mathbf{I} \right) \quad (1.1)$$

where p is the pressure, $\boldsymbol{\tau}$ is the viscous stress tensor, the proportionality constant μ is the dynamic viscosity, $\mathbf{u} = \{u_i\}_{i=1}^d$ ($d = 1, \dots, 3$) is the velocity and \mathbf{I} is the unit tensor, while the constitutive law for the specific conductive heat flux \mathbf{h}_c is described by the Fourier law

$$\mathbf{h}_c := -\lambda \nabla T \quad (1.2)$$

where λ is the thermal conductivity and T is the local temperature. The governing equations written in vector notation result¹:

- mass conservation

$$\frac{\partial \rho}{\partial t} + \nabla \cdot (\rho \mathbf{u}) = 0 \quad (1.3)$$

- momentum conservation

$$\rho \left(\frac{\partial \mathbf{u}}{\partial t} + \mathbf{u} \cdot \nabla \mathbf{u} \right) = -\nabla p + \nabla \cdot \boldsymbol{\tau} + \rho \mathbf{f} \quad (1.4)$$

- energy conservation

$$\rho \left(\frac{\partial e_i}{\partial t} + \mathbf{u} \cdot \nabla e_i \right) = \nabla \cdot (\lambda \nabla T) - p \nabla \cdot \mathbf{u} + \Phi + \dot{Q} \quad (1.5)$$

where the fluid density is indicated by ρ , the specific internal energy by e_i , whereas the term \mathbf{f} refers to external body forces per unit of mass, Φ is the power per unit of volume dissipated by the internal viscous stresses (negligible for air and water under normal situations) and can be written as follows

$$\Phi = \text{tr}(\boldsymbol{\tau} \nabla \mathbf{u}) \quad (1.6)$$

and \dot{Q} corresponds to the volumetric internal generated/dissipated power due to chemical or nuclear reactions for instance. Note that in Eq.(1.5) the work done by the non-equilibrium component of pressure is neglected [Bat67] meaning that the change of pressure of the moving fluid goes through successive thermodynamic quasi-equilibrium states.

It is useful to considering the fluid as an ideal diatomic gas with equation of state

$$\frac{p}{\rho} = RT \quad (1.7)$$

where R is the specific gas constant, with constant $\gamma = 1.4$ ratio of specific heat at constant pressure c_p and constant volume c_v . It follows that all the fluid thermodynamic

¹The angular momentum is conserved thanks to the property of the symmetric stress tensor $\boldsymbol{\sigma} = \boldsymbol{\sigma}^T$.

and physical properties depend only on two state variables, for instance (T, p) , and they have to be determined from experimental measurements or from the kinetic theory of gases. In the following a possible formulation of thermodynamic and physical properties is given:

$$\beta = -\frac{1}{\rho} \left(\frac{\partial \rho}{\partial T} \right)_p = \frac{1}{T} \quad (1.8)$$

$$\mu = \mu_0 \frac{T_0 + S_0}{T + S_0} \left(\frac{T}{T_0} \right)^{3/2} \quad (1.9)$$

$$\lambda = \frac{15}{4} R \mu \left(\frac{4}{15} \frac{\gamma}{\gamma - 1} + \frac{1}{3} \right) \quad (1.10)$$

where in Eq.(1.9) accordingly to the Sutherland's law μ_0 , T_0 and S_0 are the reference dynamic viscosity, the temperature and the Sutherland's constant which depend on the gas.

Providing appropriate initial and boundary conditions, the system of coupled equations Eq.(1.3)-(1.5) is difficult to solve. In order to simplify the complexity of the problem formulated above, it is useful to introduce the Oberbeck-Boussinesq (OB) approximation [Obe79, Bou03]. The latter is based on the following assumptions:

1. The density ρ is assumed constant in the mass, momentum and energy equations except when it causes buoyant forces;
2. All other fluid properties, like μ and λ , are assumed constant;
3. The viscous dissipation is assumed negligible, i.e. $\Phi \approx 0$.

The first hypothesis allows to rewrite Eq.(1.3) as

$$\nabla \cdot \mathbf{u} = 0 \quad (1.11)$$

which imposes the velocity field to be divergence-free and corresponds to the conservation of mass written for an incompressible fluid. Another important consequence is that acoustic phenomena are in this way discarded from the problem and that $\gamma = c_p/c_v = 1$ and consequently $c_p = c_v = c$ (see also [Pan84]).

In the present study the forcing term in Eq.(1.4) represents only the buoyancy force and is simply given by

$$\mathbf{f} = \mathbf{g} \quad (1.12)$$

where \mathbf{g} is the gravitational acceleration. The further simplification relies on first-order Taylor expansion of the density as a function of temperature only, in other words

$$\rho \approx \rho_R + \left[\left(\frac{\partial \rho}{\partial T} \right)_p \right]_{T_R} (T - T_R) = \rho_R [1 - \beta_R (T - T_R)] \quad (1.13)$$

where with the subscript “ R ” are indicated the quantity measured at the reference temperature T_R . Finally, using Eq.(1.13) in the right hand side (*rhs*), applying the second and third Oberbeck-Boussinesq hypotheses to Eqs.(1.3)-(1.5), neglecting every source/dissipation of internal heat \dot{Q} , and recalling that the internal energy of a substance can be expressed by $e_i = c_R T$, the simplified set of governing equations reads

$$\nabla \cdot \mathbf{u} = 0 \quad (1.14)$$

$$\frac{\partial \mathbf{u}}{\partial t} + \mathbf{u} \cdot \nabla \mathbf{u} = -\frac{1}{\rho_R} \nabla p + \nu_R \Delta \mathbf{u} + [1 - \beta_R(T - T_R)] \mathbf{g} \quad (1.15)$$

$$\frac{\partial T}{\partial t} + \mathbf{u} \cdot \nabla T = \kappa_R \Delta T \quad (1.16)$$

where $\nu_R = \mu_R/\rho_R$ is the kinematic viscosity at the reference temperature and $\kappa_R = \lambda_R/(\rho_R c_R)$ refers to the thermal diffusivity of the fluid at the reference temperature.

1.1.2 Validity of the Oberbeck-Boussinesq approximation

The simplified problem expressed by Eq.(1.14)-(1.16) is attractive for several applications characterized by natural or mixed convection but it has been shown to be a good approximation only under certain restrictions [GG76, Nie04, NS06]. In fact a measure of the error introduced by the hypothesis of constant density in the continuity equation can be estimated considering the ratio between the material derivative of the density and the divergence of the velocity field

$$\frac{\frac{D\rho}{Dt}}{-\rho \nabla \cdot \mathbf{u}} \quad (1.17)$$

that for an incompressible flow should be sufficiently small ($D/Dt = \partial/\partial t + (\mathbf{u} \cdot \nabla)$ being the material derivative).

Consider the exact differential of density for a perfect gas is

$$d\rho = \left(\frac{\partial \rho}{\partial T} \right)_p dT + \left(\frac{\partial \rho}{\partial p} \right)_T dp = \rho(-\beta dT + \alpha dp) \quad (1.18)$$

where α is the isothermal compressibility coefficient. Furthermore the density rate of change of a particle fluid volume with velocity \mathbf{u} is straightforward

$$\frac{d\rho}{dt} = \frac{\partial \rho}{\partial t} + \mathbf{u} \cdot \nabla \rho = \frac{D\rho}{Dt}, \quad (1.19)$$

by substitution of Eq.(1.18) in Eq.(1.19) and using the definition of speed of sound $a^2 = \gamma/(\rho \alpha)$ [Pan84] it is possible to obtain the following equation for the rate of change of density

$$\frac{D\rho}{Dt} = \rho \left(-\beta \frac{DT}{Dt} + \frac{\gamma}{\rho a^2} \frac{Dp}{Dt} \right). \quad (1.20)$$

1.1. CONTINUOUS PHASE

The second term in the *r.h.s.* can be dropped since in natural convection the acoustic phenomena are negligible, meaning that the convective velocity is small in comparison with the speed of sound (the Mach number $Ma = |\mathbf{u}|/a < 0.3$) and the pressure evolves slowly in comparison with the acoustic pressure waves. Finally, introducing appropriate scales for length L_R , velocity U_R and temperature difference ΔT , Eq.(1.17) leads to

$$\frac{\frac{Dp}{Dt}}{-\rho \nabla \cdot \mathbf{u}} = \frac{\beta \frac{DT}{Dt}}{\nabla \cdot \mathbf{u}} \approx \frac{\beta \Delta T (U_r/L_R)}{U_R/L_R} \approx \beta \Delta T. \quad (1.21)$$

The last result implies that OB approximation is valid only if the product $\beta \Delta T$ is sufficiently small. Gray *et* Giorgini [GG76] derived Eqs.(1.14)-(1.16) with a different approach, based on the linearization, in terms of T and p , of all the thermo-physical properties appearing in Eqs.(1.3)-(1.5) and simplifying terms with second order of magnitude (another different approach based on an asymptotic analysis can be found in [Boi00]). From their work the validity of the OB approximation is subject to thirteen constraints listed below

$$\left\{ \begin{array}{ll} \epsilon_1 = \beta_R \Delta T \leq \epsilon & \epsilon_2 = \alpha_R \rho_R g L_R \leq \epsilon \\ \epsilon_3 = c_R \Delta T \leq \epsilon & \epsilon_4 = d_R \rho_R g L_R \leq \epsilon \\ \epsilon_5 = r_R \Delta T \leq \epsilon & \epsilon_6 = s_R \rho_R g L_R \leq \epsilon \\ \epsilon_7 = m_R \Delta T \leq \epsilon & \epsilon_8 = n_R \rho_R g L_R \leq \epsilon \\ \epsilon_9 = e_R \Delta T \leq \epsilon & \epsilon_{10} = f_R \rho_R g L_R \leq \epsilon \\ & \epsilon_{11} = \frac{\beta_R g L_R}{c_{pR}} \leq \epsilon \\ & \epsilon_{11} \left(\frac{Pr_R}{Ra_H} \right)^{1/2} \leq \epsilon (Pr_R Ra_H)^{-1/2} \\ \epsilon_{11} \frac{T_R}{\Delta T} \leq \epsilon & \end{array} \right.$$

where c_R , d_R , e_R , f_R , m_R , n_R , r_R , s_R are fluid property coefficients defined in Gray *et al.* and the parameters Pr_R and Ra_H are the Prandtl and Rayleigh numbers expressed respectively by

$$Pr_R = \frac{\nu_R}{\kappa_R} \quad (1.22)$$

$$Ra_H = \frac{g \beta_R \Delta T L_R^3}{\nu_R \kappa_R}. \quad (1.23)$$

Now, consider the case of air at standard conditions for temperature and pressure (STP) $T_R = 293.15$ [K] and $P_R = 101.325$ [kPa] (accordingly to the National Institute of Standards and Technology, see App.(1.A)), then the three most restrictive limitations² are

$$\epsilon_1 = \beta_R \Delta T \leq 0.1 \quad (1.24)$$

² $\epsilon = 0.1$ is supposed to give a satisfactory description of the flow employing the OB formulation.

$$\epsilon_2 = \rho_R \alpha_R g L_R \leq 0.1 \quad (1.25)$$

$$\epsilon_{12} = \frac{\alpha_R g L_R}{c_{pR}} \left(\frac{T_R}{\Delta T} \right) \leq 0.1 \quad (1.26)$$

which lead to the validity range reported in Fig.(1.1). In experimental setups [Nie04,

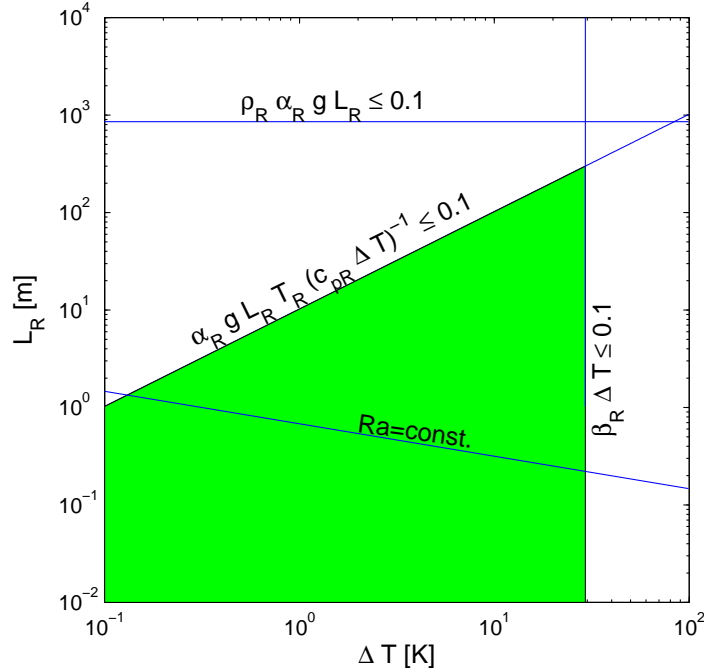


Fig. 1.1: *Region of validity of the OB approximation in air* ($T_R = 293.15$ [K], $P_R = 101.325$ [kPa]) *App.(1.A)*.

NS06], on the basis of a comparison to the Boussinesq problem at onset, the condition in Eq.(1.24) can be relaxed up to $\beta_R \Delta T < 0.2$. Here, it is important to stress that the validity range obtained depends basically on the thermo-physical properties of the real fluid at the reference conditions which in general are evaluated at the mean temperature $T_R = \frac{T_H + T_C}{2}$, where T_H and T_C are respectively the temperature at the hot and cold surfaces, whereas P_R can be taken equal to the initial pressure when the fluid is at rest. A recent study [PL07], based on thermodynamic second law analysis and accurate numerical simulations, has pinpointed that the energy equation written in its enthalpic form (i.e. retaining the work done by internal viscous forces and the term due to pressure work) allows to fulfil both the OB approximation applied only to mass and momentum equations, while satisfying at

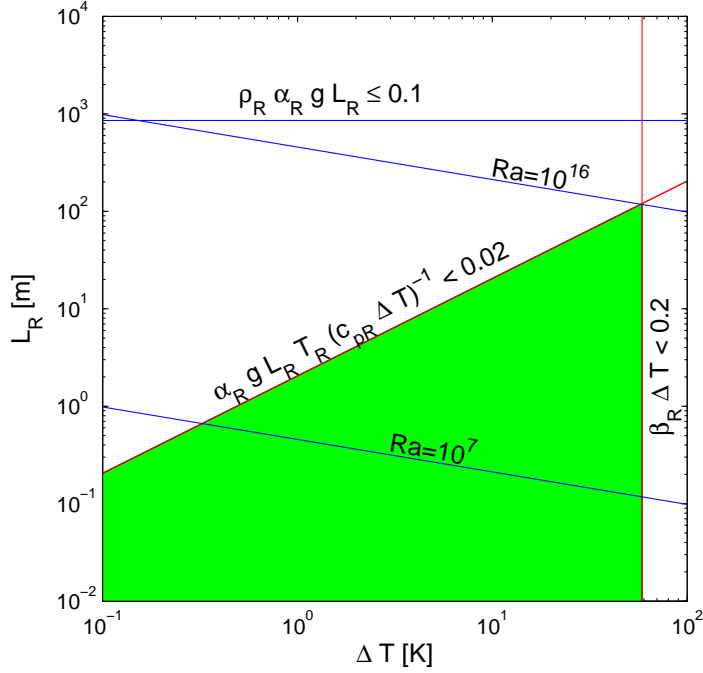


Fig. 1.2: *Extended region of validity of the OB approximation in air* ($T_R = 293.15$ [K], $P_R = 101.325$ [kPa]) *App.(1.A)*.

the same time the second law of thermodynamics which is otherwise discarded in the usual form. Their main result is that a more strict condition should apply to ϵ_{12} , i.e.

$$\frac{\alpha_R g L_R}{c_{pR}} \left(\frac{T_R}{\Delta T} \right) \leq 0.02 \quad (1.27)$$

Finally, the range of validity of the BO approximation with the new modified conditions is shown in Fig.1.2. In the next chapters the following condition has been chosen $\epsilon_1 \leq 0.15$, $\epsilon_2 \leq 0.1$ and $\epsilon_{12} < 0.02$.

1.1.3 Dimensionless Boussinesq equations

In order to reduce the number of thermo-physical parameters involved in the momentum and energy transport it is useful to write Eqs.(1.14)-(1.16) in dimensionless form introducing appropriate dimensional groups and governing dimensionless parameters. This will also provide a simpler way to understand and generalize the results obtained for a particular case in the space of the dimensionless parameters which represent, for similarity, infinite realizations with different fluids characterized by the same dimensionless parameters.

The proper way to define the dimensional groups is to consider the steady two dimensional

boundary layer (BL) problem. In fact it is well known that bounded natural convective flows always present boundary layers at the walls where, depending on the Prandtl number Pr_R , the viscous forces balance buoyancy or inertia. A schema of the two dimensional BL is shown in Fig.(1.3) where (x_1, x_2) are the position coordinates normal and parallel to the vertical wall respectively, H is the height of the wall, δ_T is the thermal BL thickness defined as the *loci* where the fluid temperature is $T = 0.99T_R$. From a scaling analysis (see also [Bej84, Le 87]) of the energy equation it follows that

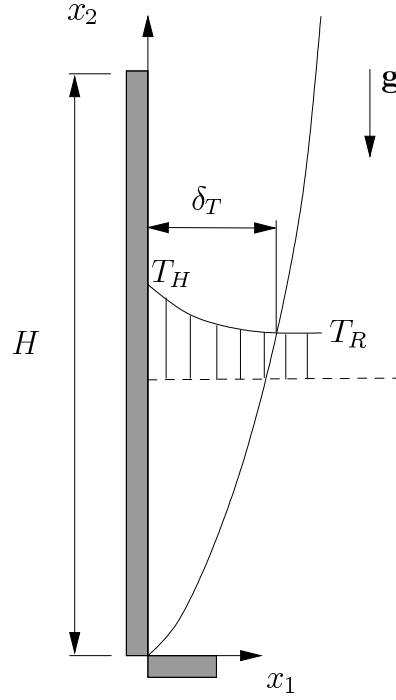


Fig. 1.3: *Temperature boundary layer along a heated vertical wall.*

$$\underbrace{u_1 \frac{\Delta T}{\delta_T}, u_2 \frac{\Delta T}{H}}_{\text{convection}} \sim \underbrace{\kappa_R \frac{\Delta T}{\delta_T^2}}_{\text{conduction}}, \quad (1.28)$$

on the other hand the same reasoning applied to the conservation of mass yields to

$$\frac{u_1}{\delta_T} \sim \frac{u_2}{H}. \quad (1.29)$$

Substituting Eq.(1.29) into Eq.(1.28) and rearranging

$$u_2 \sim \kappa_R \frac{H}{\delta_T^2}, \quad (1.30)$$

where δ_T is still unknown. Looking at the importance of each term appearing in the vertical component of the momentum equation, where the inter-play between inertia, viscous force

(friction) and buoyancy is stressed hereafter,

$$\underbrace{u_1 \frac{u_2}{\delta_T}}_{\text{inertia}}, \underbrace{u_2 \frac{u_2}{H}}_{\text{friction}}; \nu_R \frac{u_2}{\delta_T^2} \sim \underbrace{g\beta_R \Delta T}_{\text{buoyancy}}. \quad (1.31)$$

then dividing all the terms by the buoyancy scale $g\beta_R \Delta T$ and using Eq.(1.30), it follows that

$$\frac{1}{Pr_R Ra_H} \left(\frac{H}{\delta_T} \right)^4; \frac{1}{Ra_H} \left(\frac{H}{\delta_T} \right)^4 \sim 1. \quad (1.32)$$

The latter clearly shows the dependency on the Prandtl number of the relative magnitude of viscous and inertia forces compared to the buoyancy. In the case of high- Pr_R fluids ($Pr_R \gg 1$) inertia has a secondary role respect the friction which can be supposed in equilibrium with the buoyancy. Therefore the thermal boundary layer thickness is straightforward given by

$$\delta_T \sim \frac{H}{Ra_H^{1/4}} \quad (1.33)$$

and the appropriate vertical velocity scaling becomes

$$u_2 \sim \frac{\kappa_R}{H} Ra_H^{1/2}. \quad (1.34)$$

On the other hand for low- Pr_R fluids ($Pr_R \ll 1$) the inertial terms are in equilibrium with the buoyancy, hence it immediately follows

$$\delta_T \sim \frac{H}{(Pr_R Ra_H)^{1/4}} \quad (1.35)$$

and

$$u_2 \sim \frac{\kappa_R}{H} \sqrt{(Pr_R Ra_H)}. \quad (1.36)$$

The reader should note that for $Pr_R \approx 1$ both inertia and friction are of the same order of importance and cannot be neglected in the simplified equations of the boundary layer. Furthermore both scalings tend to one equation respectively, i.e.

$$\delta_T \sim \frac{H}{Ra_H^{1/4}} \quad (1.37)$$

$$u_2 \sim \frac{\kappa}{H} \sqrt{Ra_H}. \quad (1.38)$$

In order to write in dimensionless form Eqs.(1.14)-(1.16) it is useful to introduce five dimensional groups for length (L^\star), time (t^\star), velocity (U^\star), pressure (P^\star) and temperature

T^\star , as follows

$$\begin{aligned} l^\star &= H, \quad t^\star = \frac{H^2}{\kappa_R \sqrt{Ra_H}}, \quad u^\star = \frac{\kappa_R}{H} \sqrt{Ra_H} \\ p^\star &= \rho_R \left(\frac{\kappa_R}{H} \right)^2 Ra_H, \quad T^\star = \Delta T. \end{aligned} \quad (1.39)$$

The dimensionless form of the Boussinesq equations Eqs.(1.14)-(1.16) obtained by scaling each variable by its dimensional group is given by

$$\hat{\nabla} \cdot \hat{\mathbf{u}} = 0 \quad (1.40)$$

$$\frac{\partial \hat{\mathbf{u}}}{\partial \tau} + \hat{\mathbf{u}} \cdot \hat{\nabla} \hat{\mathbf{u}} = -\hat{\nabla} \hat{p} + \frac{Pr}{\sqrt{Ra_H}} \hat{\Delta} \hat{\mathbf{u}} - Pr \Theta \frac{\mathbf{g}}{|\mathbf{g}|} \quad (1.41)$$

$$\frac{\partial \Theta}{\partial \tau} + \hat{\mathbf{u}} \cdot \hat{\nabla} \Theta = \frac{1}{\sqrt{Ra_H}} \hat{\Delta} \Theta \quad (1.42)$$

where $\hat{\mathbf{u}}$ is the dimensionless velocity, τ is the dimensionless time, $\hat{p} = (p - \rho_R \mathbf{g} \cdot \mathbf{x})/p^\star$ the dimensionless pressure, $\Theta = (T - T_R)/T^\star$ the dimensionless temperature.

1.2 Aerosol dispersed solid phase

The term *aerosol* defines the solution of dispersed solid or liquid particles suspended in gaseous fluid, commonly air. It refers to the two-phase system simultaneously. The size of the dispersed phase ranges from few nano-meters to 100 micro-meters and usually the volume fraction ϕ , defined as the ratio of the total volume occupied by N_p solid particles, each one of volume V_p , and the total volume of the aerosol phase V , is very low

$$\phi = \frac{1}{V} \sum_{i=1}^{N_p} V_{p,i} \leq \epsilon. \quad (1.43)$$

with ϵ typically of the order of 10^{-6} (see also [[CST98, Cro05]]). In this range of application, the two phases can be treated with a simple one-way coupling approach, i.e. mass, momentum and energy of the dispersed phase are affected by the carrying fluid but the changes in the hydrodynamics of the latter, due to the suspended particles, are negligible as well as particle-particle collisions. Thus, a Lagrangian description of each particle is feasible and required to describe in detail the mechanisms of segregation, dispersion and deposition.

1.2.1 Governing equations

The conservation laws for a rigid, solid, point-wise, spherical particle of diameter d_p (App.(1.B)) written in vector notation are [MR83, CST98]:

- mass conservation

$$m_p = \rho_p V_p = \text{const.} \quad (1.44)$$

- momentum conservation³

$$\begin{aligned} m_p \frac{d\mathbf{v}}{dt} = & m_p \mathbf{g} + 3\pi\mu d_p (1 + Re_p^{0.687})(\mathbf{u} - \mathbf{v}) + (\nabla \cdot \boldsymbol{\sigma}) V_p + \\ & + C_L \rho [(\mathbf{u} - \mathbf{v}) \times \boldsymbol{\omega}] V_p - 3\pi\mu d_p \nu C_T \frac{\nabla T}{T} + \frac{\rho}{2} \left(\frac{D\mathbf{u}}{Dt} - \frac{d\mathbf{v}}{dt} \right) V_p + \\ & + \frac{3}{2} d_p^2 \sqrt{\pi\rho\mu} \left[\int_0^t \left(\frac{d\mathbf{u}}{d\vartheta} - \frac{d\mathbf{v}}{d\vartheta} \right) \frac{d\vartheta}{\sqrt{t-\vartheta}} + \frac{(\mathbf{u} - \mathbf{v})_0}{\sqrt{t}} \right] \end{aligned} \quad (1.45)$$

- energy equation⁴

$$m_p c_d \frac{dT_p}{dt} = Nu_d \pi \lambda_d d_p (T - T_p) \quad (1.46)$$

where m_p is the particle mass, ρ_p the particle material density, V_p the particle volume, \mathbf{v} the particle velocity, Re_p is the particle Reynolds number, $\boldsymbol{\omega} = \nabla \times \mathbf{u}$ the fluid vorticity, C_L and C_T are constants for the lift and thermophoretic forces calculated as in [GLS05] and [Cro05] respectively, c_d the particle material specific heat, Nu_p is the Nusselt number and finally λ_p is the particle material conductivity. Here below are given the relations for Re_p and Nu_p [CST98]

$$Re_p = \frac{\rho(1 - \beta\Delta T\Theta)d_p |\mathbf{u} - \mathbf{v}|}{\mu} \quad (1.47)$$

$$Nu_p = 2 + 0.6 Re_p^{1/2} Pr^{1/3} \quad (1.48)$$

All the fluid variables are measured at the particle position \mathbf{y}_p and in last term of the *r.h.s.* of Eq.(1.45)

$$\frac{d\mathbf{u}}{d\vartheta} = \left(\frac{\partial \mathbf{u}}{\partial \vartheta} + \mathbf{v} \cdot \nabla \mathbf{u} \right)_{\mathbf{y}_p}. \quad (1.49)$$

The *r.h.s.* of Eq.(1.45) describes, by order of appearance, the effect of gravity, steady-state Stokesian drag, stress gradient (also called pressure gradient), lift, thermophoresis, added

³Second order Faxen's terms are negligible since the size of the particle is of the order of few microns.

⁴The particle internal thermal resistance is here neglected since the Biot number $Bi = Nu_p \lambda / \lambda_p \ll 1$ (see also [CST98, CC99]).

mass (or virtual mass) and Basset historical force, which apart from the introduction of lift and thermophoretic forces corresponds to the Basset-Boussinesq-Oseen equation. These equations are valid in the limit of small particles $d_p/\eta_K \ll 1$ (η_K being the Kolmogorov length scale), but at the same time the Knudsen number should be large $Kn_p = 2l/d_p \gg 1$ (l being the mean free path of the fluid molecules) for considering the fluid phase as a continuum around the particle. Both conditions ensure that the flow around the particle is Stokesian, i.e. $Re_p \ll 1$, or at least does not exceed $O(1)$. The significant forces for heavy particles ($\rho_d/\rho \gg 1$ as occurs in aerosol two-phase flows) are drag and gravity [ET92], since the others are order of magnitude smaller. In the present work also lift and thermophoretic forces are retained in the model because of the strong velocity and temperature gradients in the boundary layers close to the vertical heated and cooled walls. Moreover the energy equation Eq.(1.46) is discarded in view of the non-reactive nature of the aerosol phase here considered and the relatively low temperatures involved. Finally, the particle trajectory is obtained by time integration of the kinematic definition of linear velocity

$$\mathbf{v} = \frac{d\mathbf{y}_p}{dt}. \quad (1.50)$$

where \mathbf{y}_p indicates the particle position in a Eulerian frame of reference.

1.2.2 Dimensionless particle equation of motion

For the same reasons described in Sec.1.1.3 it is important to identify appropriate dimensional groups in order to correctly describe the motion of the aerosol solid phase. The most important parameter for particle dynamics is the relaxation time $\tau_d = \frac{\rho_d d_p^2}{18\mu}$ which appears in the momentum equation Eq.(1.45) if divided by the mass of the particle m_p . This quantity is a characteristic measure of the response time of the particle dynamic system spent to adapt its velocity given a sudden change in the fluid velocity. It is straightforward to think that the sudden changes of the fluid velocity in a turbulent flow is directly induced by the velocity field fluctuations. Therefore the time scale associated with the characteristic time of turbulence or eddy turn-over time is commonly employed, for instance the Kolmogorov time scale $\tau_\eta = \sqrt{\nu/\langle\varepsilon\rangle}$ in homogeneous and isotropic turbulence ($\langle\varepsilon\rangle$ being the rate of dissipation of the turbulent kinetic energy), or wall quantities in the case of fully developed turbulent forced flows in channels/pipes $\tau^+ = \nu/u_\tau^2$ ($u_\tau = \sqrt{\tau_w/\rho}$ and τ_w is the shear stress at the wall). At the author's knowledge there is no appropriate scaling describing natural convective flows inside enclosures where a vast range of regimes (i.e. laminar, transitional and fully chaotic) occurs at the same time at different locations in the domain, moreover the presence of the temperature as active scalar increases the complexity in identifying the correct scaling since further mechanisms of production and dissipation of turbulence are introduced [Bol62]. For these reasons the same dimensional scaling quantities given

in Eq.(1.39) are used, which allow to adimensionalise the simplified particle equation of motion (PEM):

$$\begin{aligned} \frac{d\hat{\mathbf{v}}}{d\tau} = & \frac{Pr}{\beta\Delta T} \left[1 - \frac{\rho}{\rho_d}(1 - \beta\Delta T\Theta) \right] \frac{\mathbf{g}}{|\mathbf{g}|} + \frac{(1 + Re_p^{0.687})}{St} (\hat{\mathbf{u}} - \hat{\mathbf{v}}) + \\ & + C_L \frac{\rho}{\rho_d} (1 - \beta\Delta T\Theta) [(\hat{\mathbf{u}} - \hat{\mathbf{v}}) \times \hat{\boldsymbol{\omega}}] - C_T \frac{Pr}{St\sqrt{Ra_H}} \frac{\beta\Delta T}{[1 - (\beta\Delta T\Theta)^2]} \nabla\Theta \end{aligned} \quad (1.51)$$

$$\hat{\mathbf{v}} = \frac{d\hat{\mathbf{y}}_p}{d\tau} \quad (1.52)$$

where $St = \tau_d/t^\star$ is the so called Stokes number. The values of the Stokes number used in the present work are of the order $O(10^{-3})$, the particle Reynolds number is always less than unity. It should be noticed that the actual aerosol phase would be characterized by Stokes numbers $St \approx 10^{-4}$ or less, which are very time demanding from the computational point of view using the Lagrangian approach. Only the buoyancy term coming from the pressure gradient has been retained, and the local fluid density at the particle position is approximated using the dimensionless version of Eq.(1.13) in order to take into account the non-homogeneity of the temperature field which modifies the fluid density, and as a consequence the drag, the buoyancy and the lift forces, leading to sensible changes in particle segregation and deposition patterns in the case of long time integration.

Appendix

1.A Thermo-physical properties of air

Property	Symbol	Value
Gas constant	R	287 $[J(kg\ K)^{-1}]$
Density	ρ	1.2043 $[kg\ m^{-3}]$
Dynamic viscosity	μ	1.81×10^{-5} $[kg(m\ s)^{-1}]$
Thermal conductivity	λ	2.56×10^{-2} $[W(m\ K)^{-1}]$
Specific isobaric heat capacity	c_p	1003.55 $[J(kg\ K)^{-1}]$
Sepecific isochore heat capacity	c_v	716.55 $[J(kg\ K)^{-1}]$
Isobaric thermal expansion coefficient	β	3.41×10^{-3} $[K^{-1}]$
Isothermal compressibility	α	9.87×10^{-6} $[Pa^{-1}]$

Tab. 1.1: *Thermo-physical properties of air at $T_R = 293.15$ [K], $p_R = 101.325$ [kPa].*

1.B Aerosol particle aerodynamic diameter

There exists several definitions of equivalent diameter d_p for arbitrary shaped small-size aerosol particles [Dav79]. Among the others, the most important one is the so called aerodynamic diameter which is described as the diameter of a sphere with density $\rho_w = 1000 [kg m^{-3}]$ and having the same terminal velocity \hat{v}_p of the particle in a controlled quiescent environment. The settling velocity can be obtained simplifying a slightly modified version of Eq.(1.45) supposing only drag and gravity forces in equilibrium [Cro05]:

$$\hat{v}_p = \frac{\rho_p d_e^2 g C_c(d_e)}{18\mu\chi} \quad (1.53)$$

where $C_c(d_e)$ and χ are respectively the Cunningham and the dynamic shape factors: the first takes into account for the effect of slip-velocity between the particle and the surrounding fluid in the limit of $Kn_e = 2l/d_e \gg 1$, whereas the second for the irregular shape is given in Tab.(1.2). The diameter d_e introduced in Eq.(1.53) is the equivalent diameter of a sphere with the same volume of the particle. Concluding the aerodynamic diameter d_p is given by

$$d_p = d_e \sqrt{\frac{\rho_p C_c(d_e)}{\rho_w \chi C_c(d_p)}} \approx d_e \sqrt{\frac{\rho_p}{\rho_w \chi}} \quad (1.54)$$

where the approximated formula is valid if $Kn_p \approx Kn_e \gg 1$.

Shape	Aspect ratio	Dynamic factor χ
Sphere	1	1
Oblate spheroid	2	1.04
	4	1.18
	10	1.49
Prolate spheroid	2	1.05
	4	1.20
	10	1.58
Cube	1	1.08
Cylinder (orientation averaged motion)	$L/d = 2$	1.09
	$L/d = 5$	1.23
	$L/d = 10$	1.43

Tab. 1.2: *Dynamic shape factors χ from [Dav79, Cro05].*

Chapter 2

Numerical methods

The aim of the present chapter is to describe the numerical methods employed for the discretization in space and time of the dimensionless partial differential equations (PDEs) set Sec.1.1.3 as well as space interpolation and time integration needed to solve the ordinary differential equations (ODEs) given in Sec.1.2.2 and their solution.

As before the chapter organization is twofold: the first part describes the Chebyshev pseudo-spectral method on which relies the spatial discretization of the continuous phase problem, followed by the continuous-in-time solver for the solenoidal velocity field and auxiliary pressure field. Finally the time discretization technique is discussed. The second part discusses the choice of local Lagrangian polynomial interpolation for measuring the fluid quantities at the particle position and the time scheme implemented for the integration of the PEM.

2.1 Methodology for the continuous phase

2.1.1 Space discretization

Pseudospectral Chebyshev collocation method

The choice of high-order spectral methods is justified by the fact that they are characterized by very low numerical diffusion and dispersion in comparison with other low-order methods [CHQZ88]. Furthermore, it can be shown ([GO77]) that, for a infinite differentiable function, spectral methods guarantee exponential convergence, while low-order method present algebraic convergence only; as a consequence spectral methods provide the same accuracy of lower order methods with much less degrees of freedom, hence gaining in computing time if optimized numerical techniques, like FFT [DL82], are employed. The theory presented in the following refers to [GO77, CHQZ88, Pey02].

Consider the general one dimensional linear mixed initial-boundary value model problem in the domain $\bar{\Omega} = \Omega \cup \partial\Omega = [-1, +1]$ expressed by

$$\frac{\partial u(x, \tau)}{\partial \tau} = M(x, \tau)u(x, \tau) + f(x, \tau), \quad x \in \bar{\Omega}, \quad \tau \in [\tau_0, \vartheta] \quad (2.1)$$

$$u(x, \tau_0) = u^0(x), \quad x \in \bar{\Omega} \quad (2.2)$$

$$B(x)u(x, \tau) = \bar{u}(x, \tau), \quad x \in \partial\Omega, \quad t \in [\tau_0, \vartheta] \quad (2.3)$$

where $M(x, \tau)$ is the time-dependent second-order linear differential operator which includes spatial derivatives of the solution $u(x, \tau)$, $f(x, \tau)$ is the forcing term, $B(x)$ represents the linear (time-independent) boundary operator on the domain frontier with boundary condition $\bar{u}(x, \tau)$ and initial condition $u^0(x)$. Furthermore, at each time τ the unknown function $u(x, \tau)$ is an element of a Hilbert subspace $\mathcal{H}_{\mathcal{B}}$ characterized by the inner product (u, v) for all $u, v \in \mathcal{H}_{\mathcal{B}}$ and norm $\|u\| = (u, u)^{1/2}$ for which Eq.(2.3) is satisfied. In this framework it is possible to search for an approximated solution u_N in the finite dimension space $\mathcal{H}_{\mathcal{B}}^N$ that is solution of a minimization problem: at each instant $\tau \in [\tau_0, \vartheta]$ the approximated solution must satisfies

$$(R_N, \psi_j)_w = \int_{\Omega} \left[\frac{\partial u_N(x, \tau)}{\partial \tau} - M(x, \tau)u_N(x, \tau) + f(x, \tau) \right] \psi_j w dx = 0, \quad j = 0, \dots, N \quad (2.4)$$

where R_N is the residual of the PDE due to the choice of a finite subspace of dimension N in $\mathcal{H}_{\mathcal{B}}$, ψ_j are the test functions and w is the weighting function associated with the basis functions of the subspace $\mathcal{H}_{\mathcal{B}}^N$. In the case of the collocation method the test functions are translated Dirac delta functions $\psi_j = \delta(x - x_j)$ that leads the residual to be zero at the nodal or collocation points x_j , i.e. for $j = 0, \dots, N$ and $t \in [t_0, \vartheta]$. Therefore Eq.(2.4) becomes

$$\frac{\partial u_N(x_j, \tau)}{\partial \tau} - M(x_j, \tau)u_N(x_j, \tau) - f(x_j, \tau) = 0. \quad (2.5)$$

In the present work the family of basis (or trial) functions which are orthogonal with respect to the inner product in $\mathcal{H}_{\mathcal{B}}^N$ are the Chebyshev polynomials of first kind

$$T_k(x) = \cos k\Theta, \quad k = 0, \dots, N \quad (2.6)$$

where $\Theta = \cos^{-1} x$ and $-1 \leq x \leq 1$. With the aid of the trigonometric identity $\cos(k+1)\Theta + \cos(k-1)\Theta = 2\cos\Theta \cos k\Theta$ it is possible to define the recurrence relation

$$T_{k+1}(x) = 2xT_k(x) - T_{k-1}(x) \quad (2.7)$$

together with $T_0(x) = 1$ and $T_1(x) = x$ (for more details about Chebyshev polynomial properties [MH03]). The representation of the first six Chebyshev polynomials is given

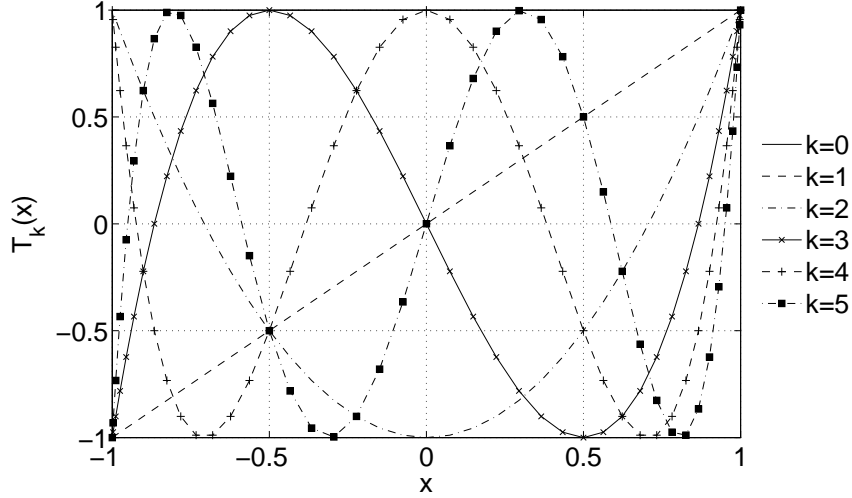


Fig. 2.1: First Chebyshev polynomials $T_k(x)$ of first kind for $k = 0, \dots, 5$.

in Fig.2.1. The Chebyshev truncated expansion of the solution $u_N(x, t)$ is defined as the following series

$$u_N(x, t) := \sum_{k=0}^N b_k(\tau) T_k(x) \quad (2.8)$$

where $b_k(\tau)$ are the expansion coefficients, also called spectral coefficients. After substitution of Eq.(2.8) in Eq.(2.4) and rearranging, the resulting semi-discrete system of ODEs written for the spectral coefficients reads

$$\sum_{k=0}^N \dot{b}_k(\tau) T_k(x_j) - \sum_{k=0}^N b_k(\tau) M(x_j, \tau) T_k(x_j) = f(\tau, x_j) \quad j = 0, \dots, N \quad (2.9)$$

where $\dot{b}_k = db_k(\tau)/d\tau$. Hence, if backward Euler scheme is used to discretize the time-derivative with step-size $\Delta\tau$ then Eq.(2.9) can be recasted in

$$\sum_{k=0}^N \left[\frac{\eta_0}{\Delta\tau} - M(x_j, \tau) \right] T_k(x_j, \tau) b_k(\tau) = f'(x_j, \tau) \quad j = 0, \dots, N \quad (2.10)$$

where η_0 is a constant introduced by the time-splitting method employed as well as the source term $f'(x_j, \tau)$ now takes into account of both the forcing $f(x_j, \tau)$ and the explicit part coming from the time discretization. Finally the algebraic linear system can be solved for the spectral coefficients inverting the matrix $\underline{A} = \{a_{jk}\}_{j,k=0}^N = \{[\eta_0/\Delta\tau - M(x_j, \tau)] T_k(x_j, \tau)\}_{j,k=0}^N$. The solution in the physical space is straightforwardly obtained using Eq.(2.8).

The collocation method allows also to formulate the problem using directly the nodal values

$u_N(x_j, \tau)$ as unknowns instead of the spectral coefficients. This is possible if the approximation of the spatial derivatives of order $p = 1, 2$ contained in $M(x_j, t)$ are evaluated at the nodal points with the aid of interpolation polynomials. Introducing the Gauss-Lobatto-Chebyshev (GLC) nodes x_j defined as the roots of the following polynomial equation of order $N + 1$

$$(1 - x^2) \frac{dT_N(x)}{dx} = 0 \quad -1 \leq x \leq 1, \quad (2.11)$$

it is possible to describe the variable $u_N(x, \tau)$ in a Lagrangian fashion using the polynomials $h_i(x)$ defined by

$$h_i(x) = \frac{(-1)^{i+1}(1 - x^2) \frac{dT_N(x)}{dx}}{\bar{c}_i N^2 (x - x_i)} \quad (2.12)$$

which satisfy the condition $h_i(x_j) = \delta_{ij}$. Thus, the variable u is approximated by the truncated Lagrangian series of order N given by

$$u_N(x, \tau) = \sum_{k=0}^N \hat{u}_k(\tau) h_k(x). \quad (2.13)$$

Further on, if $u_N^{(p)}(x_j, \tau)$ is the p -th spatial derivative of the approximated function at the nodal point x_j , then is possible to write

$$u_N^{(p)}(x_j, \tau) = \sum_{k=0}^N d_{k,j}^{(p)} u_N(x_k, \tau) \quad j = 0, \dots, N \quad (2.14)$$

where

$$d_{k,j}^{(p)} = \left(\frac{d^p h_k(x)}{dx^p} \right)_{x_j} = \left\{ \frac{d^p}{dx^p} \left[\frac{(-1)^{k+1}(1 - x^2) \frac{dT_k(x)}{dx}}{\bar{c}_k N^2 (x - x_k)} \right] \right\}_{x_j} \quad (2.15)$$

with

$$\bar{c}_k = \begin{cases} 2 & \text{if } k = 0 \\ 1 & \text{if } 1 \leq k \leq N - 1 \\ 2 & \text{if } k = N \end{cases} \quad (2.16)$$

For advection-diffusion transport equations, the coefficients $d_{k,j}^{(p)}$ are also used to compute explicitly non-linear advective terms which are eventually added to the source $f'(x_j, t)$. If Dirichlet boundary conditions are applied the resulting algebraic linear system reads

$$\underbrace{\begin{bmatrix} 1 & 0 & & \dots & 0 \\ & \underline{A}_{(N-1)(N-1)} & & & \\ & & & & \\ 0 & \dots & & 0 & 1 \end{bmatrix}}_{\underline{A}'} \underbrace{\begin{bmatrix} u_N(x_0) \\ u_N(x_1) \\ \vdots \\ u_N(x_{N-1}) \\ u_N(x_N) \end{bmatrix}}_{\underline{u}} = \underbrace{\begin{bmatrix} \bar{u}(x_0, \tau) \\ f'(x_1, \tau) \\ \vdots \\ f'(x_{N-1}, \tau) \\ \bar{u}(x_N, \tau) \end{bmatrix}}_{\underline{f}''} \quad \tau \in [\tau_0, \vartheta]. \quad (2.17)$$

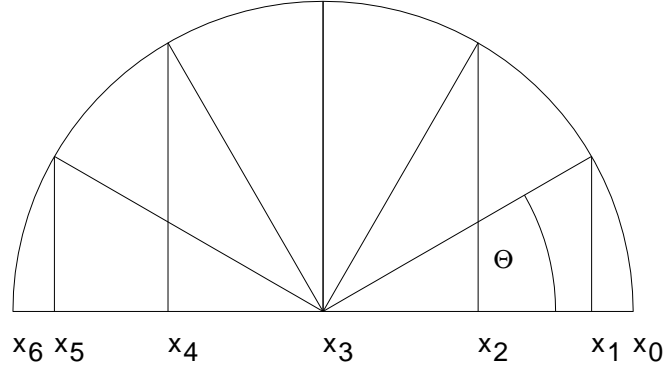


Fig. 2.2: Example of Gauss-Lobatto-Chebyshev point distribution ($N = 6$) on the unit semi-circle.

where $\underline{A}_{(N-1)(N-1)} = \{a_{jk}\}_{j,k=1}^{N-1}$ contains linear combinations of $d_{jk}^{(p)}$ and is generally full. The formulae for the first- and second-order collocation derivative coefficients read as follows (see [Pey02]):

- First-order derivative

$$d_{jk}^{(1)} = \frac{\bar{c}_j}{\bar{c}_k} \frac{(-1)^{j+k}}{(x_j - x_k)}, \quad 0 \leq j, k \leq N, \quad j \neq k \quad (2.18)$$

$$d_{jj}^{(1)} = -\frac{x_j}{2(1-x_j^2)}, \quad 1 \leq j \leq N-1 \quad (2.19)$$

$$d_{00}^{(1)} = -d_{NN}^{(1)} = \frac{2N^2 + 1}{6}, \quad (2.20)$$

- Second-order derivative

$$d_{jk}^{(2)} = \frac{(-1)^{j+k}}{\bar{c}_k} \frac{x_j^2 + x_j x_k - 2}{(1-x_j^2)(x_j - x_k)^2}, \quad 1 \leq j \leq N-1, \quad (2.21)$$

$$0 \leq k \leq N, \quad j \neq k$$

$$d_{jj}^{(2)} = -\frac{(N^2 - 1)(1 - x_j^2) + 3}{3(1 - x_j^2)^2}, \quad 1 \leq j \leq N-1 \quad (2.22)$$

$$d_{0j}^{(2)} = \frac{2}{3} \frac{(-1)^j (2N^2 + 1)(1 - x_j) - 6}{\bar{c}_j (1 - x_j)^2}, \quad 1 \leq j \leq N \quad (2.23)$$

$$d_{Nj}^{(2)} = \frac{2}{3} \frac{(-1)^{N+j} (2N^2 + 1)(1 + x_j) - 6}{\bar{c}_j (1 + x_j)^2}, \quad 0 \leq j \leq N-1 \quad (2.24)$$

$$d_{00}^{(2)} = d_{NN}^{(2)} = \frac{N^4 - 1}{15}. \quad (2.25)$$

Finally, it may be useful to recall that

$$d_{jk}^{(2)} = \sum_{i=0}^N d_{ji}^{(1)} d_{ik}^{(1)}. \quad (2.26)$$

Extension to multidimensional domain

The extension of the previous results to multidimensional domain $\bar{\Omega} = [-1, 1]^d$ with $d = 2, 3$ is possible thanks to the introduction of the tensor product operator which allows significant simplifications in the application of the linear operator to the vector $\mathbf{u} = \{u_i\}_{i=1}^d$ [DFM02]. First of all the GLC collocation points of a tensorized domain are given by

$$\mathcal{G}_{(N_1 \dots N_d)} := \bigotimes_{i=1}^d \mathcal{G}_{N_i}(x_i) \quad (2.27)$$

where $\mathcal{G}_{N_i}(x_i)$ are the i -th one-dimensional set of N_i ordered GLC points in the x_i space direction. The approximated vector function $\mathbf{u}_{(N_1 \dots N_d)}(\mathbf{x}, \tau)$ is expressed by the tensor product of the independent one dimensional basis functions $T_i(x_i)$

$$\mathbf{u}_{(N_1 \dots N_d)}(\mathbf{x}, \tau) = \sum_{i_1=0}^{N_1} \cdots \sum_{i_d=0}^{N_d} \mathbf{b}_{(i_1 \dots i_d)}(\tau) T_1(x_1) \cdots T_d(x_d) \quad (2.28)$$

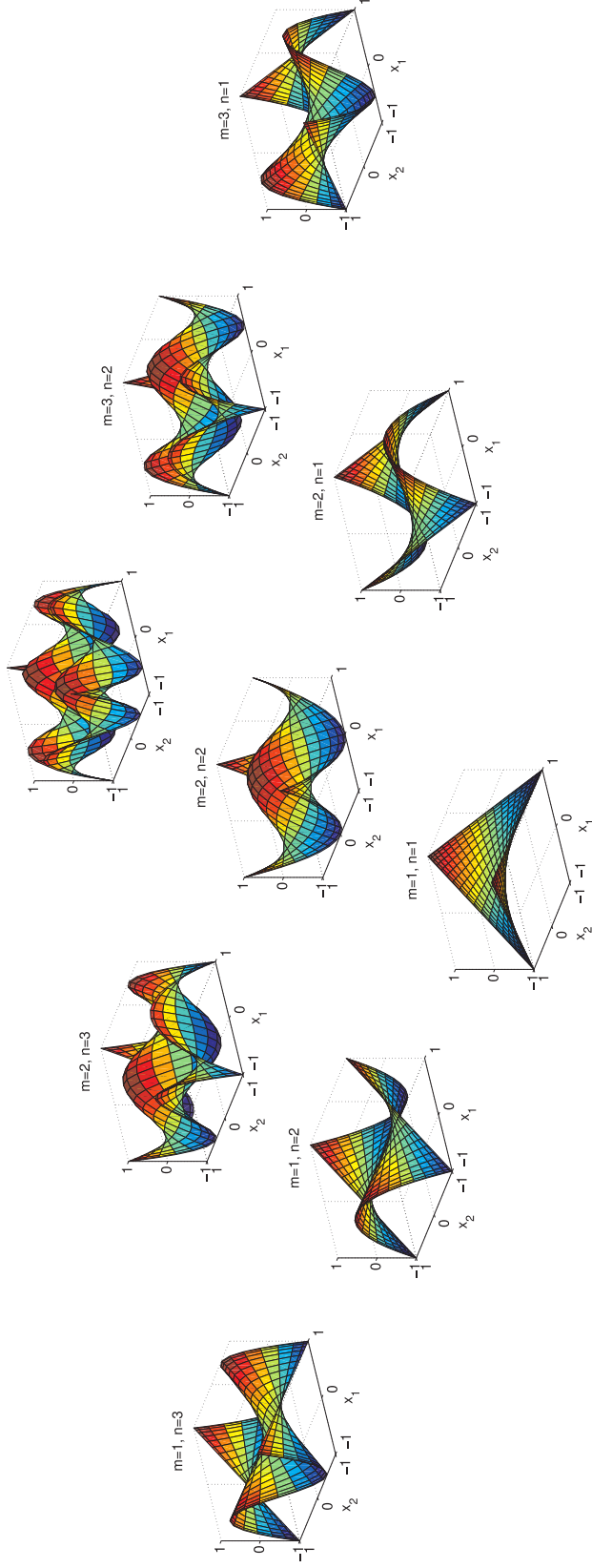
where the spectral coefficients $\mathbf{b}_{(i_1 \dots i_d)}(\tau) = \mathbf{u}(x_1^{i_1}, \dots, x_d^{i_d}, \tau)$. Examples of tensorized Chebyshev basis functions for the case $d = 2$ and $N_1 = N_2 = 3$ are given in Fig.(2.3). Finally, also the derivation operators are described by tensorized products of the operators $\tilde{D}_i^{(p)}$ as shown below for $d = 2$

$$\underline{D}_{x_1}^{(p)} = \underline{I}_{x_2} \otimes \tilde{D}_{x_1}^{(p)}, \quad \underline{D}_{x_2}^{(p)} = \tilde{D}_{x_2}^{(p)} \otimes \underline{I}_{x_1}, \quad (2.29)$$

and for $d = 3$

$$\underline{D}_{x_1}^{(p)} = \underline{I}_{x_3} \otimes \underline{I}_{x_2} \otimes \tilde{D}_{x_1}^{(p)}, \quad \underline{D}_{x_2}^{(p)} = \underline{I}_{x_3} \otimes \tilde{D}_{x_2}^{(p)} \otimes \underline{I}_{x_1}, \quad \underline{D}_{x_3}^{(p)} = \tilde{D}_{x_3}^{(p)} \otimes \underline{I}_{x_2} \otimes \underline{I}_{x_1}. \quad (2.30)$$

Fig. 2.3: Two-dimensional representation of Chebyshev basis functions $N_1 = N_2 = 3$ for $n = 1, \dots, 3$ and $m = 1, \dots, 3$.



2.1.2 Solver

In order to solve Eqs.(1.29)-(1.28) the projection-diffusion technique described in [BKL94, LL00, LPLD06] is used. Briefly, this method relies on a non-splitting consistent formulation of the Boussinesq equations which provides an efficient and accurate way of computing the instantaneous pressure field, thus ensuring the incompressibility of the velocity field without the introduction of spurious modes.

Let \mathbf{u}^* be the intermediate acceleration vector defined by the relation

$$\mathbf{u}^* := \frac{\partial \mathbf{u}}{\partial \tau} - \frac{Pr}{\sqrt{Ra}} \Delta \mathbf{u}, \quad (2.31)$$

then the first step consists of solving the following problem projecting the intermediate field in a divergence-free space:

- projection step

$$\mathbf{u}^* + \nabla p = -\mathbf{u} \cdot \nabla \mathbf{u} + Pr \Theta \frac{\mathbf{g}}{|\mathbf{g}|} \quad \text{in } \Omega' \quad (2.32)$$

$$\nabla \cdot \mathbf{u}^* = 0 \quad \text{in } \bar{\Omega} \quad (2.33)$$

$$\mathbf{u}^* \cdot \mathbf{n} = \left(\frac{\partial \mathbf{u}}{\partial \tau} - \frac{Pr}{\sqrt{Ra}} \Delta \mathbf{u} \right) \cdot \mathbf{n} \quad \text{on } \partial \Omega \quad (2.34)$$

where \mathbf{n} is the unit vector normal to $\partial \Omega$ and $\Omega' := \{\Omega_i\}_{i=1}^d$ are subdomains without the boundaries in the x_i direction.

The second and last step simply employs the definition of \mathbf{u}^* and together with the velocity boundary conditions results

- diffusion step

$$\frac{\partial \mathbf{u}}{\partial \tau} - \Delta \mathbf{u} = \mathbf{u}^* \quad \text{in } \Omega \quad (2.35)$$

$$\mathbf{u} = \mathbf{0} \quad \text{in } \partial \Omega. \quad (2.36)$$

Applying the spatial discretization described in the previous section the problem Eq.(2.32)-(2.34) is written as

$$\underline{\mathbf{u}}^* + \underline{\mathbf{G}} p = \underline{\mathbf{f}}'(\underline{\mathbf{u}}) \quad \text{in } \bar{\Omega} \quad (2.37)$$

$$\underline{\mathbf{D}} \cdot \underline{\mathbf{u}}^* = 0 \quad \text{in } \bar{\Omega} \quad (2.38)$$

where the matrices $\underline{\mathbf{D}}$ and $\underline{\mathbf{G}}$ are the divergence and the restricted gradient collocation operators respectively, whereas $\underline{\mathbf{f}}'(\underline{\mathbf{u}})$ represents the modified *r.h.s.* of Eq.(2.32) containing

also the terms coming from the discretized boundary conditions Eq.(2.34). Finally, the substitution of Eq.(2.37) in Eq.(2.38) leads to the pseudo-Poisson operator for the pressure

$$\underline{\mathbf{D}} \cdot \underline{\mathbf{G}}' p = \underline{\mathbf{D}} \cdot \underline{\mathbf{f}}'(\underline{\mathbf{u}}) \quad (2.39)$$

providing that

$$\frac{\partial p}{\partial \mathbf{n}} = \left[[\underline{\mathbf{G}} \times (\underline{\mathbf{G}} \times \underline{\mathbf{u}})] + Pr \underline{\Theta} \frac{\underline{\mathbf{g}}}{|\underline{\mathbf{g}}|} \right] \cdot \mathbf{n}. \quad (2.40)$$

Because the velocity field \mathbf{u} is unknown the above problem is not yet solvable and an extrapolation technique is needed.

The fully discretized problem

The discretization in time of Eqs.(2.32)-(2.36) is based on a second order backward differentiation formula (BDF2) for the pure diffusive second step, where the diffusive terms are treated implicitly for stability reasons, whilst the non-linear advective terms are extrapolated with second order time accurate formula [KIO91]. Concerning the time discretization, the first projection step Eq.(2.39) can now be written for the time level $\tau = (n + 1)\Delta\tau$ ($\Delta\tau$ being the discrete advancing time-step)

$$\underline{\mathbf{D}} \cdot \underline{\mathbf{G}}' p^{n+1} = \underline{\mathbf{D}} \cdot \underline{\mathbf{f}}'{}^{n+1}(\underline{\mathbf{u}}) \quad (2.41)$$

where the source term $\underline{\mathbf{f}}'(\underline{\mathbf{u}})$, containing the boundary conditions for the pressure Eq.(2.39) which now reads

$$\frac{\partial p^{n+1}}{\partial \mathbf{n}} = \left[- \left(\sum_{i=0}^{J_e-1} \zeta_i [\underline{\mathbf{G}} \times (\underline{\mathbf{G}} \times \underline{\mathbf{u}}^{n-i})] \right) + Pr \underline{\Theta}^{n+1} \frac{\underline{\mathbf{g}}}{|\underline{\mathbf{g}}|} \right] \cdot \mathbf{n} \quad (2.42)$$

whereas for internal nodes $\underline{\mathbf{f}}''(\underline{\mathbf{u}})$ is equal to

$$\underline{\mathbf{f}}'{}^{n+1}(\underline{\mathbf{u}}) = \left[- \left(\sum_{i=0}^{J_e-1} \zeta_i [\underline{\mathbf{u}}^{n-i} \cdot \underline{\mathbf{G}} \underline{\mathbf{u}}^{n-i}] \right) + Pr \underline{\Theta}^{n+1} \frac{\underline{\mathbf{g}}}{|\underline{\mathbf{g}}|} \right] \quad (2.43)$$

J_e being the order of the extrapolator and ζ_i the associated weights given in Tab.(2.1). Finally, the second step discretized in time and space becomes

$$\underline{\mathbf{H}}'_u \underline{\mathbf{u}}^{n+1} = \left[- \frac{\sum_{i=0}^{J_e-1} \xi_i \underline{\mathbf{u}}^{n-i}}{\Delta\tau} - \left(\sum_{i=0}^{J_e-1} \zeta_i \underline{\mathbf{u}}^{n-i} \cdot \underline{\mathbf{G}} \underline{\mathbf{u}}^{n-i} \right) + Pr \underline{\Theta}^{n+1} \frac{\underline{\mathbf{g}}}{|\underline{\mathbf{g}}|} - \underline{\mathbf{G}} p^{n+1} \right] \quad (2.44)$$

$\underline{\mathbf{H}}'_u = \frac{Pr}{\sqrt{Ra}} \underline{\mathbf{D}} \cdot \underline{\mathbf{G}} - \frac{\eta_0}{\Delta\tau} \underline{\mathbf{I}}$ being the modified Helmholtz operator that contains the Dirichlet boundary condition $\underline{\mathbf{u}} = \underline{\mathbf{0}}$ on the nodes of the boundaries $\partial\Omega$, η_0 and ξ_i are constants

depending on the order J_i of the implicit BDF scheme (Tab.(2.1)). The discretization of the energy equation can be recasted as a Helmholtz problem where the operator

$$\underline{H}'_{\Theta} = \frac{1}{\sqrt{Ra}} \underline{\mathbf{D}} \cdot \underline{\mathbf{G}} - \frac{\eta_0}{\Delta\tau} \underline{I} \quad (2.45)$$

contains temperature Dirichlet and Neumann boundary conditions depending on the problem set-up. In general it will look like

$$\underline{H}'_{\Theta} \underline{\Theta}^{n+1} = \left[-\frac{\sum_{i=0}^{J_i-1} \xi_i \underline{\Theta}^{n-i}}{\Delta\tau} - \left(\sum_{i=0}^{J_e-1} \zeta_i \mathbf{u}^{n-i} \cdot \underline{\mathbf{G}} \underline{\Theta}^{n-i} \right) \right]. \quad (2.46)$$

The inversion of the full matrices on the *l.h.s.* is performed with the fast-diagonalization algorithm by Haldenwang *et al.* [HLAD84] which allows the filtering of the spurious pressure modes [ABG95] arising in the pressure operator in Eq.(2.41). The algorithm to perform the inversion of the Helmholtz operators is briefly described in the following few steps:

- Preprocessing stage: computation of the one-dimensional matrices \underline{B}_i of order $N_i - 1$ with $i = 1, \dots, d$, coming from the matrix multiplication in the Helmholtz operator $\underline{\mathbf{D}} \cdot \underline{\mathbf{G}} = \sum_{i=1}^d \underline{B}_i$, and successive diagonalization of these matrices to produce the \underline{E}_i and $\underline{\Lambda}_i$, the eigenvector and eigenvalue matrices respectively. Then it is possible to recast the 3D Helmholtz problem for a general discretized scalar quantity $\underline{\phi}$ (which can be the temperature or a component of the velocity field) as a matrix tensor product

$$(\underline{E}_3 \otimes \underline{E}_2 \otimes \underline{E}_1)(\underline{\Lambda}_3 \otimes \underline{I}_2 \otimes \underline{I}_1 + \underline{I}_3 \otimes \underline{\Lambda}_2 \otimes \underline{I}_1 + \underline{I}_3 \otimes \underline{I}_2 \otimes \underline{\Lambda}_1)(\underline{E}_3^{-1} \otimes \underline{E}_2^{-1} \otimes \underline{E}_1^{-1})\underline{\phi} = \underline{f}' \quad (2.47)$$

- Computation of the modified source \underline{f}' term which has to include the boundary conditions;
- Scanning each spatial direction successively, one applies the corresponding \underline{E}_i^{-1} operator to the *r.h.s.* to produce the term of the full diagonal representation;
- The solution is recovered, by the successive application of the \underline{E}_i operators and by the appropriate use of the boundary conditions.

Finally, it is important to note that, due to the explicit treatment of the non-linear terms, the integration time-step has to respect the Courant–Friedrichs–Lewy (CFL) condition which in the present work is computed as follows

$$CFL = \max \left\{ \left| \frac{u_1(x_i)\Delta\tau}{\Delta x_{1,i}} \right| + \dots + \left| \frac{u_d(x_i)\Delta\tau}{\Delta x_{d,i}} \right| \right\}_{i=0}^{\mathcal{N}} < CFL_{MAX} \quad (2.48)$$

2.1. METHODOLOGY FOR THE CONTINUOUS PHASE

where $\mathcal{N} = \prod_{i=1}^d N_i$ is the total number of collocation points, $\Delta x_{k,i}$ represents the distance between two neighboring points measured along the k -th direction and CFL_{MAX} is the maximum CFL number allowed by the chosen explicit extrapolation scheme [Ler99]. The implemented algorithm uses $J_i = J_e = 2$ after the first time-step, whereas $J_i = J_e = 1$ for the first one. First the temperature field $\underline{\Theta}^{n+1}$ is solved from Eq.(2.46) and then the pressure \underline{p}^{n+1} from Eq.(2.41) and finally velocity field $\underline{\mathbf{u}}^{n+1}$ from Eq.(2.44).

Weights	Order 1	Order 2	Order 3	Order 4
η_0	1	3/2	11/6	25/12
ξ_0	1	2	3	4
ξ_1	0	-1/2	-3/2	-3
ξ_2	0	0	1/3	4/3
ξ_3	0	0	0	-1/4
ζ_0	1	2	3	4
ζ_1	0	-1	-3	6
ζ_2	0	0	1	4
ζ_3	0	0	0	-1

Tab. 2.1: *The weights (η_0, ξ_i) for the implicit BDF schemes and (ζ_i) for the explicit extrapolation schemes.*

2.2 Methodology for the aerosol dispersed phase

2.2.1 Interpolation

As seen in the previous chapter, the PEM requires the knowledge of flow quantities measured at the particle position \mathbf{Y}_d in order to be solved. This information can be retrieved by simply interpolating the solution fields at the Eulerian grid nodes. Hence two possible approaches can be considered:

- direct summation or spectral interpolation;
- local interpolation.

The first choice is straightforward since the Chebyshev pseudo-spectral method employed for the continuous phase provides direct access to the spectral representation of the solution fields with the advantage to conserve the full spectral accuracy when determining the interpolated quantities with no need of any searching algorithm; the main disadvantage is that the computational costs increase as $O(N_p N^d \log N)$ ($d = 1, \dots, 3$ being the domain space dimension supposing $N_1 = \dots = N_d = N$ and N_p the number of particles) [YP88]. The second technique is the most commonly used in the literature and requires a searching algorithm to find the closest GLC grid point from the particle position in order to define the local knots of the cell where to perform the interpolation. It has been shown that globally the second technique only requires $O(N_p K^{2d})$ (K being the number of knots of the local interpolation method in each direction) for a Lagrangian interpolation method on a rectilinear grid. Balachandar *et al.* [BM89] and Kontomaris *et al.* [KHM92] showed that 6th-order Lagrangian interpolation gives sufficiently accurate results on Lagrangian statistics of homogeneous isotropic turbulence. The homogeneous periodic boundary conditions applied in that case allows to always consider an optimal cell centered interpolation around the particle (see particle *a* in Fig.2.4). On the other hand the presence of wall boundaries in non-homogeneous turbulent flows forces to use one-side interpolation with a (slight) increment in the interpolation error, or to decrease the order of the interpolator up to linear interpolation when the wall distance of the particle is less than the wall distance of the corresponding first node inside the fluid domain, with an increase of the interpolation error. More complex interpolation schemes designed to avoid this problem involves direct summation in the non-homogeneous direction (hence preserving the spectral accuracy), combining Lagrangian, Hermite or cubic polynomial, with Chebyshev interpolation [KHM92]. In the present case this latter approach would lead to full spectral interpolation because the domain is fully confined.

On the basis of the results reported in the literature the interpolation based on 6th-order Lagrangian polynomial (which uses the GLC grid points of the fluid mesh) has been cho-

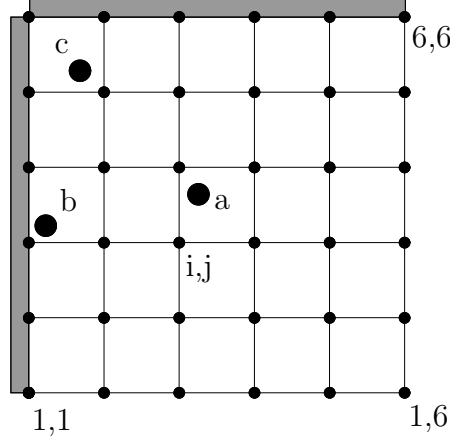


Fig. 2.4: Schematic representation of the local grid used by a sixth order Lagrangian interpolator for three different particles away and close to the boundaries.

sen with one-side interpolation (see particles *b-c* in Fig.2.4) and the description of the methodology is briefly presented in the following.

Lagrangian interpolation

Given K distinct nodes x_i with $i = 0, \dots, K - 1$ belonging to the interval $[x_0, x_{K-1}]$ and the corresponding values $f(x_i, t) = f_i(t)$ of the function $f = f(x, t)$ to be interpolated, then the Lagrangian polynomial interpolation of order K of f , is given by

$$I_N f(x, \tau) = \sum_{i=0}^{K-1} f_i(\tau) l_i(x) \quad (2.49)$$

where l_i are the characteristic polynomials expressed by

$$l_i(x) := \prod_{\substack{j=0 \\ j \neq i}}^{K-1} \frac{x - x_j}{x_i - x_j} \quad (2.50)$$

which satisfies the property $l_i(x_j) = \delta_{ij}$. Figure 2.5 shows the characteristic functions for $K = 6$ where the knots are uniformly spaced. Furthermore, Lagrangian polynomial interpolation satisfies the general property of interpolants, i.e.

$$I_N f(x_i, \tau) = f(x_i, \tau) \quad (2.51)$$

which expresses the exactness of the interpolated function at the knots where the function is known.

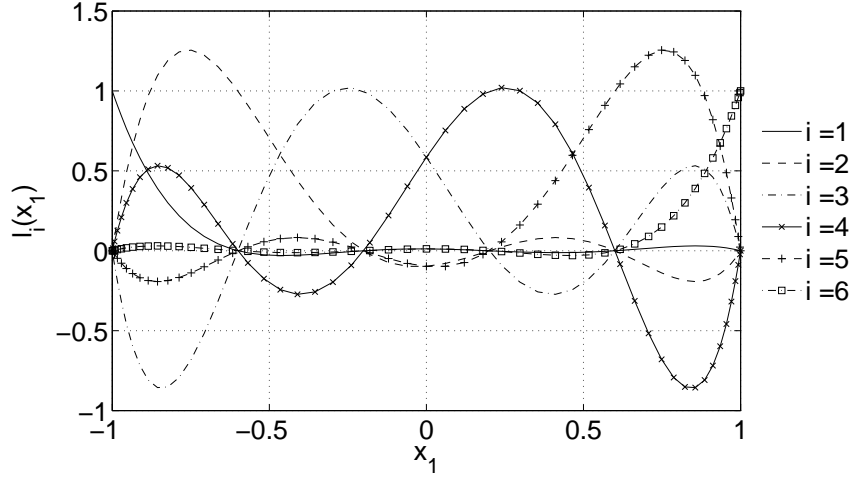


Fig. 2.5: Lagrangian characteristic functions l_i for $K = 6$ and $i = 1, \dots, N$.

Moreover, the extension to multidimensional domains where tensorization applies is straightforward:

the d -dimensional versions of Eq.(2.49) becomes

$$I_{(K_1 \dots K_d)} f(\mathbf{x}, t) = \sum_{i_1=0}^{K_1} \cdots \sum_{i_d=0}^{K_d} f_{(i_1 \dots i_d)}(t) l_1(x_1) \cdots l_d(x_d). \quad (2.52)$$

where K_i are the orders of the interpolators in each spatial direction and the characteristic functions l_i can be easily computed from Eq.(2.50) for each direction, respectively (Fig.2.6). Finally a 6-th order Lagrangian interpolator with one-side interpolation on the GLC nodes

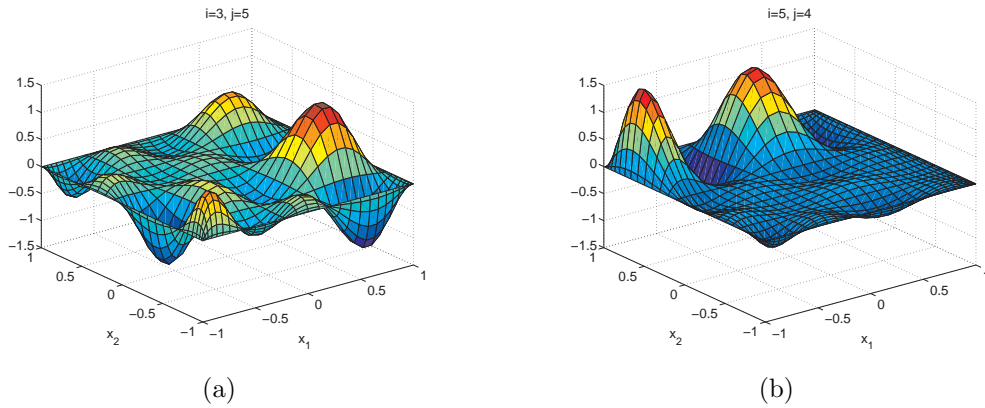


Fig. 2.6: Two-dimensional representation of Lagrangian characteristic functions $l_3 l_5$ (a), $l_5 l_4$ (b) with $K_1 = K_2 = 6$ and uniformly spaced knots.

has been chosen.

2.2.2 Time integration

A general ODEs system of N scalar equations can be reduced to its *autonomous* form by the introduction of the new differential equation $\dot{x}_{N+1} = 1$ (where the upper dot means time derivation) together with the appropriate initial conditions

$$\dot{\underline{\mathbf{x}}} = \underline{\mathbf{f}}(\underline{\mathbf{x}}), \quad \underline{\mathbf{x}}(\tau_0) = \underline{\mathbf{x}}^0. \quad (2.53)$$

In order to integrate Eq.(2.53) a classical Explicit 4th-order Runge-Kutta (ERK4) scheme has been chosen for its properties of large stability and good convergence. A brief description of the algorithm is given in the following. More details about the theoretical aspects of the Runge-Kutta methods are in [But87, QSS07].

Explicit Runge-Kutta method

The idea behind the derivation of Runge-Kutta (RK) methods is to impose that the highest number of terms of the Taylor expansion of the numerical solution of the ODE system $\tilde{\underline{\mathbf{x}}}(\tau)$ coincide with the terms appearing in the Taylor expansion of the exact solution $\underline{\mathbf{x}}(\tau)$. Usually this leads to an infinite number of possible combinations of coefficients for each RK method of order r . It is also worth to recall that RK methods are one-step algorithms with multiple internal time-level evaluations (stages). Moreover, the convergence order q of an explicit RK method with r stages cannot be greater than r , in particular it has been shown that the optimum occurs for $r = q = 4$ whilst if $r \geq 5$ then $q < r$ [But87].

The general form of a RK method with r internal stages and integration time step $\Delta\tau$ reads

$$\tilde{\underline{\mathbf{x}}}^{n+1} = \tilde{\underline{\mathbf{x}}}^n + \Delta\tau \sum_{i=1}^r b_i \underline{\mathbf{k}}_i \quad (2.54)$$

with the coefficients

$$\underline{\mathbf{k}}_i = \underline{\mathbf{f}} \left(\tilde{\underline{\mathbf{x}}}^n + \sum_{j=1}^r a_{ij} \underline{\mathbf{k}}_j \right), \quad i = 1, \dots, r \quad (2.55)$$

where $\tilde{\underline{\mathbf{x}}}_{n+1}$ is the numerical solution of the ODE system at the $(n+1)$ -th time step and $\tilde{\underline{\mathbf{x}}}_n$ is the numerical solution at the previous iteration. The algorithm is fully determined by the coefficients $\mathbf{b} = (b_i)$ and $\mathbf{A} = (a_{ij})$ collected in the Butcher array as shown below

$$\begin{array}{c|cc|cccc} & & c_1 & a_{11} & a_{12} & \cdots & a_{1r} \\ \mathbf{c} & \mathbf{A} & c_2 & a_{21} & a_{22} & & a_{2r} \\ & & \vdots & \vdots & & \ddots & \vdots \\ & & c_r & a_{r1} & a_{r2} & \cdots & a_{rr} \\ \hline & \mathbf{b}^T & & b_1 & b_2 & \cdots & b_r \end{array} \quad (2.56)$$

where the elements of $\mathbf{c} = (c_i)$ indicate the position within the step and satisfy

$$c_i = \sum_{j=1}^r a_{ij}, \quad i = 1, \dots, r \quad (2.57)$$

whereas the elements of $\mathbf{b} = (b_i)$ shows how the final result depends on the derivatives computed at the various stages and for consistency must verify the following condition

$$\sum_{i=1}^r b_i = 1. \quad (2.58)$$

If the matrix \mathbf{A} is strictly lower triangular, i.e. the coefficient a_{ij} are equal to zero for $j \geq i$ then the method is explicit and needs only a total number of coefficients equal to $r(r+1)/2$.

Finally, the corresponding Butcher array for a classical ERK4 is provided

$$\begin{array}{c|cccc} 0 & 0 & 0 & 0 & 0 \\ 1/2 & 1/2 & 0 & 0 & 0 \\ 1/2 & 0 & 1/2 & 0 & 0 \\ 1 & 0 & 0 & 1 & 0 \\ \hline & 1/6 & 1/3 & 1/3 & 1/6 \end{array} \quad . \quad (2.59)$$

and the array of coefficients \mathbf{k}_i can now be explicitly evaluated by

$$\mathbf{k}_i = \mathbf{f} \left(\tilde{\mathbf{x}}^n + \sum_{j=1}^{i-1} a_{ij} \mathbf{k}_j \right), \quad i = 1, \dots, r. \quad (2.60)$$

It is possible to define the linear model problem in the form

$$\dot{x} = \lambda x, \quad x(\tau_0) = x^0 \quad (2.61)$$

for which the ERK4 integration scheme presents the following stability region Fig.2.7 ([But87]). A direct measure of the maximum time-step $\Delta\tau$ allowed for the integration of the PEM would require also the knowledge of characteristic of the linearized dynamics of the flow system (because of the drag, lift and thermophoretic forces that depends on the flow quantities) which is out of the scope of this thesis. Anyway, in order to choose the appropriate integration time-step, a set of tests have been run. The most strict criterion among the CFL condition for the fluid, the stability conditions of the ERK4 method and the Nyquist sampling theorem in relation to the particle relaxation time, has yielded a time-step around one tenth of the time-step required by the CFL condition of the fluid and at least one third of the particle relaxation time. The exact values for each case considered in this work will be specified later on in the text.

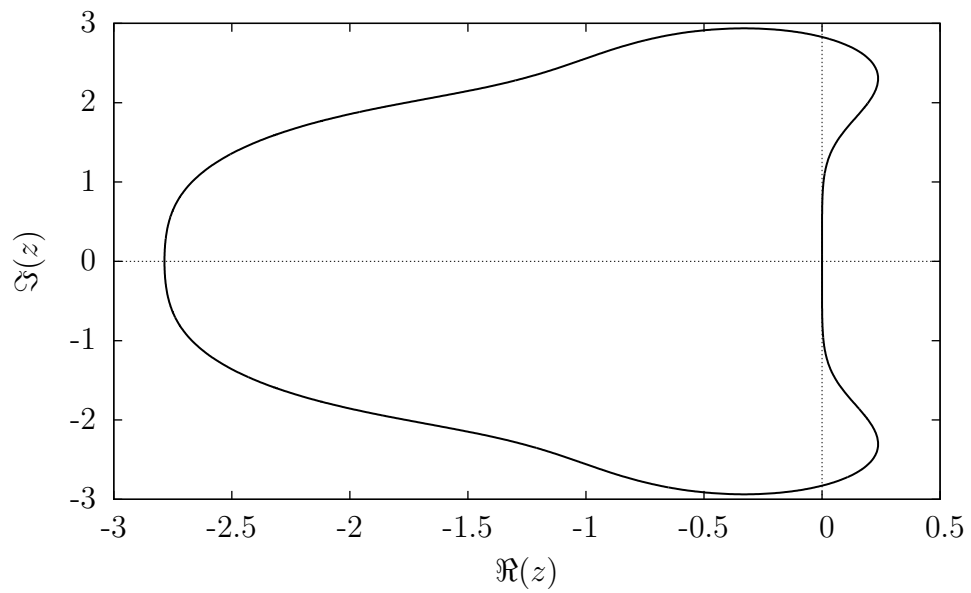


Fig. 2.7: *Stability region for ERK4 method: points in the complex plane contained inside the closed curve are stable.*

Chapter 3

Differentially heated cavity: Two dimensional investigations

Several topics are discussed in the present chapter. First of all, the benchmark setup is described and laminar steady-state results obtained for three different Rayleigh numbers (10^5 , 10^6 , 10^7) are compared with those already published in the literature. A detailed description of the main flow patterns and characteristic quantities, namely velocity and temperature profiles, temperature stratification, Nusselt number and wall shear stress is provided.

In the second part of the chapter the attention is focused on unsteady chaotic flows at high Rayleigh numbers ($Ra = 10^9$, 10^{10}), and the study of first and second order moments are provided, including important terms appearing in the mean Navier-Stokes equations and in the turbulent kinetic energy and temperature variance transport equations like the production and rate of dissipation of the turbulent kinetic energy and temperature variance. The reader should be aware that these quantities give information which is not truly related to the actual turbulent flow which is intrinsically three-dimensional but illustrate in first approximation the trend and the basic features of the chaotic flows at high Rayleigh numbers.

The third and last section deals with the depletion mechanisms for three sets of aerosol particles of different sizes for the two unsteady chaotic cases above mentioned. The evolution in time of the particle number fraction and the deposition profiles at the bottom wall are presented. The influence of lift is discussed in more detail since it will be shown that is the reason of particle deposition on the vertical cold wall, and also the thermophoretic effect will be addressed.

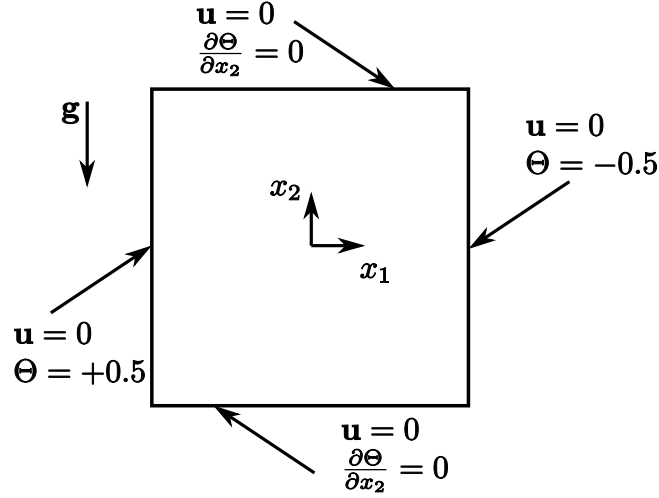


Fig. 3.1: Schematic representation of the square DHC with boundary conditions.

3.1 Steady laminar flows

Differentially heated cavities (DHC) are closed systems where two opposite vertical walls are differentially heated while the rest is considered adiabatic. The heating process is the only responsible mechanism of the motion of the contained working fluid which is subject to a local change of density at the thermally active walls, resulting in a buoyancy driving force that induces a large recirculation of fluid.

3.1.1 Benchmark configuration

Since the pioneering work of de Vahl Davis and Jones [dVD83, dVDJ83] in the eighties the thermal flow in the two dimensional heated square cavity filled by air ($Pr = 0.71$) became a numerical benchmark problem because it is a simple setting for testing accuracy and efficiency of numerical methods for solving the incompressible Navier-Stokes equations. The schema of the geometry configuration in the dimensionless space is shown in Fig. 3.1 for a dimensionless square domain $\Omega = [-0.5, +0.5]^2$ together with the thermal and velocity boundary conditions. The dimensionless governing equations are here recalled (the symbol “^” has been dropped for the sake of simplicity)

$$\nabla \cdot \mathbf{u} = 0 \tag{3.1}$$

$$\frac{\partial \mathbf{u}}{\partial \tau} + \mathbf{u} \cdot \nabla \mathbf{u} = -\nabla p + \frac{Pr}{\sqrt{Ra_H}} \Delta \mathbf{u} - Pr \Theta \frac{\mathbf{g}}{|\mathbf{g}|} \tag{3.2}$$

$$\frac{\partial \Theta}{\partial \tau} + \mathbf{u} \cdot \nabla \Theta = \frac{1}{\sqrt{Ra_H}} \Delta \Theta \quad (3.3)$$

with the following boundary conditions for velocity and temperature

$$\mathbf{u}(x_1 = \pm 0.5, x_2, \tau) = \mathbf{0} \quad \forall x_2 \in [-0.5, +0.5], \quad (3.4)$$

$$\mathbf{u}(x_1, x_2 = \pm 0.5, \tau) = \mathbf{0} \quad \forall x_1 \in [-0.5, +0.5], \quad (3.5)$$

$$\Theta(x_1 = \pm 0.5, x_2, \tau) = \mp 0.5 \quad \forall x_2 \in [-0.5, +0.5], \quad (3.6)$$

$$\frac{\partial \Theta}{\partial x_2}(x_1, x_2 = \pm 0.5, \tau) = 0 \quad \forall x_1 \in [-0.5, +0.5]. \quad (3.7)$$

The initial conditions imposed are

$$\mathbf{u}_0 = \mathbf{u}(x_1, x_2, \tau = 0) = \mathbf{0} \quad \text{in } \Omega, \quad (3.8)$$

$$\Theta_0 = \Theta(x_1, x_2, \tau = 0) = -x_1 \quad \text{in } \Omega \quad (3.9)$$

the latter corresponds to the steady solution of the one-dimensional Fourier law in a homogeneous linear solid material and is used up to $Ra_H = 10^5$, whereas for $Ra_H > 10^5$ the fields are initialized using the fields obtained from previous calculations at lower Rayleigh number. The comparison of several quantities obtained in the present work with those provided in [dVD83, Le 87, Le 91, TLB00] is performed spanning three orders of magnitude of the Rayleigh number, namely $Ra_H = 10^5, 10^6, 10^7$, and the results are reported in Tab.3.2. The quantities under investigation are:

- The maximum of the absolute value of velocity components $|u_1|_{Max}, |u_2|_{Max}$ in the whole domain and their location $(x_1, x_2)_{Max}$;
- The maximum of the absolute value of the horizontal velocity component along the vertical centerline $|u_1|_{0,Max}$ and its location $x_{2,Max}$;
- The maximum of the absolute value of the vertical velocity component along the horizontal centerline $|u_2|_{0,Max}$ and its location $x_{1,Max}$;
- The maximum of the absolute value of the stream-function $|\psi|_{Max}$ in the whole domain and its location $(x_1, x_2)_{Max}$;
- The stream-function value at the center of the cavity $|\psi|_0$;
- The maximum of the local Nusselt number at the hot wall $Nu_{H,Max}$;
- The mean Nusselt number at the hot wall \overline{Nu}_H ;
- The mean Nusselt number at the vertical centerline \overline{Nu}_M ;

Here, the stream-function is defined in such a way that

$$u_1(x_1, x_2) = \frac{\partial}{\partial x_2} \psi(x_1, x_2), \quad (3.10)$$

$$u_2(x_1, x_2) = -\frac{\partial}{\partial x_1} \psi(x_1, x_2), \quad (3.11)$$

whereas the local Nusselt number is defined as

$$\mathbf{Nu} := -\nabla\Theta + \sqrt{Ra_H} \mathbf{u}\Theta \quad (3.12)$$

and its space averaging along a line \mathcal{L} , lying on the plane (x_1, x_2) , of length L and unit normal vector \mathbf{n} , is given by

$$\overline{Nu}_L = \frac{1}{L} \int_L \mathbf{Nu}_{\mathcal{L}} \cdot \mathbf{n} \, dl. \quad (3.13)$$

The maximum values and their location are searched using a multidimensional Newton's method coupled with a 6th-order Lagrangian interpolation for the present results, whilst Richardson's extrapolation has been used in [dVD83] where several solutions have been computed with a second-order central difference scheme on different grids ranging from 11×11 to 81×81 . In [Le 91], the pseudo-spectral solutions have been interpolated on a uniform Cartesian 1001×1001 grid and the values reported correspond to the maxima on the new discretized domain; Tric *et al.* [TLB00] have used a second-order Lagrangian interpolation technique on the Chebyshev grid. The values and positions obtained are in excellent agreement with the published references. The only discrepancy is encountered in the Nusselt number ¹ at the vertical centerline. It is known that in the present configuration from the first law of thermodynamic the latter quantity has to be equal to the Nusselt number at the hot wall. The present work and the one of Tric *et al.* perform better than the others which show a lack of convergence in their calculations since a larger error is registered in the two Nusselt numbers.

It is known that steady solutions of the Oberbeck-Boussinesq equations in symmetric geometries present the so called centro-symmetry properties (see also [CGS02]) expressed by

$$(u_i, p, \Theta)(x_1, x_2) = -(u_i, -p, \Theta)(+0.5 - x_1, +0.5 - x_2). \quad (3.14)$$

The latter relation has been used in order to assert the convergence of the computation. The error in the centro-symmetry for a general quantity ϕ is evaluated as

$$\mathcal{E}_{cs}(|\phi|) = \frac{|\phi(x_1, x_2)| - |\phi(+0.5 - x_1, +0.5 - x_2)|}{|\phi|_{Max}} \leq \epsilon \quad (3.15)$$

¹Gauss-Lobatto-Chebyshev quadrature rule is employed in the present work.

3.1. STEADY LAMINAR FLOWS

	$Ra_H = 10^5$ ($N_1 = N_2 = 129$)			$Ra_H = 10^6$ ($N_1 = N_2 = 129$)			$Ra_H = 10^7$ ($N_1 = N_2 = 129$)		
	$\ \mathcal{E}_{cs}\ _\infty$	$\ \mathcal{E}_{cs}\ _1$	\mathcal{S}	$\ \mathcal{E}_{cs}\ _\infty$	$\ \mathcal{E}_{cs}\ _1$	\mathcal{S}	$\ \mathcal{E}_{cs}\ _\infty$	$\ \mathcal{E}_{cs}\ _1$	\mathcal{S}
u_1	1.214E-11	4.675E-12	1.44E-10	9.529E-10	2.278E-10	1.29E-9	5.404E-8	5.293E-9	4.27E-9
u_2	6.347E-12	2.448E-12	1.04E-10	7.483E-10	1.312E-10	8.97E-10	2.866E-8	2.697E-9	2.61E-8
p	1.852E-11	1.855E-12	1.23E-10	1.603E-9	8.525E-10	2.94E-10	7.344E-8	4.023E-8	4.16E-9
Θ	2.160E-11	3.446E-12	4.39E-9	8.839E-10	5.639E-10	1.59E-8	3.202E-8	2.256E-8	4.81E-8

Tab. 3.1: *Max-norm, 1-norm of the error in the centro-symmetry property and spectral coefficient ratio \mathcal{S} for each field at $Ra = 10^5, 10^6, 10^7$.*

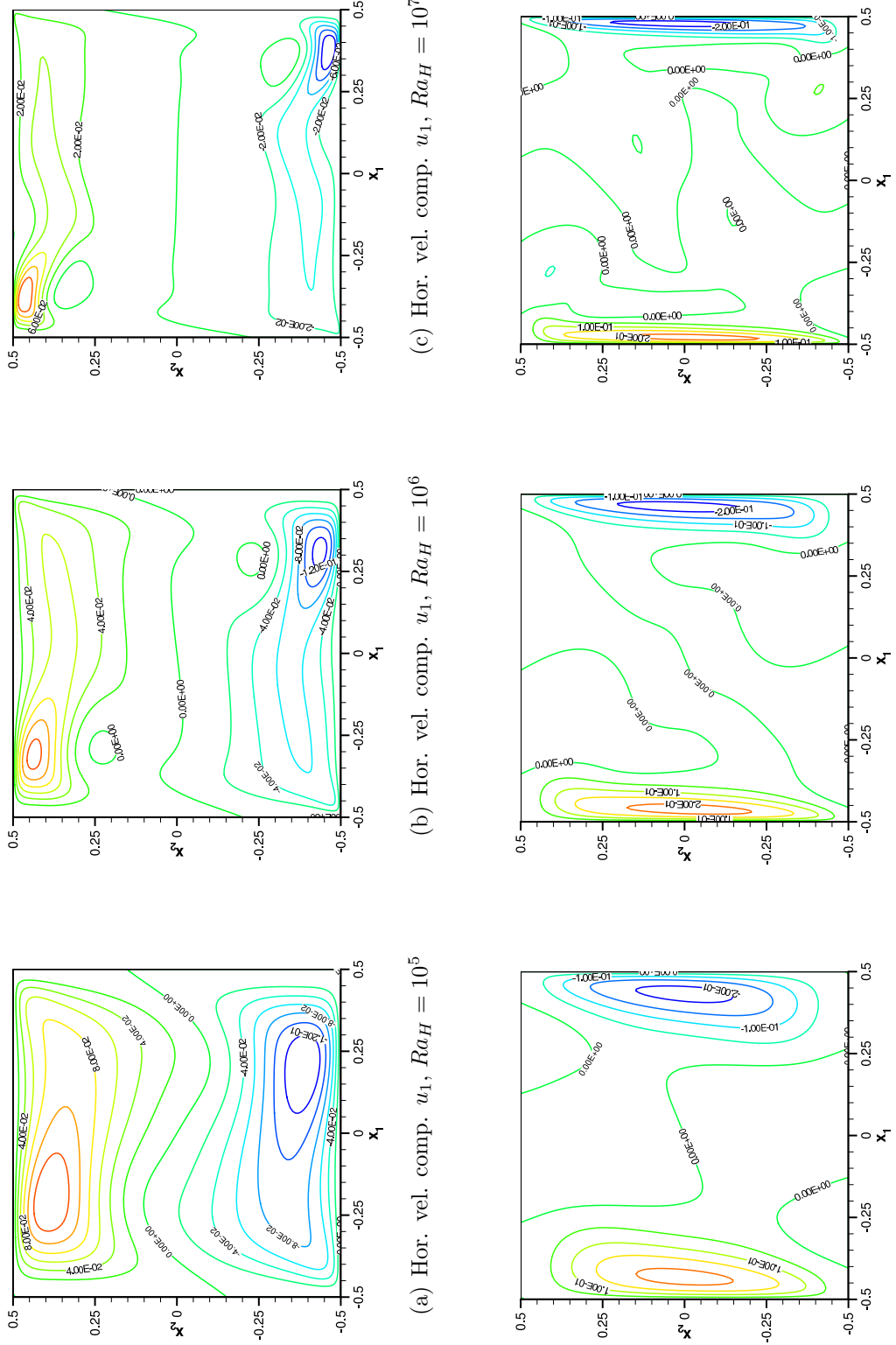
that should be less than a certain ϵ fixed here at 10^{-7} . Together with this, the ratio of the smallest to the largest spectral coefficients \mathcal{S} is also used to assert the convergence of the computation. It is commonly accepted that the order of magnitude of \mathcal{S} should be less or equal to $O(10^{-4})$ even for turbulent flows. In the present work this condition is fully satisfied. Tab.3.1 shows the max-norm ($\|\phi\|_\infty$) and 1-norm ($\|\phi\|_1 = \int_\Omega |\phi| d\Omega$) of the error in the centro-symmetry at the different Rayleigh numbers for the different grids.

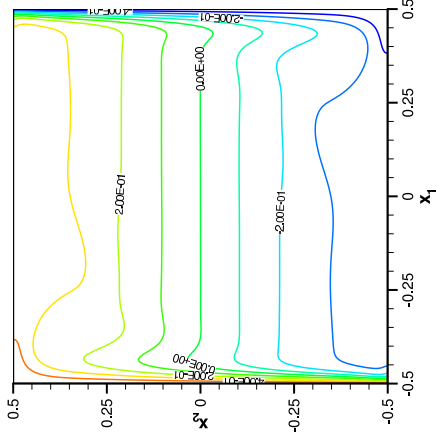
CHAPTER 3. DIFFERENTIALLY HEATED CAVITY: TWO DIMENSIONAL
INVESTIGATIONS

	Present	[dVD83]	[Le 91]	[Le 87]	[TLB00]	
$Ra_H = 10^5$	Grid	129×129	Extrapolated	–	65×65	51×51
	$ u_1 _{Max}$	0.1388	–	–	–	–
	(x_1, x_2)	(0.2034, –0.3894)	–	–	–	–
	$ u_2 _{Max}$	0.2171	–	–	–	–
	(x_1, x_2)	(0.4340, –0.0017)	–	–	–	–
	$ u_1 _{0,Max}$	0.1099	0.1098	–	0.1099	0.1097
	(x_2)	(0.3546)	(0.3550)	–	(0.3550)	(0.354)
	$ u_2 _{0,Max}$	0.2170	0.2169	–	0.2171	0.2169
	(x_1)	(0.4341)	(–0.4340)	–	(–0.434)	(–0.4340)
	$ \psi _{Max}$	0.0304	0.0304	–	0.0304	–
	(x_1, x_2)	(0.2155, –0.1015)	(–0.2150, 0.1010)	–	(–0.2150, 0.1010)	–
	$ \psi _0$	0.0288	0.0288	–	0.0288	–
	$Nu_{H,Max}$	7.720	7.717	–	7.720	–
	(x_2)	(–0.4179)	(–0.4190)	–	(–0.4180)	–
	\overline{Nu}_H	4.5216	4.509	–	4.522	4.522
\overline{Nu}_M	4.5216	4.519	–	4.523	4.522	
$Ra_H = 10^6$	Grid	129×129	Extrapolated	73×73	65×65	51×51
	$ u_1 _{Max}$	0.1287	–	–	–	–
	(x_1, x_2)	(0.3115, –0.4374)	–	–	–	–
	$ u_2 _{Max}$	0.2211	–	–	–	–
	(x_1, x_2)	(0.4633, 0.0310)	–	–	–	–
	$ u_1 _{0,Max}$	0.0648	0.0646	0.0648	0.0648	0.0648
	(x_2)	(0.3499)	(0.3500)	(0.3500)	(0.3500)	(0.3410)
	$ u_2 _{0,Max}$	0.2206	0.2206	0.2206	0.2206	0.2205
	(x_1)	(0.4622)	(–0.4620)	(–0.4620)	(–0.4625)	(–0.4620)
	$ \psi _{Max}$	0.0168	0.0168	0.0168	0.0168	–
	(x_1, x_2)	(0.3496, –0.0467)	(–0.3490, 0.0470)	(–0.3500, 0.0470)	(–0.2150, 0.1010)	–
	$ \psi _0$	0.0164	0.0163	0.0164	0.01639	–
	$Nu_{H,Max}$	17.535	17.925	17.536	17.536	–
	(x_2)	(–0.4607)	(–0.4622)	(–0.4610)	(0.480)	–
	\overline{Nu}_H	8.825	8.817	8.825	8.825	8.825
\overline{Nu}_M	8.825	8.799	8.852	8.826	8.825	
$Ra_H = 10^7$	Grid	129×129	–	81×81	–	51×51
	$ u_1 _{Max}$	0.1229	–	–	–	–
	(x_1, x_2)	(0.3771, –0.4661)	–	–	–	–
	$ u_2 _{Max}$	0.2218	–	–	–	–
	(x_1, x_2)	(0.4793, 0.3495)	–	–	–	–
	$ u_1 _{0,Max}$	0.0470	–	0.0470	–	0.0470
	(x_2)	(–0.3793)	–	(0.379)	–	(0.379)
	$ u_2 _{0,Max}$	0.2211	–	0.2211	–	0.2214
	(x_1)	(0.4787)	–	(–0.4790)	–	(–0.479)
	$ \psi _{Max}$	9.5339×10^{-3}	–	9.5387×10^{-3}	–	–
	(x_1, x_2)	(0.4140)	–	(–0.414)	–	–
	$ \psi _0$	9.2850×10^{-3}	–	9.2850×10^9	–	–
	$Nu_{H,Max}$	39.3947	–	39.3947	–	–
	(x_2)	(–0.4820)	–	(–0.4820)	–	–
	\overline{Nu}_H	16.5231	–	16.523	–	16.522
\overline{Nu}_M	16.5231	–	16.523	–	16.522	

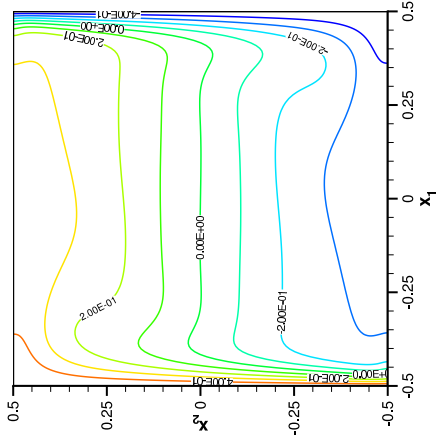
Tab. 3.2: Comparison of 2d DHC flow results with the benchmark data of [dVD83, Le 91, Le 87, TLB00] for $Ra_H = 10^5, 10^6, 10^7$.

Fig. 3.2: Contour plots of velocity components u_1, u_2 for $Ra_H = 10^5, 10^6, 10^7$.

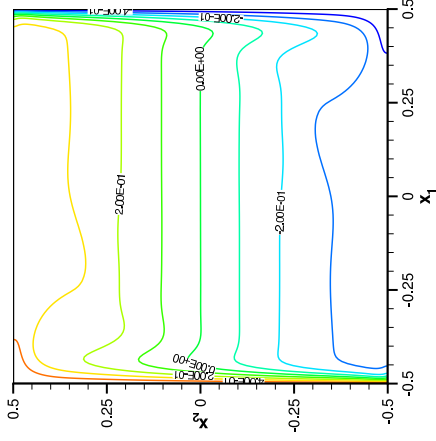




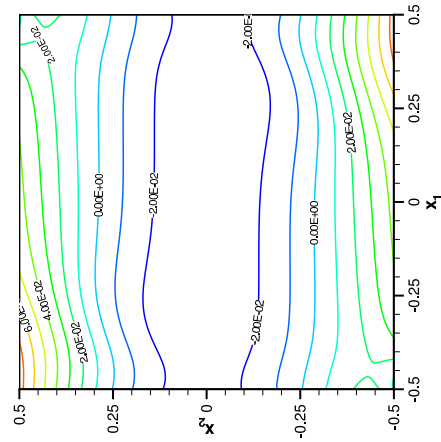
(a) Temperature Θ , $Ra_H = 10^5$



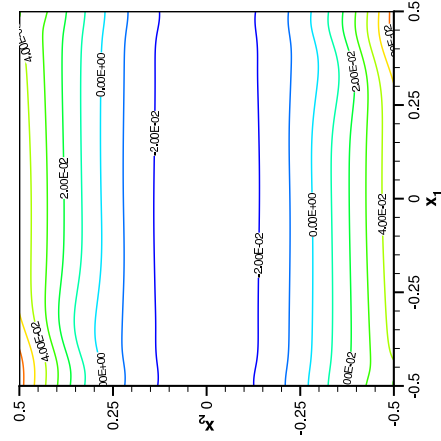
(b) Temperature Θ , $Ra_H = 10^6$



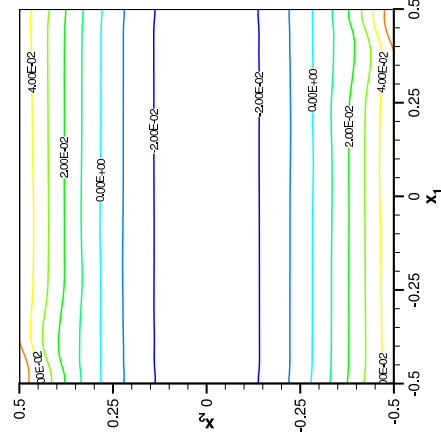
(c) Temperature Θ , $Ra_H = 10^7$



(d) Pressure p , $Ra_H = 10^5$



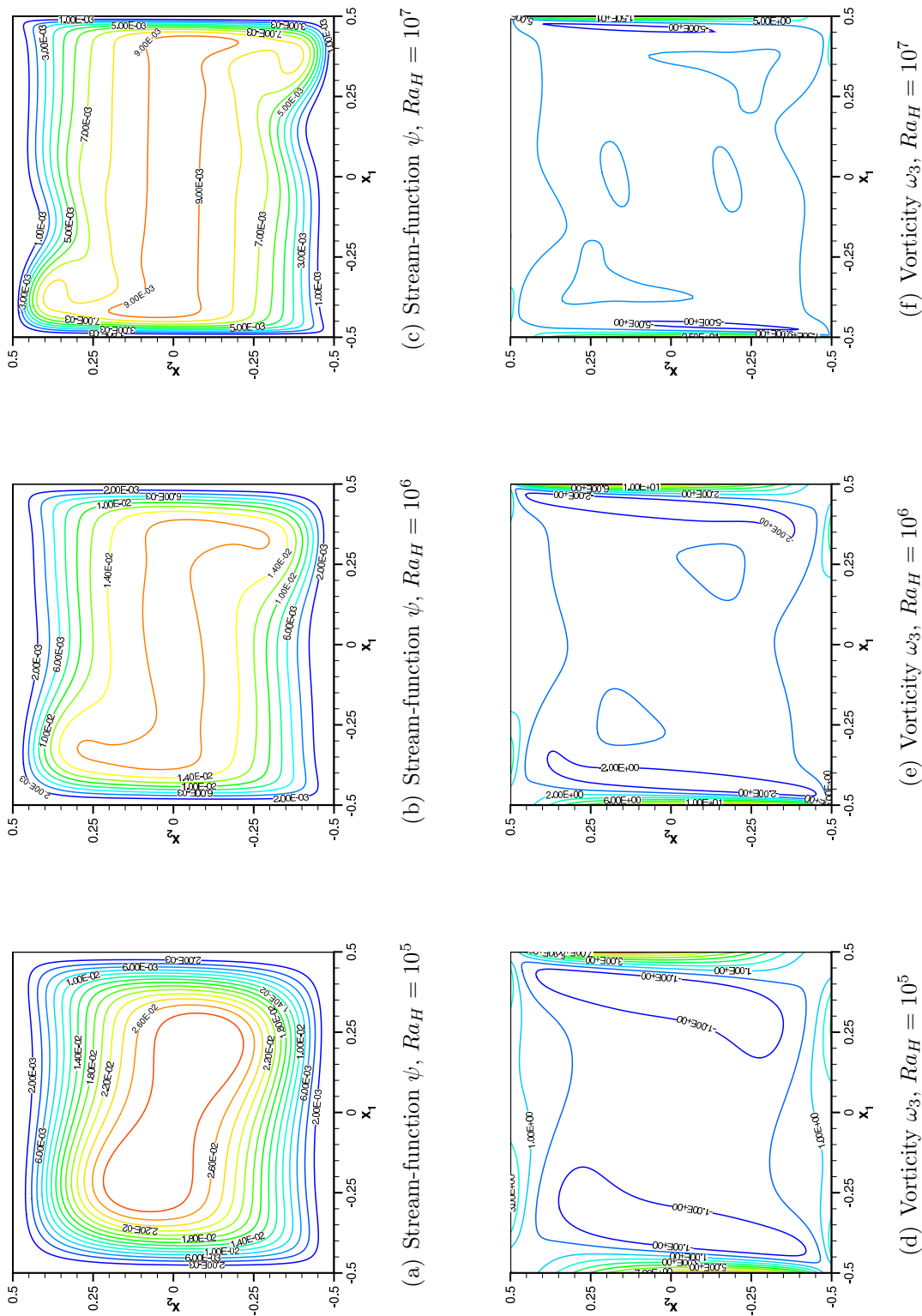
(e) Pressure p , $Ra_H = 10^6$

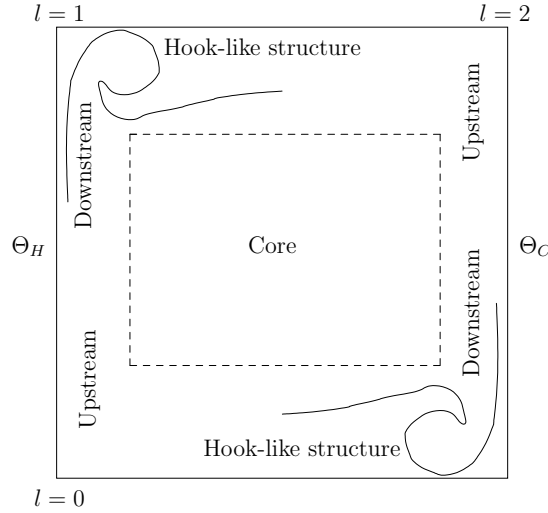


(f) Pressure p , $Ra_H = 10^7$

Fig. 3.3: Contour plots of temperature Θ and pressure p for $Ra_H = 10^5, 10^6, 10^7$.

Fig. 3.4: Contour plots of stream-function ψ and vorticity ω_3 for $Ra_H = 10^5, 10^6, 10^7$.





Results and discussion

The velocity, pressure, temperature fields together with the stream-function and vorticity are shown in Figs.3.2-3.4. First of all, it should be noted that for Rayleigh number $Ra_H = 10^5$ the velocity fields are characterized by interacting large horizontal boundary layers (BLs) with their maxima located at $x_1 \approx \pm 0.2$ close to the horizontal adiabatic walls. Moreover, the vertical BLs attached at the vertical walls already do not interact together and present maxima around mid-height. The temperature and pressure fields show the tendency to stratify in the core region, even if only the temperature field shows high gradients close to the vertical walls, stressing that the heat does not diffuse directly into the core but is convected by the flow in the upper/lower part of the cavity. The stream-function ψ presents two centro-symmetric lobes where it reaches its maxima. At Rayleigh $Ra_H = 10^6$ the horizontal BLs begin to split as shown in Fig.3.3(b), the high velocity regions become smaller and is shifted towards the upper and lower turning corners. The vertical BLs get narrowed as expected according to Eq.(1.33) and counter-flow is found in the immediately outer part of the vertical BLs. An increased stratification is depicted in the central region, even if the temperature near the adiabatic walls tends to be more uniform along the horizontal direction. The beginning of the formation of a hook-like structure can be seen in the stream-function Fig.3.4(b) (refer to the schema in Fig.3.1.1) where the two lobes now are completely separated. A further increasing of the Rayleigh number ($Ra_H = 10^7$) results in a very small increase of the maximum vertical velocity, thanks to the appropriate scaling, whereas the vertical boundary layers become thinner. In the outer part of the vertical plumes the presence of counter-flow is enhanced since the lobes leave the central region which is now almost quiescent. The horizontal BLs almost disappear because of the diffusion of momentum and temperature in the upper and bottom regions where the adiabatic walls reduce the stratification effect. The hook-like pattern

is now well established as it can be noted in Fig.3.4(c). Concerning the vorticity it is important to note that the maximum values are always located at the vertical boundaries, whereas at the horizontal adiabatic walls the zones of relatively high local vorticity get smaller in size.

More in detail, Fig.3.5 shows the vertical velocity component at the hot wall for three different heights ($x_2 = -0.3, 0, +0.3$) versus the scaled dimensionless distance from the wall

$$x^- := d Ra_H^{1/4} \quad (3.16)$$

where d is the given simply by

$$d = x_1 + 0.5 \quad (3.17)$$

It should be noted that the scaling proposed in Eq.(1.38) well represents the behavior at high Rayleigh numbers along the whole height of the cavity even if for $x_2 = +0.3$ the agreement is less satisfactory in the outer part of the BLs due to the presence of the developing hook-like structure. Besides that, although the scaling is perfectly respected at mid-height for all the Rayleigh, in the case of $Ra_H = 10^5$, the discrepancies are more important at the top and the bottom. The latter behavior is related to the difference in the temperature distribution in the regions closed to the horizontal adiabatic walls, which presents higher gradients in the horizontal direction than the cases at higher Rayleigh as already depicted in Fig.3.3(a). Moreover, a sensible discrepancy is encountered between the experimental [KJ83] and the computed profiles at half height. This behavior has been related to the fact that, in the experiment, the horizontal walls are not perfectly insulated as it will be shown later. The temperature BLs are shown along the vertical hot wall in Fig.3.6. It should be noted how the scaling proposed in Sec.1.1.3 for the thermal BL now performs well along the whole height and very close to the wall. Small discrepancies are encountered at the top corner where the hook-like structure is present. Temperature profiles on the vertical mid-line are presented in Fig.3.7 together with experimental results performed at $Ra_H = 1.89 \times 10^5$ by Krane *et al.* in [KJ83]. It is evident from the experimental results that the horizontal walls were not perfectly adiabatic showing how it is difficult to perform a direct comparison. It has been shown [SXJ⁺04] that even applying experimental temperature profile at the top and bottom walls does not solve completely the problem, suggesting that another effect can be the source of error in the computation like the presence of heat transfer due to radiation. To the author's knowledge there are very few works in the literature dealing with radiation in the differentially heated cavity flow [CCO04, WXL06, BBAHZ08] and the results do not clarify completely the issue. Moreover, it is worth to say that the absolute value of the temperature at the horizontal walls increases with the Rayleigh number due to stratification $\varsigma = \partial\Theta/\partial x_2$. In Fig.3.9 the shear stress at the

vertical hot wall, defined by

$$\tau_w := \frac{Pr}{\sqrt{Ra_H}} \left(\frac{\partial u_1}{\partial x_2} + \frac{\partial u_2}{\partial x_1} \right)_{x_1=-0.5} \quad (3.18)$$

and at the top horizontal wall, expressed by

$$\tau_w := \frac{Pr}{\sqrt{Ra_H}} \left(\frac{\partial u_2}{\partial x_1} + \frac{\partial u_1}{\partial x_2} \right)_{x_2=+0.5} \quad (3.19)$$

is plotted against the half perimeter length l starting from the left-bottom corner ($x_1 = x_2 = -0.5$) to the right-upper one clockwise (see schema in Fig.3.1.1). It is interesting to observe that the maximum value of τ_w at vertical hot wall ($0 \leq l \leq 1$) occurs before the location of the vertical velocity maximum, meaning that there is a play between the thickening and the increase of the vertical velocity which gives the maximum of the shear stress before the location of maximum velocity. Downstream the peak of shear stress, for $Ra_H > 10^5$ and $0.5 \leq l \leq 0.8$, there is a region characterized by linear decrease since the vertical component of velocity diminishes whereas the boundary layer continues to increase its thickness. At the ceiling ($1 \leq l \leq 2$) it deserves attention the case $Ra_H = 10^7$ where the shear stress is equal to zero, showing the beginning of detachment. Another point to stress is that the length of low shear stress gets larger with increasing the Rayleigh number, meaning that the horizontal momentum transfer at the top wall (and symmetrically at the bottom one) is strongly influenced by the adiabatic boundary condition which tends to increase the isothermal zones in the vicinity of the horizontal boundary, thus avoiding the formation of a thermal BL and as a consequence the formation of a natural convective BL. Finally, the scaled local Nusselt number defined in Eq.(3.12) is presented in Fig.3.10. It clearly appears that the maximum of the heat transfer occurs upstream at the very beginning of the BL formation. For a large section of the wall the Nusselt number decrease almost exponentially (linear zone) up to the point where the flow turns inside the cavity transferring momentum from the vertical component of velocity to the horizontal one. Further downstream the Nusselt number dramatically reduces.

3.2 Chaotic flows

Above the critical Rayleigh number $Ra_c^{2d} = 1.82 \times 10^8$ (see also [XL06]) the DHC flows get unsteady and reach the chaotic regime for $Ra_H \geq 10^9$. In order to study the statistical properties of these chaotic systems, two large databases have been created at $Ra_H = 10^9, 10^{10}$ using as initial conditions interpolated fields from solutions obtained at lower Rayleigh.

3.2. CHAOTIC FLOWS

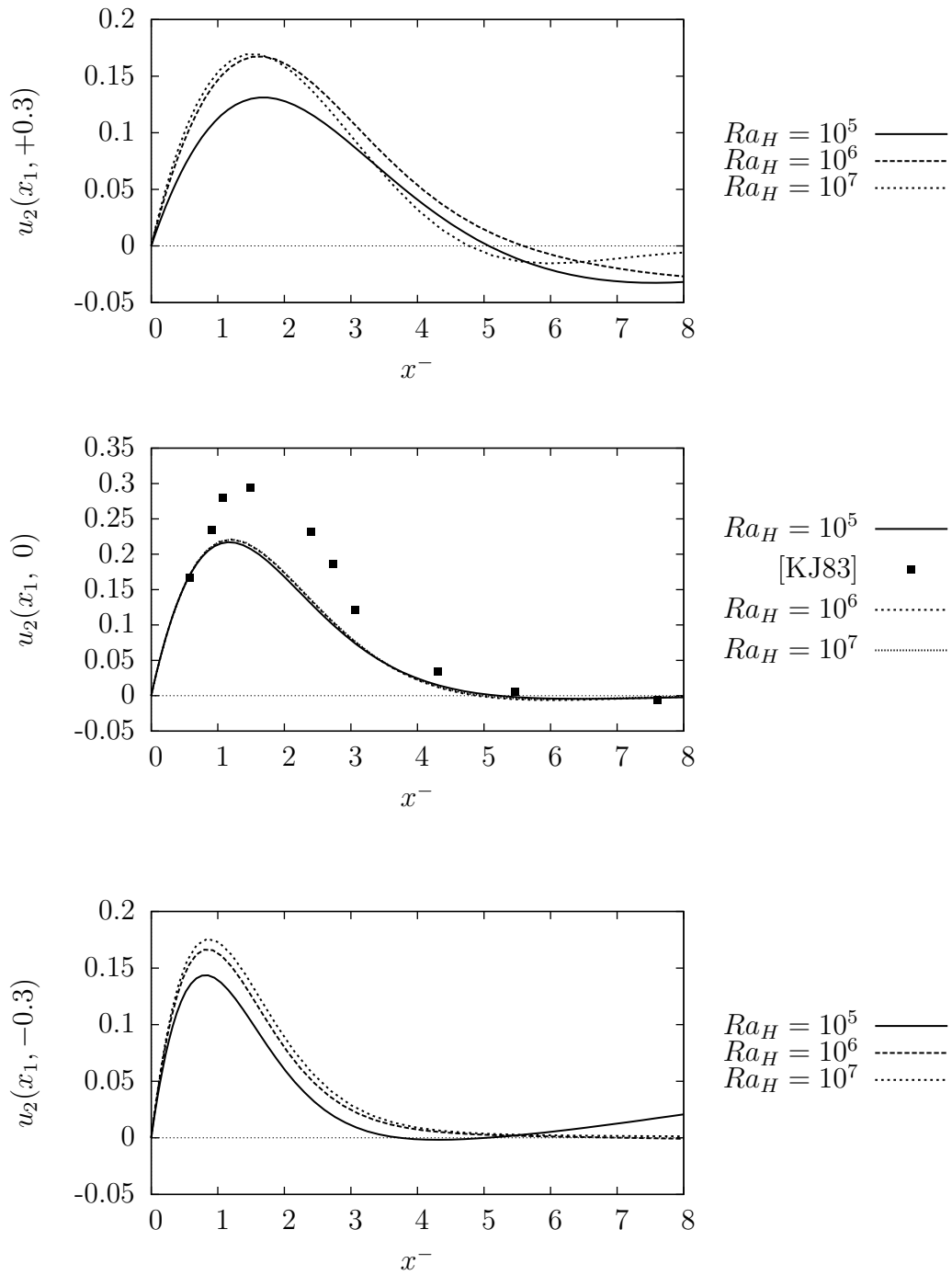


Fig. 3.5: Vertical velocity component profiles at different heights $x_2 = -0.3, 0.0, +0.3$ with respect to x^- .

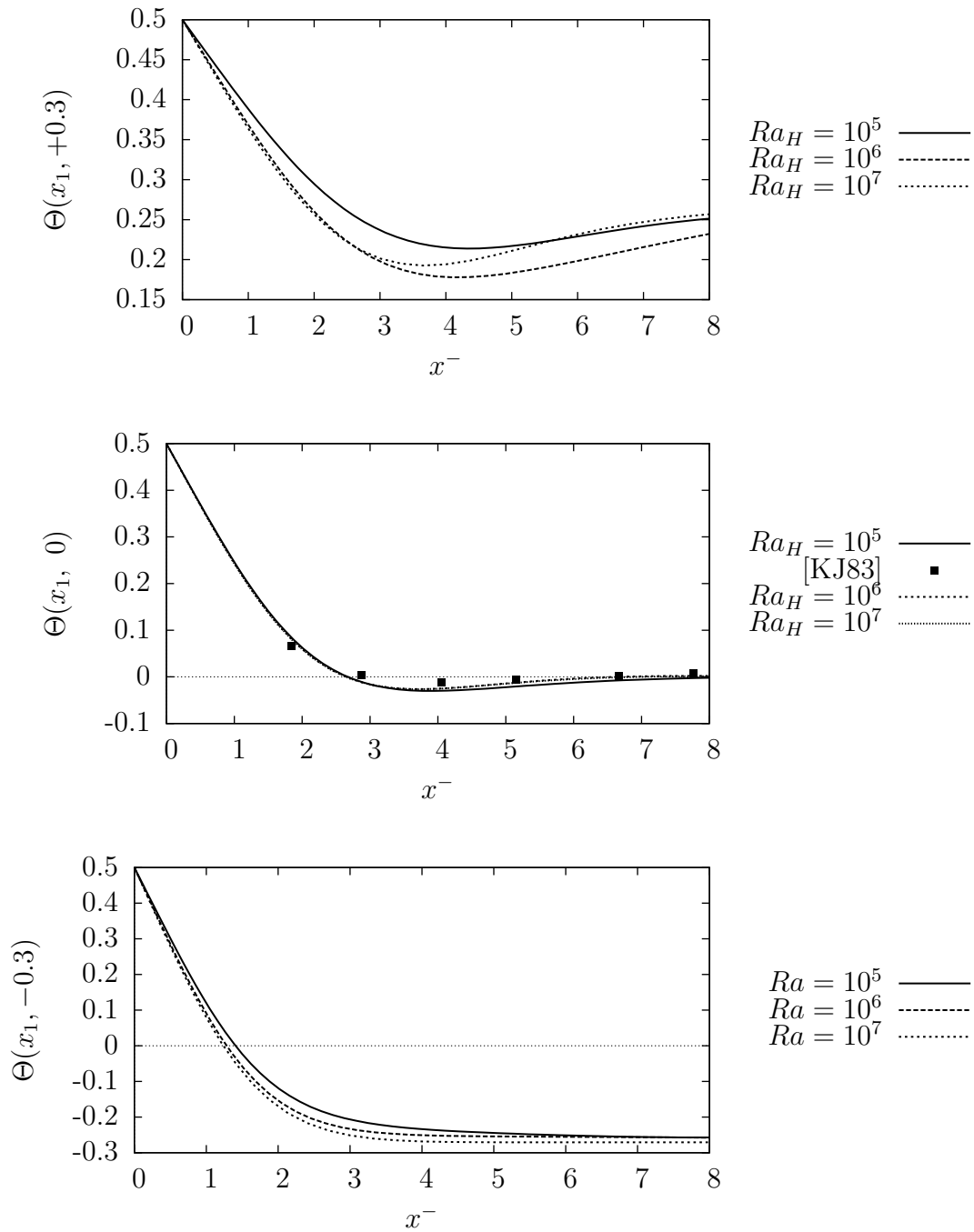


Fig. 3.6: Temperature profiles at different heights $x_2 = -0.3, 0.0, +0.3$ with respect to x^- .

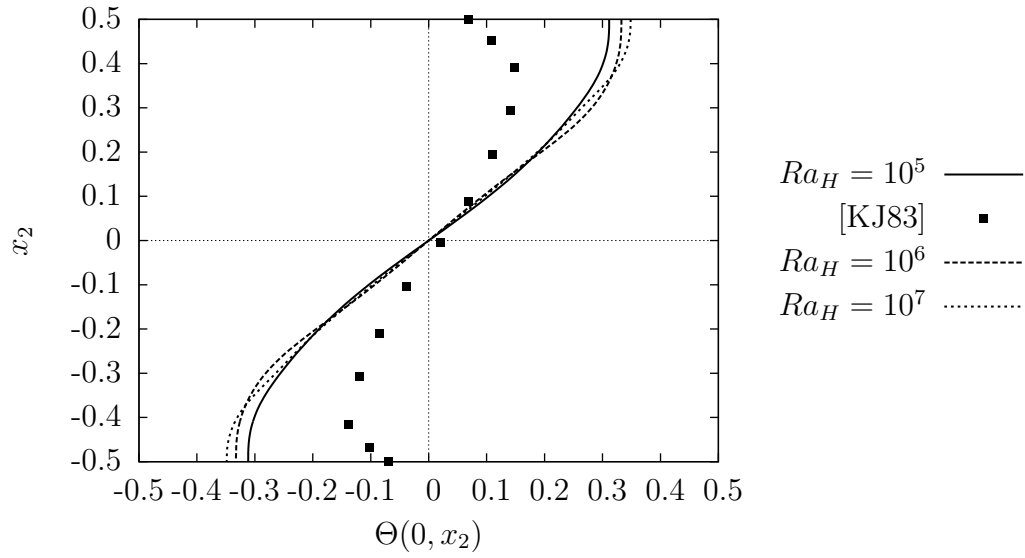


Fig. 3.7: Temperature profiles along the vertical mid-line $x_1 = 0$.

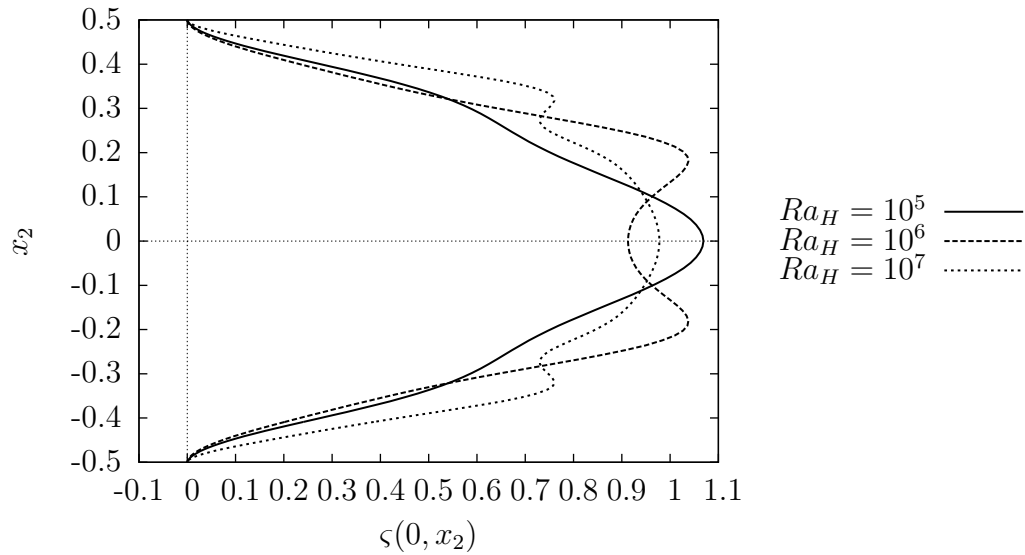


Fig. 3.8: Temperature stratification coefficient ζ along the vertical mid-line $x_1 = 0$.

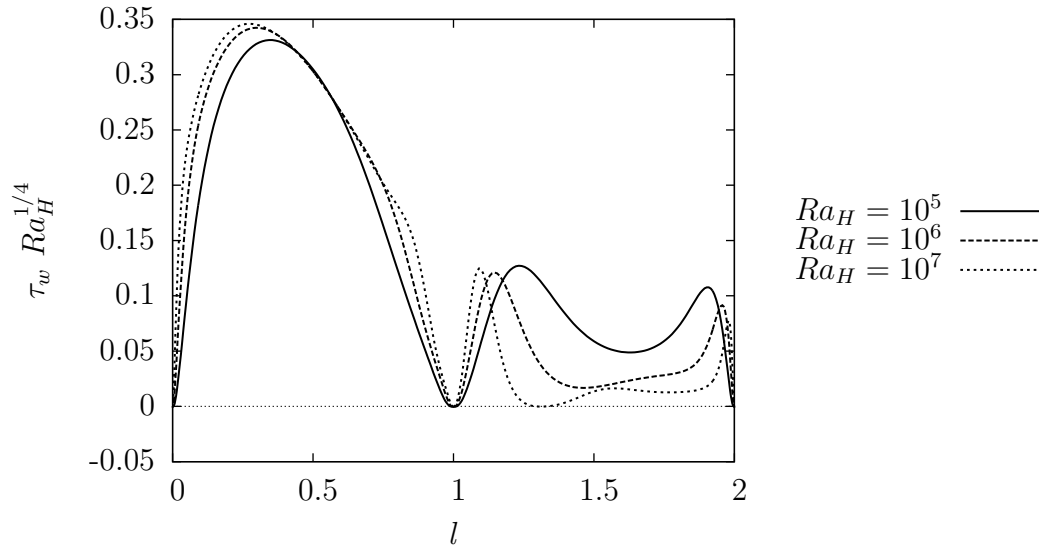


Fig. 3.9: Shear stress τ_w along the half cavity perimeter l .

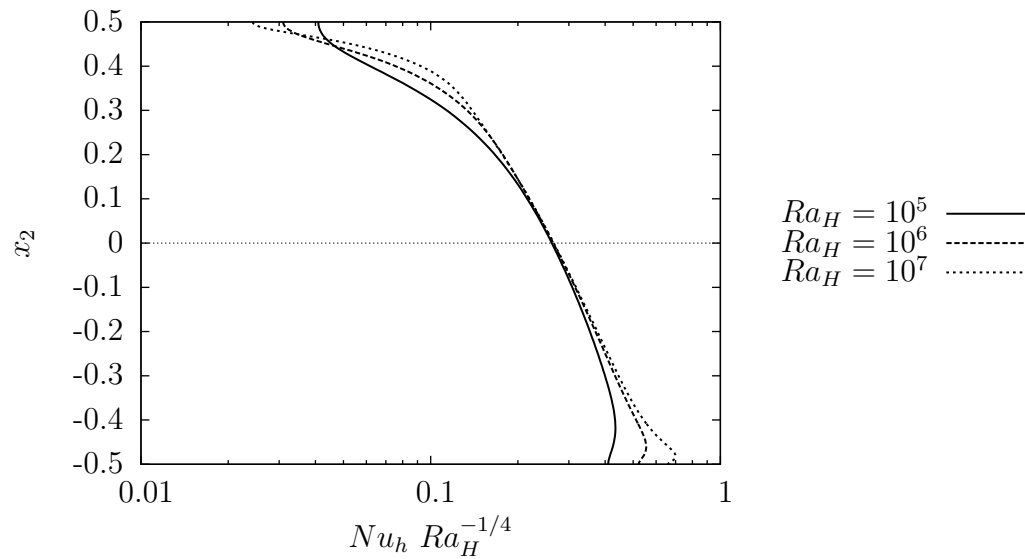


Fig. 3.10: Local Nusselt number profile at the hot wall.

3.2. CHAOTIC FLOWS

Ra_H	$N_1 = N_2$	$min(\Delta x_i)$	$max(\Delta x_i)$	$\Delta\tau$	Sampl. freq.	Ave. time	$max(\mathcal{S})$
10^9	257	3.8×10^{-5}	6.1×10^{-3}	2.5×10^{-3}	10	1050.0	1.40×10^{-8}
10^{10}	321	2.4×10^{-5}	5.0×10^{-3}	1.0×10^{-3}	20	1760.0	9.88×10^{-6}

Tab. 3.3: *Computational parameters: polynomial degrees N_1, N_2 , minimum and maximum grid size Δx_i , integration timestep $\Delta\tau$, number of frames per unit of time, averaging time and ratio of spectral coefficients .*

The possible influence in the statistics of a change in the boundary conditions at the initial stage of the computations has been avoided letting this numerical perturbations fading away before starting the sampling of the database. The number of iterations needed to dissipate the effect of a change in the boundary conditions depends on the difference between the Rayleigh numbers employed and the grid, but in general it is of the order $O(\sqrt{\Delta Ra_H})$ (see [PI80, LQB98]). The averaging time is taken sufficiently large to ensure low residuals in the time-averaged momentum and energy equations as will be discussed further on in the text. A summary of the computational parameters is provided in Tab.3.3. The author would like to stress again that these statistical quantities give informations which are not truly related to the actual turbulent flow which is intrinsically three-dimensional but illustrate in first approximation the trend and the basic features of the chaotic flows at high Rayleigh numbers.

Mean fields

According to the Reynolds decomposition, statistically steady fields with variables in time and space $\phi(\mathbf{x}, \tau)$ can be easily described as the sum of their mean value in time $\langle\phi(\mathbf{x})\rangle$ and their fluctuating component $\phi'(\mathbf{x}, \tau)$ resulting in

$$\phi(\mathbf{x}, \tau) = \langle\phi(\mathbf{x})\rangle + \phi'(\mathbf{x}, \tau). \quad (3.20)$$

In the following all the quantities indicated with $\langle\cdot\rangle$ and \cdot' represent the time averaged and fluctuating part of the field under investigation. The flow structures that characterize the laminar regime are also present in the averaged fields [LQB98], for instance the two separate velocity and thermal boundary layers at the active walls, the recirculating pockets at the downstream corners, the temperature stratification in the core region and the global centro-symmetry. The comparison of the mean horizontal component of velocity $\langle u_1 \rangle$ shown in Fig.3.11(a) and Fig.3.11(d) puts in evidence counter rotating currents in the core between the linear stratified zone and the lower and upper almost isothermal ones for the highest Rayleigh number. These counter rotating currents represent a departure from the laminar or slightly turbulent regimes previously published in the literature when

adiabatic horizontal walls are present, while it has been detected at lower Rayleigh numbers in [PD01] and other works where linear or experimental temperature profiles have been imposed as boundary condition at the horizontal walls. The vertical velocity profiles in Fig.3.11(b) and Fig.3.11(e) differ from the fact that at $Ra_H = 10^{10}$ the BL thickness drastically increases around $x_2 = 0.25$ at the hot wall and symmetrically at the cold wall. Thus, in those zones the loss of momentum is due to the transfer of momentum from the mean fields to the fluctuating ones which eventually will enhance the chaotic mixing and will influence the shear stress and the heat transfer at the walls. It is also important to note that the temperature stratified zone gets narrowed due to the diffusion which enlarges the almost isothermal upper and lower regions close to the adiabatic walls (Fig.3.12(a) and Fig.3.12(c)). For a more detailed discussion about the influence of the stratification and the sustainment of the internal gravity waves refer to [LQB98]. Moreover, the time-averaged stream-function shows two completely different patterns: for $Ra_H = 10^9$ (Fig.3.12(b)) the two recirculating pockets are still close to the upper-left and bottom-right corners, on the other hand for $Ra_H = 10^{10}$ the recirculating pockets are shifted towards the mid height (Fig.3.12(d)). Further on, the pressure field in Fig.3.11(f) at the highest Rayleigh presents modifications at the active walls where the transition of the BLs occurs. Time-averaged vertical velocity $\langle u_2 \rangle$ and temperature $\langle \Theta \rangle$ profiles at the hot wall are shown for three different altitudes ($x_2 = -0.3, 0.0, 0.3$), as function of the variable x^- defined as the distance from the wall scaled by $Ra_H^{-1/4}$, see Fig.3.13-3.14. The thermal scaling proposed in Eq.(1.37) works for the laminar or quasi-laminar regime ($x_2 < 0.1$) of the developing boundary layer, for both velocity and temperature, but when the layer becomes fully chaotic ($Ra_H = 10^{10}$) the present scaling fails. In fact the intense mixing registered at $x_2 = 0.3$ provokes a large decrease in the peak velocity, the absence of temperature local minima and a sensible increase of the BL thickness. One issue dealing with the boundary layer scaling is that in such closed geometries the turning of the impinging jets induced by the horizontal walls leads to a transfer of momentum from one velocity component to the other avoiding a single behavior in the transfer of momentum and heat in the boundary layer. In conclusion, the lack of momentum of the vertical boundary layer of the mean fields, when progressively reaching downstream the horizontal walls, is not only due to turbulent mixing, as occurs in natural convective boundary layers along an infinite flat plane, but also because of the interplay between the two components of velocity during the turn (this point will be discussed later on). This is also a reason for the inadequacy of the turbulent scales proposed so far in the literature.

The time-averaged temperature profiles along the vertical centerline are shown in Fig.3.15. It is clear that the linear stratified core region tends to reduce with the increase of the Rayleigh number and as observed in the laminar case (see Fig.3.7), the absolute value of the mean temperature at the horizontal walls increases. This leads to a configuration

where hotter and colder environments get closer in the middle, where secondary counter flows arise.

A simple way to identify the extension of the laminar boundary layers at the active walls is to look at the local transfer of momentum and heat. In fact, the transition region at the vertical layers is characterized by a sudden decrease of the mean shear stress and also the enhanced convective heat transfer due to the ejection of unsteady hot/cold buoyant eddies that will then dissipate in the upper/lower isothermal regions. In Fig.3.16 the profiles obtained for the two different Rayleigh numbers are plotted as function of l (the semi-perimeter starting from the bottom-left corner to the upper-right corner in clockwise direction). It is important to note that, unlike the steady-laminar solutions, the maximum value of τ_w shifts downstream from the hot wall for higher Ra_H and an almost constant shear stress region takes place at $0.8 \leq s \leq 0.9$ where the flow is fully turbulent, whereas for $Ra_H = 10^9$ the constant shear-stress region is rather narrowed, indicating that the flow is only weakly turbulent, or in the transition regime. As second instance, at the top horizontal wall it is possible to observe that the mean flow does not present the characteristic separation zone for $Ra_H = 10^{10}$, which is identified by zero shear stress for both detachment and reattachment (see Fig.3.16). Finally, the reader should note the small values in the shear stress along the horizontal wall, where the thermal boundary layer does not exist and the velocity BL is rather weak.

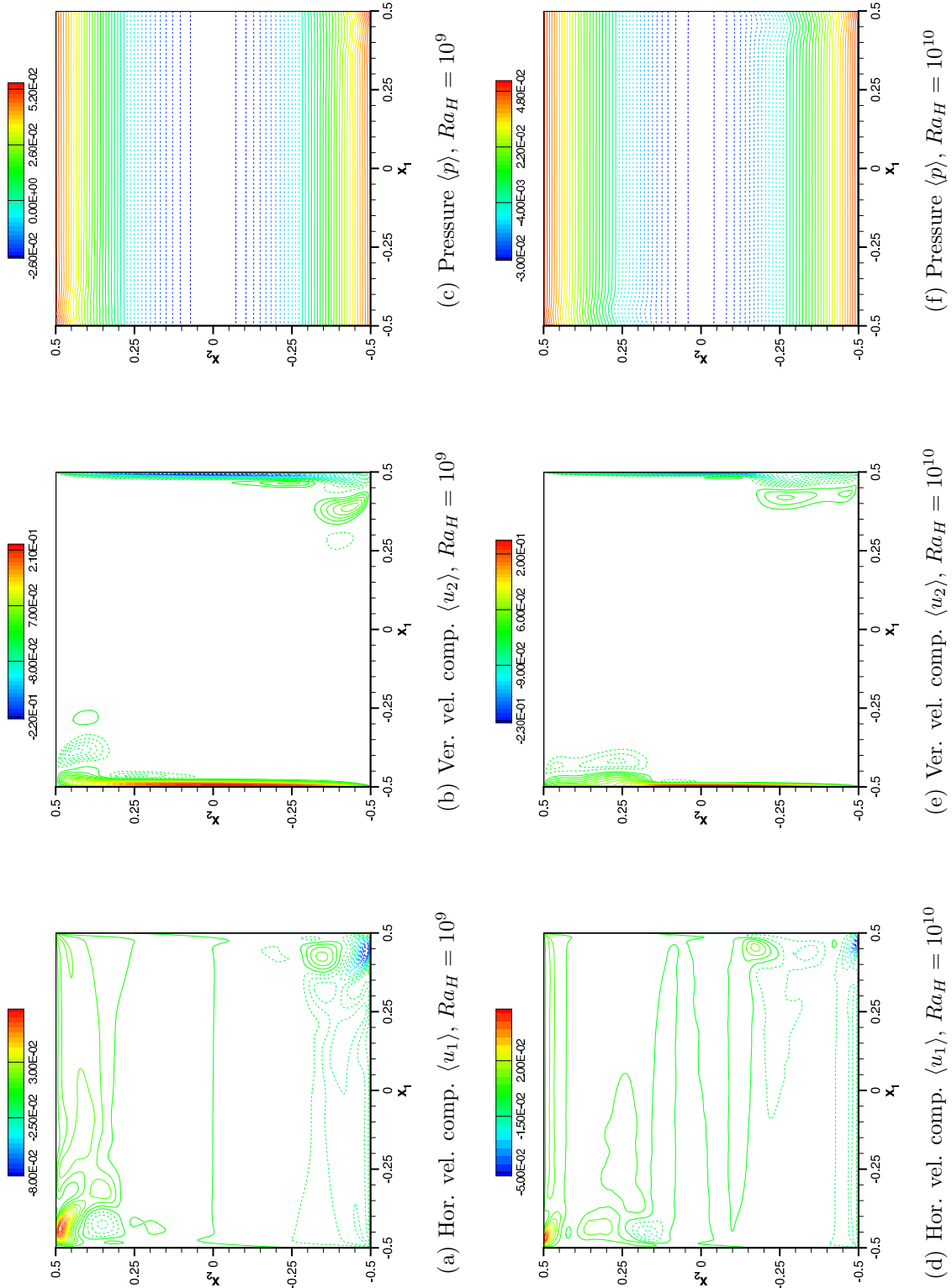


Fig. 3.11: Time-averaged velocity components and pressure contour plots at $Ra_H = 10^9, 10^{10}$.

Concerning the heat transfer at the active wall, the time averaged local Nusselt number $\langle Nu_h \rangle$ is presented in Fig.3.17. The heat flux is again maximum at the very beginning of the boundary layer but for the highest Rayleigh number a local maximum is depicted at $x_2 \approx 0.2$ due to transition to turbulence which breaks the exponential decay. Furthermore, the last downstream part of the vertical wall is more efficient regarding the heat transfer at high Rayleigh, probably because the corner pocket has shifted upstream.

Reynolds stresses and turbulent heat flux

The three independent components of the Reynolds stress tensor together with the two components of the turbulent heat flux are presented in Fig.3.18-3.19 . It is immediately clear that for $Ra_H = 10^9$ the intensity of the fluctuations is very high in the corner regions interested by the recirculating pockets and extends towards the opposite vertical wall due to the fact that the turning and the diffusion of the impinging jets is fully chaotic. Moreover, for the case $Ra_H = 10^{10}$ the maxima are located upstream where the BL becomes unstable, besides that the pattern of the fluctuation intensities and cross-terms, like $\langle u'_i u'_j \rangle$ and $\langle \Theta' u'_i \rangle$, develops more along the vertical direction than before. It is interesting also to note that the cross-terms $\langle u'_1 u'_2 \rangle$ and $\langle \Theta' u'_1 \rangle$ present positive values very close to the vertical boundaries for both Rayleigh numbers, whereas $\langle \Theta' u'_2 \rangle$ changes of sign, meaning that the turbulent mixing reduces the total mean flux in the vertical direction. It also appears (Fig.3.18(c) and Fig3.18(f)) that even if the BLs are laminar for at least two-thirds of the cavity height, the counter-flows in the outer part of the ascending/descending jets are more unstable producing a more chaotic environment just outside the thermal plumes.

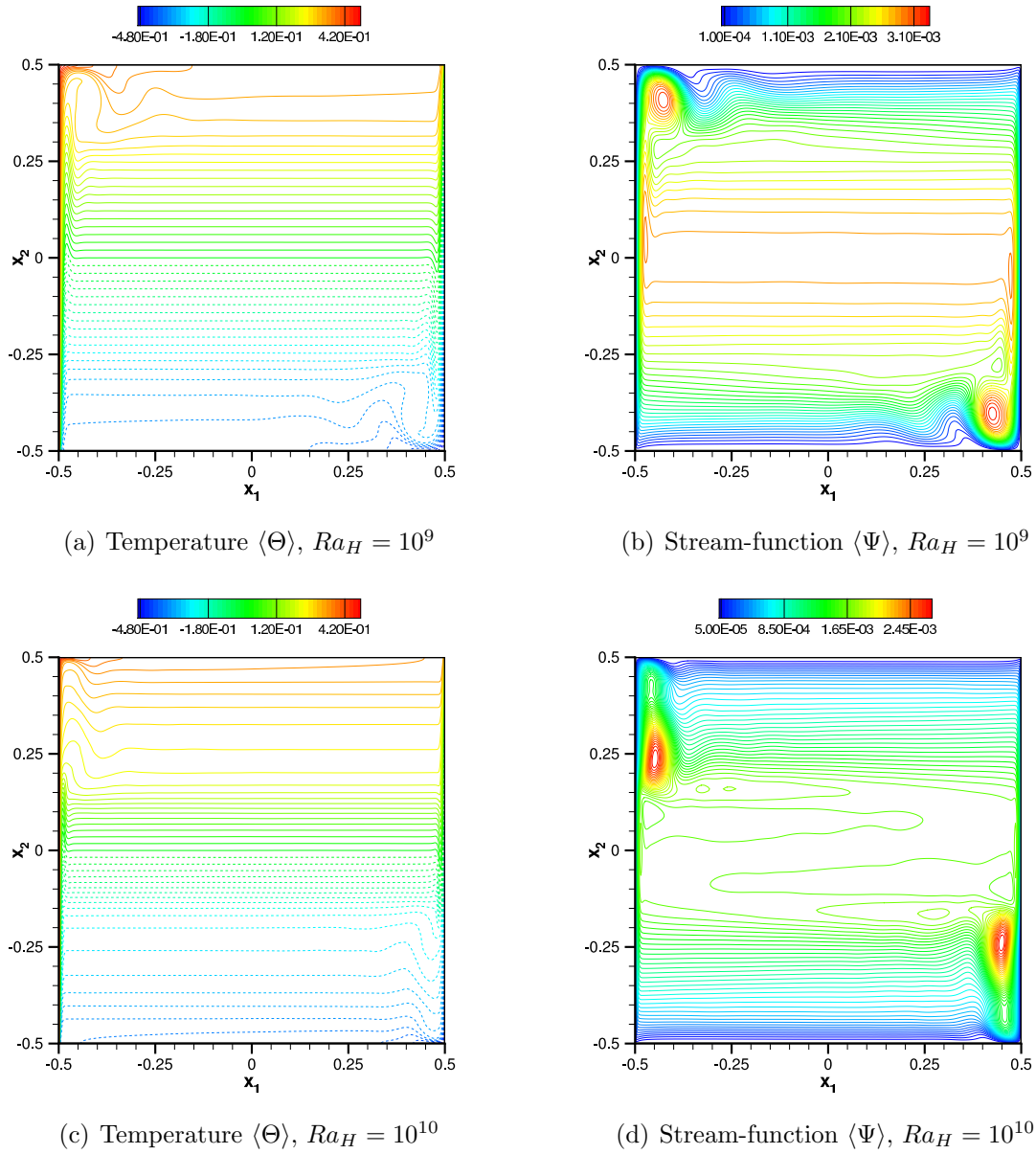


Fig. 3.12: *Time-averaged temperature and stream-function contour plots at $Ra_H = 10^9, 10^{10}$.*

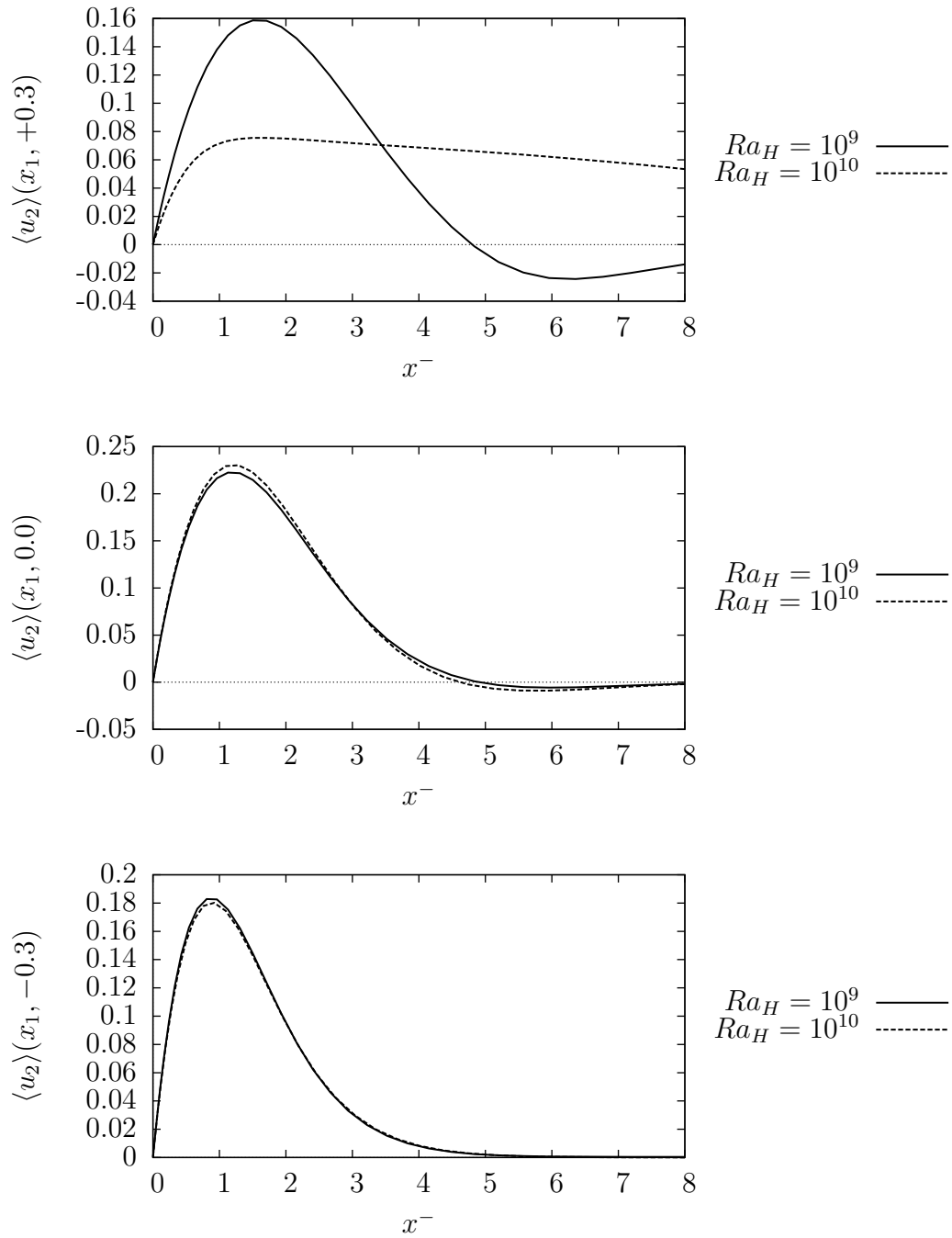


Fig. 3.13: Time-averaged vertical component velocity profiles at different heights $x_2 = -0.3, 0.0, +0.3$ with respect to x^- .

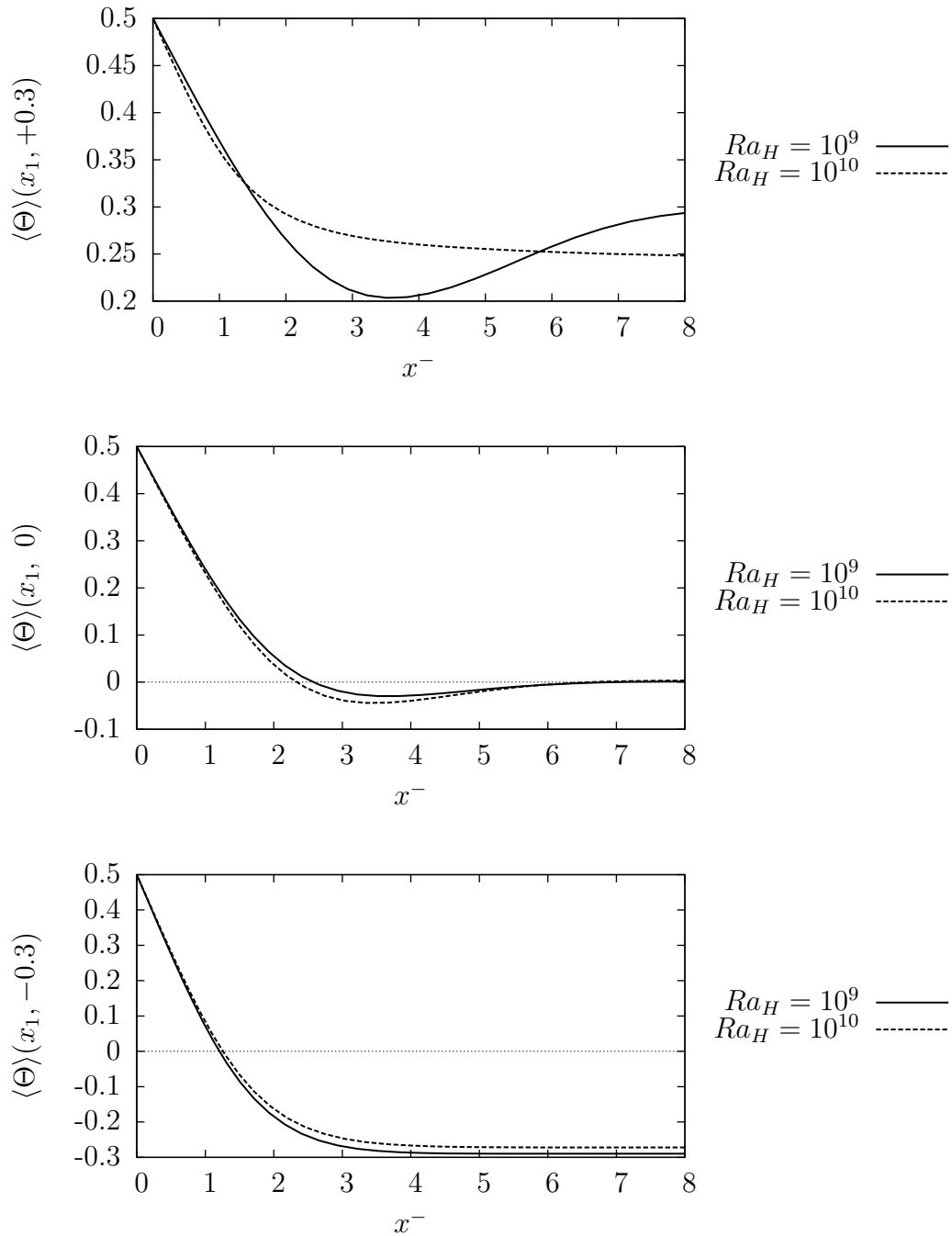


Fig. 3.14: Time-averaged temperature profiles at different heights $x_2 = -0.3, 0.0, +0.3$ with respect to x^- .

3.2. CHAOTIC FLOWS

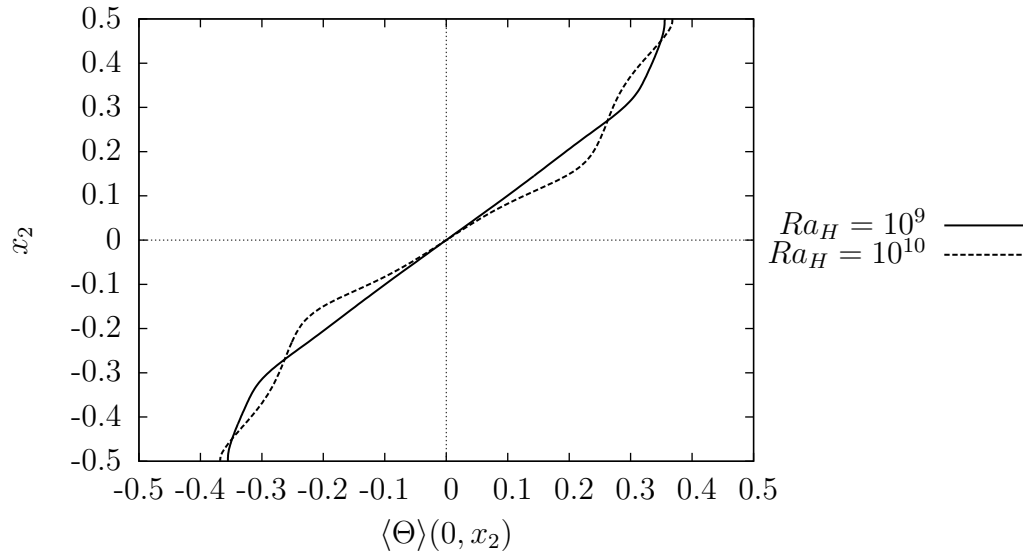


Fig. 3.15: Time-averaged temperature profile along the vertical center-line.

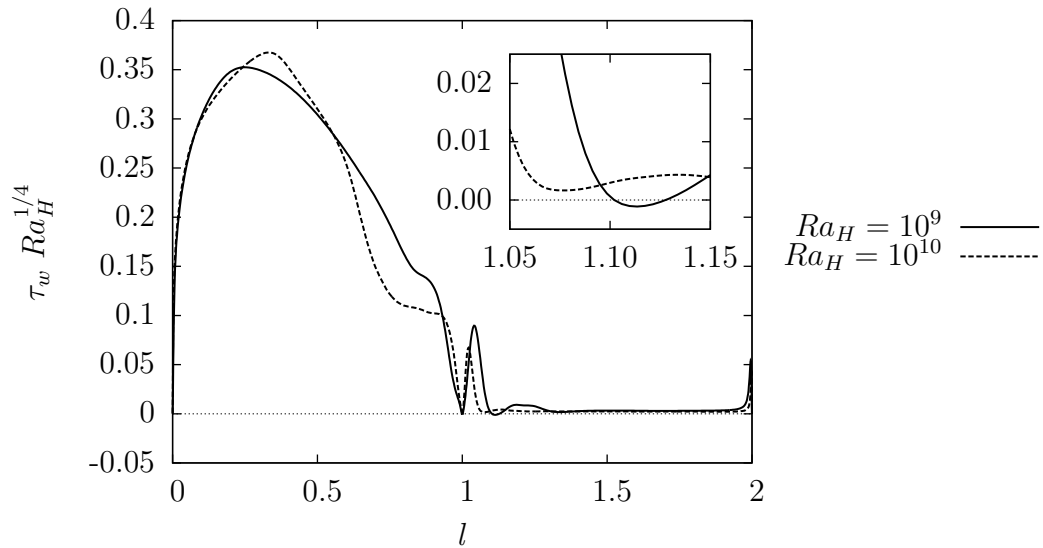


Fig. 3.16: Time-averaged shear stress $\langle \tau_w \rangle$ along the half cavity perimeter l .

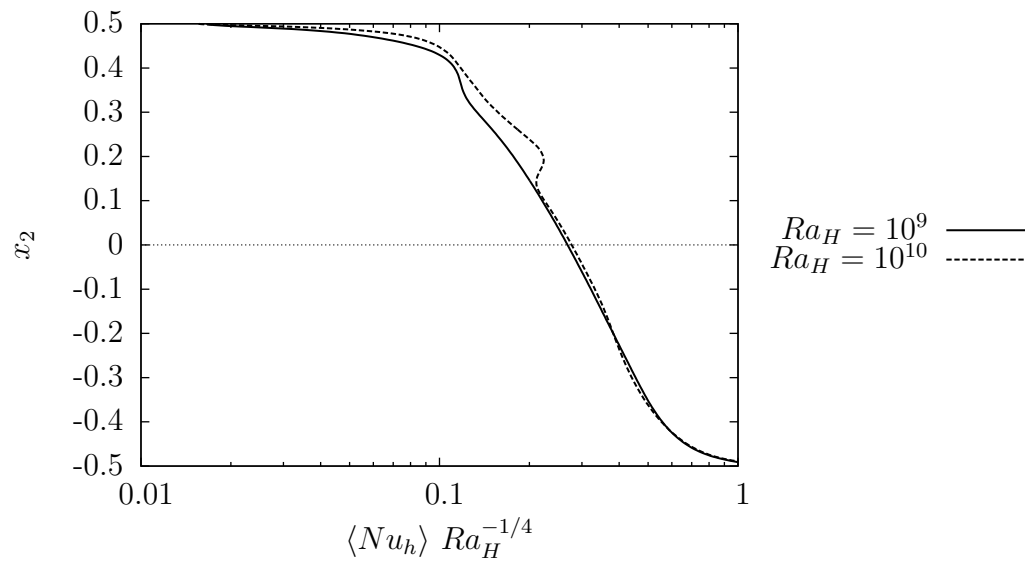


Fig. 3.17: *Time-averaged local Nusselt number $\langle Nu_h \rangle$ profile at the hot wall.*

3.2. CHAOTIC FLOWS

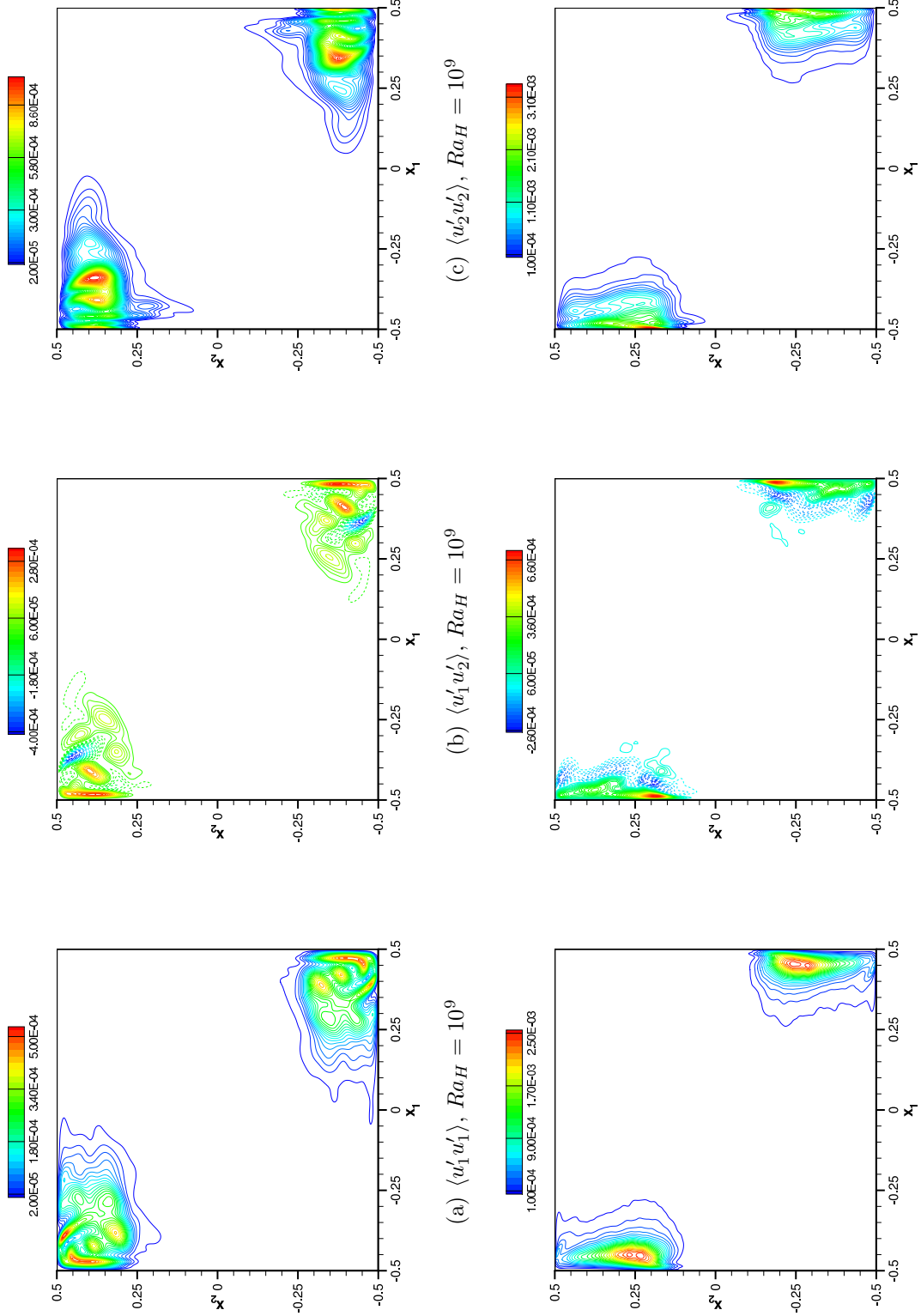


Fig. 3.18: Reynolds-stress components contour plots at $Ra_H = 10^9, 10^{10}$.

	$\ Res(\langle u_1 \rangle)\ _\infty$	$\ Res(\langle u_1 \rangle)\ _1$	$\ Res(\langle u_2 \rangle)\ _\infty$	$\ Res(\langle u_2 \rangle)\ _1$	$\ Res(\langle \Theta \rangle)\ _\infty$	$\ Res(\langle \Theta \rangle)\ _1$
$Ra_H = 10^9$	8.3×10^{-5}	1.2×10^{-6}	8.9×10^{-5}	1.2×10^{-6}	1.1×10^{-4}	1.5×10^{-6}
$Ra_H = 10^{10}$	5.3×10^{-4}	2.8×10^{-5}	3.5×10^{-4}	1.9×10^{-5}	4.1×10^{-3}	1.2×10^{-5}

Tab. 3.4: *Max-norm and 1-norm of the residuals R of the time-averaged momentum and energy conservation laws.*

3.2.1 Time-averaged momentum and energy budgets

The dimensionless governing equations of the mean quantities written with the Einstein convection read (see also [MY07])

$$\frac{\partial \langle u_i \rangle}{\partial x_i} = 0 \quad (3.21)$$

$$\frac{\partial \langle u_i \rangle}{\partial \tau} + \underbrace{\langle u_j \rangle \frac{\partial \langle u_i \rangle}{\partial x_j}}_{CTM} = - \underbrace{\frac{\partial \langle p \rangle}{\partial x_i}}_{PG} + \underbrace{\frac{Pr}{\sqrt{Ra_H}} \frac{\partial^2 \langle u_i \rangle}{\partial x_j^2}}_{VD} - \underbrace{\frac{\partial \langle u'_i u'_j \rangle}{\partial x_j}}_{RS} + \underbrace{Pr \langle \Theta \rangle \delta_{i2}}_{BT} \quad (3.22)$$

$$\frac{\partial \langle \Theta \rangle}{\partial \tau} + \underbrace{\langle u_i \rangle \frac{\partial \langle \Theta \rangle}{\partial x_i}}_{CTT} = \underbrace{\frac{1}{\sqrt{Ra_H}} \frac{\partial^2 \langle \Theta \rangle}{\partial x_i^2}}_{TD} - \underbrace{\frac{\partial \langle u'_i \Theta' \rangle}{\partial x_i}}_{THF}. \quad (3.23)$$

where $\langle u'_i u'_j \rangle$ and $\langle \Theta' u'_i \rangle$ are the Reynolds stress tensor and the turbulent heat flux respectively. For a statistically steady flow the accumulation terms, identified by the time-derivatives, are zero. Thus, the balances defined as the residual Res of the mean Boussinesq equations at every collocation point,

$$Res(\langle u_i \rangle) = \left| \langle u_j \rangle \frac{\partial \langle u_i \rangle}{\partial x_j} + \frac{\partial \langle u'_i u'_j \rangle}{\partial x_k} + \frac{\partial \langle p \rangle}{\partial x_i} - \frac{Pr}{\sqrt{Ra_H}} \frac{\partial^2 \langle u_i \rangle}{\partial x_j^2} - Pr \langle \Theta \rangle \delta_{i2} \right| \quad (3.24)$$

$$Res(\langle \Theta \rangle) = \left| \langle u_j \rangle \frac{\partial \langle \Theta \rangle}{\partial x_j} + \frac{\partial \langle \Theta' u'_j \rangle}{\partial x_k} - \frac{1}{\sqrt{Ra_H}} \frac{\partial^2 \langle \Theta \rangle}{\partial x_j^2} \right| \quad (3.25)$$

give a measure of the variation in time of the mean velocity and temperature fields which ideally should be zero. For the present calculations, in both cases the 1-norm of the residuals are of the order $O(10^{-4})$ or less, as shown in Tab.3.4. The low residuals in the averaged fields are a proof of the correctness of the sampling frequency and the length of the averaging time of the databases. In Fig.3.20 are shown some terms appearing in the vertical component of the averaged momentum equation (in particular the convective, pressure gradient and Reynolds stress terms). Focusing the attention on the hot wall ($x_1 = -0.5$), it is possible to see that above a certain height ($x_2 \approx 0.25$) apart from the laminar sublayer where the viscous effects are important, two terms contributes for the convective term, the pressure gradient and the Reynolds stresses. In particular the pressure

3.2. CHAOTIC FLOWS

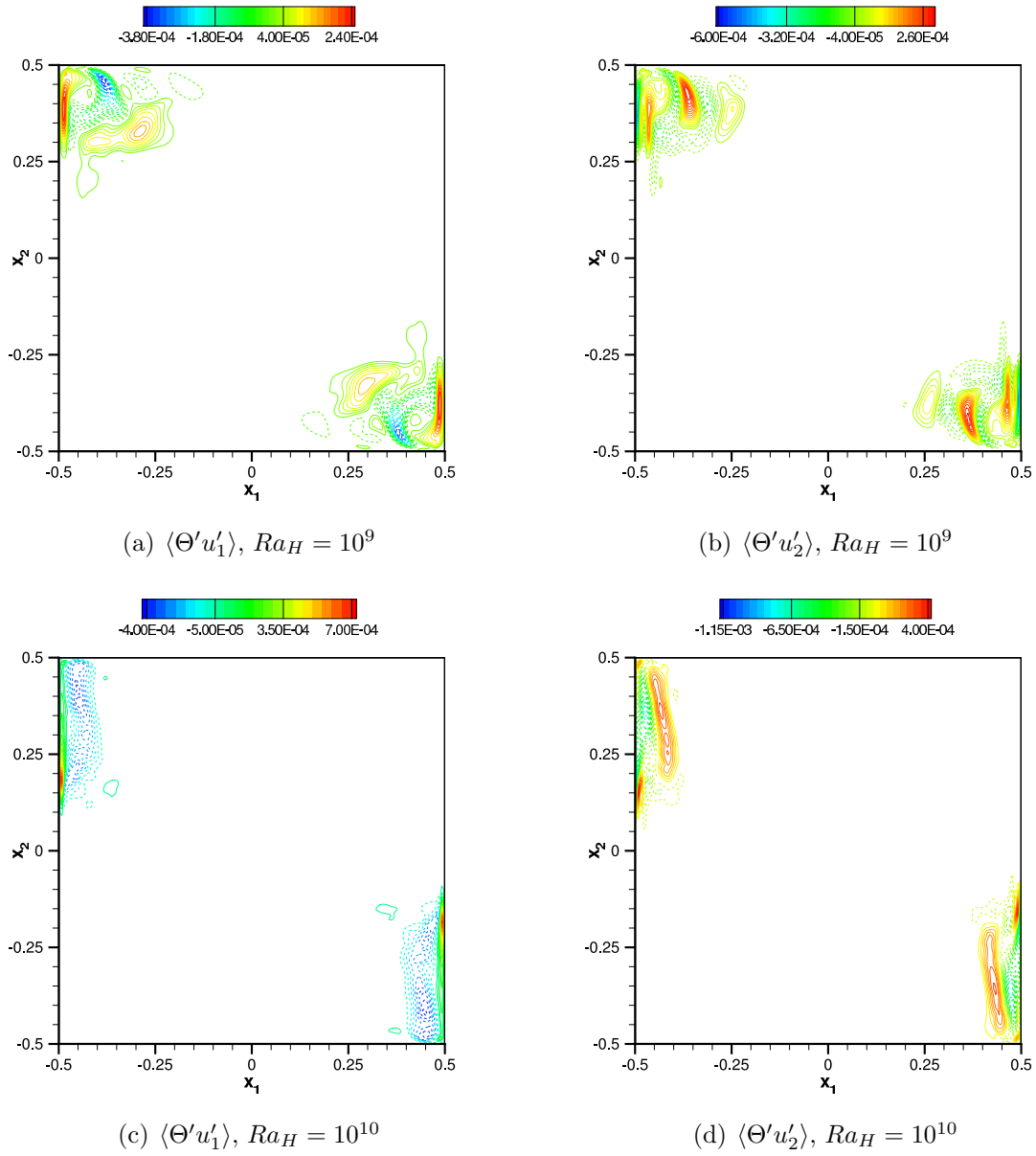


Fig. 3.19: *Time-averaged temperature and stream-function contour plots at $Ra_H = 10^9, 10^{10}$.*

gradient is the most important one when the fluid is obliged to turn at the cavity corner. Moreover, the maximum of the pressure gradient is not located at the wall as it would be expected for an impinging jet (with the manifestation of maximum pressure values due to the dynamic pressure) but it takes place slightly upstream. All the terms appearing in Eq.(3.22) for the vertical component of velocity are plotted along the horizontal and vertical centerlines in Fig.3.21-3.22 (the horizontal component is not shown because of relatively less importance), as well as the budgets of the energy equations in Fig.3.23-3.24. It is important to stress that close to the wall the Buoyancy Term (BT) is perfectly balanced by the Viscous Diffusion (VD) for both Rayleigh numbers, even if a small contribution is given by the convective terms around $x^- \approx 1$. In the vertical centerline the striking result is that the BT is balanced perfectly by only the Pressure Gradient (PG).

It is common idea that in natural convection the pressure field is not as important as in forced convection but it is actually strongly related to the vertical temperature field. This result can be explained by taking the divergence of Eq.(3.22), a Poisson operator for the time-averaged pressure is obtained:

$$\frac{\partial^2 \langle p \rangle}{\partial x_i^2} = Pr \frac{\partial \langle \Theta \rangle}{\partial x_2} - \frac{\partial^2 \langle u'_i u'_j \rangle}{\partial x_i \partial x_j} - \frac{\partial^2 (\langle u_i \rangle \langle u_j \rangle)}{\partial x_i \partial x_j}. \quad (3.26)$$

Since far from the active walls it is reasonable to assume $\partial \cdot / \partial x_1 \approx 0$ (in particular from the continuity equation Eq.(3.21) it comes $\partial \langle u_2 \rangle / \partial x_2 \approx 0$), and also $\langle u'_2 u'_2 \rangle \approx 0$, Eq.(3.26) simplifies in

$$\frac{\partial^2 \langle p \rangle}{\partial x_2^2} \approx Pr \frac{\partial \langle \Theta \rangle}{\partial x_2} \quad (3.27)$$

which integrated yields $\partial \langle p \rangle / \partial x_2 = Pr \langle \Theta \rangle + C$ where C is a constant to be determined. The boundary condition to apply can be found by simplifying with the same approach as before the second component of the mean momentum (Eq.3.22). This leads to impose the following boundary conditions at the horizontal adiabatic walls

$$\frac{\partial \langle p \rangle}{\partial x_2} (x_1, x_2 \pm 0.5) = Pr \langle \Theta \rangle (x_1, x_2 = \pm 0.5) \quad (3.28)$$

which leads to $C = 0$.

Concerning the energy budgets it is straightforward to see in Fig.3.23 that along the horizontal centerline the Convective Term (CTT) must be balanced only by the Thermal Diffusion (TD) because the flow is laminar, but in the vertical direction the influence of the turbulent fluxes is relatively sensible and gets the same order of magnitude as the other terms for very high Rayleigh numbers as shown in Fig.3.24.

3.2. CHAOTIC FLOWS

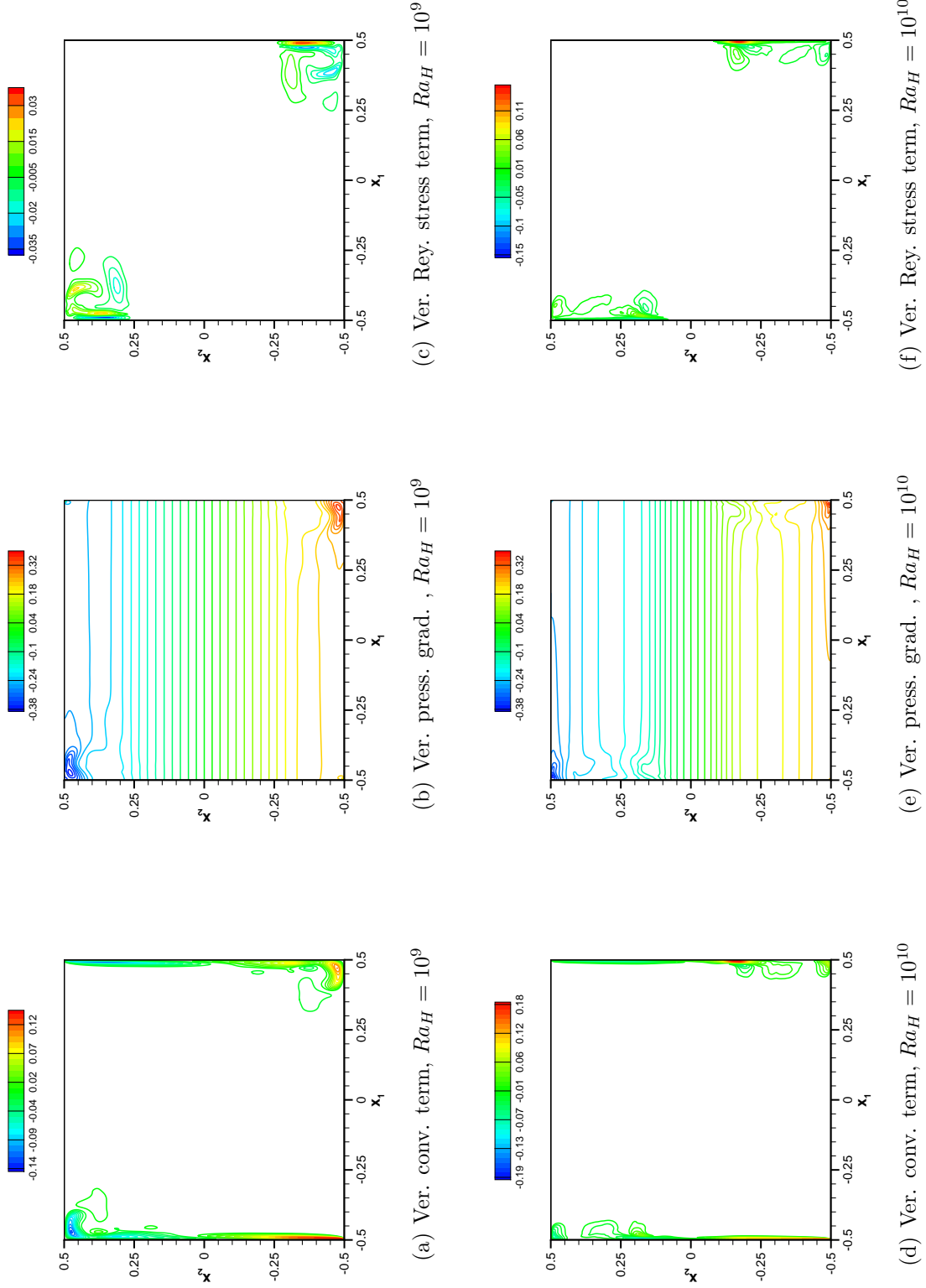


Fig. 3.20: Time-averaged vertical component of Convective, Pressure gradient and Reynolds stresses terms for $Ra_H = 10^9, 10^{10}$.

Ra_H	$\langle e \rangle Ra_H^{1/4}$	$\overline{\langle K \rangle} Ra_H^{1/4} (\%)$	$\bar{k} Ra_H^{1/4} (\%)$
10^9	7.43×10^{-2}	$6.63 \times 10^{-2} (89)$	$8.01 \times 10^{-3} (11)$
10^{10}	9.64×10^{-2}	$6.01 \times 10^{-2} (62)$	$3.63 \times 10^{-2} (38)$

Tab. 3.5: *Total averaged kinetic energy scaled by $Ra_H^{1/4}$ and its repartition between mean flow $\overline{\langle K \rangle}$ and fluctuating part \bar{k} with percentage.*

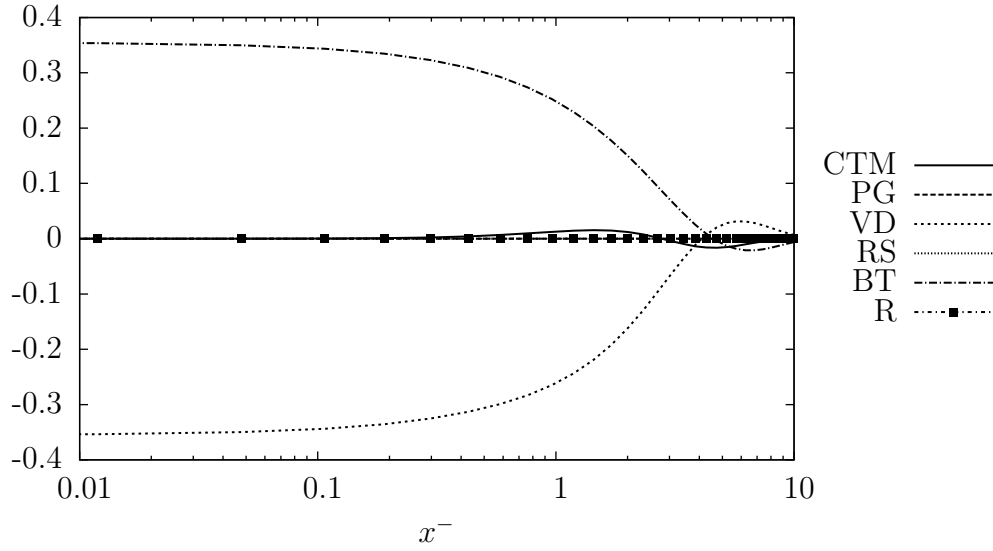
3.2.2 Turbulent kinetic energy and temperature variance budgets

In Tab.3.5 the averaged total kinetic energy $\langle e \rangle$, defined as

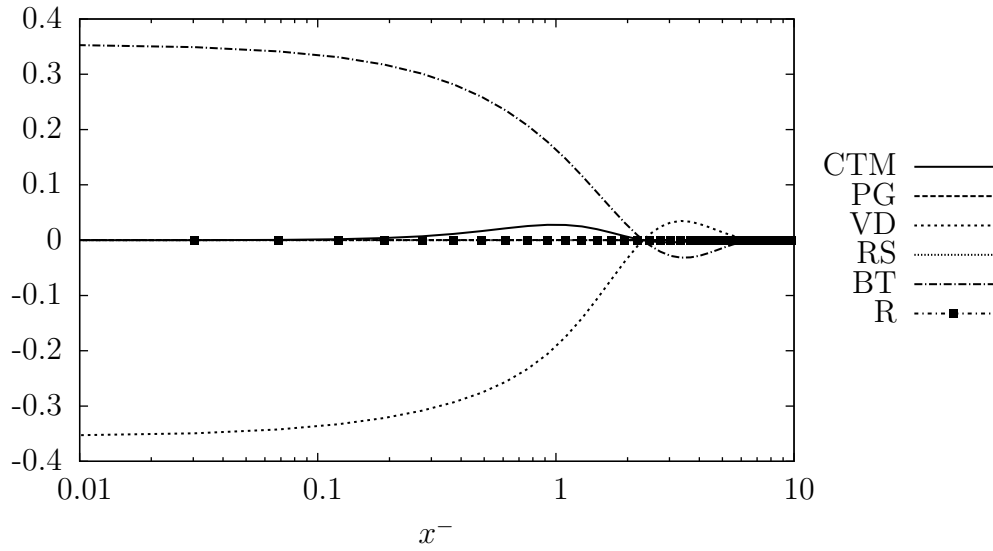
$$\langle e \rangle = \overline{\langle K \rangle} + \bar{k} = \int_{\Omega} \underbrace{\frac{1}{2} \langle u_i \rangle^2}_{\langle K \rangle} d\Omega + \int_{\Omega} \underbrace{\frac{1}{2} \langle u'_i u'_i \rangle}_{k} d\Omega \quad (3.29)$$

is reported together with its two components $\overline{\langle K \rangle}$ and \bar{k} . It is important to emphasize that the percentage of mean total specific kinetic energy contained in the fluctuating field k increases sensibly from 11% at $Ra_H = 10^9$ up to 38% at $Ra_H = 10^{10}$. The used scaling is justified by the fact that for a wide range of Rayleigh numbers the total kinetic energy scaled by $Ra_H^{1/4}$ is approximatively constant as depicted in Fig.3.25. This can be explained considering that the mass of fluid which contains the major amount of kinetic energy (i.e. in motion) scales as $\delta_{th.} \propto Ra^{-1/4}$ in comparison with the total mass of fluid contained in the cavity (see also [TSOPS07]). This holds for well established convective laminar and weakly turbulent flows, whereas it does not hold in the conductive regime $Ra_H < 10^4$ and probably for very high Rayleigh numbers. Iso-contours of the turbulent kinetic energy distribution k are shown in Fig.3.26(a)-3.26(c). As already mentioned, the regions of high fluctuating intensity are located at the corner. Furthermore, the k field gets wider and developed upstream the boundary layer for $Ra_H = 10^{10}$ confirming the earlier transition with respect to the lower Rayleigh number. According to the transport equation of the mean turbulent kinetic energy and temperature variance $\langle \Theta' \Theta' \rangle$

$$\begin{aligned} \frac{\partial k}{\partial t} + \langle u_j \rangle \frac{\partial k}{\partial x_j} &= \frac{\partial}{\partial x_j} \left(\frac{Pr}{\sqrt{Ra_H}} \frac{\partial k}{\partial x_j} - \langle u'_j k' \rangle - \langle u'_j p' \rangle \right) \\ \underbrace{- \langle u'_i u'_j \rangle \frac{\partial \langle u_i \rangle}{\partial x_j}}_P &\quad \underbrace{- \frac{Pr}{\sqrt{Ra_H}} \left\langle \frac{\partial u'_i}{\partial x_j} \frac{\partial u'_i}{\partial x_j} \right\rangle}_D \quad \underbrace{+ Pr \langle u_i \Theta' \rangle \delta_{i,2}}_G \end{aligned} \quad (3.30)$$

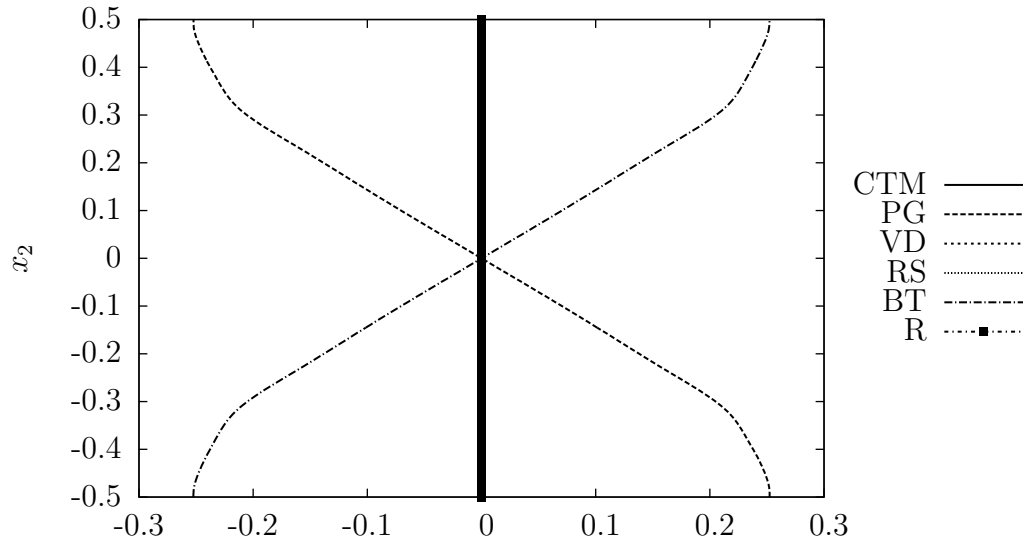


(a) $Ra_H = 10^9$

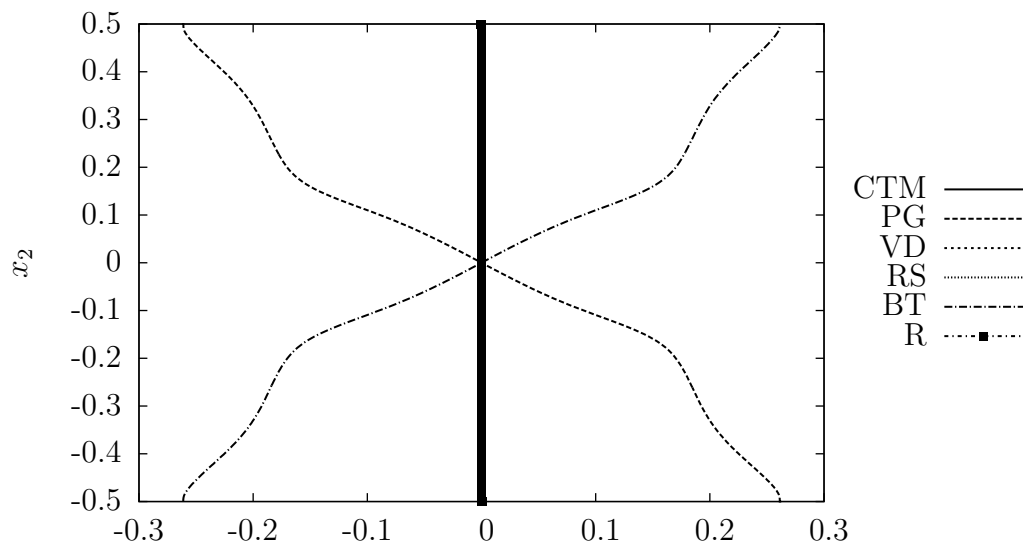


(b) $Ra_H = 10^{10}$

Fig. 3.21: Time-averaged Navier-Stokes budgets along the horizontal centerline ($x_2 = 0$) for $Ra_H = 10^9, 10^{10}$ with respect to x^- : Convective Term (CTM), Pressure Gradient (PG), Viscous Diffusion (VD), Reynolds Stresses (RS), Buoyancy Term (BT) and Residual (R).

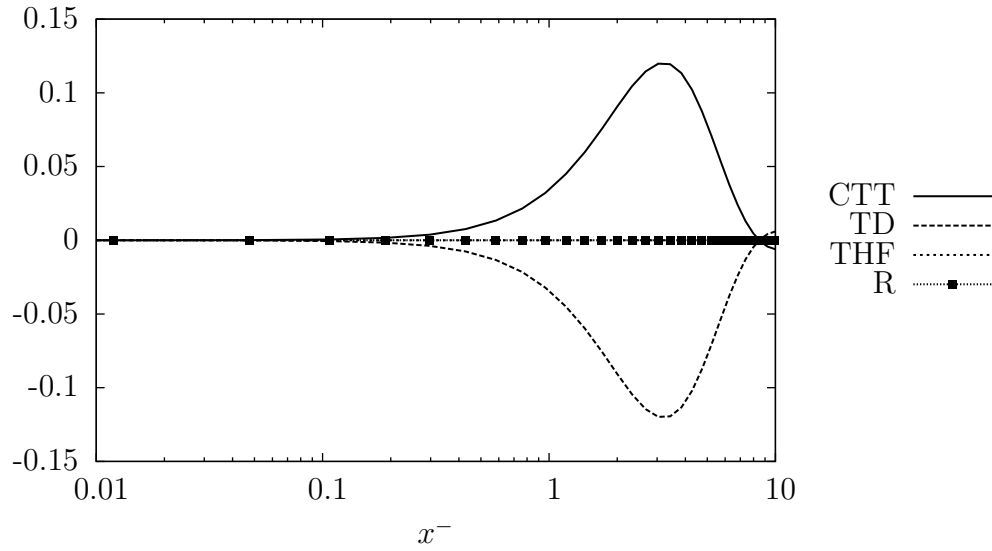


(a) $Ra_H = 10^9$

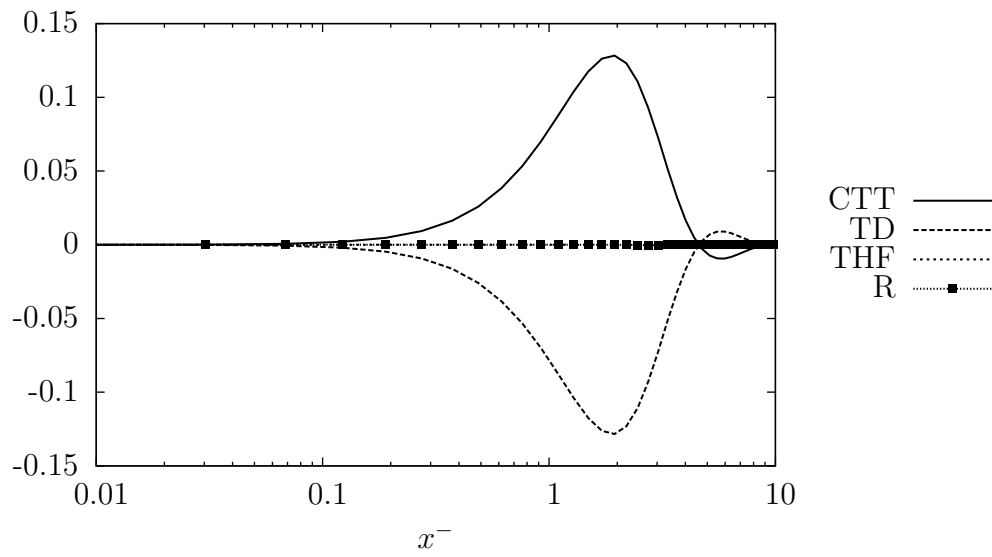


(b) $Ra_H = 10^{10}$

Fig. 3.22: Time-averaged Navier-Stokes budgets along the vertical centerline ($x_1 = 0$) for $Ra_H = 10^9, 10^{10}$: Convective Term (CTM), Pressure Gradient (PG), Viscous Diffusion (VD), Reynolds Stresses (RS), Buoyancy Term (BT) and Residual (R).

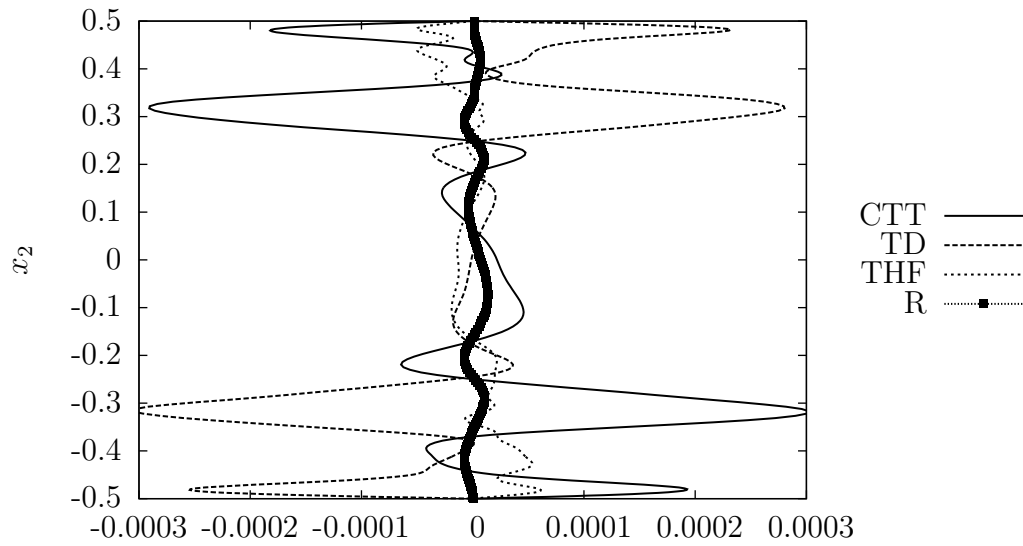


(a) $Ra_H = 10^9$

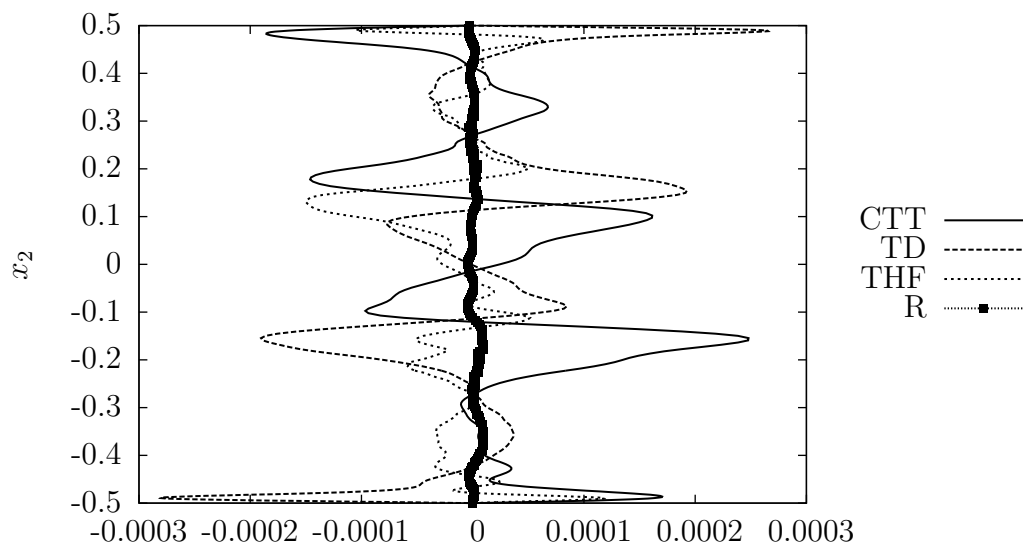


(b) $Ra_H = 10^{10}$

Fig. 3.23: *Time-averaged energy budgets along the horizontal centerline ($x_2 = 0$) for $Ra_H = 10^9, 10^{10}$ with respect to x^- : Convective Term (CTT), Thermal Diffusion (TD), Turbulent Heat Flux (THF) and Residual (R).*



(a) $Ra_H = 10^9$



(b) $Ra_H = 10^{10}$

Fig. 3.24: Time-averaged energy budgets along the vertical centerline ($x_1 = 0$) for $Ra_H = 10^9, 10^{10}$: Convective Term (CTT), Thermal Diffusion (TD), Turbulent Heat Flux (THF) and Residual (R).

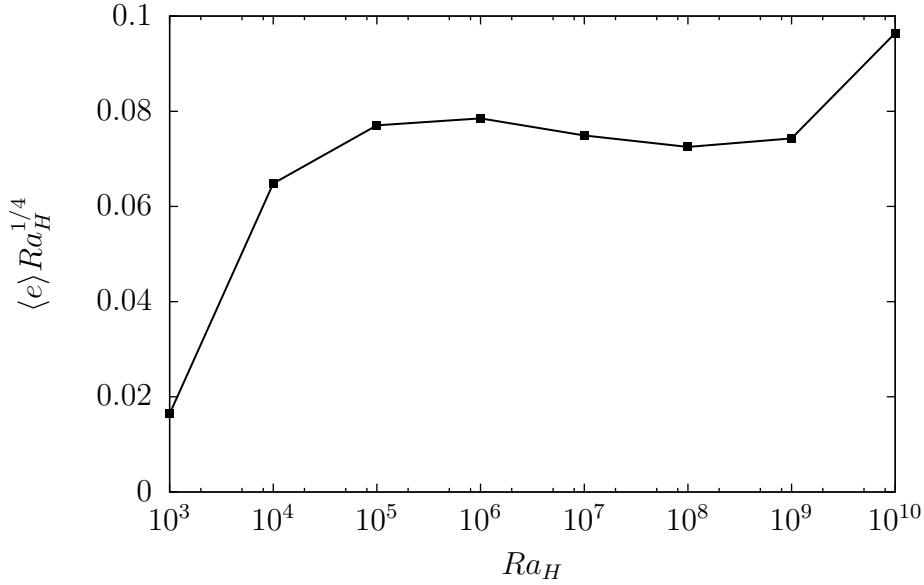


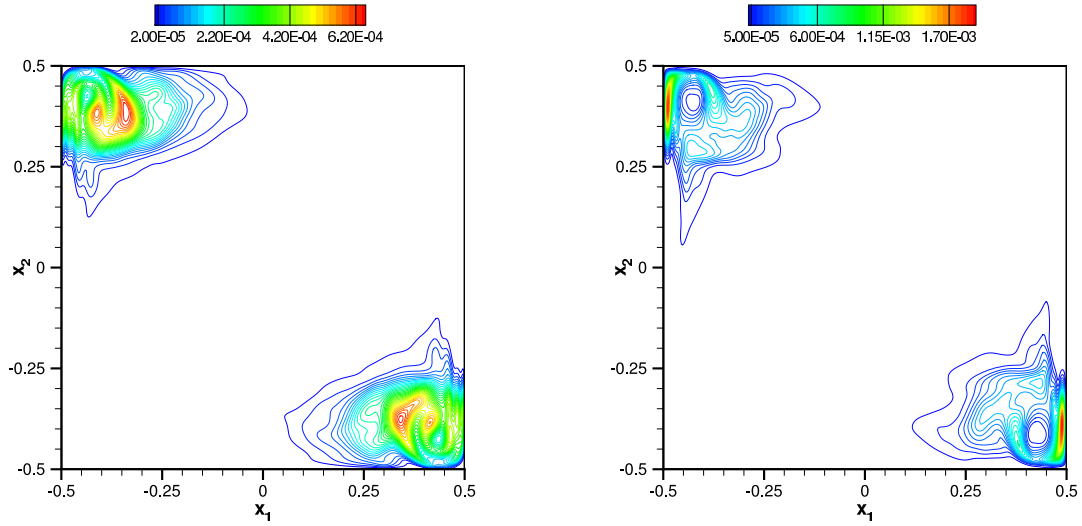
Fig. 3.25: Total kinetic energy scaled by $Ra_H^{1/4}$ as a function of Rayleigh number Ra_H .

	$\max P $ (x_1, x_2)	$\max G $ (x_1, x_2)	$\max D $ (x_1, x_2)	$\max P_\Theta $ (x_1, x_2)	$\max D_\Theta $ (x_1, x_2)
$Ra_H = 10^9$	2.3×10^{-3} (0.4819, -0.3403)	8.6×10^{-4} (0.4937, -0.3621)	3.5×10^{-3} (0.5000, -0.3536)	2.9×10^{-3} (0.4904, -0.3492)	2.4×10^{-3} (0.4991, -0.3826)
$Ra_H = 10^{10}$	9.3×10^{-3} (-0.4903, 0.1592)	1.7×10^{-3} (-0.4959, 0.1684)	1.3×10^{-2} (-0.5000, 0.1731)	2.0×10^{-2} (-0.4946, 0.1684)	2.0×10^{-2} (0.4999, -0.1959)

Tab. 3.6: Maximum values and position of turbulent kinetic energy and temperature variance production and dissipation.

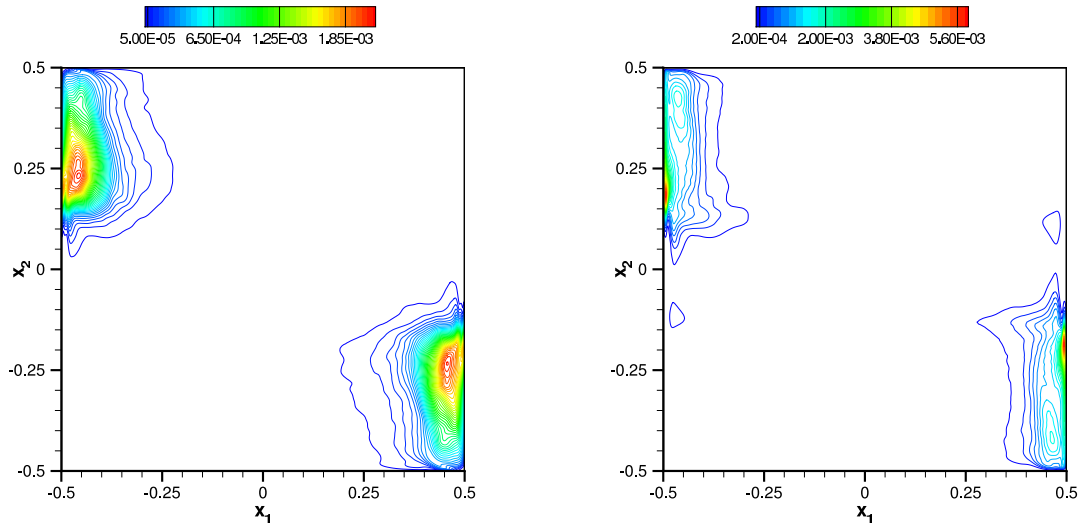
$$\begin{aligned}
 \frac{\partial \langle \Theta' \Theta' \rangle}{\partial t} + \langle u_j \rangle \frac{\partial \langle \Theta' \Theta' \rangle}{\partial x_j} &= \left(\frac{1}{\sqrt{Ra_H}} \frac{\partial \langle \Theta' \Theta' \rangle}{\partial x_j} - \langle u_j' \Theta' \Theta' \rangle \right) \\
 \underbrace{-2 \langle \Theta' u_j' \rangle \frac{\partial \langle \Theta \rangle}{\partial x_j}}_{P_\Theta} &\quad \underbrace{- \frac{2}{\sqrt{Ra_H}} \left\langle \frac{\partial \Theta'}{\partial x_j} \frac{\partial \Theta'}{\partial x_j} \right\rangle}_{D_\Theta}
 \end{aligned} \tag{3.31}$$

the terms that determine the production P , G , P_Θ and dissipation D , D_Θ , are shown in Fig.3.27 as function of x^- for $x_2 = 0.3$ and their maximum values in the entire domain are given in Tab.3.6. The maximum of k along the line is located between $10 \leq x^- \leq 25$, moreover it is interesting to mention that for $Ra_H = 10^{10}$ the profile is monotone up to the peak while for $Ra_H = 10^9$ presents several local maxima and minima. This is due to the fact that, in the latter case, the profile is measured where the vertical boundary layer gets unstable and ejects eddies, whereas outside the unstable boundary layer the fluctuations



(a) Turbulent kinetic energy k , $Ra_H = 10^9$

(b) Temperature variance $\langle \Theta' \Theta' \rangle$, $Ra_H = 10^9$



(c) Turbulent kinetic energy k , $Ra_H = 10^{10}$

(d) Temperature variance $\langle \Theta' \Theta' \rangle$, $Ra_H = 10^{10}$

Fig. 3.26: Turbulent kinetic energy and temperature variance contour plots at $Ra_H = 10^9, 10^{10}$.

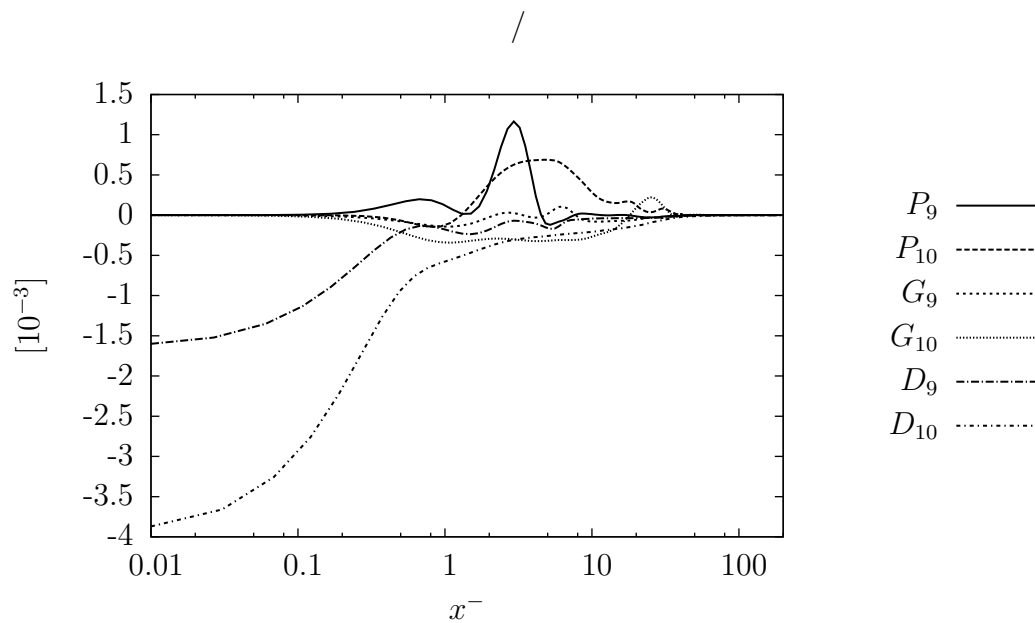
coming from the large corner recirculating pocket are more intense. On the other hand for $Ra_H = 10^{10}$ both the ejection of eddies and the recirculating pocket are located upstream the measuring line. Comparing the terms of production P in Fig.3.27(a) the reader should note that at $x^- \approx 0.75$ the production term $P_{10} < 0$ whereas $P_9 > 0$ leading to a completely different mechanism of sustainment of the mean turbulent kinetic energy, furthermore for $10 \leq x^- \leq 25$, P_{10} is significantly larger than P_9 .

Concerning the production due to buoyancy G , it appears that for high Rayleigh number this term dissipates the mean turbulent kinetic energy suggesting that $\langle u'_2 \Theta' \rangle < 0$. In fact, in a thermally stably stratified medium a vertical displacement of a fluid particle results in a local negative fluctuation of temperature and vice versa for a negative vertical displacement. This explanation, however does not apply for $Ra_H = 10^9$ where G_9 is slightly positive. The reason can be found on the local temperature profile which shows neutral or even unstable stratification in the neighborhood. About the viscous dissipation terms D , they are maximum at the wall and fast decrease before $x^- = 1$ even if D_{10} remains larger than D_9 and comparable with G_{10} further deep in the core of the cavity. The temperature variance $\langle \Theta' \Theta' \rangle$ iso-contours are shown in Fig.3.26(b)-3.26(d). The regions interested by high temperature variance activity are also those where the terms of $\langle \Theta' \Theta' \rangle$ are plotted in Fig.3.27(b). Unlike the production term in the mean turbulent kinetic energy, P_Θ is positive for both cases even if it approaches zero for $x^- \approx 7.5$ at $Ra_H = 10^9$ because of the almost neutral stratification as said before. On the other hand the dissipation D_Θ becomes really important at $Ra_H = 10^{10}$ and close to the wall.

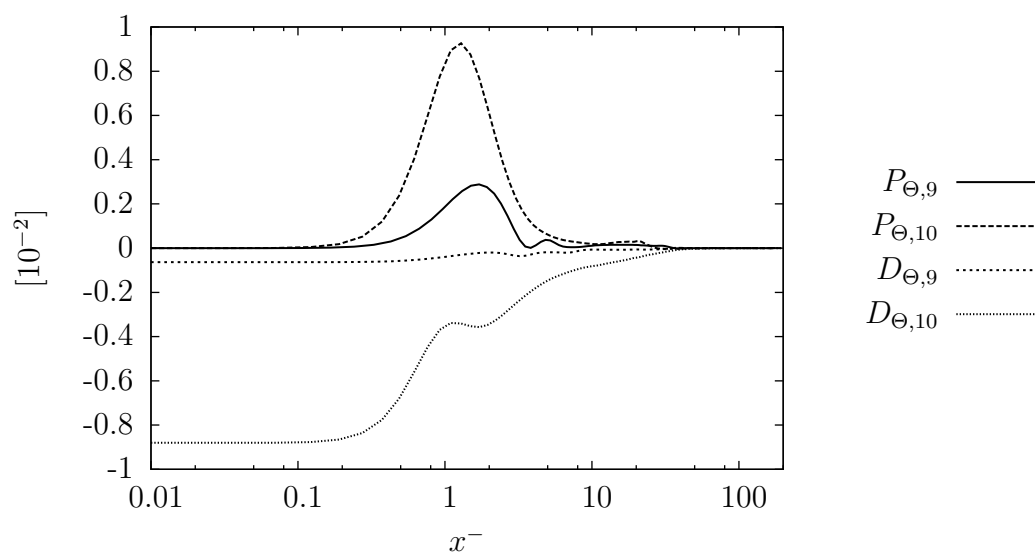
3.3 Particle deposition

The mechanisms of particle sedimentation in closed geometries with turbulent natural convective currents represent an important issue for example in nuclear engineering: during a severe nuclear accident in a Pressurized Water Reactor (PWR) which involves the rupture of at least one pipe of the steam generator bundle of the primary side for instance [CHGR⁺03]. The water coolant, which is in direct contact with the radioactive fuel rods, is sprayed through the rupture in the steam generator vessel and in the most dangerous case further aerosol leakage can contaminate the containment environment. The recirculating currents are caused by the temperature difference between hot walls and other surfaces due to the melting of the core and the cold walls affected by steam condensation. From an engineering point of view the most important parameter for the design of the different containment ambients is the deposition velocity C_d which relates the instantaneous density flux of aerosol j_p through the particle concentration C_p [Ree83]. The relation reads simply

$$j_p = C_d C_p. \tag{3.32}$$



(a) Turbulent kinetic budgets



(b) Temperature variance budgets

Fig. 3.27: Budget profiles of the turbulent kinetic energy transport equations and temperature variance transport equation for $Ra_H = 10^9, 10^{10}$ along the horizontal line $x_2 = +0.3$.

It has been proved from experiments and computations that in forced bounded flows the deposition velocity is function of the particle Stokes number [LA74, RS76, Ree83]. It is also known that after a certain amount of time, particles of a given diameter accumulate in the the laminar sub-layer in regions delimited by instantaneous regions of low speed (the so called low speed streaks). Moreover the turbulent instantaneous realization of the Reynolds stresses generates sweep and ejection events that mix the particles to fill always the same amount of volume, leading to a constant averaged deposition velocity in time (i.e. the concentration of the dispersed phase is expressed by an exponential decay law). As it will be shown later, in the present case, the mechanism of sweeps and ejections does not hold at the horizontal walls, because of the lack of strong and turbulent boundary layer, and only partially at the active vertical walls, the deposition velocity exhibits a strong dependency in time during the first few seconds after particle release (this is mainly due to the choice made for estimating the particle concentration).

The computational parameters for the particle simulations are summarized in Tab.3.7.

When the flow is well established, one hundred thousand particles are injected at the same time inside the domain at random positions, each particle having a velocity equal to the fluid velocity. The particle tracking is carried on together with the fluid in the way that particle positions and velocities are immediately updated after the calculation of a new fluid field solution remaining anyway in the one-way coupling framework. When dealing with multiphase flows the integration time-step has to be set in order to capture the dynamics of the two phases. In dilute systems, usually the play is between the CFL condition of the fluid and the relaxation time of the tracked particles: generally, in the case of channel flows the leading parameter is the CFL number. On the contrary, it appears that DHC flow are characterized by low velocities so that the CFL limit results in a much larger time-step than the relaxation time suitable for the smallest particles here investigated (at least an order of magnitude). The latter quantity then imposes a much stronger limitation in the integration time-step also on the fluid phase. In view of that, three sets of particles at $Ra_H = 10^9$ have been tracked separately, meaning that the three sets are advanced in time with different time-steps. The time step must be at least less than one half of each single Stokes number in order to be consistent with the Nyquist sampling theorem, and resolve adequately the particle motion. For the case $Ra_H = 10^{10}$ the tracking has been performed using only the time-step proportional to almost one tenth of the smallest Stokes number because of the enhanced turbulence and also because the size of the time-step can lead to different evolutions of instantaneous flows in chaotic or turbulent regime, as depicted in [Ler99]. It has been found anyway that there are no appreciable differences in the particle statistics between the two methodologies and in the most expensive 3D calculations the first approach will be employed. Finally, the walls are considered perfectly absorbing, meaning that when a particle hits any boundary surface it sticks to it and is immediately

Ra_H	N_p	$d_p[\mu\text{m}]$	$\rho_p[\text{kg m}^{-3}]$	St	$\Delta\tau$	τ_f
10^9	1×10^5	15	1000	1.26×10^{-3}	5.00×10^{-4}	134
"	"	25	"	3.50×10^{-3}	5.00×10^{-4}	160
"	"	35	"	6.86×10^{-3}	1.00×10^{-3}	"
10^{10}	1×10^5	15	1000	8.59×10^{-4}	1.00×10^{-4}	160
"	"	25	"	2.39×10^{-3}	"	"
"	"	35	"	4.68×10^{-3}	"	"

Tab. 3.7: *Particle tracking computational parameters: Rayleigh number Ra_H , total number of particles injected N_p , particle aerodynamic diameter d_p , particle density ρ_p , Stokes number St , integration time step $\Delta\tau$, final time τ_f .*

removed.

3.3.1 Deposition velocity

In Fig.3.28-3.30, instantaneous particle distributions at three different instants (namely $\tau = 5, 25, 125$) are shown in the case of $Ra_H = 10^9, 10^{10}$ for the three particle diameters ($d_p = 15, 25, 35 [\mu\text{m}]$). It is possible already to see that small particles do not deposit as quickly as the larger ones since they closely follow the flow likewise tracers. This tendency is enhanced if the Rayleigh number increases also due to the particular dimensional scales used in the present work that leads to decrease the Stokes number when increasing the Rayleigh number (the opposite occurs in channel flows for instance [SM09]), hence the particles will be more affected by the drag force. An interesting feature of this flow is that the local concentration at the bottom wall remains the same until the core region gets particle-free and almost no clustering (i.e. particle accumulation) is observed from a qualitative point of view. Moreover the unsteadiness of the hook-like structure at the top left affects the pattern of the particles giving a wavelike motion to the particle in the upper part of the cavity and afterwards periodic structures are also visible along the vertical hot wall produced by strong ejections of the hook-like structure. Further on, it is also possible to observe that the cold jet gets rapidly free of particles, meaning that the joint action of drag and gravity together with the fact that the cold boundary layer remains laminar for a long distance are an efficient mechanism of enhancing deposition. The influence of lift and thermophoretic forces will be addressed later but it can be stated that their influence is not of major importance. Finally a zone where particles are suspended is depicted clearly at the hot wall where the drag force remains sufficiently strong and in the opposite direction of the gravity term. This latter result was experimentally found in [YKHK96]. The extension of this region depends both on the particle size and the Rayleigh number: the theoretical

model proposed in the following will be able to address this issue. The time evolution of the suspended particle fraction N_a/N_p (N_a is the actual number of airborne particles) is shown in Fig.3.31 for two Rayleigh numbers and three diameters. Two different behaviors can be depicted from the profiles:

- Most of the particles deposit during the first phase for $d_p = 25, 35 [\mu\text{m}]$ while the mass flux, defined as the time derivative of the suspended particles is approximately constant. This observation does not hold for small particles.
- During the second part the mass flux decreases abruptly and the profiles are characterized by periodic deposition events caused by the presence of the unsteady ejections that occur downstream the hot wall.

From a quantitative point of view the *l.h.s.* of Eq.(3.32) can be described as the opposite of the rate of change of the total airborne particle mass per surface unit, i.e.

$$j_p = -\frac{m_p}{S} \frac{dN_a}{dt} \quad (3.33)$$

where m_p is the mass of a single particle of a given diameter d_p , S is the surface interested by the deposition, and N_a is the number of particle suspended in the domain at time t . All the airborne particles N_a are assumed perfectly mixed in the domain. Hence the actual concentration can be written as

$$C_p = \frac{m_p N_a}{V}. \quad (3.34)$$

Finally, it is possible to write Eq.(3.32) in differential form as

$$-\frac{1}{S} \frac{dN_a}{dt} = C_d \frac{N_a}{V} \quad (3.35)$$

and the instantaneous deposition velocity coefficient results

$$C_d = -\frac{V}{N_a S} \frac{dN_a}{dt} \quad (3.36)$$

Integration of Eq.(3.36) from time t to $(t + \Delta t)$ yields to the final equation of a mean deposition velocity coefficient at time t which depends also on the time-step used by the integration.

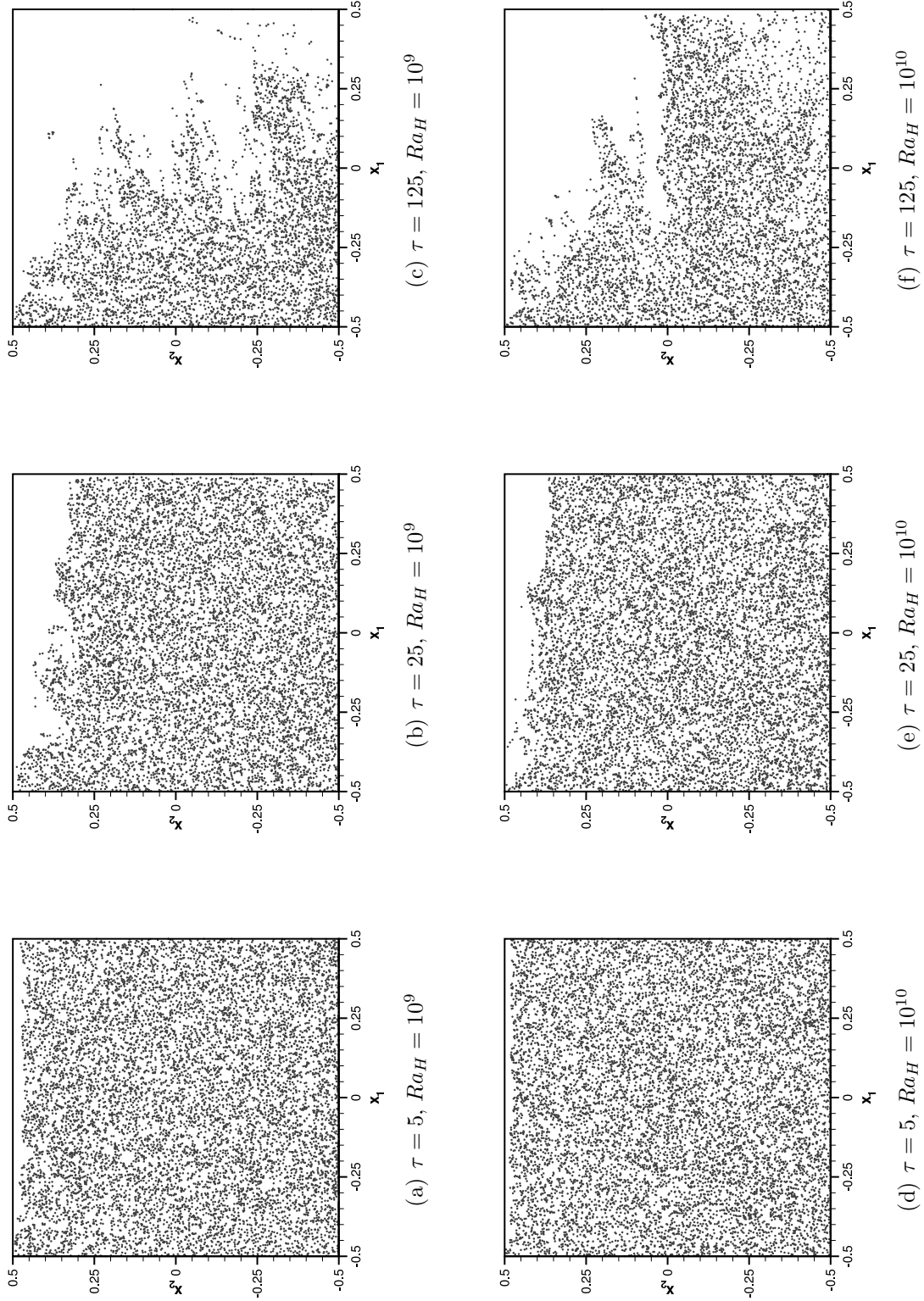


Fig. 3.28: Three instantaneous snapshots of particle distribution at time $\tau = 5, 25, 125$ for $Ra_H = 10^9, 10^{10}$ and $d_p = 15[\mu\text{m}]$.

3.3. PARTICLE DEPOSITION

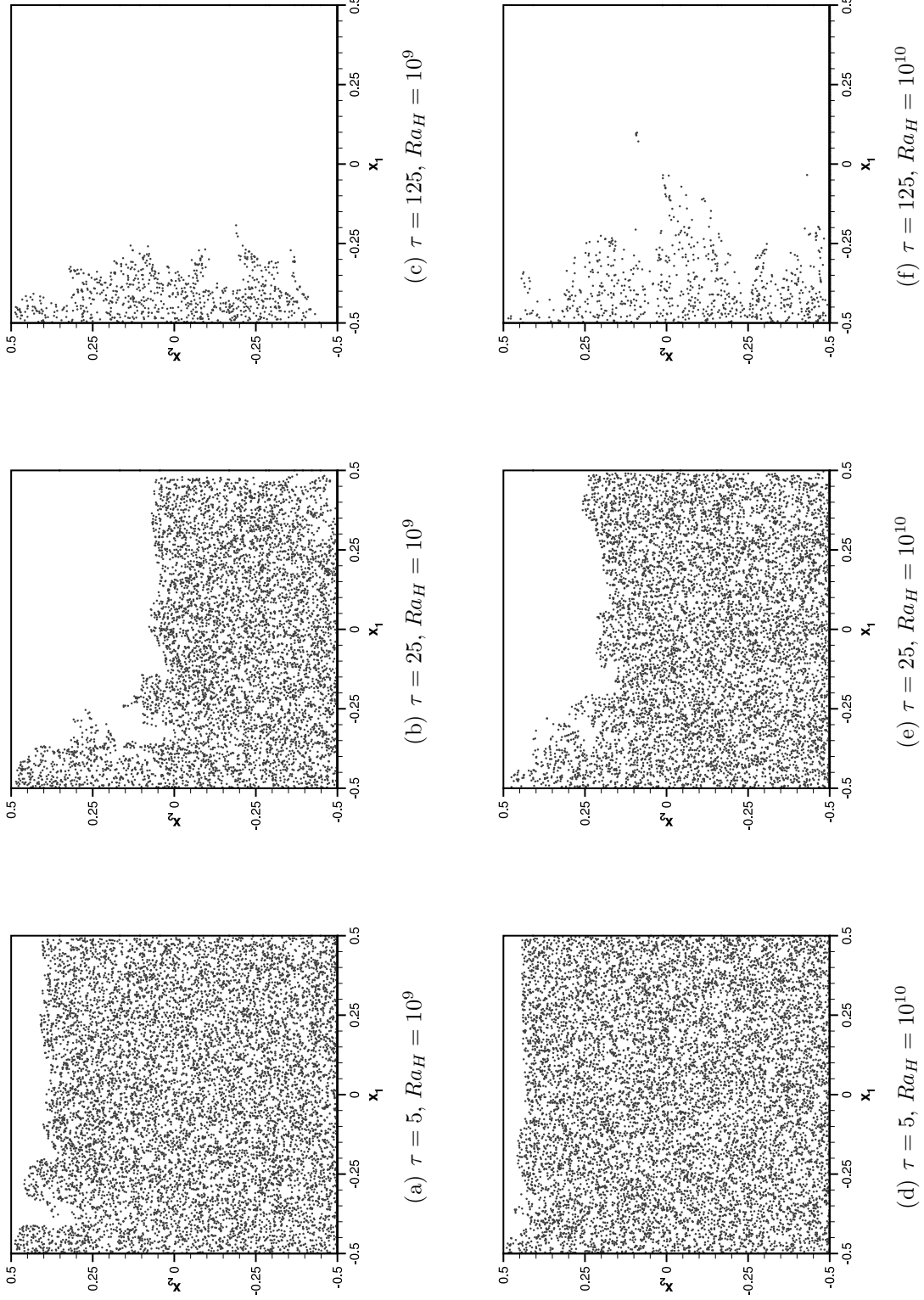


Fig. 3.29: Three instantaneous snapshots of particle distribution at time $\tau = 5, 25, 125$ for $Ra_H = 10^9, 10^{10}$ and $d_p = 25[\mu\text{m}]$.

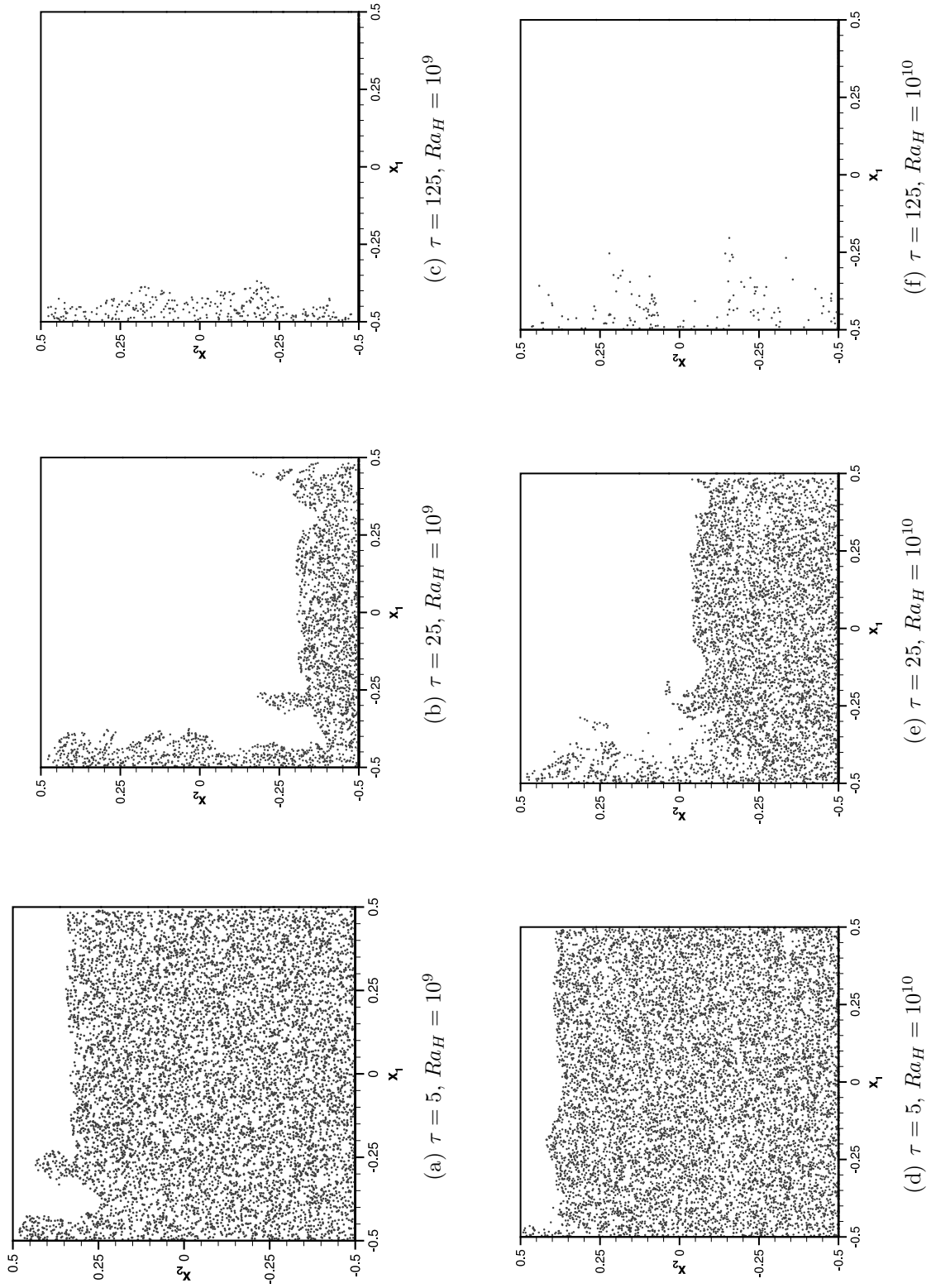


Fig. 3.30: Three instantaneous snapshots of particle distribution at time $\tau = 5, 25, 125$ for $Ra_H = 10^9, 10^{10}$ and $d_p = 35$ [μm].

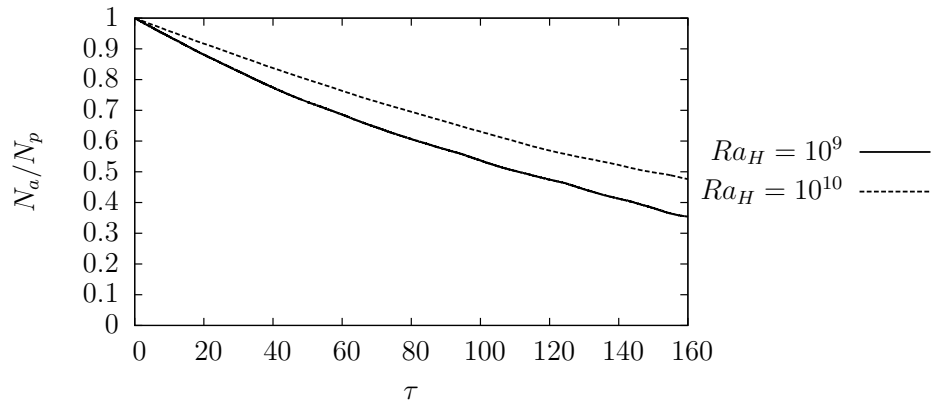
The resulting dimensionless deposition velocity coefficient \mathcal{C}_d reads

$$\mathcal{C}_d = \frac{C_0}{\Delta\tau} \ln \left(\frac{N_a(\tau)}{N_a(\tau + \Delta\tau)} \right) \quad (3.37)$$

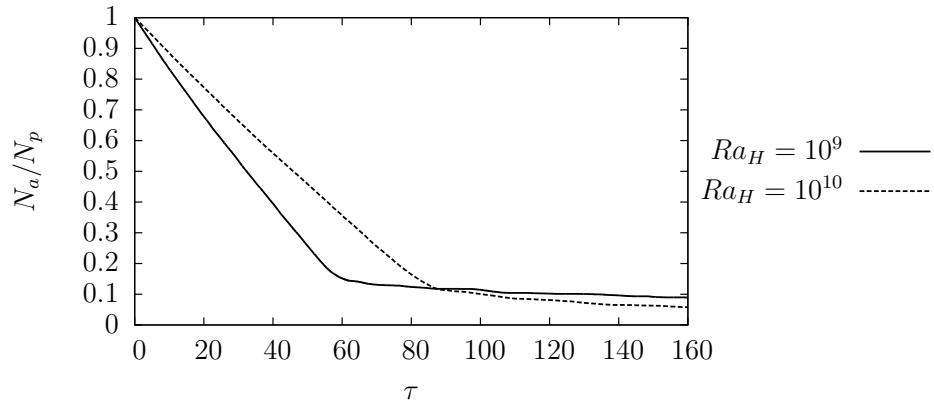
where C_0 is a constant which depends on the ratio of the dimensionless volume and the dimensionless surface taken into consideration. In the present case $C_0 = 1$. The correspondent values of the deposition velocity coefficient are presented in Fig.3.32.

Influence of lift and thermophoretic forces

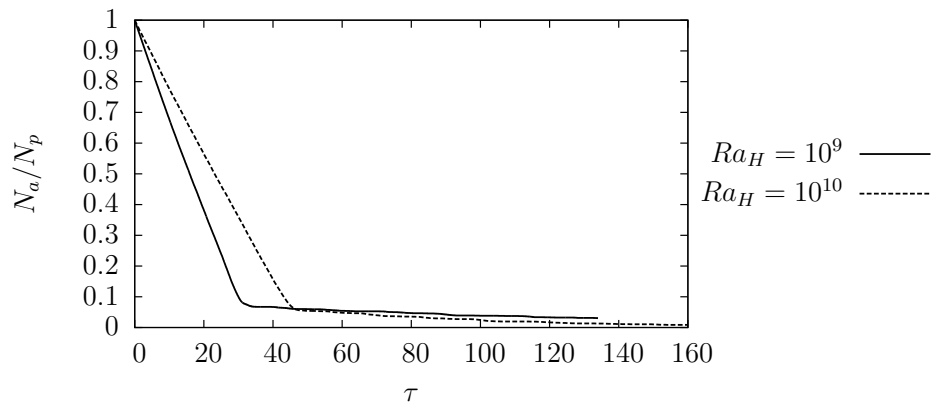
Particles deposit basically at the bottom wall as depicted in Fig.3.33-3.34 which show the probability density function to find particles at the bottom walls defined as $\mathcal{P} = \Delta n_d / (\Delta S N_p)$ (such that it is equal to one only when the deposition is completed) for three different instants (Δn_d is the number of deposited particles contained in a element surface ΔS of the wall). The lack of particles in the vicinity of the cold wall is due to the fact that those particles that come from the cold jet are injected by the eddy towards the mid line instead of impinging directly on the bottom left corner. On the other hand, the maximum that occurs in vicinity of the hot wall is justified by the fact that there is a mean horizontal recirculating flow that blows all the core particles, located in the lower half cavity, towards the hot wall, and at later times, because also those which are suspended in the hot plume tend to deposit slowly in the same region. Besides the depletion of particles at the bottom wall it has been found that few particles actually deposit also at the cold vertical wall, the particular shape of the mean vertical velocity boundary layers (Fig.3.11(b)-3.11(e)) and the presence of the gravitational field lead to a characteristic mechanism of deposition due to the lift at the cold wall. As depicted in the schema of Fig.3.36 on the cold wall there exists a component of the lift force that drives the particles directly towards the wall. Starting from the velocity maximum the lift force changes its direction and helps the particles to move away from the boundary layer region going towards the inner core. Since the introduction of the thermophoretic term, a drift in the opposite direction of the temperature gradient is experienced by all aerosol particles. Concerning the hot wall the behavior is inverse. In other words the lift and the thermophoretic force drive particles away from the wall if the particles are between the wall and the mean vertical velocity maximum, whereas the fluid exerts a force directed towards the velocity maximum if the particles are suspended in the vicinity of the outer part of the velocity boundary layer. The time evolution of particle deposition at the cold wall is shown in Fig.3.35 where n_t refers to the number of particles stuck at the cold wall. The reader should note that larger deposition occurs for big particles because the magnitude of the lift force is proportional to the norm of the relative velocity which increases for big particles. Hence, it is possible to say that the influence of the thermophoretic force is negligible in comparison with the lift. In fact



(a) $d_p = 15\mu\text{m}$



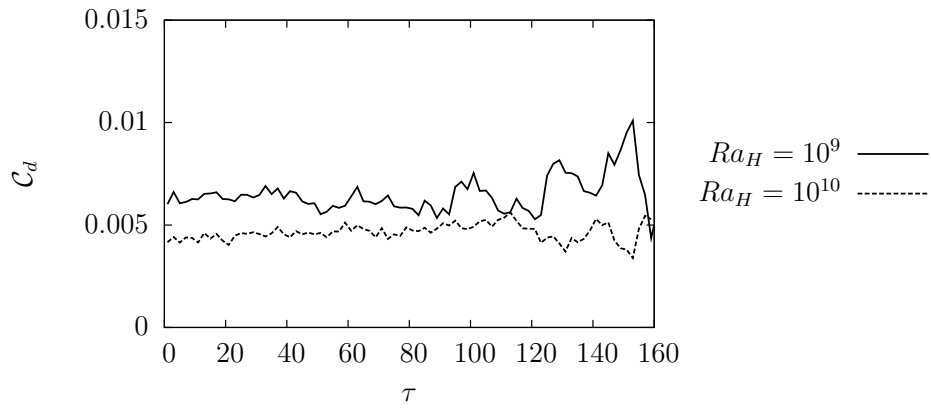
(b) $d_p = 25\mu\text{m}$



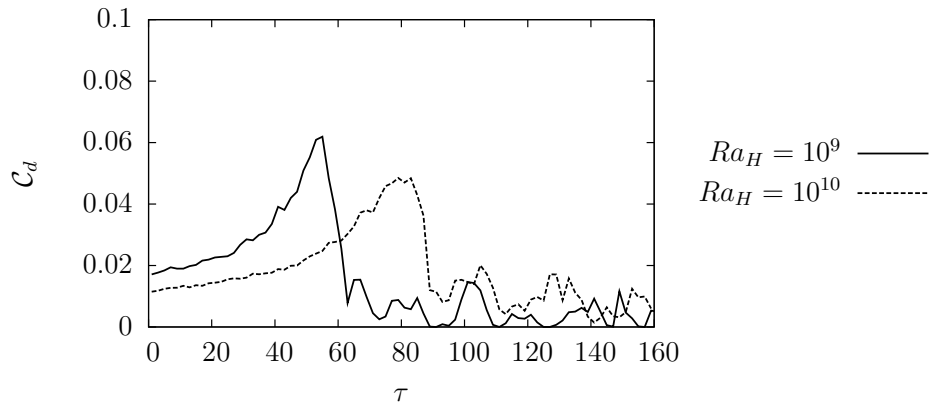
(c) $d_p = 35\mu\text{m}$

Fig. 3.31: Time evolution of the suspended particle number fraction for three sets of particles at $Ra_H = 10^9, 10^{10}$.

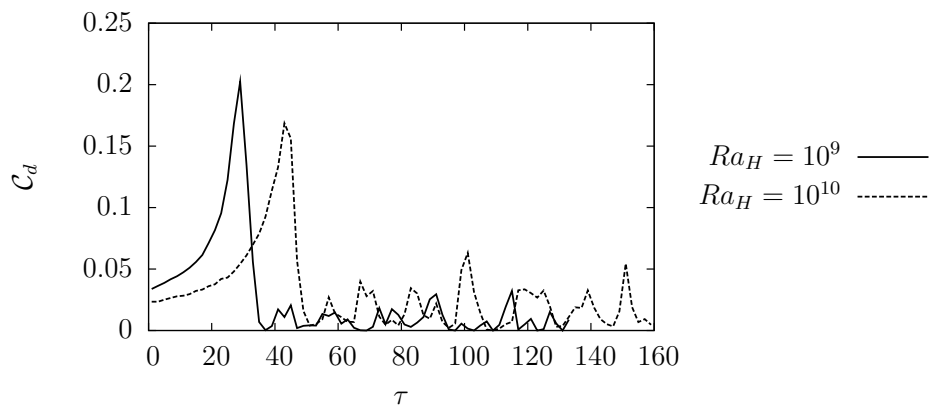
3.3. PARTICLE DEPOSITION



(a) $d_p = 15\mu\text{m}$

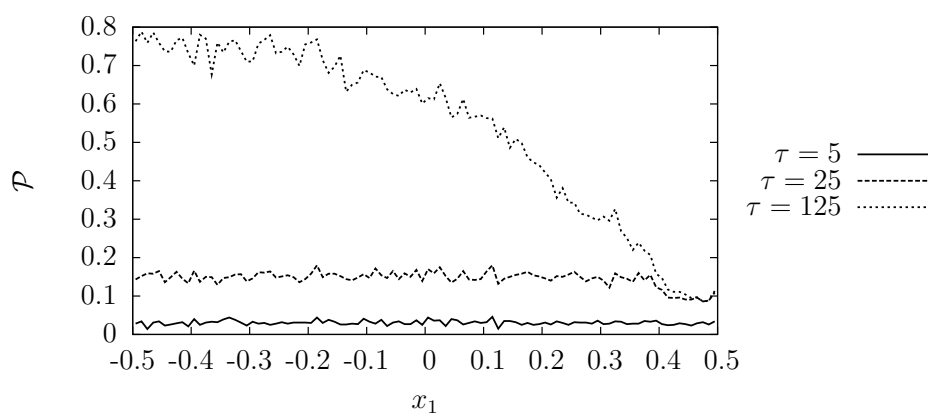


(b) $d_p = 25\mu\text{m}$

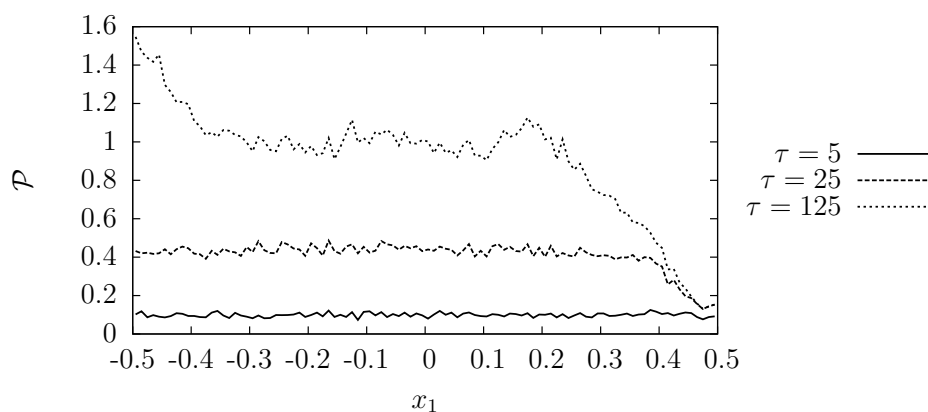


(c) $d_p = 35\mu\text{m}$

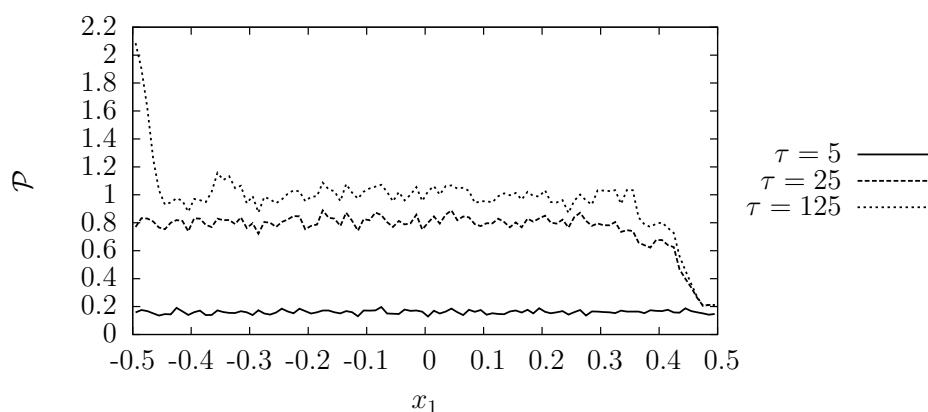
Fig. 3.32: Time evolution of the deposition velocity coefficient for three sets of particles at $Ra_H = 10^9, 10^{10}$.



(a) $d_p = 15\mu\text{m}$



(b) $d_p = 25\mu\text{m}$



(c) $d_p = 35\mu\text{m}$

Fig. 3.33: Particle probability density function at the bottom wall for the three sets of particles at three different times for $Ra_H = 10^9$.

3.3. PARTICLE DEPOSITION

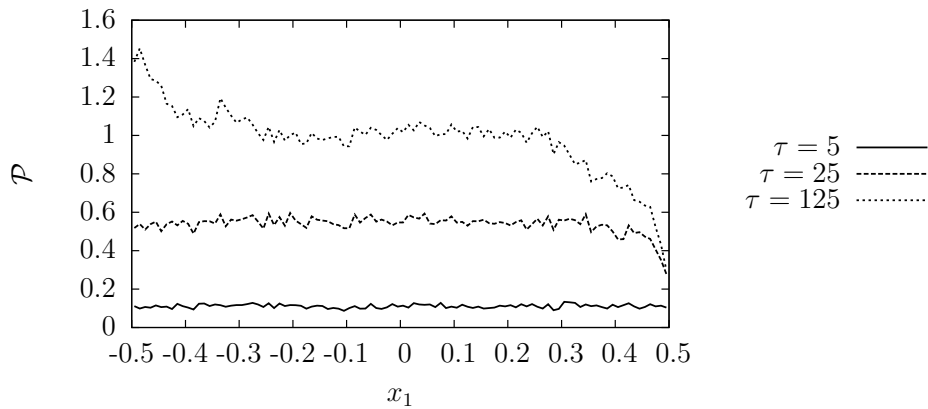
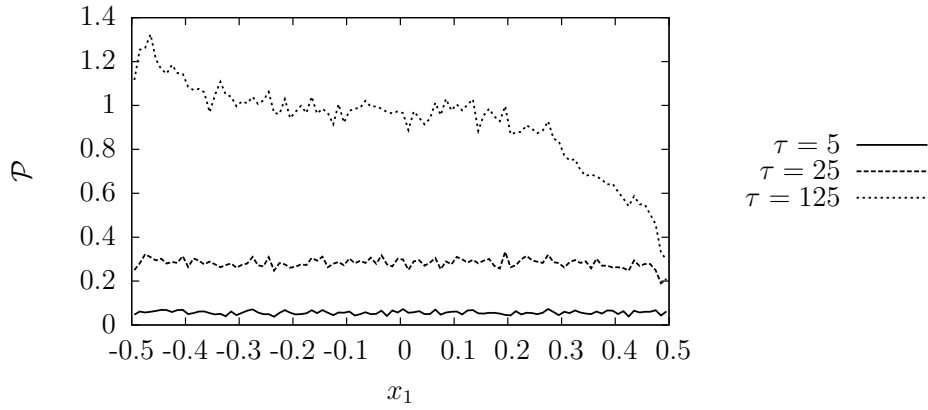
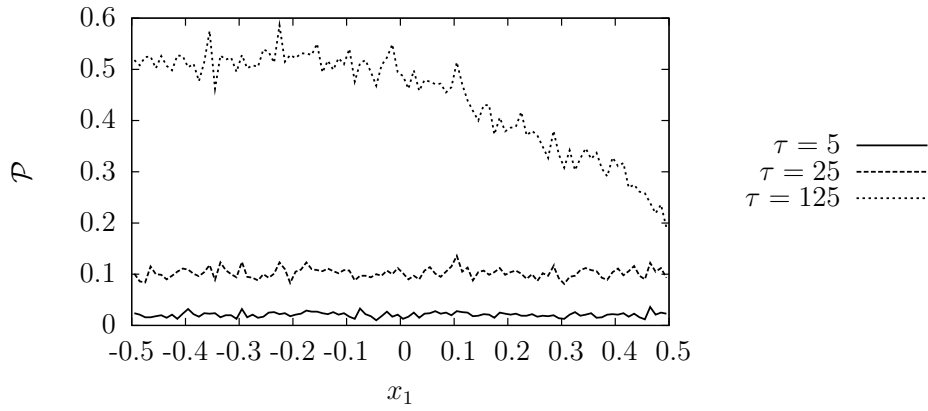


Fig. 3.34: Particle probability density function at the bottom wall for the three sets of particles at three different times for $Ra_H = 10^{10}$.

thermophoresis gets important for smaller particles (i.e. for higher Knudsen numbers) as expressed in Eq.(1.51) but this trend is not remarked in the measurements. Finally, since the deposition at the cold wall takes place at the very first instants for a small amount of particles (less than 0.2%) the phenomenon has to be related to the random distribution of the particles at the injection time. Those that are injected sufficiently close to the cold wall will deposit quickly under the effect of the lift force.

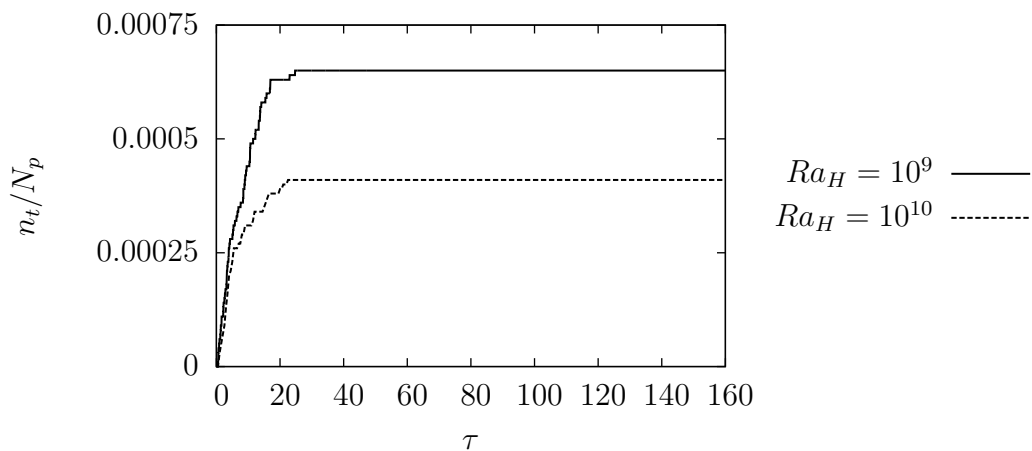
3.3.2 Segregation parameter: correlation dimension

In aerosol engineering it is also important to know if particles accumulate or segregate in particular regions of the flow field in order to understand if particle clusters can influence momentum or thermal characteristics of the carrier fluid, or in reacting flows to see if certain reaction can be enhanced or not in certain locations of the domain. The correlation dimension (also referred as fractal dimension) measures the degree of organization of the particle patterns [GP83]. The methodology to measure the correlation dimension as described in [FKE94] consists first in choosing a base particle and counting the number of particles $\mathcal{N}(r)$ within a certain distance r of the base particle. This procedure has to be performed for a large number of base particles. The resulting ensemble averaged value over all the chosen base particles gives the correlation number characteristic of the swarm of suspended particles. If \mathcal{N} scales with r^0 then particles tend to be clustered in point wise structures; if \mathcal{N} scales with r^1 it means that particles structures are filament wise, and so on for surfaces and volumes. Furthermore, it is important to say that in the case of incompressible flow the upper bound for the correlation dimension is equal to the dimension of the domain d . In the present case particles will be perfectly uniformly distributed if \mathcal{N} scales with r^2 . In Fig.3.37 the correlation dimension defined as

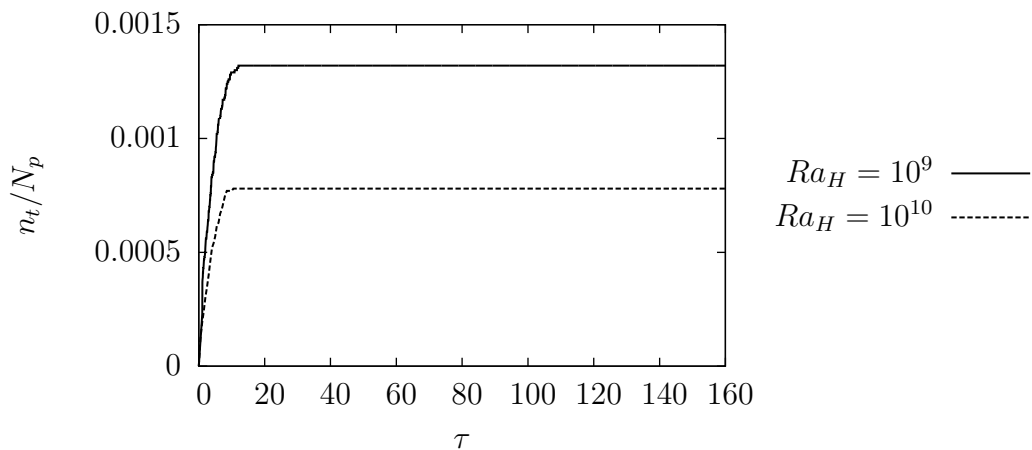
$$\mathcal{D} := \frac{d \ln(\mathcal{N}(r))}{d \ln(r)} \quad (3.38)$$

measured at $\tau = 125$ is plotted against the particle size. The small and medium size particles are characterized by a uniform distribution even under the action of the flow field and do not show particular tendency to cluster. The effect of the Rayleigh number is again negligible for very small particles whilst for medium and big particles it plays a fundamental role. In fact, it appears that turbulent motions and the corner eddy at the hot wall influence strongly the structures/patterns of big size particles. The reason is found in the fact that the ejection events are more frequent and intense at high Rayleigh number so that they affect big particles, resulting in a correlation dimension of approximatively 1.4 because of the formation of elongated horizontal structures as depicted in (Fig.3.30(c)-3.30(f)). For Rayleigh $Ra_H = 10^9$ the ejections are very weak and large particles are less affected. Furthermore, at a given Rayleigh number the trend of the correlation dimension shows

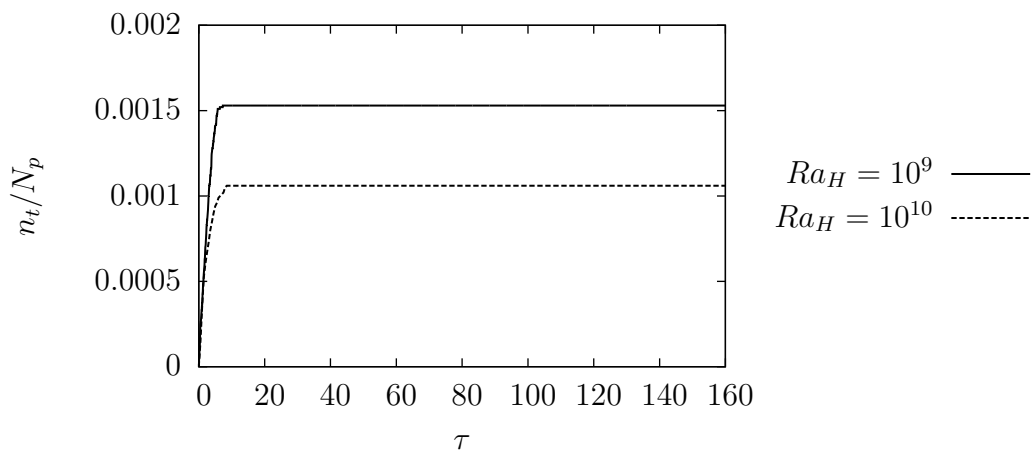
3.3. PARTICLE DEPOSITION



(a) $d_p = 15\mu\text{m}$



(b) $d_p = 25\mu\text{m}$



(c) $d_p = 35\mu\text{m}$

Fig. 3.35: Time evolution of the cumulative fraction of particle deposited at the cold wall for three sets of particles at $Ra_H = 10^9, 10^{10}$.

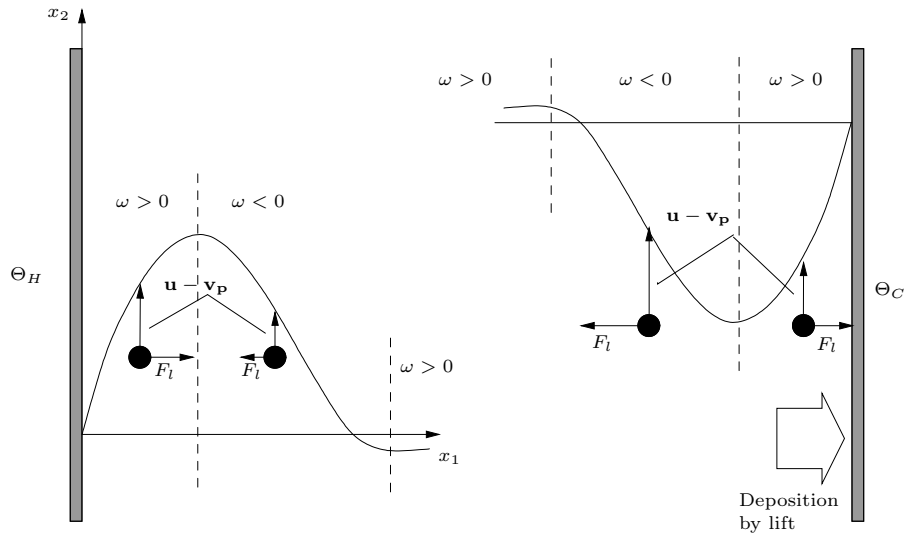


Fig. 3.36: Schematic representation of the deposition mechanism due to lift. \mathbf{F}_l lift force, Θ_H hot wall, Θ_C cold wall, $\mathbf{u} - \mathbf{v}_p$ particle relative velocity, $\omega = \omega_3$ fluid vorticity.

that increasing in the particle diameter yields to departure from the uniform distribution as expected from the theory, and the cluster along the hot boundary layer develops mainly along one dimension (i.e. x_2), so to reach the theoretical limit $\mathcal{D} \rightarrow 1$.

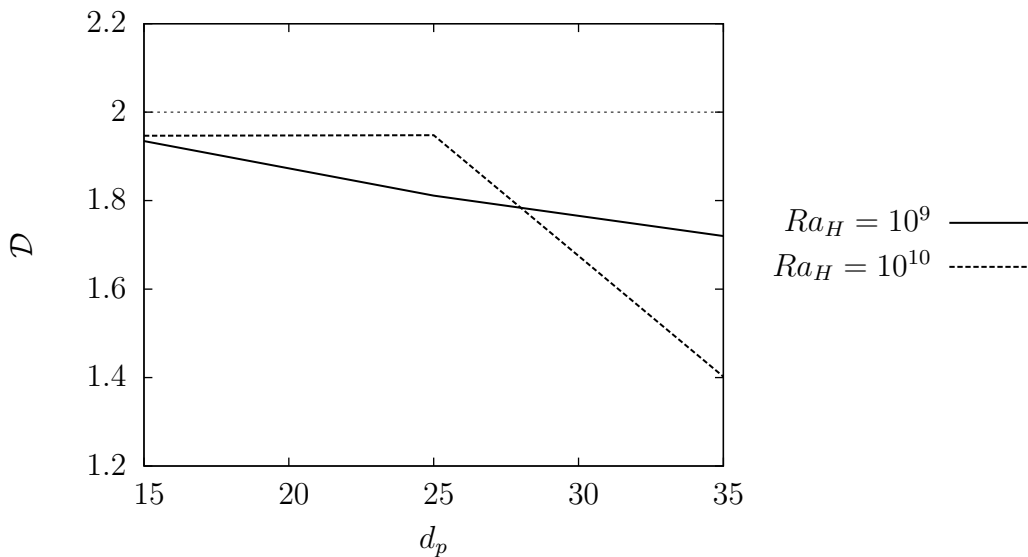


Fig. 3.37: Correlation dimension for three sets of particles at time $\tau = 125$ for $Ra_H = 10^9, 10^{10}$.

Chapter 4

Differentially heated cavity: Three dimensional investigations

In the following paragraphs three laminar benchmark cases at different Rayleigh numbers ($Ra_H = 10^4, 10^5, 10^6$) are compared with the results provided in the literature and a detailed discussion about the more significant features of the three dimensional differentially heated cavity is provided.

The second part of the chapter is devoted to the study of the turbulent flow at ($Ra_H = 10^9, 5 \times 10^9$). Following the same structure proposed in the previous chapter, first and second order statistics are discussed as well as the time averaged Navier-Stokes equations, and the most important terms appearing in the turbulent kinetic energy and temperature variance equations. Anisotropy maps and time-signal analysis (probability density functions, autocorrelation function and power spectral densities) are used to characterize the turbulence inside the cavity. Finally the description of the mechanism that produces turbulent kinetic energy is explained.

The third and last part treats the problem of deposition of three sets of particles of aerodynamic diameter $d_p = 15, 25, 35$ [μm] at $Ra_H = 10^9$ and a simple theoretical deposition model is proposed to interpret the numerical results obtained.

4.1 Steady laminar flows

A cubical enclosure is filled with air ($Pr = 0.71$) at the reference temperature of $T_R = 293.15[\text{K}]$. Two opposite vertical walls are kept at uniform temperature with an imposed temperature difference between them of $42.97[\text{K}]$, the other four walls are adiabatic. The schema of the cavity and the boundary conditions are shown in Fig.4.1. The fluid motion is described by the Boussinesq equations Eq.(1.14)-(1.16), recalled here, in vector

dimensionless form (the symbol “ \wedge ” has been dropped for the sake of simplicity)

$$\nabla \cdot \mathbf{u} = 0 \quad (4.1)$$

$$\frac{\partial \mathbf{u}}{\partial \tau} + \mathbf{u} \cdot \nabla \mathbf{u} = -\nabla p + \frac{Pr}{\sqrt{Ra}} \Delta \mathbf{u} - Pr \Theta \frac{\mathbf{g}}{|\mathbf{g}|} \quad (4.2)$$

$$\frac{\partial \Theta}{\partial \tau} + \mathbf{u} \cdot \nabla \Theta = \frac{1}{\sqrt{Ra}} \Delta \Theta \quad (4.3)$$

with the following boundary conditions for velocity and temperature

$$\mathbf{u} = \mathbf{0} \quad \text{in } \partial\Omega \quad (4.4)$$

$$\Theta(x_1 = \pm 0.5, x_2, x_3, \tau) = \mp 0.5 \quad \forall (x_2, x_3) \in [-0.5, +0.5]^2, \quad (4.5)$$

$$\frac{\partial \Theta}{\partial x_2}(x_1, x_2 = \pm 0.5, x_3, \tau) = 0 \quad \forall (x_1, x_3) \in [-0.5, +0.5]^2, \quad (4.6)$$

$$\frac{\partial \Theta}{\partial x_3}(x_1, x_2, x_3 = \pm 0.5, \tau) = 0 \quad \forall (x_1, x_2) \in [-0.5, +0.5]^2. \quad (4.7)$$

The initial conditions imposed for the laminar steady-state are

$$\mathbf{u}_0 = \mathbf{u}(x_1, x_2, x_3, \tau = 0) = \mathbf{0} \quad \text{in } \Omega, \quad (4.8)$$

$$\Theta_0 = \Theta(x_1, x_2, x_3, \tau = 0) = -x_1 \quad \text{in } \Omega. \quad (4.9)$$

It is well known that steady solutions of the OB equations in symmetric geometries present the so called centro-symmetry properties (see also [CGS02, dXD03]) expressed by

$$(u_i, p, \Theta)(x_1, x_2, x_3) = -(u_i, -p, \Theta)(+0.5 - x_1, +0.5 - x_2, x_3), \quad (4.10)$$

and in addition a planar symmetry with respect to $x_3 = 0$,

$$(u_1, u_2, u_3, p, \Theta)(x_1, x_2, x_3) = (u_1, u_2, -u_3, p, \Theta)(x_1, +x_2, x_3 - 0.5). \quad (4.11)$$

The previous two relations have been used in order to assert the convergence of the simulation together with the ratio of the smallest and largest spectral coefficients. Tab.4.1 shows the max-norm ($\|\cdot\|_\infty$) and 1-norm ($\|\cdot\|_1$) of the error in the symmetry properties at the different Rayleigh numbers for different meshes. The comparison of several quantities obtained in the present work with those provided in [TLB00, WS04] is performed spanning three orders of magnitude of Rayleigh numbers ($Ra_H = 10^4, 10^5, 10^6$), and the results are reported in Tab.4.2-4.3. The quantities under investigation are:

- The maximum of the absolute value of velocity components $|u_1|_{Max}, |u_2|_{Max}, |u_3|_{Max}$ in the whole domain and their location $(x_1, x_2, x_3)_{Max}$;

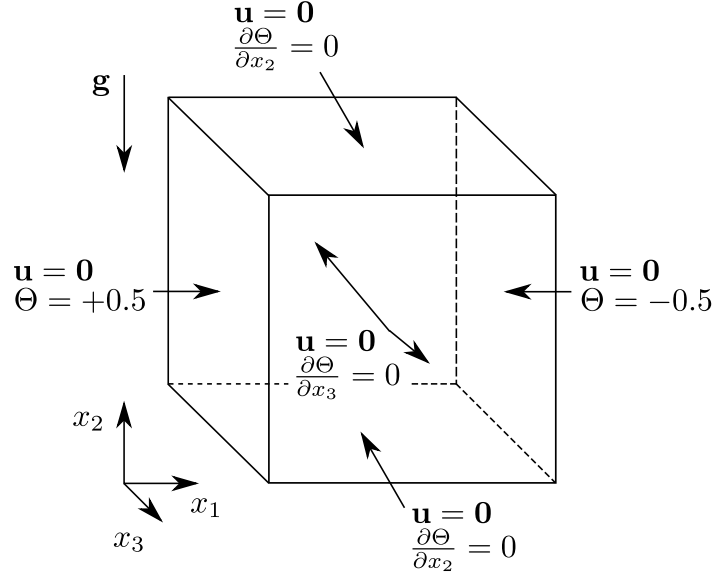


Fig. 4.1: Schematic representation of the cubical DHC with boundary conditions.

- The maximum of the absolute value of the horizontal velocity component in the vertical streamwise mid-plane ($x_3 = 0$) $|u_1|_{p,Max}$ and its location $(x_1, x_2)_{p,Max}$;
- The maximum of the absolute value of the vertical velocity component along the vertical streamwise mid-plane $|u_2|_{p,Max}$ and its location $(x_1, x_2)_{p,Max}$;
- The maximum of the absolute value of the horizontal velocity component along the vertical centerline $|u_1|_{l,Max}$ and its location $x_{2,Max}$;
- The maximum of the absolute value of the vertical velocity component along the horizontal centerline $|u_2|_{l,Max}$ and its location $x_{1,Max}$;
- The spanwise component of the vorticity vector measured at the cavity center $|\omega_3|_c = \left| \frac{\partial u_2}{\partial x_1} - \frac{\partial u_1}{\partial x_2} \right|_{\mathbf{x}=\mathbf{0}}$;
- The stratification coefficient at the cavity center $|\varsigma|_c = \left| \frac{\partial \Theta}{\partial x_2} \right|_{\mathbf{x}=\mathbf{0}}$;
- The mean Nusselt number at the hot wall \overline{Nu}_H ;
- The mean Nusselt number at the vertical spanwise mid-plane \overline{Nu}_M ;

The Nusselt numbers at the wall or at the mid-plane is a straightforward extension of the two dimensional Eq.(3.13)

$$Nu_S = \frac{1}{S} \int_S \mathbf{Nu}_S \cdot \mathbf{n} \, ds \quad (4.12)$$

Regarding the techniques employed in the present work and in [TLB00] for the identification of the maxima and their positions we refer to the previous chapter. Note that in [WS04], the solutions are obtained by a fourth-order central difference scheme (the governing equations are written in vorticity-vector potential form), and Richardson extrapolation together with least square method are used to find the maxima and their positions. The maximum values and their positions reported in Tab.4.2-4.3 are in good agreement with those published in [TLB00]. Some discrepancies are detected between the present results and [WS04] probably because their simulations did not fully converge (as the difference in the Nusselt numbers at the hot and mid planes suggests) and also because of the spatial discretization method employed on rather coarse grids.

		$\ \mathcal{E}_{cs}\ _\infty$	$\ \mathcal{E}_{cs}\ _1$	$\ \mathcal{E}_{pt}\ _\infty$	$\ \mathcal{E}_{pt}\ _1$	\mathcal{S}	
$Ra_H = 10^4$	$N_i = 65$	u_1	2.4×10^{-11}	9.6×10^{-12}	2.6×10^{-11}	2.3×10^{-16}	1.3×10^{-7}
		u_2	1.6×10^{-11}	8.0×10^{-12}	1.4×10^{-11}	5.5×10^{-16}	1.9×10^{-7}
		u_3	6.4×10^{-11}	8.0×10^{-12}	3.7×10^{-10}	6.4×10^{-15}	2.0×10^{-6}
		p	3.7×10^{-11}	1.5×10^{-11}	1.2×10^{-10}	1.6×10^{-15}	1.1×10^{-5}
		Θ	3.4×10^{-11}	3.6×10^{-11}	9.8×10^{-12}	2.9×10^{-17}	1.9×10^{-8}
$Ra_H = 10^5$	$N_i = 129$	u	3.9×10^{-10}	9.5×10^{-11}	3.6×10^{-10}	1.4×10^{-15}	2.8×10^{-8}
		u_2	3.1×10^{-10}	4.2×10^{-11}	1.5×10^{-10}	3.4×10^{-16}	1.7×10^{-8}
		u_3	2.4×10^{-10}	2.4×10^{-10}	4.9×10^{-10}	1.6×10^{-14}	1.9×10^{-7}
		p	7.1×10^{-10}	3.5×10^{-10}	2.9×10^{-9}	1.4×10^{-16}	4.1×10^{-6}
		Θ	3.6×10^{-10}	2.4×10^{-10}	6.7×10^{-11}	7.5×10^{-18}	3.5×10^{-9}
$Ra_H = 10^6$	$N_i = 129$	u	1.4×10^{-8}	2.2×10^{-9}	1.2×10^{-8}	6.7×10^{-14}	1.5×10^{-7}
		u_2	9.2×10^{-9}	1.2×10^{-9}	3.8×10^{-9}	2.0×10^{-14}	7.5×10^{-8}
		u_3	1.2×10^{-8}	1.2×10^{-9}	2.3×10^{-8}	9.6×10^{-13}	1.0×10^{-6}
		p	2.1×10^{-8}	1.1×10^{-8}	1.0×10^{-7}	1.8×10^{-15}	5.3×10^{-6}
		Θ	1.0×10^{-8}	6.8×10^{-9}	4.0×10^{-9}	2.8×10^{-16}	1.4×10^{-8}

Tab. 4.1: *Max-norm, 1-norm of the error in the planar and centro-symmetry properties and spectral coefficient ratio \mathcal{S} for each field at $Ra_H = 10^4, 10^5, 10^6$.*

4.1. STEADY LAMINAR FLOWS

	Present	[TLB00]	[WS04]	
$Ra_H = 10^4$	Grid	65^3	81^3	Extrapolated
	$ u_1 _{Max}$	0.1672	0.1672	–
	(x_1, x_2, x_3)	(0.0197, 0.3249, 0)	(0.0196, 0.3250, 0)	–
	$ u_2 _{Max}$	0.1898	0.1898	–
	(x_1, x_2, x_3)	(0.3834, 0.0269, –0.2309)	(–, 0.0206, 0.2308)	–
	$ u_3 _{Max}$	0.0216	0.0216	–
	(x_1, x_2, x_3)	(0.3823, 0.3448, –0.2826)	(0.3823, 0.3447, 0.2826)	–
	$ u_1 _{p,Max}$	0.1672	0.1672	–
	(x_1, x_2)	(0.0197, 0.3249)	(0.0196, 0.3250)	–
	$ u_2 _{p,Max}$	0.1868	0.1868	–
	(x_1, x_2)	(0.3870, 0.0219)	(0.3870, 0.0219)	–
	$ u_1 _{l,Max}$	0.1670	0.1672	0.1672
	(x_2)	(0.3262)	(0.3244)	(0.3250)
	$ u_2 _{l,Max}$	0.1863	0.1862	0.1867
	(x_1)	(0.3841)	(0.3802)	(–0.3823)
	$ \omega_3 _c$	0.9284	–	0.9284
	$ \zeta _c$	0.8622	–	0.8634
\overline{Nu}_H	2.0551	2.0542	2.0624	
\overline{Nu}_M	2.0551	–	2.0636	
$Ra_H = 10^5$	Grid	129^3	81^3	Extrapolated
	$ u_1 _{Max}$	0.1389	0.1388	–
	(x_1, x_2, x_3)	(0.1840, –0.3873, –0.2203)	(–0.1841, 0.3873, 0.2203)	–
	$ u_2 _{Max}$	0.2247	0.2247	–
	(x_1, x_2, x_3)	(0.4304, 0.603×10^{-2} , –0.3736)	(0.4304, 0.604×10^{-2} , 0.3736)	–
	$ u_3 _{Max}$	0.0301	0.0307	–
	(x_1, x_2, x_3)	(–0.4175, –0.3800, –0.3390)	(0.4175, 0.3801, 0.3390)	–
	$ u_1 _{p,Max}$	0.1362	0.1362	–
	(x_1, x_2)	(0.1864, –0.3848)	(–0.1865, 0.3848)	–
	$ u_2 _{p,Max}$	0.2070	0.2069	–
	(x_1, x_2)	(0.4368, 0.1005)	(0.4368, 0.1000)	–
	$ u_1 _{l,Max}$	0.1191	0.1188	0.1193
	(x_2)	(–0.3536)	(0.3535)	(0.3500)
	$ u_2 _{l,Max}$	0.2069	0.2062	0.2076
	(x_1)	(0.4361)	(0.4330)	(–0.4323)
	$ \omega_3 _c$	0.2153	–	0.2168
	$ \zeta _c$	1.0824	–	1.0867
\overline{Nu}_H	4.3370	4.3370	4.3665	
\overline{Nu}_M	4.3370	–	4.3648	

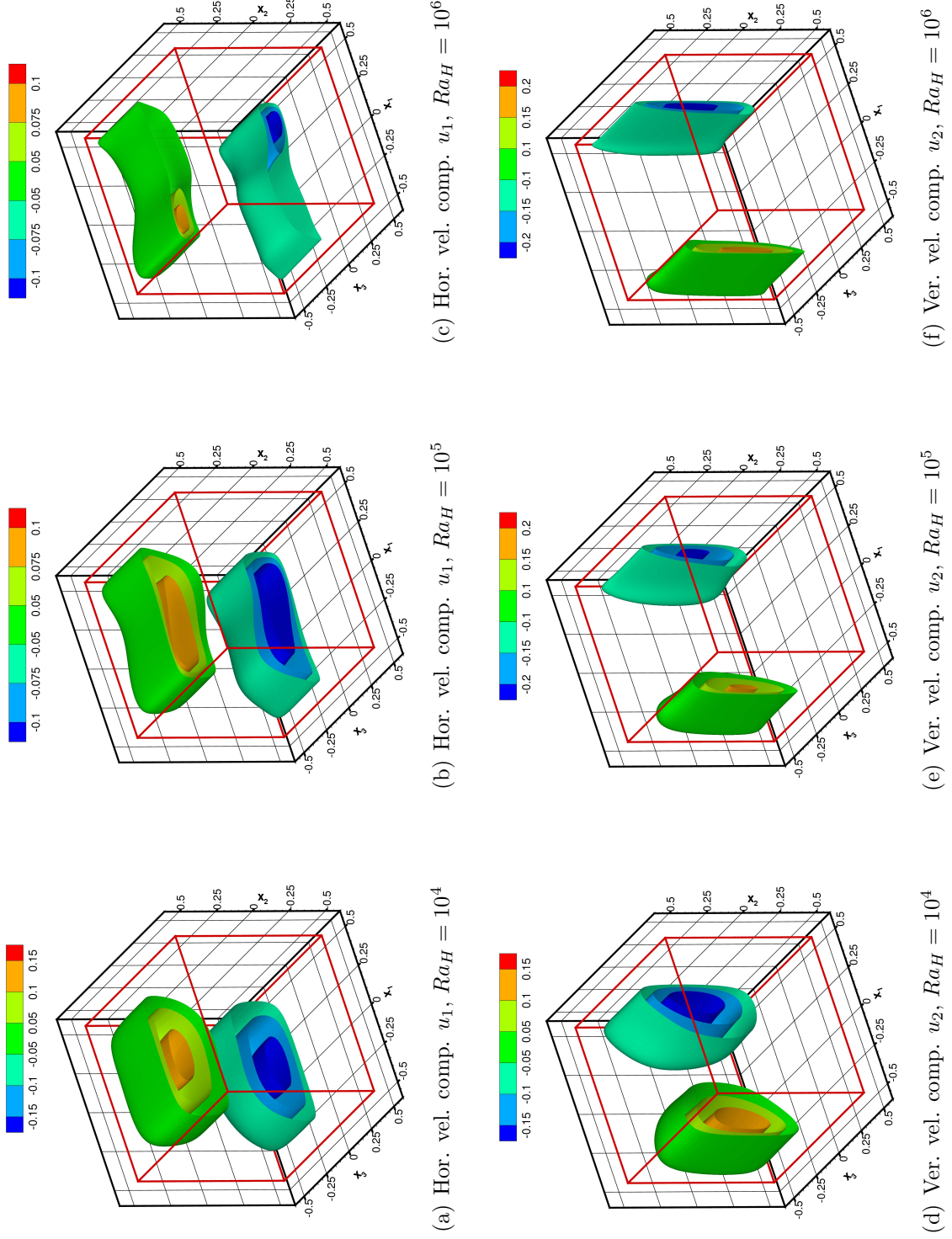
Tab. 4.2: Comparison of 3D DHC flow results with the benchmark data of [TLB00, WS04] for $Ra_H = 10^4, 10^5$.

CHAPTER 4. DIFFERENTIALLY HEATED CAVITY: THREE DIMENSIONAL
INVESTIGATIONS

	Present	[TLB00]	[WS04]
$Ra_H = 10^6$	Grid	129 ³	81 ³ Extrapolated
	$ u_1 _{Max}$	0.1270	0.1270
	(x_1, x_2, x_3)	(0.3056, -0.4365, -0.2997)	(-0.3057, 0.4365, 0.2997)
	$ u_2 _{Max}$	0.2367	0.2367
	(x_1, x_2, x_3)	(0.4604, 0.0265, 0.2498)	(0.4604, 0.0265, 0.2499)
	$ u_3 _{Max}$	0.0256	0.0256
	(x_1, x_2, x_3)	(-0.4512, -0.4168, -0.3983)	(0.4518, 0.4148, 0.3983)
	$ u_1 _{p,Max}$	0.1235	0.1235
	(x_1, x_2)	(0.3133, -0.4366)	(-0.3133, 0.4366)
	$ u_2 _{p,Max}$	0.2183	0.2183
	(x_1, x_2)	(0.4638, 0.0353)	(0.4638, 0.0353)
	$ u_1 _{l,Max}$	0.0683	0.0682
	(x_2)	-0.3556()	(0.3536)
	$ u_2 _{l,Max}$	0.2175	0.2176
	(x_1)	(0.4626)	(-0.4669)
	$ \omega_3 _c$	0.1144	-
	$ \zeta _c$	0.9086	-
	\overline{Nu}_H	8.6402	8.6407
	\overline{Nu}_M	8.6402	-

Tab. 4.3: Comparison of 3D DHC flow results with the benchmark data of [TLB00, WS04] for $Ra_H = 10^6$.

Fig. 4.2: Horizontal and vertical velocity component iso-surfaces at $Ra_H = 10^4, 10^5, 10^6$.



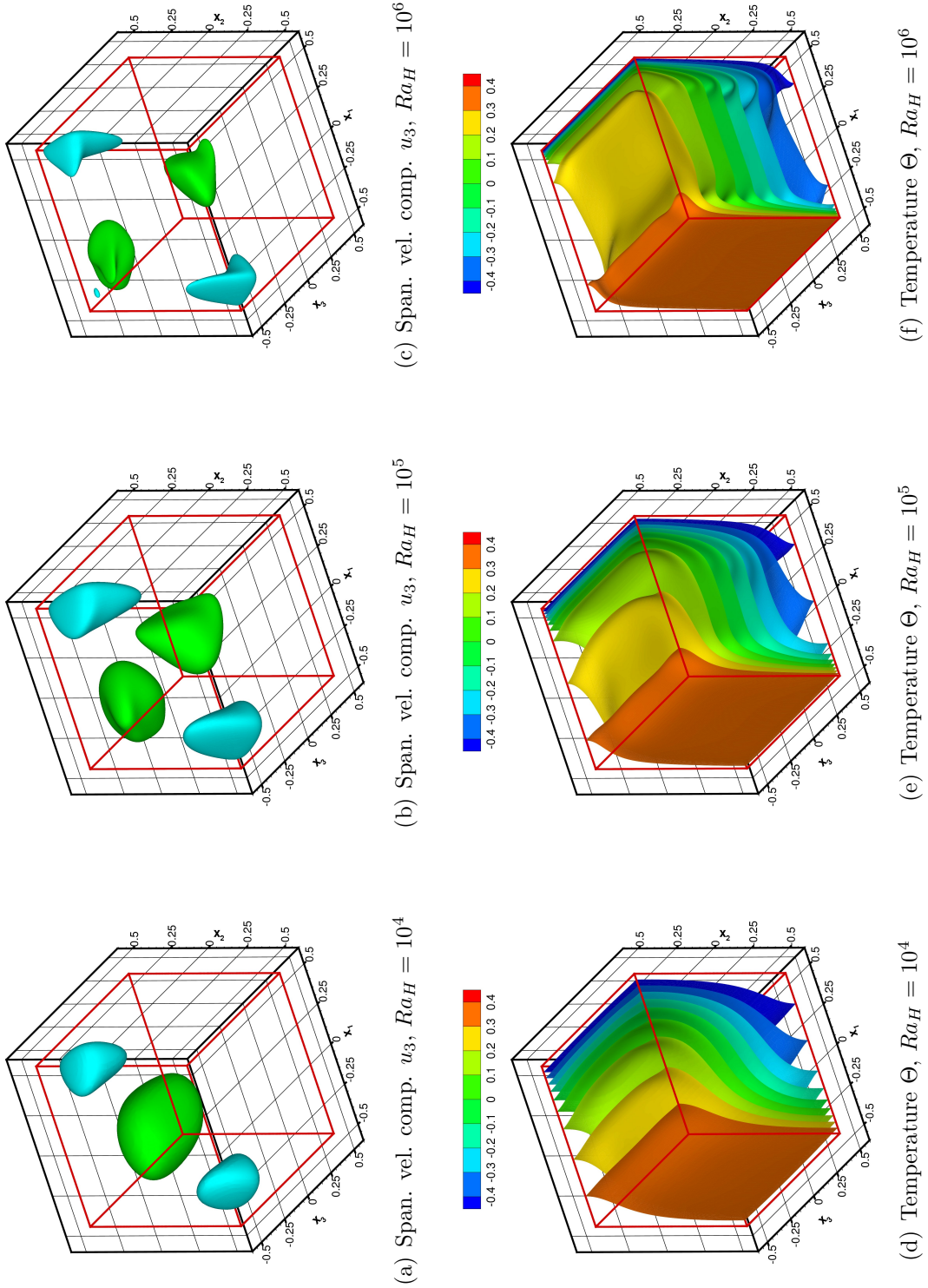


Fig. 4.3: Iso-surface plots of spanwise velocity component $u_3 = -0.07, 0.1$ and temperature Θ for $Ra_H = 10^4, 10^5, 10^6$.

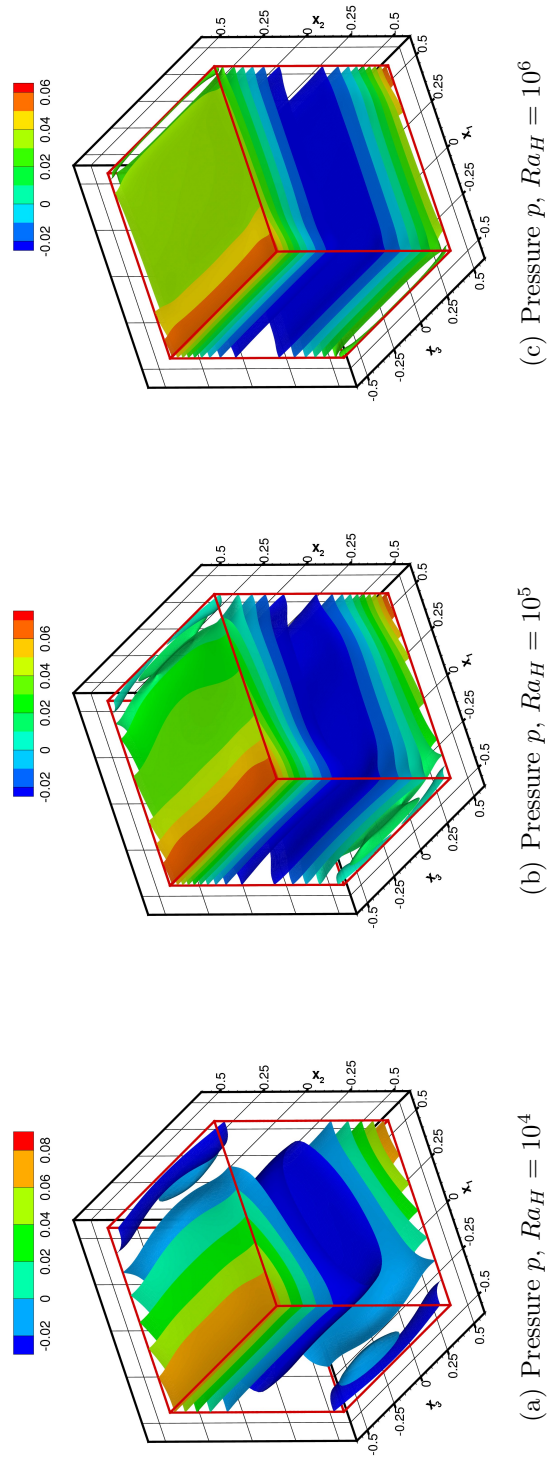


Fig. 4.4: *Iso-surface plots of pressure p for $Ra_H = 10^4, 10^5, 10^6$.*

Results and discussion

Velocity, temperature and pressure iso-surfaces for $x_3 \leq 0$ (half domain) are shown in Fig.4.2-4.4. First of all the reader should note that the presence of the lateral walls induces a multilayer onion-like structures for all the velocity fields. At $Ra_H = 10^4$ the horizontal velocity component shows two interacting Boundary Layers (BLs) with maximum and minimum located at $x_1 \approx 0$ and $x_3 \approx 0$. As seen for the two-dimensional calculations, with increasing the Rayleigh number the horizontal velocity maximum and minimum shift towards the corners where the flow turns from the vertical to the horizontal direction while the BLs separate. Furthermore it is possible to observe the diffusion of the momentum right after the turning in Fig.4.3(c) (green iso-surfaces). In Fig.4.3(d)-4.3(f) are shown the iso-surfaces of the vertical velocity component that clearly depicts the decrease in size of the vertical BL thickness with the increase of the Rayleigh numbers. Hence, it appears that for increasing Rayleigh number the laminar flow structures tend to be less and less influenced by the two side walls leading to a quasi two-dimensional flow away from the lateral adiabatic walls. Anyway the variation of the third component of velocity at the corners introduces one term in the continuity equation leading to a peculiar shape at the sides of the horizontal velocity component iso-surfaces with high velocity values that extend towards the opposite active wall (this result is also reflected in the local Nusselt number distribution on the mid-plane in [BH06]). It is clear from the spanwise component of velocity (Fig.4.3) that at low Rayleigh number there exists mass flux that drives fluid particles from the lateral walls towards the center of the cavity and back to the top and bottom walls. For higher Rayleigh numbers the transport of fluid particles takes place near the corner regions. A negative spanwise velocity characterizes the flow close to the edges where suction events take place due to the formation of the vertical natural convective boundary layers. The temperature iso-surfaces underline the increase of the vertical stratification as the Rayleigh number increases. In fact, it is possible to say that for $Ra_H = 10^4$ the transfer of energy is mixed between conduction and convection whereas at $Ra_H = 10^6$ the conductive transport becomes negligible in comparison with the convective one. The reader should also notice that at high Rayleigh numbers the top and bottom regions are characterized by a weak temperature gradient in the vertical direction thanks to the adiabatic horizontal walls. Finally the pressure fields (Fig.4.4) confirm the finding that the pressure behaves in the same way as the temperature (i.e. it stratifies) because it balances the buoyancy force in the vertical direction appearing in the momentum equation. Departures from this behavior are localized at the suction edges and where the vertical jets impinge the horizontal walls. More in detail, Fig.4.5 shows the vertical velocity profiles against the scaled distance from the vertical hot wall x^- (Eq.(3.16)) at three different heights (namely $x_2 = -0.3, 0.0, 0.3$) on the streamwise mid-plane ($x_3 = 0$). In the present cases the scaling of the momentum BL well describes the thickening of the vertical velocity profile at the mid-height, whereas

that observation does not hold at top and bottom of the cavity. Because in the lowest Rayleigh number case the conduction is not negligible in comparison with the convection. Furthermore, it is interesting to note the presence of counter flows in the outer part of the vertical BLs. The velocity profiles obtained experimentally in [KJ83, MJHL08] do not match those of the present simulations basically because of the fact that in both experiments the four lateral walls are not perfectly adiabatic. On the other hand the thermal BLs (see Fig.4.6) match very well for the two largest Rayleigh values at the bottom and mid-height, whereas due to impingement and the influence of conduction the scaling does not apply at the top of the hot wall. The vertical temperature profiles at the center-line (Fig.4.7) clearly enlighten an almost linear stratification of flow and the tendency to increase the zones of approximate constant temperature at the top and the bottom walls induced by the thermal insulation. Moreover, the local temperature stratification plotted in Fig.4.8 against the vertical direction is compatible with those presented in the two dimensional case (see Fig.3.8). The largest components of the momentum flux at the hot and top walls are shown in Fig.4.9, where

$$\tau_{w,x_2} = \tau_{12} = \frac{Pr}{\sqrt{Ra_H}} \left(\frac{\partial u_1}{\partial x_2} + \frac{\partial u_2}{\partial x_1} \right)_{x_1=-0.5}, \quad (4.13)$$

and

$$\tau_{w,x_1} = \tau_{21} = \frac{Pr}{\sqrt{Ra_H}} \left(\frac{\partial u_2}{\partial x_1} + \frac{\partial u_1}{\partial x_2} \right)_{x_2=+0.5}. \quad (4.14)$$

The maximum of the wall shear stresses occurs at the hot wall before mid-height. As previously observed in the 2D cases, on the top wall with increasing the Rayleigh number the streamwise component of the shear stress becomes smaller indicating the fact that the formation of a boundary layer is contrasted by the almost isothermal fluid in the neighbors. Moreover, the lateral walls do not affect in a sensible way the momentum transfer as the Rayleigh number increases. This statement will be also confirmed in the following section. And finally the reader should note the absence of detachment on the top wall because of the relatively low Rayleigh numbers (indeed in the two-dimensional calculations detachment and reattachment regions occur only for $Ra_H > 10^7$). Concluding this section, it is important to stress how the adiabatic walls affect the Nusselt number distribution also on the active walls (see Fig.4.10). In fact, it is possible to see that close to the lateral walls ($x_3 = \pm 0.5$) there is a defect in the heat transfer due to local decrease of the temperature gradient normal to the active wall induced by a weaker convective boundary layer. As already stressed, the effect becomes less and less important as the Rayleigh number increases.

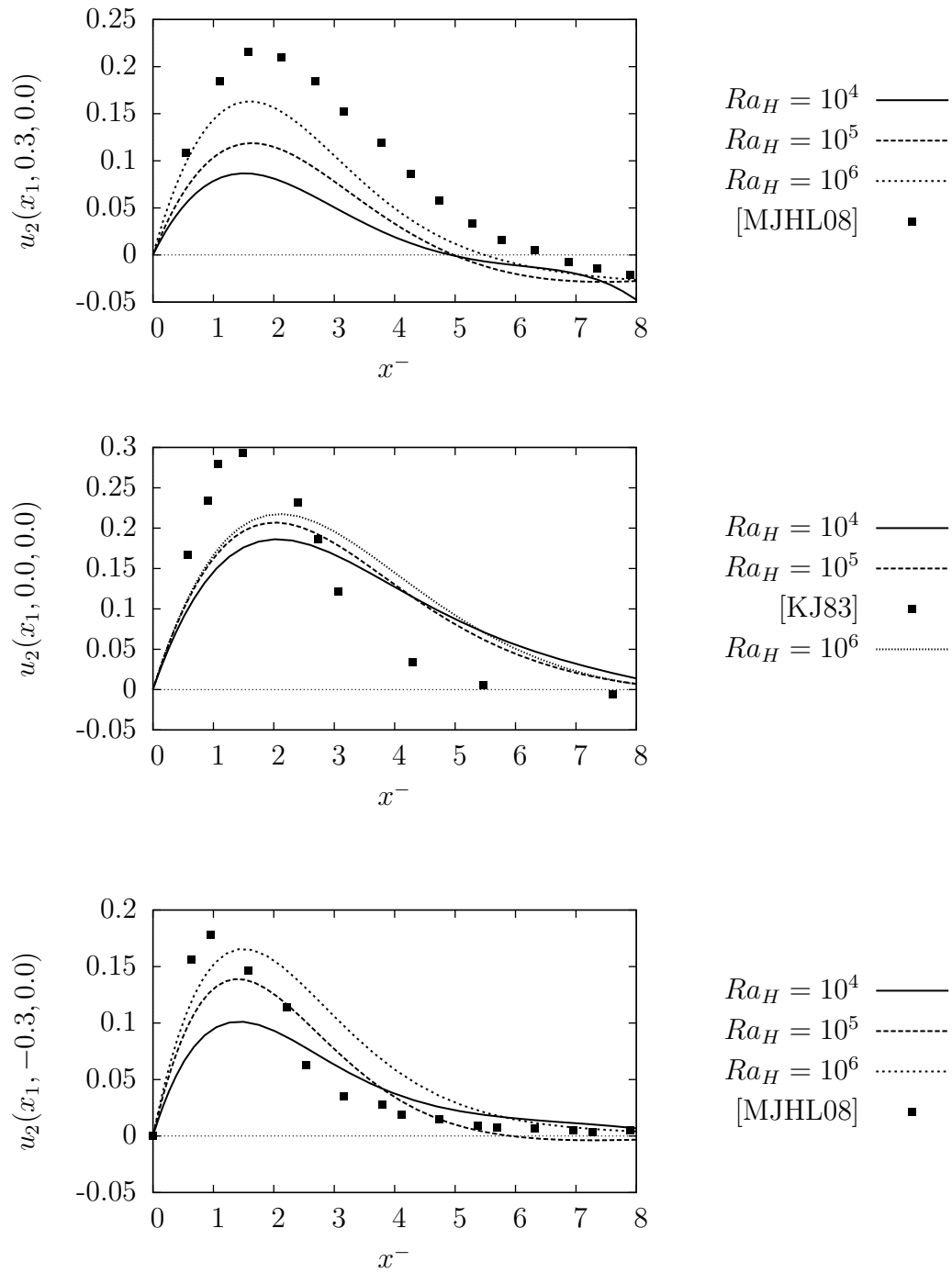


Fig. 4.5: Vertical velocity component profiles at the mid-plane ($x_3 = 0$) for different heights $x_2 = -0.3, 0.0, +0.3$ with respect to the distance from the hot wall x^- .

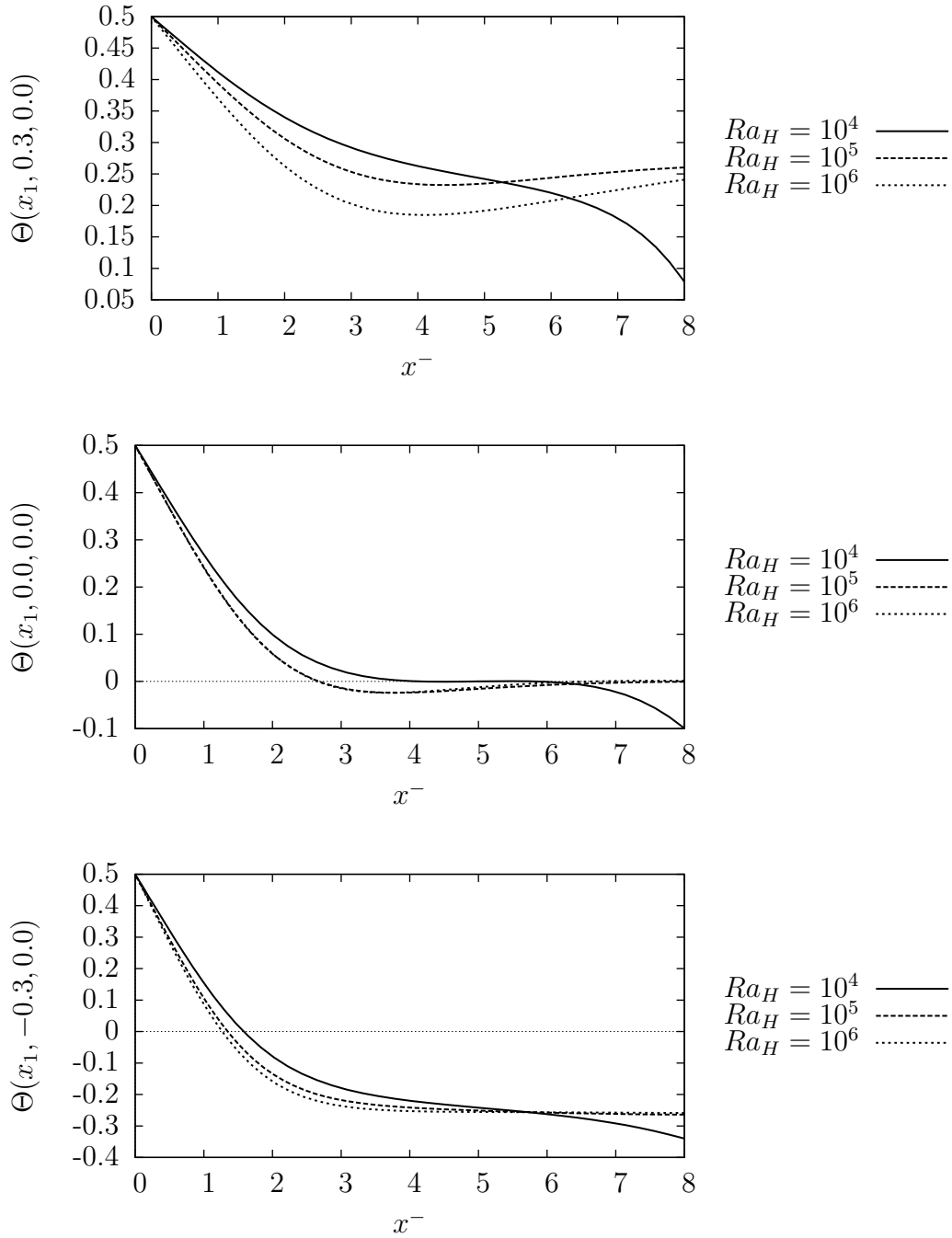


Fig. 4.6: Temperature profiles at the mid-plane ($x_3 = 0$) for different heights $x_2 = -0.3, 0.0, +0.3$ with respect to the distance from the hot wall x^- .

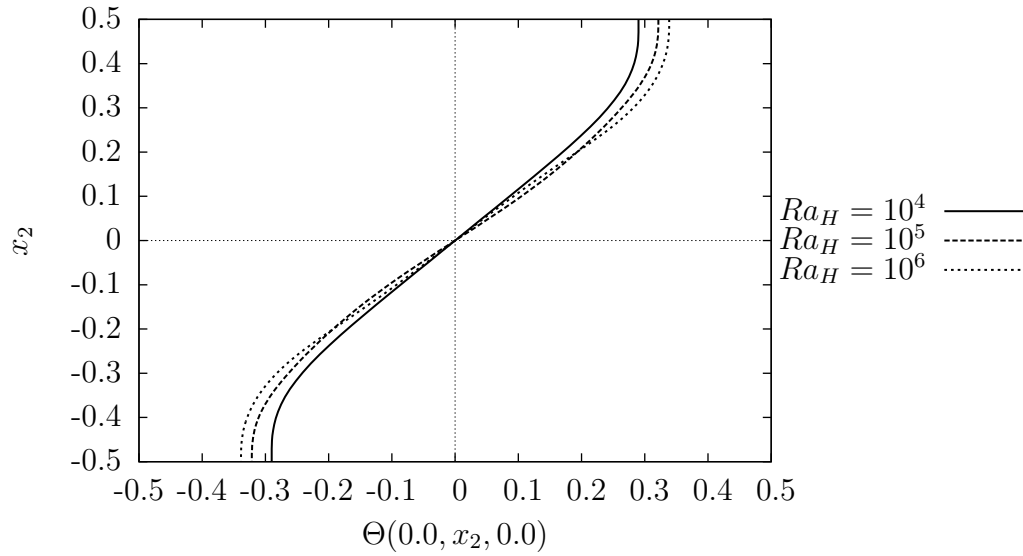


Fig. 4.7: *Temperature profiles along the vertical center-line.*

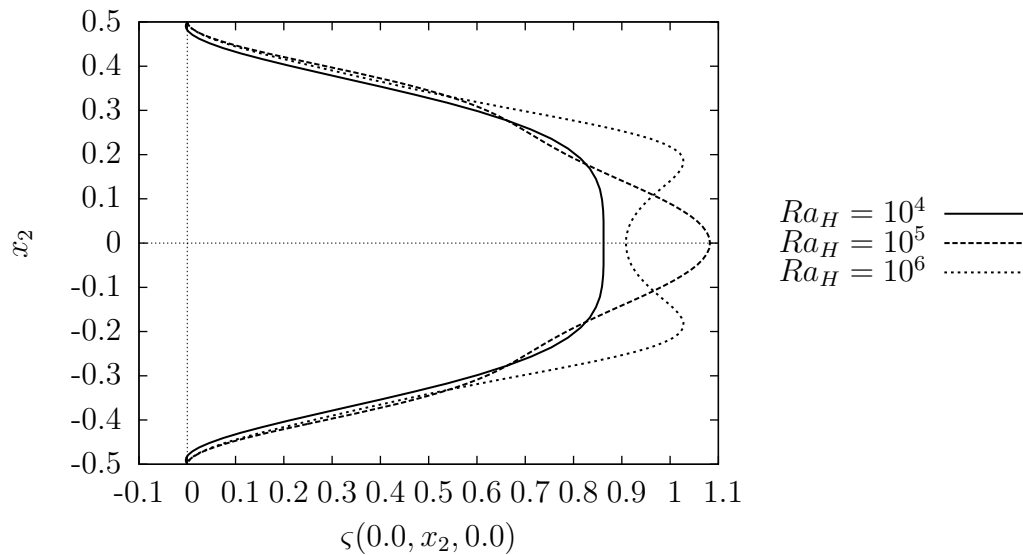


Fig. 4.8: *Temperature stratification coefficient ζ along the vertical center-line.*

4.1. STEADY LAMINAR FLOWS

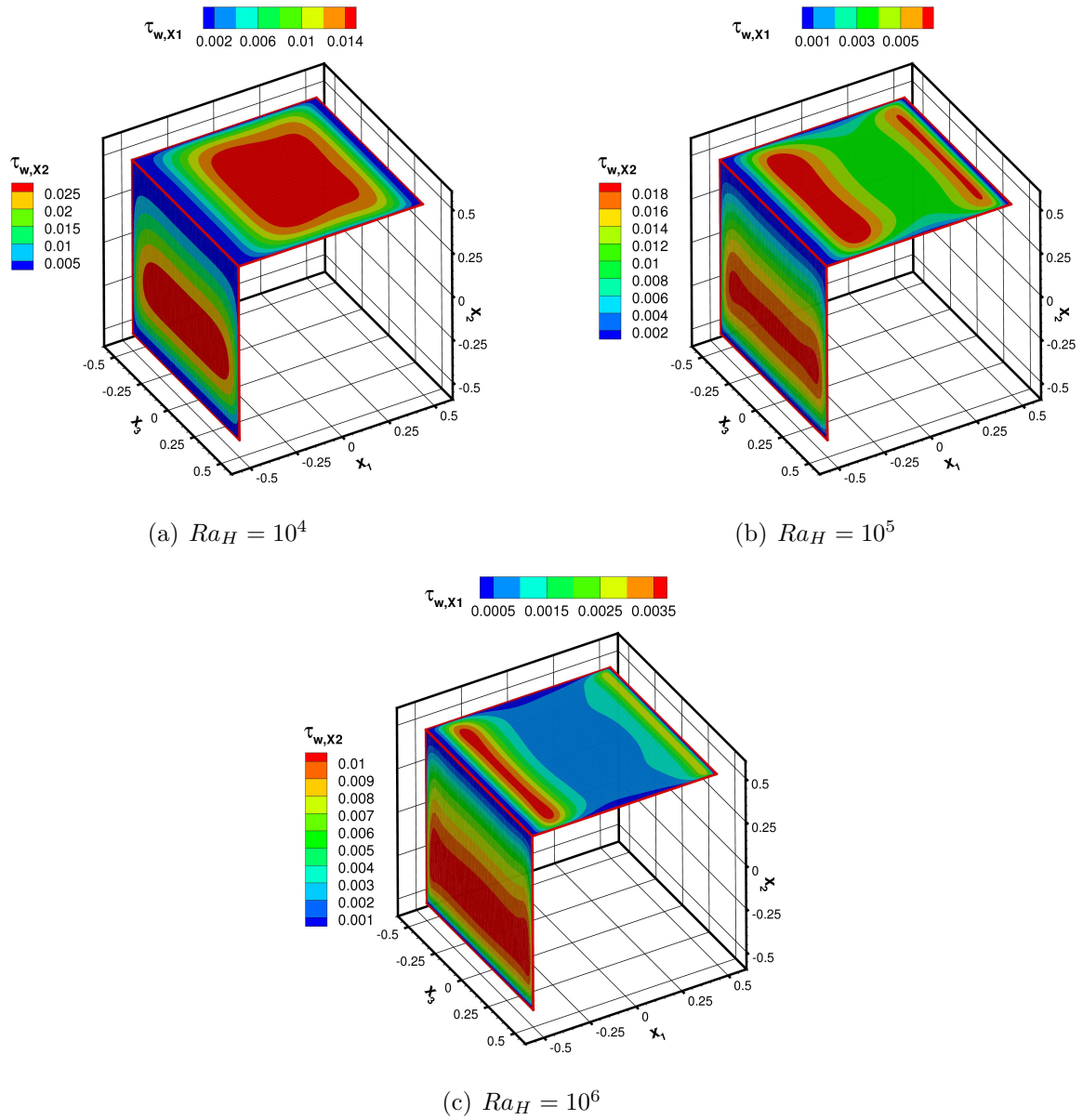


Fig. 4.9: Iso-contours of the shear stress components along x_1 and x_2 , on the top and hot walls respectively, for $Ra_H = 10^4, 10^5, 10^6$.

4.2 Turbulent flow

Above the critical Rayleigh number which has been found to be $Ra_c^{3D} \approx 3.3 \times 10^7$ (see [JH96, TLB00]) the flow becomes periodic and at $Ra_H = 10^9$ is expected to be turbulent ([Fus94]). To the author's knowledge only [JH96, TLB00, ?, dXD03] reported accurate results of direct numerical simulations in a fully enclosed cubical domain at slightly sub-critical and critical Rayleigh numbers ($Ra_c \approx 3.3 \times 10^7$), in order to address the identification of the mechanism which yields the first transition to unsteadiness (due to Kelvin-Helmholtz instability of the turning and detaching impinging jets at the horizontal walls away from the lateral walls), and supercritical Rayleigh number for characterizing the time averaged flows and turbulence intensity ($Ra = 1.5 \times 10^9$). In [dXD03] the authors put in evidence that at the first bifurcation for $Ra_c = 3.2 \times 10^7$ there is formation of vortex structures at the end of the vertical active walls near the median plane. Moreover a further increment of the Rayleigh number up to $Ra_H = 10^8$ shows a return to steady state solution of the flow, whereas for $Ra_H \geq 3 \times 10^8$ the flow becomes newly unsteady (due to the vertical boundary layer instability). In the present work not such a behaviour (i.e. the return to steadiness) has been remarked when looking at the solutions spanning from $Ra_H = 3.3 \times 10^7$ to $Ra_H = 10^8$, this is probably also due to the short total integration time used in the present research that aimed to reach higher Rayleigh numbers. Some snapshots of the instantaneous temperature iso-contours at the streamwise vertical midplane are shown in Fig.4.11-4.12 for $Ra_H = 10^9$. It is important to notice that the instantaneous flow has lost the symmetry properties (even if the centro- and plane-symmetry still hold for the mean fields). Furthermore, the time evolution shows the unsteadiness of the flow in the turning corner regions. In fact the hook-like structures (created by the diffusion of the turning jets) change of curvature resulting in a wide open hook or in more close hook structure. This behavior is almost periodic in time and it is the origin of the gravity waves that take place in the stratified core region and will be related later on to the mechanism of enhanced production of turbulent kinetic energy. In order to study the statistical properties of these chaotic systems, a large database has been created using as initial conditions interpolated fields, solutions at lower Rayleigh number. The possible influence in the statistics of the change of the initial boundary conditions at the initial stage of the computations has been avoided letting this numerical perturbation fading away before starting the sampling of the database. The dimensionless time needed to dissipate the effect of the sudden change in the boundary conditions depends on the difference between the Rayleigh numbers employed and on the grid, but in general it is of the order $O(\sqrt{\Delta Ra_H})$ ([PI80, LQB98]). The averaging time is taken sufficiently large to ensure low residuals in the time-averaged momentum and energy equations as it will be discussed later on in the text. A summary of the computational parameters is provided in Tab.4.5.

4.2. TURBULENT FLOW

	$\ \mathcal{E}_{cs}\ _\infty$	$\ \mathcal{E}_{cs}\ _1$	$\ \mathcal{E}_{ps}\ _\infty$	$\ \mathcal{E}_{ps}\ _1$	\mathcal{S}
$\langle u_1 \rangle$	4.268×10^{-2}	2.581×10^{-3}	1.324×10^{-2}	2.814×10^{-6}	7.319×10^{-6}
$\langle u_2 \rangle$	3.226×10^{-2}	6.017×10^{-4}	3.588×10^{-3}	6.293×10^{-7}	3.203×10^{-6}
$\langle u_3 \rangle$	1.545×10^{-1}	4.609×10^{-3}	1.047×10^{-1}	3.233×10^{-5}	3.000×10^{-5}
$\langle p \rangle$	2.464×10^{-3}	1.822×10^{-4}	2.355×10^{-3}	9.568×10^{-8}	3.103×10^{-6}
$\langle \Theta \rangle$	1.229×10^{-2}	3.877×10^{-4}	7.922×10^{-4}	1.041×10^{-7}	4.597×10^{-7}

Tab. 4.4: *Max- and one- norms of errors committed in the centro- and planar- symmetries and ratio of the smallest to the largest spectral coefficients.*

4.2.1 Mean fields

As stated in the previous section the mean fields preserve the centro- and plane- symmetries and table Tab.4.4 reports the max- and one- norms.

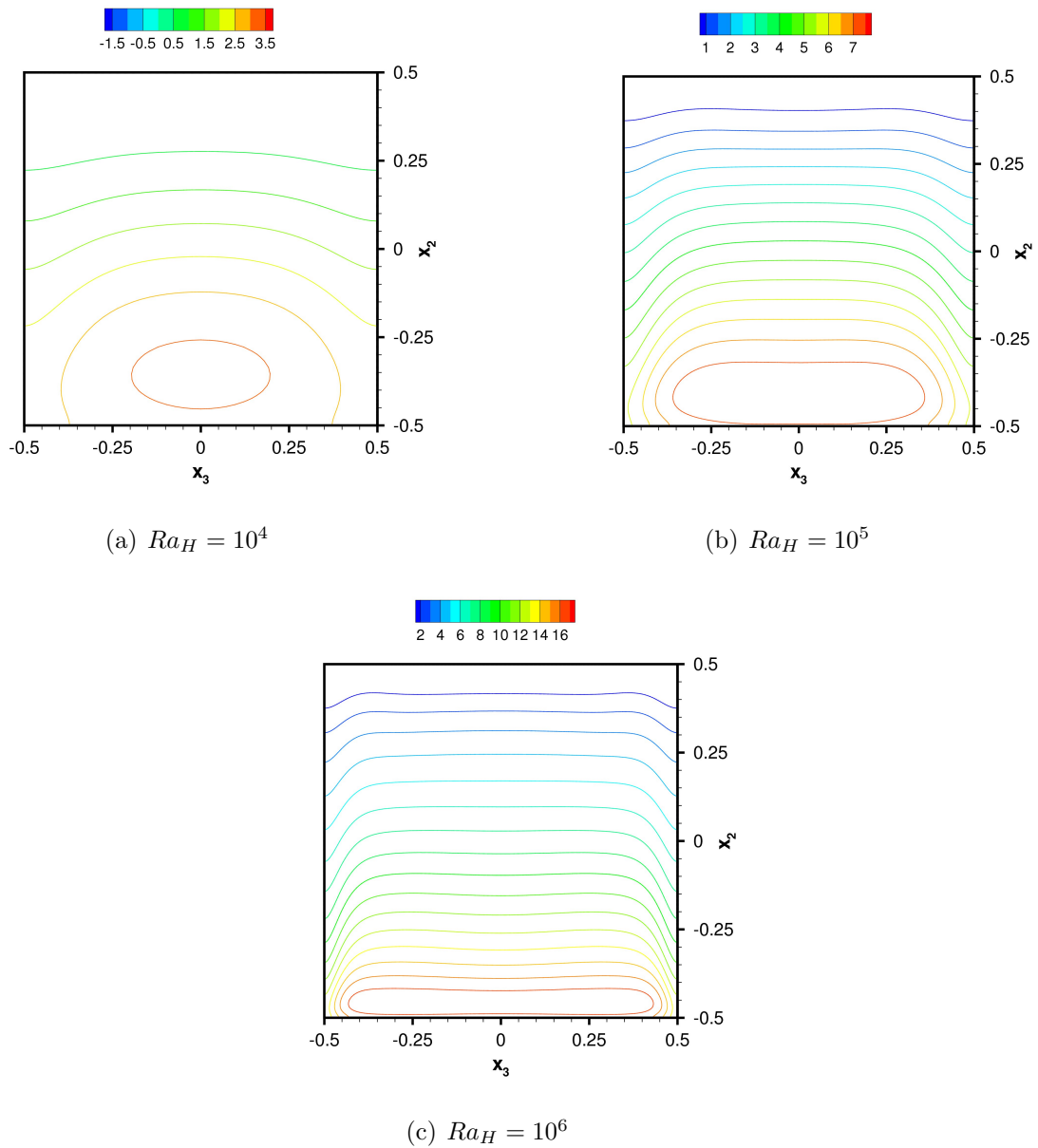


Fig. 4.10: Local Nusselt number contours at the hot wall for $Ra_H = 10^4, 10^5, 10^6$.

4.2. TURBULENT FLOW

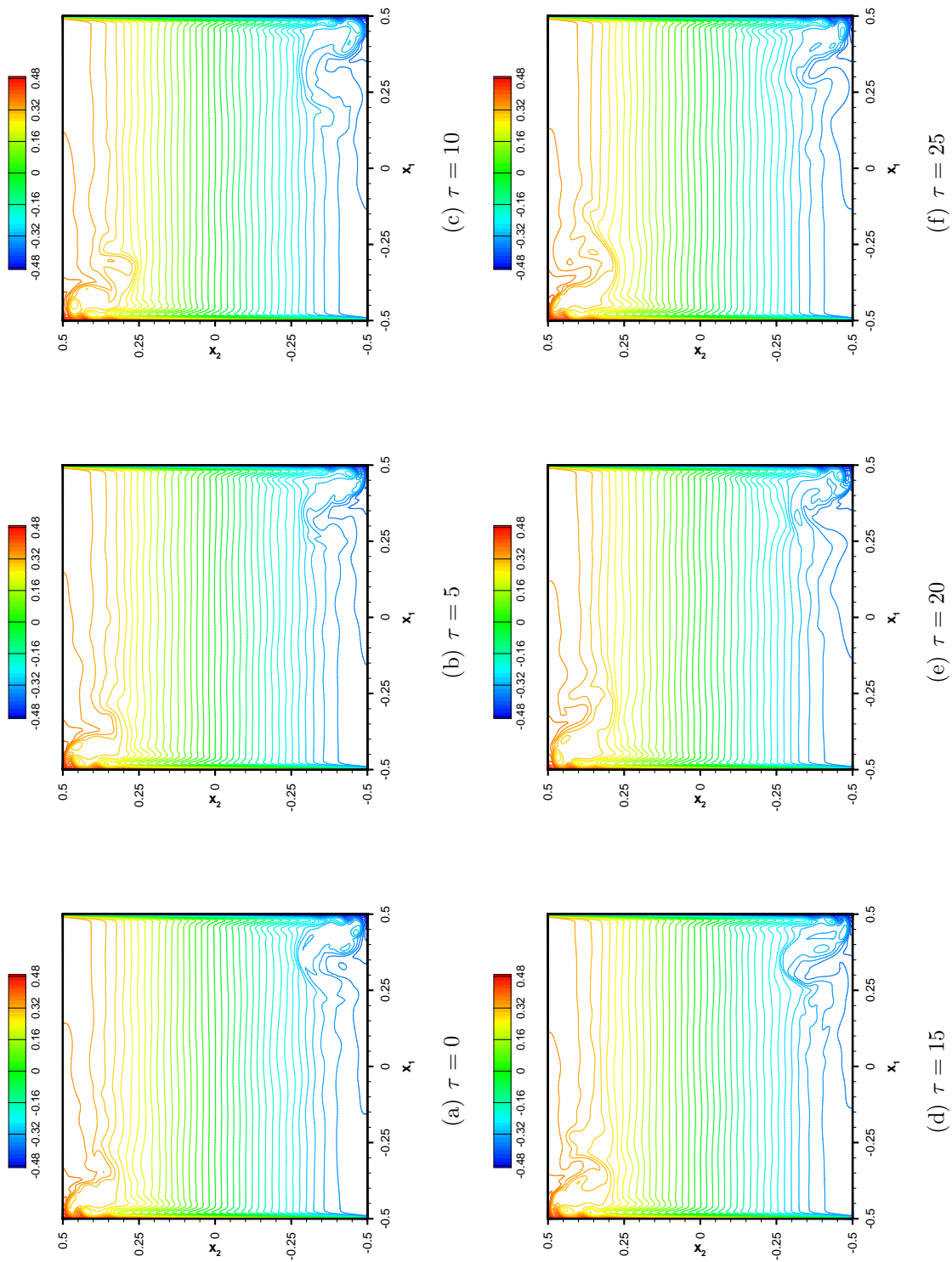


Fig. 4.11: Instantaneous contour plots of the temperature field Θ at the midplane $x_3 = 0$ for $Ra_H = 10^9$ at each $\Delta\tau = 5$.

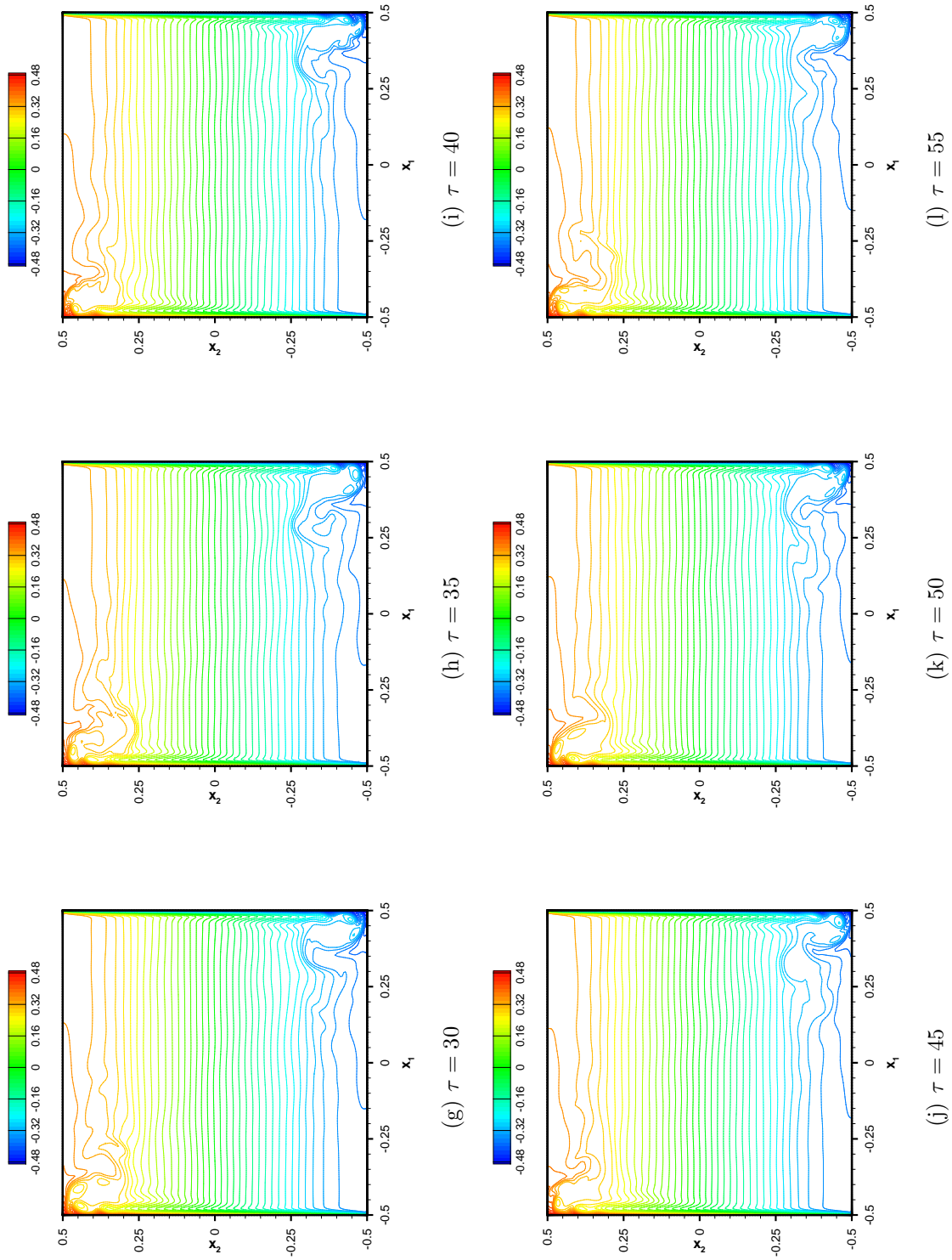


Fig. 4.12: Instantaneous contour plots of the temperature field Θ at the midplane $x_3 = 0$ for $Ra_H = 10^9$ at each $\Delta\tau = 5$.

4.2. TURBULENT FLOW

Ra_H	$N_1 = N_2 = N_3$	$min(\Delta x_i)$	$max(\Delta x_i)$	$\Delta\tau$	Sampl. freq.	Ave. time
10^9	169	8.742×10^{-5}	9.394×10^{-3}	5×10^{-3}	10	470.0

Tab. 4.5: *Computational parameters: polynomial degrees N_1, N_2, N_3 , minimum and maximum grid size Δx_i , integration time-step $\Delta\tau$, number of frames per unit of time and averaging time.*

It appears that the three-dimensional mean flow is subject to a degradation of the centro-symmetry property and this is actually the result of modes that lead to transition to unsteadiness that are no longer centro-symmetric and because of the finite size of the database, on the other hand the plane symmetry is orders of magnitude less than the centro-symmetry indicating that the spanwise instability modes are less crucial. Following the analysis performed in the two-dimensional case, the mean profiles of the vertical velocity component and the temperature measured at the mid-plane ($x_3 = 0$) at three different heights are reported in Fig.4.13-4.14 for $Ra_H = 10^9$. The profiles resemble closely those obtained in the two dimensional calculations shown in Fig.3.13-3.14 for the same Rayleigh number (as comparison are reported also the 2D velocity and temperature profiles at $x_2 = +0.3$). Hence, there is confirmation of the fact that as the Rayleigh number increases the three-dimensionality of the mean flow is negligible at the active walls. The profiles of the mean temperature field along the vertical centerline and the stratification coefficient (Fig.4.15-4.16) show, again, a clear stratified core region ($\zeta \approx 1$) and the top/hot and bottom/cold zones where the vertical spatial temperature changes are small. In fact due to the adiabatic horizontal walls and the heat flow transported mainly by convection, the local neighborhood close to the top and bottom wall present almost uniform temperature spatial distribution. The Nusselt number distribution at the hot wall (Fig.4.17) shows a very high peak at the bottom. In fact it appears that this configuration of cavity does not take too much advantage from the turbulent flow at moderately high Rayleigh numbers because of the vertical stratification that inhibits the heat transfer downstream at the active walls. In the same way the shear stress at the hot and top walls (Fig.4.19) follows the behavior already described in Chap.3.2 showing detachment and reattachment zones at the top wall close to the edge where the jet turns. The three-dimensional distributions of the time-averaged velocity components, temperature and pressure are provided in Fig.4.20. All the characteristics described in the two-dimensional flow at $Ra_H = 10^9$ can be extended to the present case in the whole domain but very close to the adiabatic side walls. Besides that three-dimensional effects become more important for the horizontal and spanwise component of velocity. In fact, the occurrence of a modulated wavy-like pattern is clearly visible in the spanwise direction of the streamwise velocity component right after the wall jets have negotiated the corners. This behavior is a direct consequence of the instability

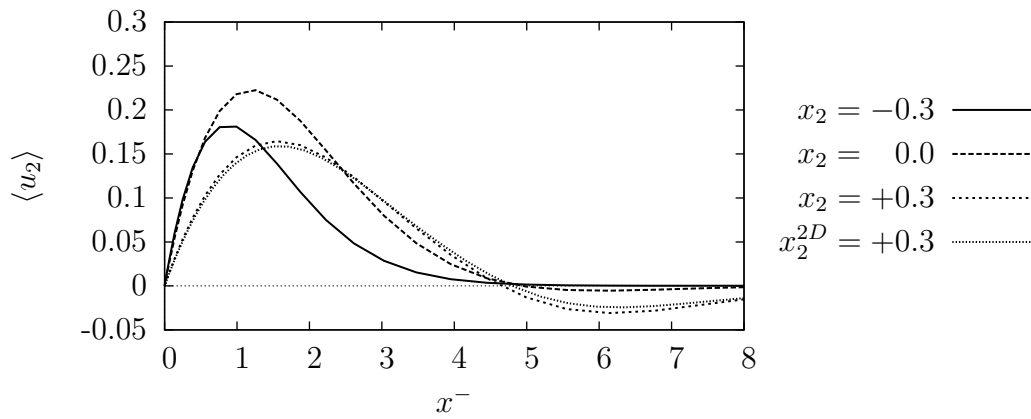


Fig. 4.13: Time-averaged vertical component velocity profiles at different heights $x_2 = -0.3, 0.0, +0.3$ on the mid-plane $x_3 = 0$ with respect to x^- .

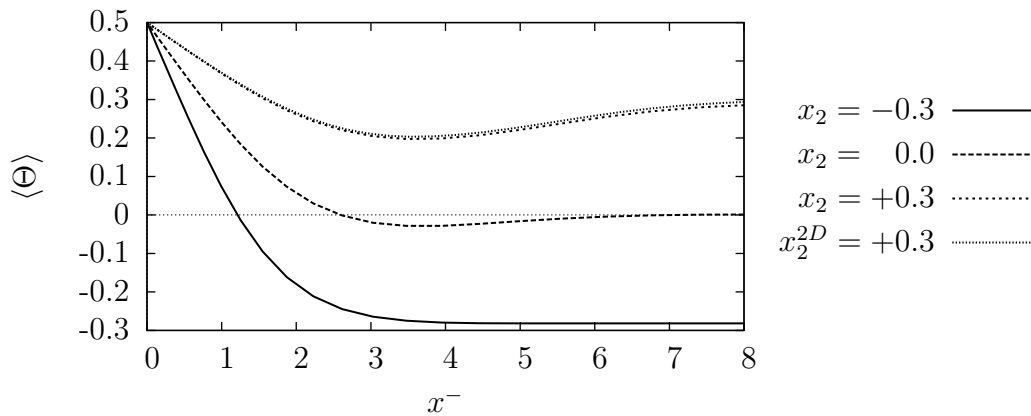


Fig. 4.14: Time-averaged temperature profiles at different heights $x_2 = -0.3, 0.0, +0.3$ on the mid-plane $x_3 = 0$ with respect to x^- .

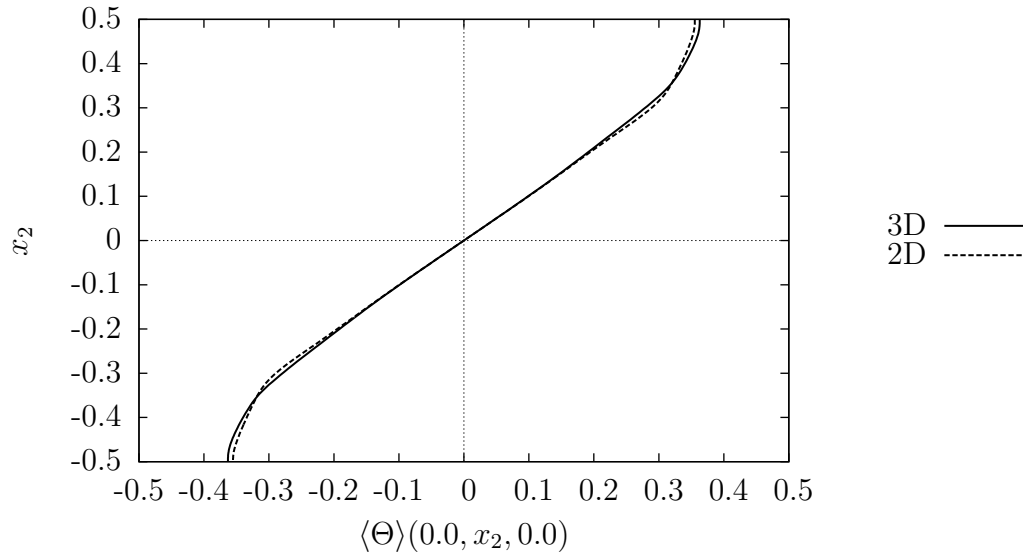


Fig. 4.15: *Time-averaged temperature profile along the vertical center-line.*

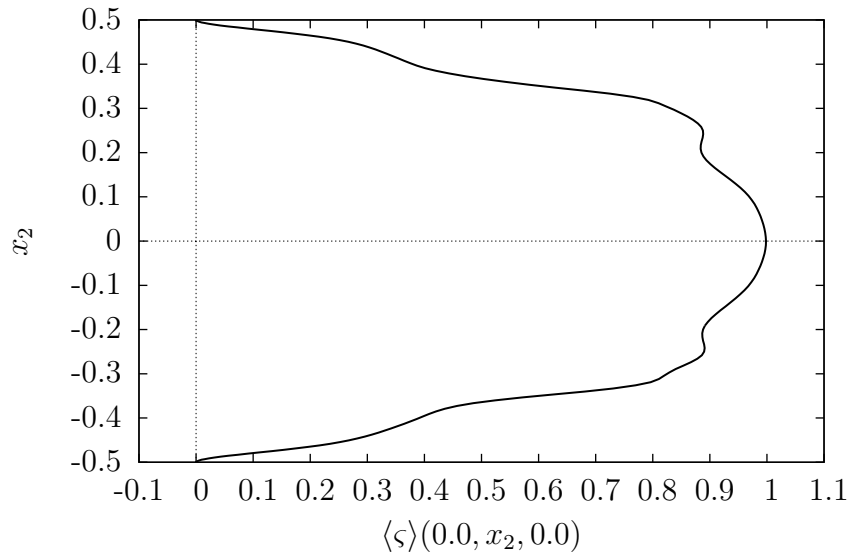


Fig. 4.16: *Time-averaged temperature stratification coefficient along the vertical center-line.*

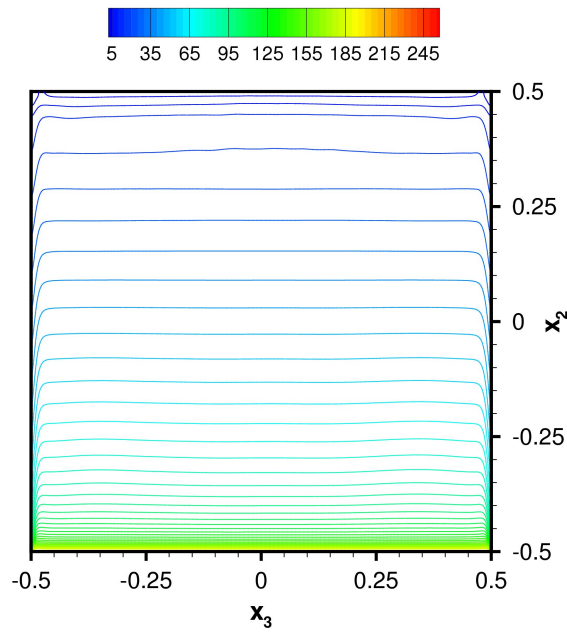


Fig. 4.17: *Time-averaged Nusselt number distribution at the hot wall ($x_1 = -0.5$) for $Ra_H = 10^9$.*

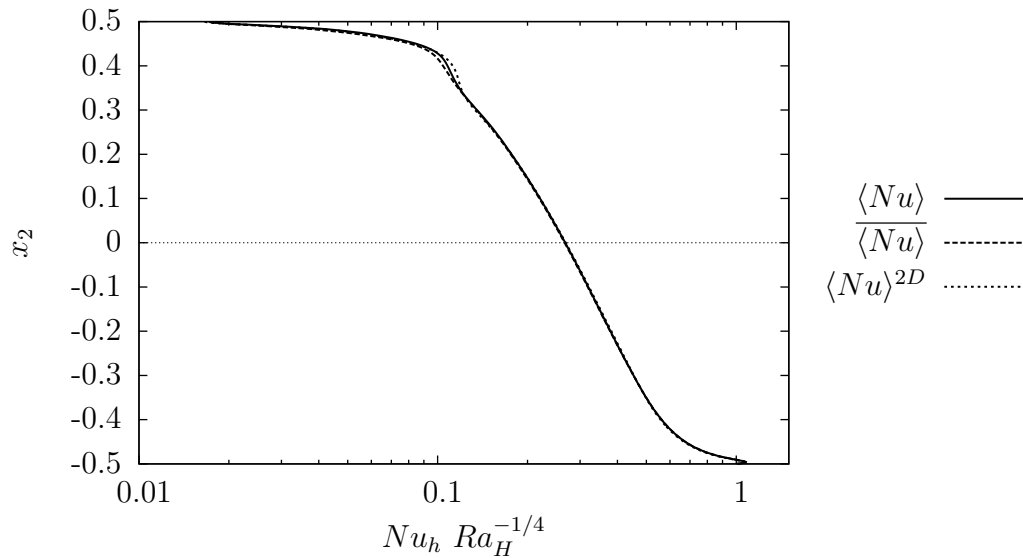


Fig. 4.18: *Comparison of time-averaged Nusselt profile along the hot wall centerline $\langle Nu \rangle$, the 3D spanwise mean $\overline{\langle Nu \rangle}$ and the two dimensional distribution $\langle Nu \rangle^{2D}$ at $Ra_H = 10^9$.*

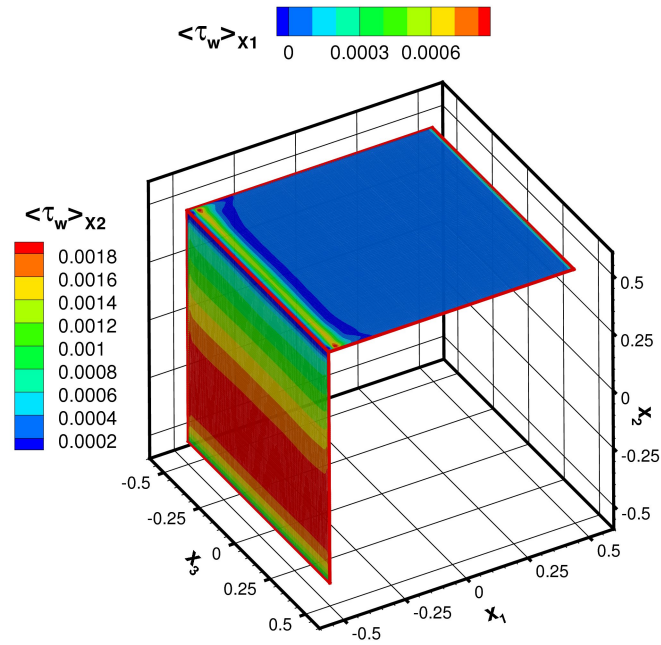


Fig. 4.19: Time-averaged shear stress vertical and horizontal components (τ_{12} and τ_{21}) at the hot and top wall respectively at $Ra_H = 10^9$.

mechanism and the Reynolds stresses will present the same characteristics.

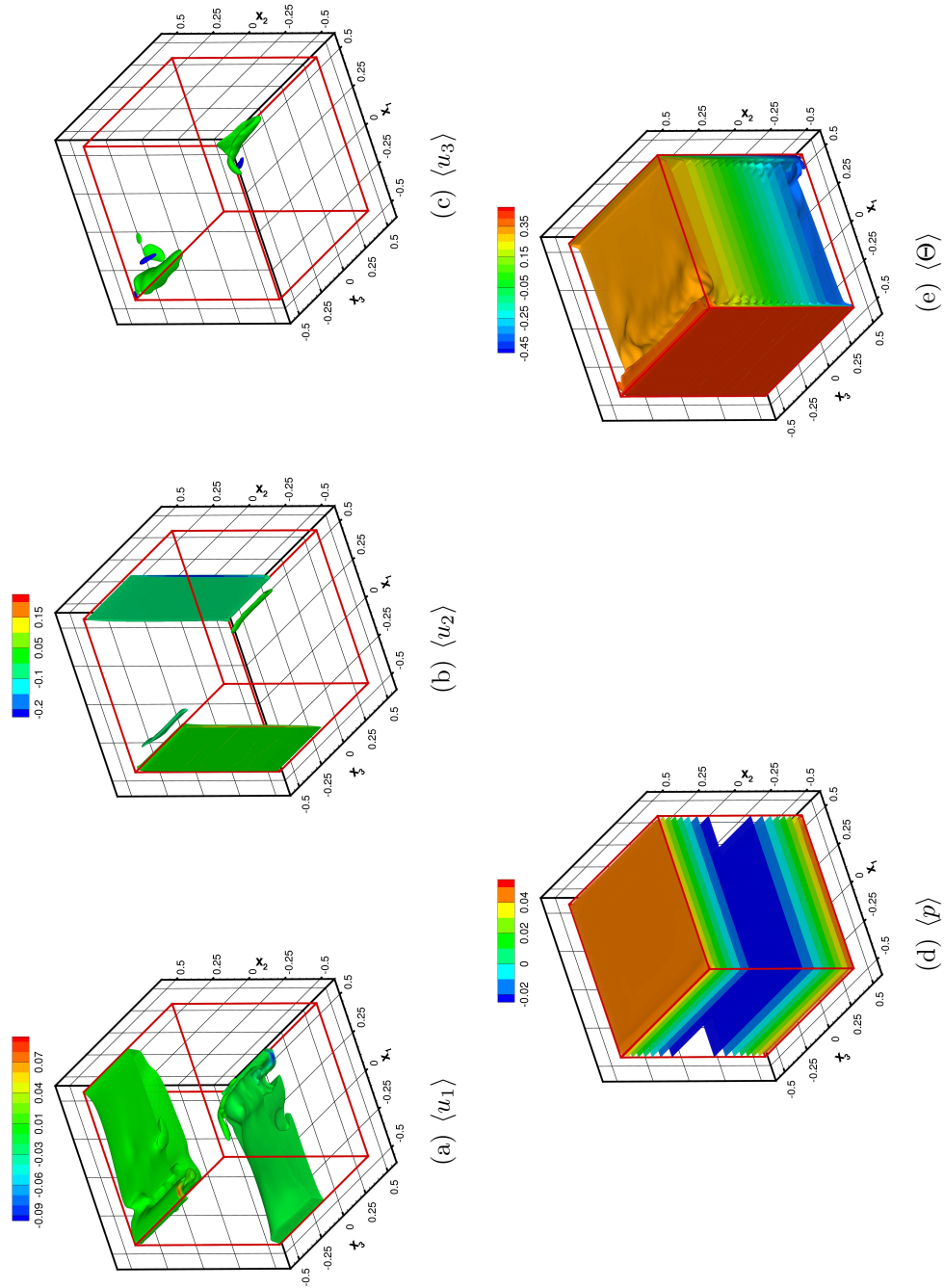


Fig. 4.20: Time-averaged velocity (limited to $x_3 \leq 0$), pressure and temperature fields at $Ra_H = 10^9$. Iso-surfaces levels in Fig.4.20(c) are $-0.01, 0.007$

Reynolds stresses and turbulent heat flux

The spatial distribution of the components $\langle u'_i u'_j \rangle$ of the Reynolds stress tensor is reported in Fig.4.21 in the region $x_3 < 0$. It is worth to remark that the quantities under investigation show three-dimensional structures with a wavy character along the spanwise direction. This is due to the mechanism that drives the flow to unsteadiness as stated in [JH96, HL96]. Indeed, Janssen *et al.* [HL96] have found that the Kelvin-Helmholtz type instability related to the separation of the flow from the horizontal adiabatic walls is modulated along the spanwise direction with a characteristic wave-length resulting in a three-dimensional wavy patterns¹ that persists also at Rayleigh numbers two orders of magnitude larger than the critical Rayleigh number ($Ra_c^{3D} \approx 3.3 \times 10^7$). Hence, even if the mean flow shows basically two dimensional features in the boundary layers (i.e. no wave motion is encountered) and the instability mechanism is the same as for the square cavity, the latter has an intrinsic three-dimensional nature that manifests downstream the separation at the horizontal walls.

It should be noted that the maxima of the velocity covariances are located in different regions depending on the velocity component considered. The covariance of the fluctuations of the horizontal velocity component shows high intensity along the active walls in the outer part of the time-averaged boundary layer. On the other hand the variance of the vertical velocity fluctuations $\langle u'_2 u'_2 \rangle$ (Fig.4.21) reaches its maxima in the region interested by the unsteady hook-like structures. Moreover, the latter term provides the main contribution to the turbulent kinetic energy k , since the spanwise fluctuation covariance $\langle u'_3 u'_3 \rangle$ is characterized by low intensity with respect to the others (at least one order of magnitude less). Moreover, as already depicted in the two-dimensional simulations presented in the previous chapter, there exists some turbulent activity in the outer part of the laminar boundary layer where vertical counter flow occurs.

Concerning the off diagonal terms $\langle u'_i u'_j \rangle$, $i \neq j$ of the symmetric Reynolds stress tensor, it is noteworthy to say that even in the fully three-dimensional case the term $\langle u'_1 u'_2 \rangle$ shows high positive values in the region where the boundary layer undergoes oscillations generating Tollmien-Schlichting waves. Furthermore it is located in the thin region between the mean velocity maximum and the outer counterflow. This peculiarity of the Reynolds stresses has been found also in [TSOPS07] for a cavity with an aspect ratio (height/length) of four. Finally it is also noteworthy to say that modest turbulent activity is always present in the region affected by the unsteady hook-like structure.

¹This behavior can be enhanced or reduced depending on the Prandtl number and cavity spanwise aspect ratio.

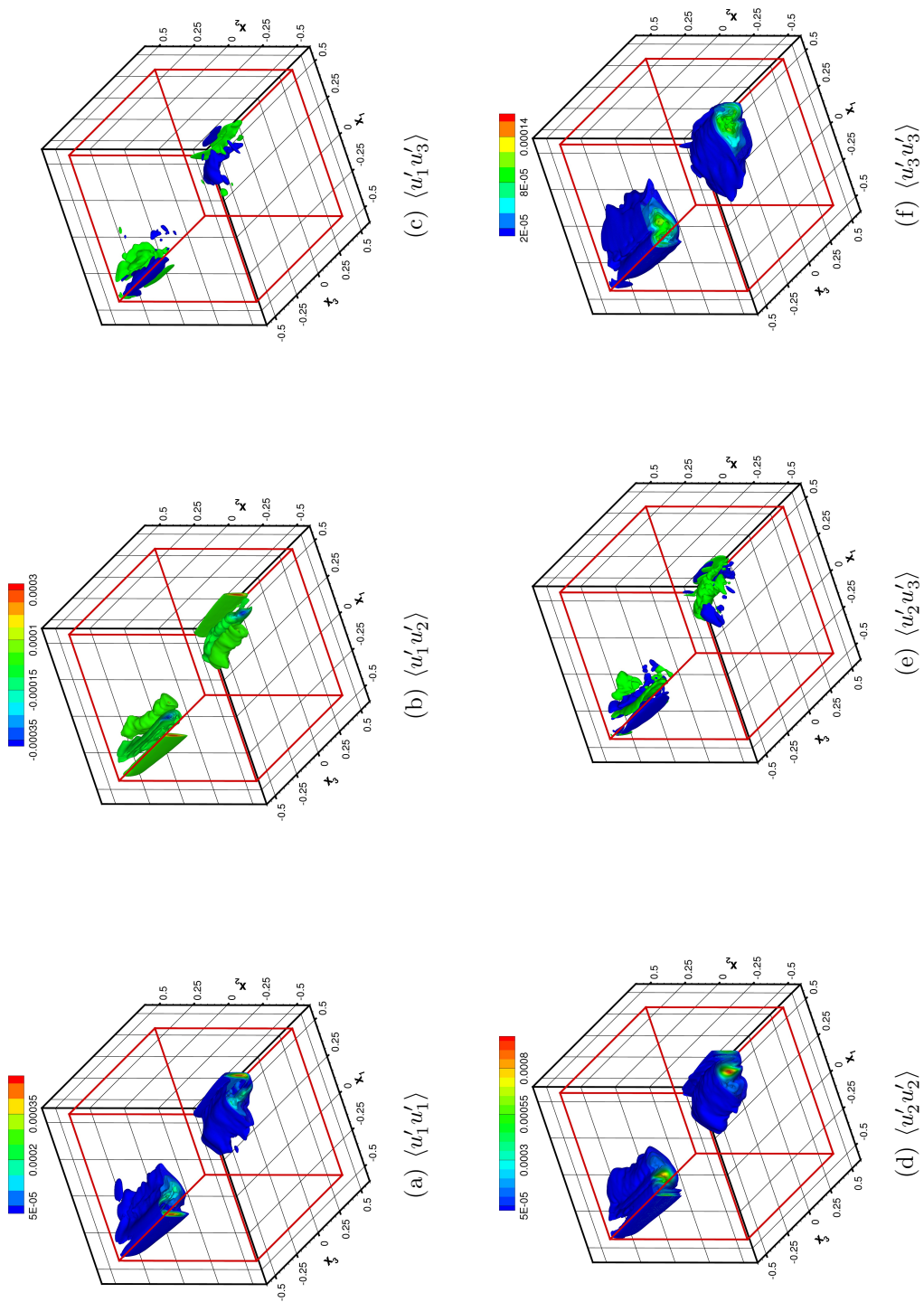


Fig. 4.21: Reynolds-stresses distribution limited to $x_3 \leq 0$. Levels for $\langle u_1' u_3' \rangle = \langle u_2' u_3' \rangle = \pm 2 \times 10^{-5}$.

4.2. TURBULENT FLOW

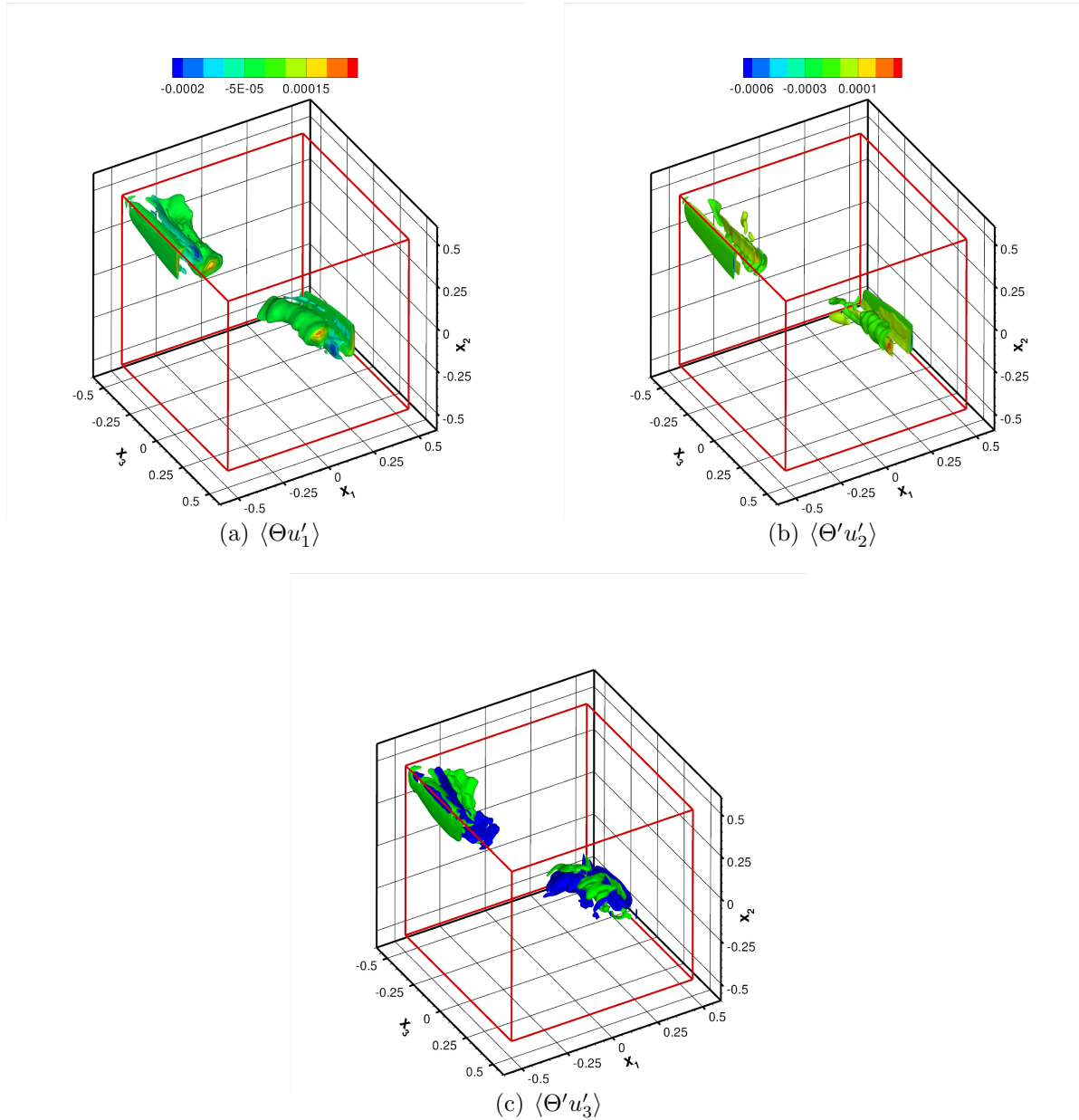


Fig. 4.22: Turbulent heat flux in the half domain $x_3 < 0$. Levels for $\langle \Theta u'_3 \rangle = \pm 2 \times 10^{-5}$

Continuing the analysis of the turbulent quantities it is important to describe the behavior of the turbulent heat flux $\langle \Theta u'_i \rangle$ (Fig.4.22). One interesting and unexpected property of the turbulent heat flux is that its vertical component, i.e. $\langle \Theta u'_2 \rangle$, shows negative values along the turbulent vertical boundary layers working against the mean convective heat flux $\langle \Theta u_2 \rangle$ that is positive and streamwise directed. As seen before for the Reynolds stress

	$\ Res(\langle u_1 \rangle)\ _1$	$\ Res(\langle u_2 \rangle)\ _1$	$\ Res(\langle u_3 \rangle)\ _1$	$\ Res(\langle \Theta \rangle)\ _1$
$Ra_H = 10^9$	3.054×10^{-5}	8.924×10^{-5}	1.299×10^{-5}	6.010×10^{-5}

Tab. 4.6: *One-norm of the residuals of the time-averaged momentum and energy transport equations.*

terms $\langle u'_i u'_j \rangle$, all the quantities related to the spanwise fluctuations are very weak and located close to the adiabatic side walls.

4.2.2 Time-averaged momentum and energy budgets

The dimensionless governing equations of the mean quantities written in index notation read ([MY07])

$$\frac{\partial \langle u_i \rangle}{\partial x_i} = 0 \quad (4.15)$$

$$\frac{\partial \langle u_i \rangle}{\partial \tau} + \underbrace{\langle u_j \rangle \frac{\partial \langle u_i \rangle}{\partial x_j}}_{CTM} = - \underbrace{\frac{\partial \langle p \rangle}{\partial x_i}}_{PG} + \underbrace{\frac{Pr}{\sqrt{Ra_H}} \frac{\partial^2 \langle u_i \rangle}{\partial x_j^2}}_{VD} - \underbrace{\frac{\partial \langle u'_i u'_j \rangle}{\partial x_j}}_{RS} + \underbrace{Pr \langle \Theta \rangle \delta_{i2}}_{BT} \quad (4.16)$$

$$\frac{\partial \langle \Theta \rangle}{\partial \tau} + \underbrace{\langle u_i \rangle \frac{\partial \langle \Theta \rangle}{\partial x_i}}_{CTT} = \underbrace{\frac{1}{\sqrt{Ra_H}} \frac{\partial^2 \langle \Theta \rangle}{\partial x_i^2}}_{TD} - \underbrace{\frac{\partial \langle u'_i \Theta' \rangle}{\partial x_i}}_{THF}. \quad (4.17)$$

where $\langle u'_i u'_j \rangle$ and $\langle \Theta' u'_i \rangle$ are the Reynolds stress tensor and the turbulent heat flux respectively. Theoretically, for a statistically steady flow the accumulation terms, identified by the time-derivatives, are zero. In practice, the balances defined as the residual Res of the mean Boussinesq equations at every collocation point,

$$Res(\langle u_i \rangle) = \left| \langle u_j \rangle \frac{\partial \langle u_i \rangle}{\partial x_j} + \frac{\partial \langle u'_i u'_j \rangle}{\partial x_k} + \frac{\partial \langle p \rangle}{\partial x_i} - \frac{Pr}{\sqrt{Ra_H}} \frac{\partial^2 \langle u_i \rangle}{\partial x_j^2} - Pr \langle \Theta \rangle \delta_{i2} \right| \quad (4.18)$$

$$Res(\langle \Theta \rangle) = \left| \langle u_j \rangle \frac{\partial \langle \Theta \rangle}{\partial x_j} + \frac{\partial \langle \Theta' u'_j \rangle}{\partial x_k} - \frac{1}{\sqrt{Ra_H}} \frac{\partial^2 \langle \Theta \rangle}{\partial x_j^2} \right| \quad (4.19)$$

give a measure of the error introduced by selecting a finite number of samples in a finite time interval. For the present calculations, in both cases the 1-norm of the residuals are of the order $O(10^{-4})$ or less, as shown in Tab.4.6. The low residuals in the averaged fields are a proof of the correctness of the sampling frequency and the length of the averaging time of the databases. It is worth to note that the iso-surfaces of $\langle u'_1 u'_2 \rangle$ show a sort of wavy shape along the spanwise direction that can be related to the spanwise disturbances that lead to unsteadiness as pinpointed in [HL96]. The terms appearing in the second component of

the mean momentum conservation law evaluated at the horizontal and vertical center-lines are shown in Fig.4.23. Close to the active walls ($0 \leq x^- \leq 2$) the dominant terms are the buoyancy force and the viscous one and they interest almost all the boundary layer thickness. Not completely negligible is the contribution of the convective part that becomes comparable to the BT and VD for $x^- > 1$. On the other hand the budgets along the vertical centerline show again a play between two dominant effects: again the buoyancy force but this time the pressure gradient. The main reason is due to the occurrence of thermal stratification away from the active vertical walls and downstream the expansion after the plumes have negotiated the corner regions as explained in Sec.3.2.1. Furthermore it is also important to note that the budgets of the horizontal and spanwise components of the mean Navier-Stokes equations are several orders of magnitude less than those appearing in the second component, stressing that the energy and momentum coupling through the buoyancy term causes strong effects along the vertical direction (either in the boundary layers either in the core region) that are balanced by the mean fields rather than the turbulent ones. In fact Fig.4.24 depicts the mean momentum budgets of the first component of the velocity along the vertical direction, for which the buoyancy does not play any direct role, that convective term (CTM), pressure gradient (PG), viscous dissipation (VD) and Reynolds stresses (RS) are comparable between $0.2 < x_2 < 0.4$ ($-0.4 < x_2 < -0.2$ for symmetry). It is worth to notice that pressure and viscous effects are both positive (around $x_2 \approx 0.35$) in order to balance the Reynolds stresses and the convective term which becomes important. It is possible to see that the horizontal motion is decelerated by diffusion and by an adverse pressure gradient. Moreover, very close to the adiabatic walls the largest forces are those coming from the viscous dissipation and the pressure gradient. Referring to Fig.4.25, the time-averaged energy budgets along the horizontal centerline show again a similar behavior to the two dimensional square cavity (Fig.3.23).

4.2.3 Turbulence characterization

Natural convective turbulence is quantified by the turbulent kinetic energy $k = \langle u'_i u'_i \rangle / 2$ and temperature variance $\langle \Theta' \Theta' \rangle$ (Fig. 4.26(a)). The maximum of the turbulent kinetic energy is located in the center of the hook-like structure ($p^{kmax} = (-0.3469, 0.3601, -0.1113)$) as for $\langle u'_2 u'_2 \rangle$. The wavy modulation in the spanwise direction is still recognizable. The total mean kinetic energy $\langle e \rangle$ and its decomposition in the kinetic energy contained in the mean flow $\overline{\langle K \rangle} = 1/2 \langle u_i \rangle^2$ and in the turbulent flow $\overline{k} = 1/2 \overline{u'_i u'_i}$ is shown in Tab.4.7. It can be seen how the turbulent kinetic energy represents only the five percent of the total averaged kinetic energy of the flow. In comparison with the values reported in Tab.3.5, the three dimensional turbulence appears to be less strong than in the two dimensional case because of the spanwise modulation of the regions interested by a relatively high fluc-

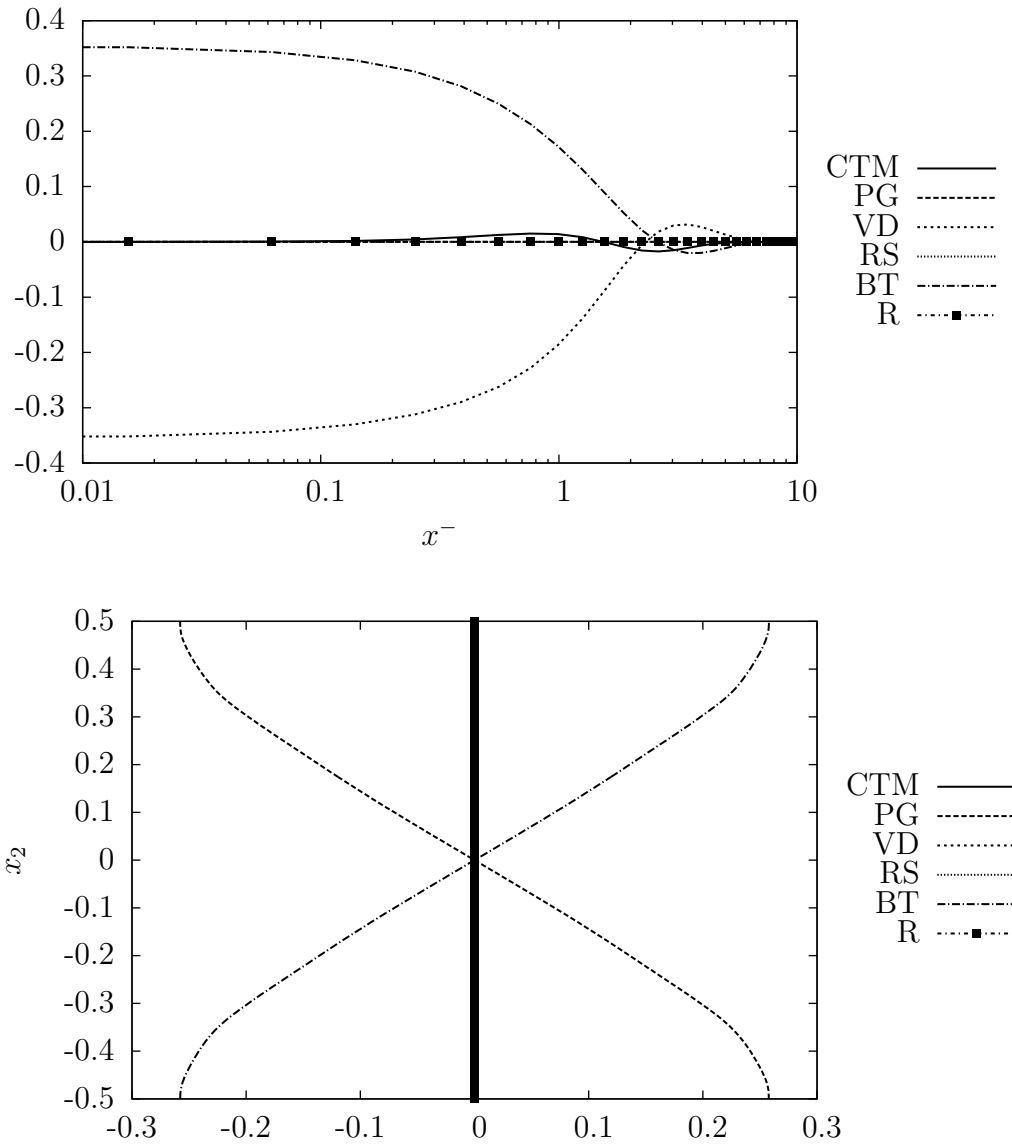


Fig. 4.23: Budget profiles of the second component of the time-averaged Navier-Stokes equations along the horizontal (top) and vertical centerline (bottom): Convective Term (CTM), Pressure Gradient (PG), Viscous Diffusion (VD), Reynolds Stresses (RS), Buoyancy Term (BT) and Residual (R).

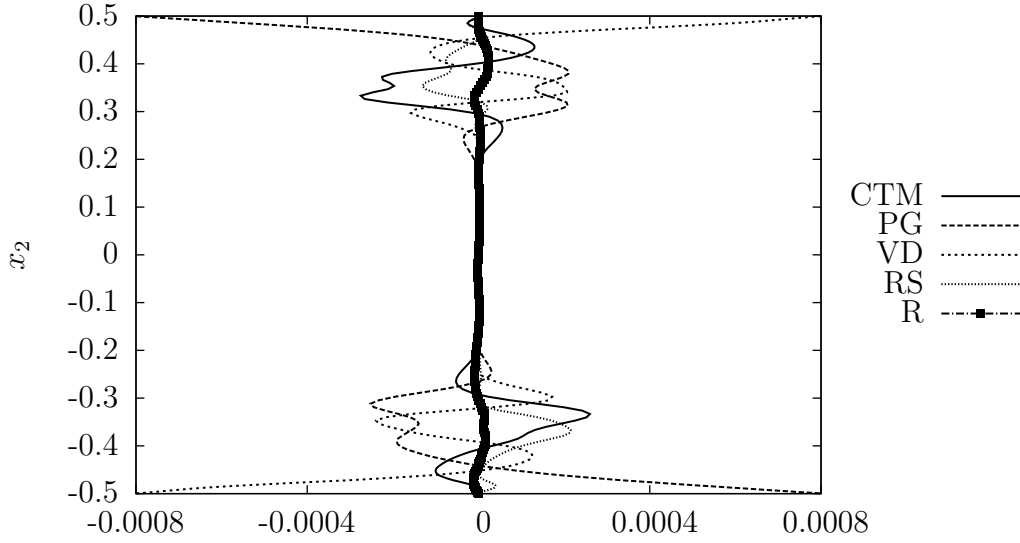


Fig. 4.24: Budget profiles of the first component of the time-averaged Navier-Stokes equations along the vertical centerline: Convective Term (CTM), Pressure Gradient (PG), Viscous Diffusion (VD), Reynolds Stresses (RS) and Residual (R).

$\langle e \rangle Ra_H^{1/4}$	$\overline{\langle K \rangle} Ra_H^{1/4} (\%)$	$\bar{k} Ra_H^{1/4} (\%)$
6.99×10^{-2}	$6.63 \times 10^{-2} (95.0)$	$3.60 \times 10^{-3} (5.0)$
$0.5 \overline{\langle u'_1 u'_1 \rangle} Ra^{1/4} (\%)$	$0.5 \overline{\langle u'_2 u'_2 \rangle} Ra^{1/4} (\%)$	$0.5 \overline{\langle u'_3 u'_3 \rangle} Ra^{1/4} (\%)$
$1.07 \times 10^{-3} (1.5)$	$1.77 \times 10^{-3} (2.5)$	$7.60 \times 10^{-4} (1.0)$

Tab. 4.7: Total averaged kinetic energy scaled by $Ra_H^{1/4}$ and its repartition between mean flow $\overline{\langle K \rangle}$ and turbulent part \bar{k} in each single component $0.5 \overline{\langle u'_i u'_i \rangle}$ for $Ra_H = 10^9$.

tuation intensity. Furthermore, it is also interesting to show that the largest contribution to the term \bar{k} comes from $\langle u'_2 u'_2 \rangle$, even if there is not a predominant term between the fluctuation components since they represent each one just few percents of $\langle e \rangle$. Concerning the temperature variance, the maximum is located close to the active walls downstream the vertical laminar boundary layers. Both distribution are in agreement on the symmetric plane $x_3 = 0$ with the two dimensional results. The one-dimensional profiles of the turbulent kinetic energy and the temperature variance computed along the midplane $x_3 = 0$ at $x_2 = 0.3$ are presented in Fig.4.27. It is possible to note that the peak of k is around $x^- \approx 30$ outside the boundary layer but in the corner eddy. The presence of the latter structure causes also the local maxima closer to the wall. Alike the turbulent kinetic energy the temperature variance $\langle \Theta' \Theta' \rangle$ shows a peak at $x^- \approx 30$. Moreover it presents less local

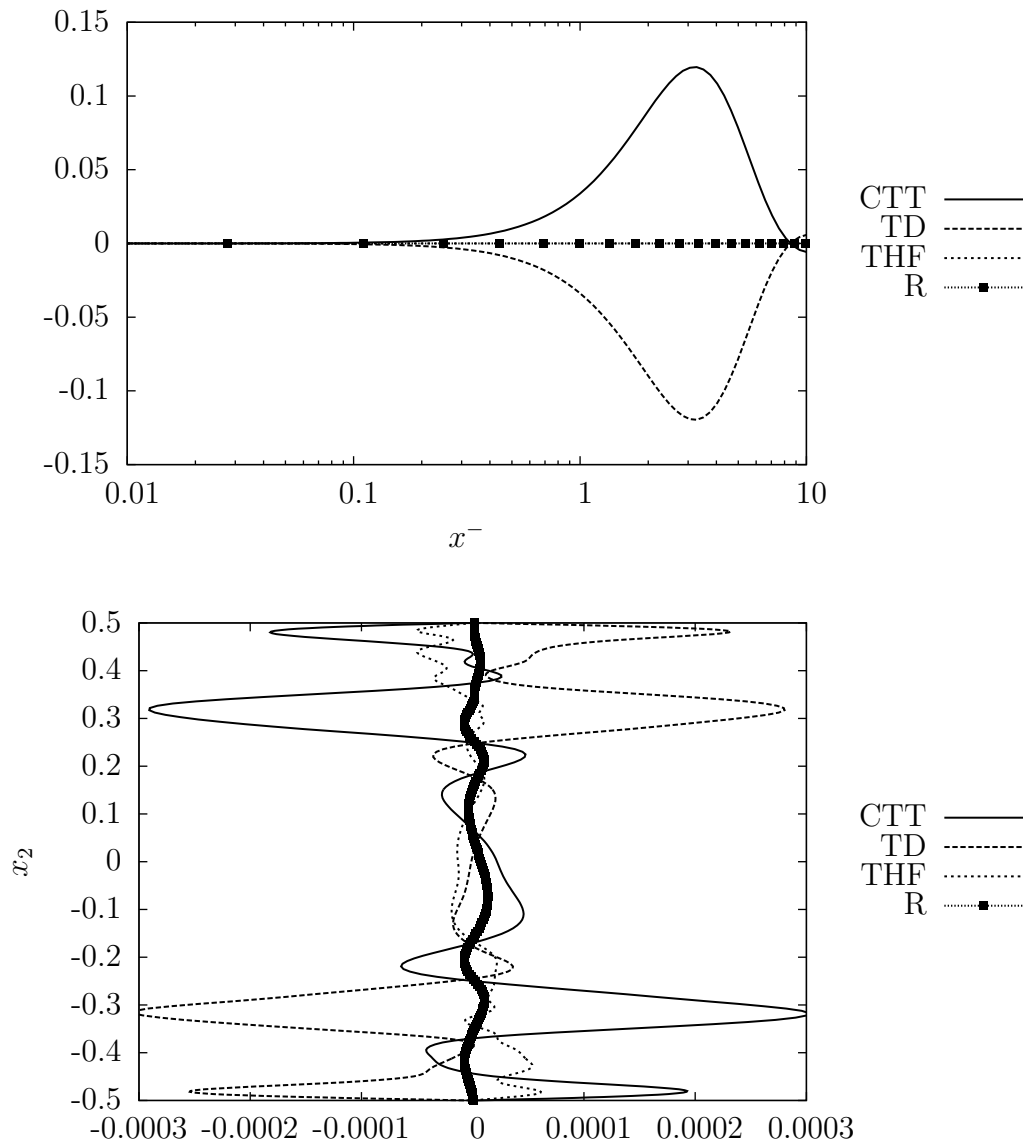


Fig. 4.25: Budget profiles of the time-averaged energy equation along the horizontal and vertical centerline: Convective Term (CTT), Thermal Diffusion (TD), Turbulent Heat Flux (THF) and Residual (R).

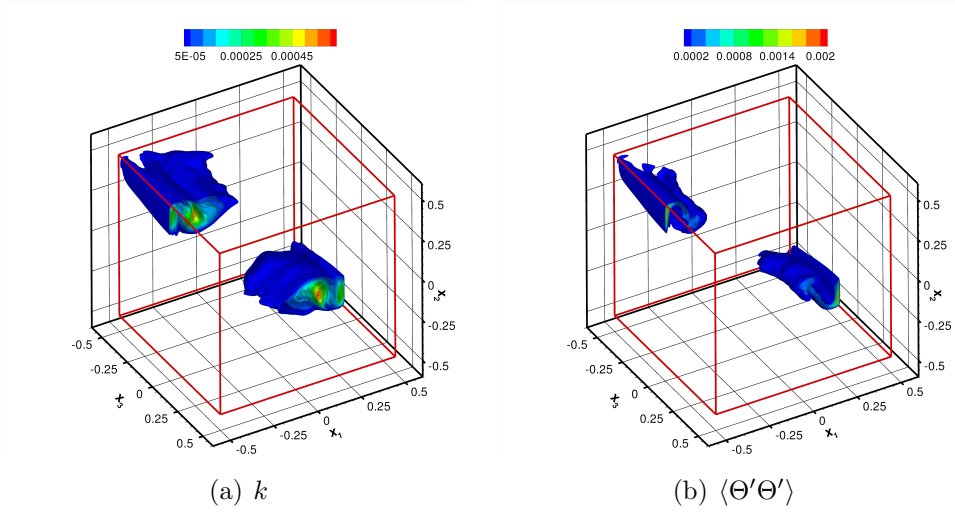


Fig. 4.26: Iso-surfaces of turbulent kinetic energy and temperature variance for $x_3 < 0.0$ with respect to x^- .

extrema. Furthermore the transport equations written in index notation of such quantities read

$$\begin{aligned} \frac{\partial k}{\partial \tau} + \langle u_j \rangle \frac{\partial k}{\partial x_j} &= \frac{\partial}{\partial x_j} \left(\frac{Pr}{\sqrt{Ra_H}} \frac{\partial k}{\partial x_j} - \langle u'_j k' \rangle - \langle u'_j p' \rangle \right) \\ &\quad - \underbrace{\langle u'_i u'_j \rangle \frac{\partial \langle u_i \rangle}{\partial x_j}}_P - \underbrace{\frac{Pr}{\sqrt{Ra_H}} \left\langle \frac{\partial u'_i}{\partial x_j} \frac{\partial u'_i}{\partial x_j} \right\rangle}_D + \underbrace{Pr \langle u_i \Theta' \rangle \delta_{i,2}}_G \end{aligned} \quad (4.20)$$

$$\begin{aligned} \frac{\partial \langle \Theta' \Theta' \rangle}{\partial \tau} + \langle u_j \rangle \frac{\partial \langle \Theta' \Theta' \rangle}{\partial x_j} &= \left(\frac{1}{\sqrt{Ra_H}} \frac{\partial \langle \Theta' \Theta' \rangle}{\partial x_j} - \langle u'_j \Theta' \Theta' \rangle \right) \\ &\quad - \underbrace{2 \langle \Theta' u'_j \rangle \frac{\partial \langle \Theta \rangle}{\partial x_j}}_{P_\Theta} - \underbrace{\frac{2}{\sqrt{Ra_H}} \left\langle \frac{\partial \Theta'}{\partial x_j} \frac{\partial \Theta'}{\partial x_j} \right\rangle}_{D_\Theta} \end{aligned} \quad (4.21)$$

In Fig.4.28 the maximum of the production P appears around $x^- = 3$ and for G it is worth to note that it is always negative but mainly acting as a source term for $2.5 \leq x^- \leq 7.5$. Finally the dissipation D has strong influence for $x^- \leq 1$. Unlike the production term P , P_Θ is always positive and with the first maximum peak around $x^- \approx 2$. Finally the level of temperature variance dissipation rate is rather low in comparison with D . In order to characterize the turbulence of the present flow configuration it is necessary to sample time-series of velocity and temperature fluctuations in the cavity. The choice of the sampling points is rather difficult since the turbulence does not present any homogeneous direction and the statistics shows a rather high degree of anisotropy.

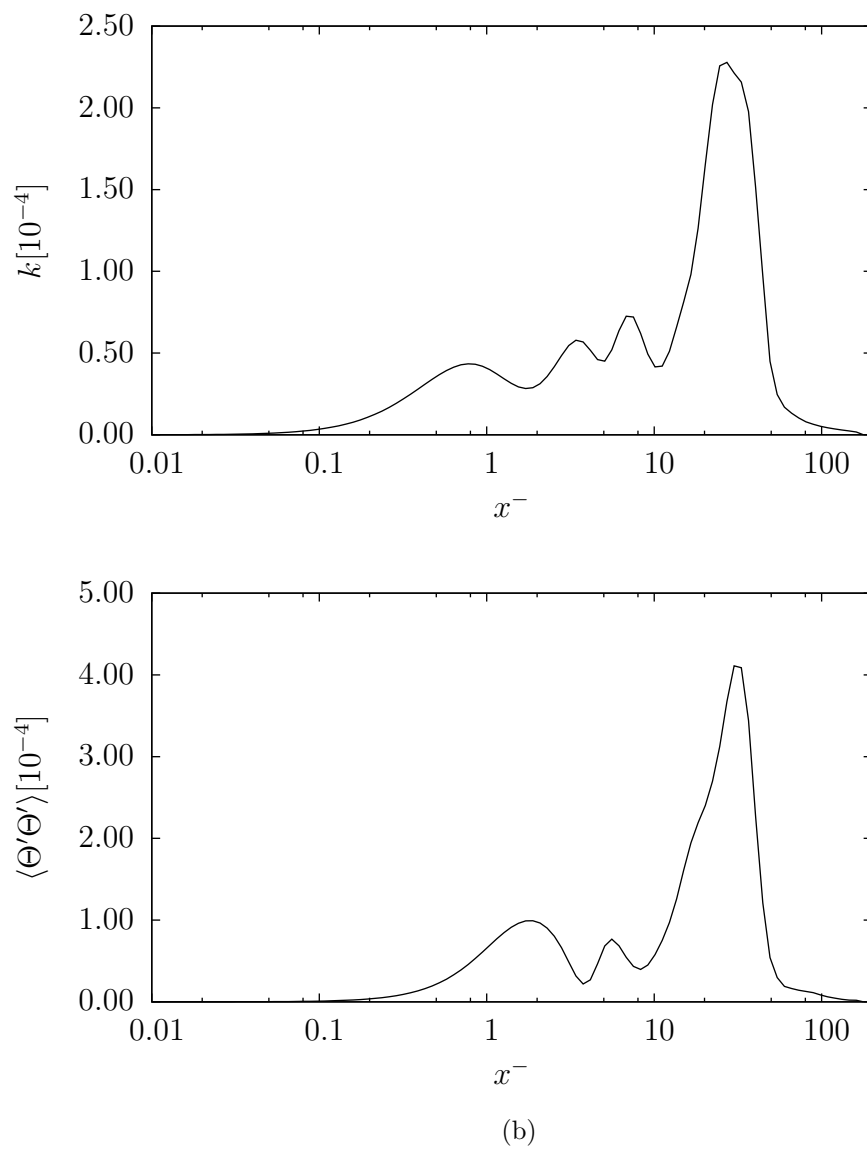


Fig. 4.27: *Turbulent kinetic energy k and temperature variance $\langle \Theta' \Theta' \rangle$ profiles in the mid-plane at $x_2 = +0.3$.*

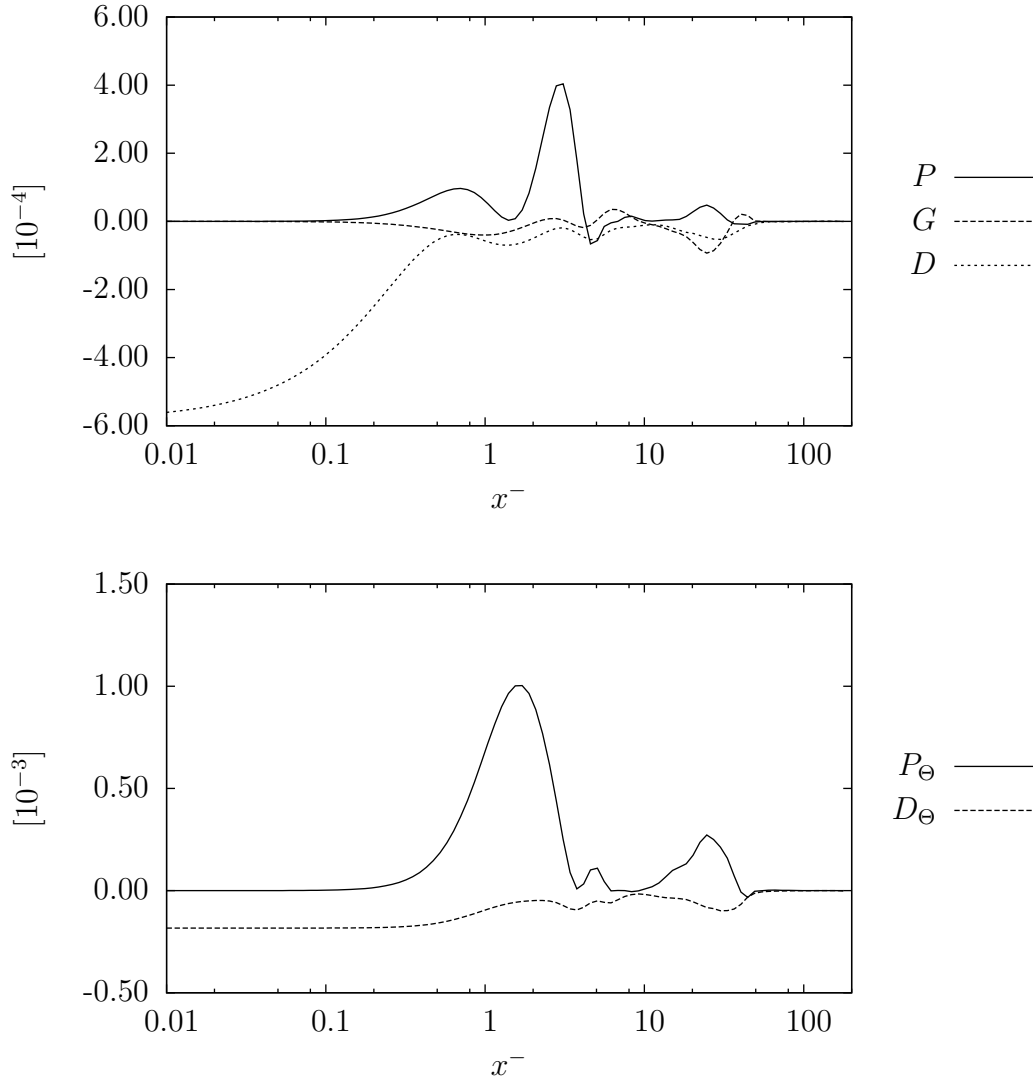


Fig. 4.28: Budget profiles of the turbulent kinetic energy and temperature variance production and dissipation terms for $Ra_H = 10^9$ along the horizontal line $x_2 = +0.3$ in the midplane $x_3 = 0$: P turbulent kinetic energy production due to mean shear stress, G production due to buoyancy effect, D turbulent kinetic energy dissipation rate; P_Θ temperature variance production due to mean temperature gradient, D_Θ temperature variance dissipation rate.

Anisotropy map

In order to quantify the degree of turbulence anisotropy author have used the anisotropy map [CL01, Pei99] that maps the second and third invariants² (II and III respectively) of the anisotropy tensor $\mathbf{B} = b_{ij} = \langle u'_i u'_j \rangle / (2k) - 1/3\delta_{ij}$ defined as function of the eigenvalues e_i of \mathbf{B} in the following way

$$\text{II} = \frac{1}{2}[(\text{tr}(\mathbf{B}))^2 - \text{tr}(\mathbf{B}^2)] = e_1 e_2 + e_2 e_3 + e_1 e_3 \quad (4.22)$$

$$\text{III} = \det(\mathbf{B}) = \prod_{i=1}^3 e_i. \quad (4.23)$$

The results presented in Fig.4.30 show the probability density function (PDF) of the second and third invariants of the anisotropy tensor in regions of the domain characterized by three levels of turbulent kinetic energy (i.e. $k/k_{max} = 0.4 \div 0.6$, $k/k_{max} = 0.6 \div 0.8$, $k/k_{max} = 0.8 \div 1$ respectively). It is important to notice that for a moderate level of turbulence intensity ($0.4 < k/k_{max} < 0.6$) the turbulence itself can be homogeneous (point (0,0) in the plane of the second and third invariants), axisymmetric, or even one dimensional (i.e. the shape of the turbulent structures presents one dominant preferential direction and the structures can be imagined as filaments). On the other hand, the high values of the PDF along the right branch of the map indicates that it is mostly probable that the turbulent structures resemble cigar-like shape. Increasing the level of relative turbulent kinetic energy leads to a reduced differentiation of the turbulent structures with a shift of the PDF towards the one dimensional state. For very high level of k (Fig.4.30(c)) the PDF is even more narrowed meaning that the most of the turbulent structures that contains the higher amount of energy are axial-symmetric with an elongated axis. Indeed it can be shown (Fig.4.26) that the region characterized by high turbulence intensity are distributed along the axis formed by the three-dimensional hook-like structure. From this analysis, two-dimensional disk-like structures are not present at all for a moderate level of turbulence (i.e. $k/k_{max} > 0.6$). The instantaneous coherent structures (i.e. turbulent eddies) are shown in Fig.4.29 at three different times, together with the instantaneous contour of the local Nusselt number and the wall shear-stress at the hot vertical active surface. The reader should note that a system of coupled spanwise elongated vortices grow at a certain height of the cavity and it is then advected along the hot wall until it breaks in smaller structures after the turning point (the same mechanism repeats symmetrically at the cold wall). Furthermore, it appears that because of the lateral walls the vortices during their development tend to bend at both extremities. It has also to be said, anyway, that this kind of structures are typical of transition regions and do not belong to fully developed turbulent

²The first invariant $\text{I} = \text{tr}(\mathbf{B}) = 0$.

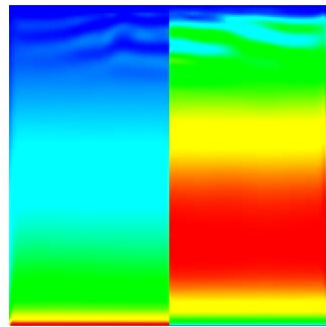
boundary layers flows for which the orientation of the coherent structures result aligned to the stream-wise direction (i.e. the so-called horseshoe/hairpin vortices). Moreover, the presence of vortices close to the active hot surface leads to local high velocity and temperature gradients hence inducing instantaneous local maxima of heat transfer and shear stresses at the vertical walls.

Auto-Correlation Function and Power Spectral Density

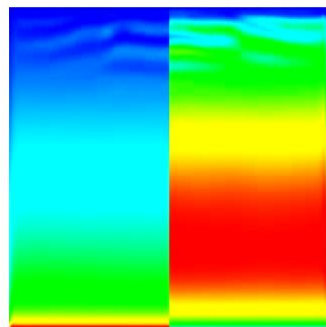
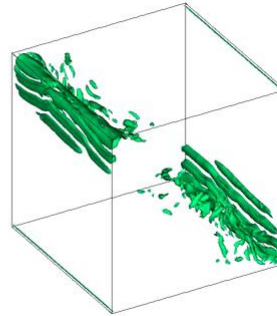
In order to characterize the turbulence in the cavity, the point of maximum turbulent kinetic energy has been chosen. In fact, as we have seen from the anisotropy maps in Fig.4.30 for values of turbulent kinetic energy larger than $0.6k_{max}$, a large amount of events show the same type of structures (elongated and axisymmetric). This means that on average the time-signal produces similar auto- and cross-correlations in a large region where intense turbulent activity takes place. Hence, the information obtained from the analysis of time history of the selected point at the location of maximum k would be “representative” of a rather large ensemble of turbulent events located at the turbulent corner regions. The time series of velocity components, temperature fluctuations are shown in Fig.4.31-4.32. It immediately appears that the introduction of energy in the signal is drastically reduced in comparison with the time evolution of the fluctuating flow quantities at the point of maximum turbulent kinetic energy production. The correspondent discrete Probability Density Functions (PDF) of the first four signals is provided in Fig.4.33. Let us notice that the PDFs of u'_1 and u'_3 show a Gaussian behavior (with a large variance in the case of u'_1), meaning that the time realizations tend to cluster around the expected value (i.e. the mean value), whereas the PDF of the fluctuations of the second component of velocity present two regions where the data cluster at the extrema indicating a global bimodal distribution. The PDF of the temperature fluctuations is the only one presenting a long tail on the right side corresponding to a positive skewness of the distribution. Moreover, as already been stated, due to the weakness of the turbulent flow and the influence of periodic events (i.e. the periodic motion of the hook-like structure and the wave-like instability of the vertical boundary layers) the fluctuating quantities still show high correlation (around 0.1) in their time signals as depicted in Fig.4.35-4.36 by the Auto-Correlation Function (ACF) in time $R_{\phi\phi}(\Delta\tau)$, given for a general statistically steady quantity $\phi(\tau) = \langle\phi\rangle + \phi'$ as

$$R_{\phi\phi}(\Delta\tau) = \langle[\phi(\tau) - \langle\phi\rangle][\phi(\tau + \Delta\tau) - \langle\phi\rangle]\rangle. \quad (4.24)$$

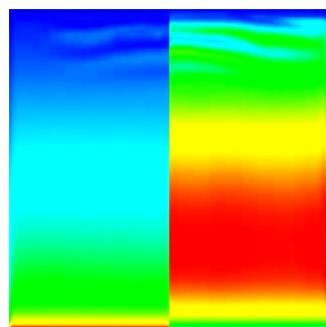
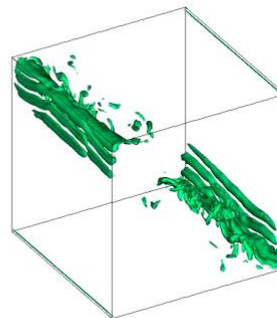
It appears that each signal is correlated with itself (with a correlation coefficient around 0.1) even for very large time distances $\Delta\tau$ for all the signals. This means that periodic patterns are hidden in the fluctuating time signal. Let us emphasize that, apart from $R_{u_3u_3}$ which presents very frequent peaks (this is due to the particular position of the sampling point



(a) $\tau = 5$



(b) $\tau = 25$



(c) $\tau = 125$

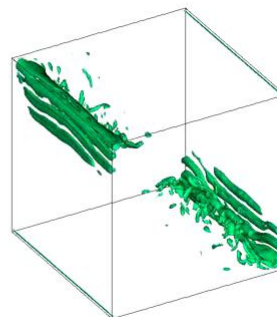
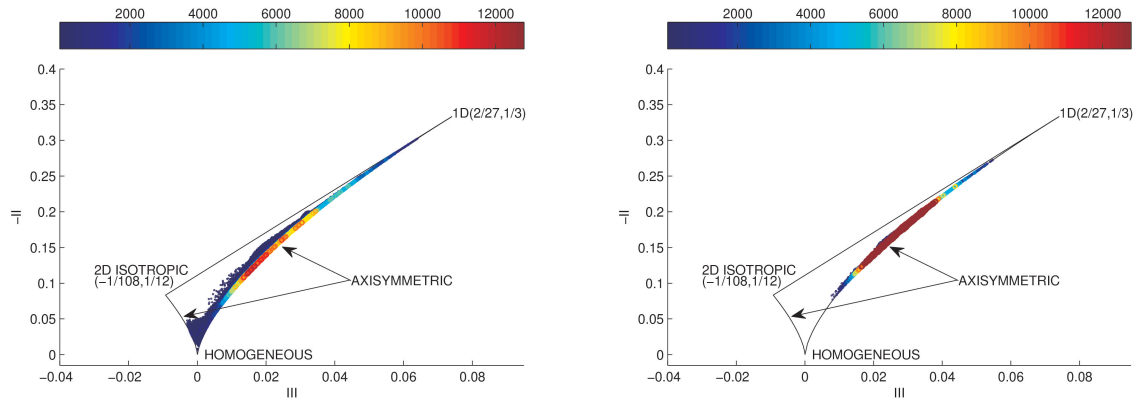


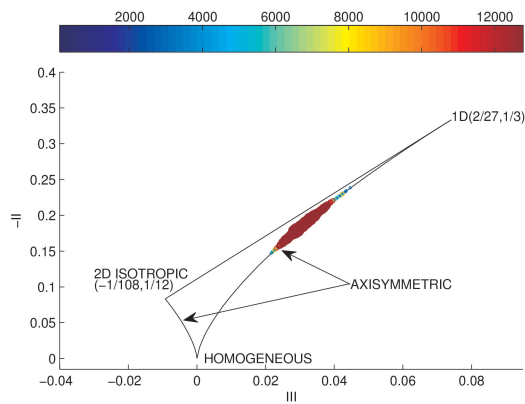
Fig. 4.29: On the left: iso-contours of the instantaneous vertical component of the shear stress at the wall ($-0.5 \leq x_3 \leq 0$) and instantaneous local Nusselt number iso-contours ($0 \leq x_2 \leq 0.5$). On the right: instantaneous coherent structures identified by $\lambda_2 = -0.5$.

4.2. TURBULENT FLOW



(a) $0.4 < k/k_{max} \leq 0.6$

(b) $0.6 < k/k_{max} \leq 0.8$



(c) $0.8 < k/k_{max} \leq 1$

Fig. 4.30: Probability density function of the second and third invariants of the anisotropy tensor \mathbf{B} in regions characterized by three different levels of turbulent kinetic energy k .

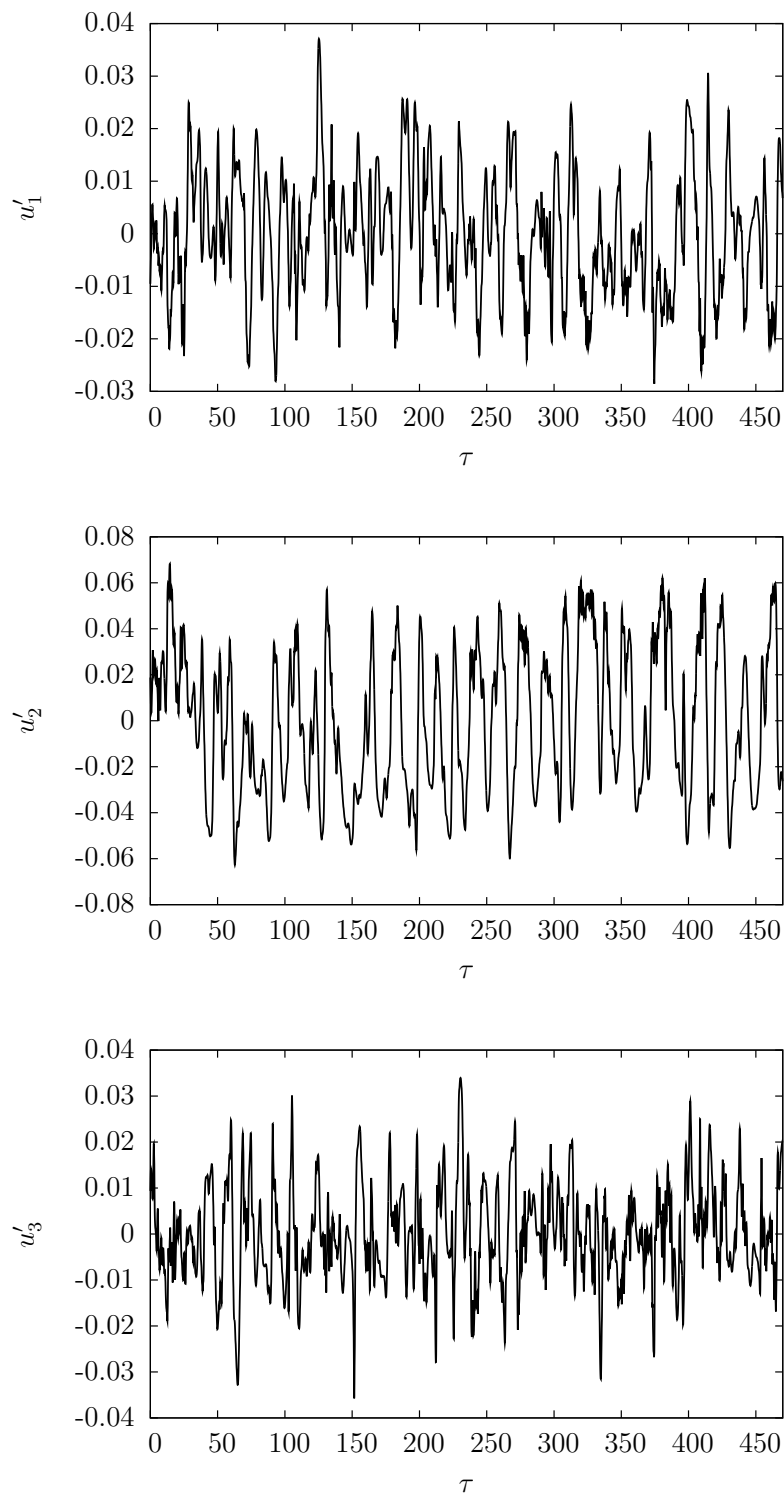


Fig. 4.31: *Time-history of the fluctuating part of the three velocity components sampled at the point of maximum turbulent kinetic energy $p^{k_{max}} == (-0.3469, 0.3601, -0.1113)$.*

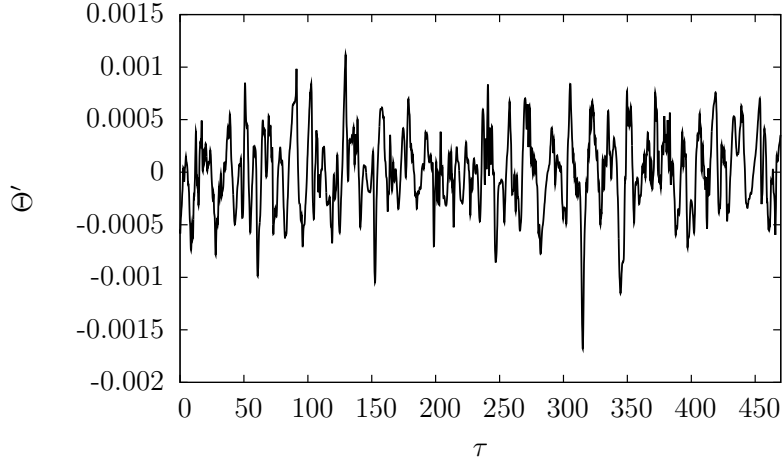


Fig. 4.32: *Time-history of the temperature fluctuations sampled at the point of maximum turbulent kinetic energy $p^{k_{max}} == (-0.3469, 0.3601, -0.1113)$.*

that lays on symmetry mid-plane $x_3 = 0$), the other autocorrelation coefficients manifest high peaks that repeat at distance of about $10 \div 20$ time distance. The auto-correlation function is useful to estimate the integral time-scale \mathcal{T} of the time signal. This quantity provides information on the longest time where the signal is correlated with itself. From a theoretical viewpoint the integral time scale is measured as

$$\mathcal{T} = \int_0^{\infty} R_{\phi\phi}(\Delta\tau)d(\Delta\tau). \quad (4.25)$$

In practice, since the auto-correlation function is measured over a finite time distance ($\Delta\tau$) and because the signal presents non negligible correlation and negative loops also for large values of the time distances, the numerical integration of Eq.(4.25) is not trivial and can lead to wrong estimations due to the poor convergence in the tails of the ACF. Thus, two alternative methods proposed in the literature are used in order to estimate \mathcal{T} :

1. Integration up to the first root (zero-crossing) \mathcal{T}_0 [KP95];
2. Integration up to the first minimum \mathcal{T}_{min} [Tri88].

The corresponding values are reported in Tab.4.8. It appears that the maximum time for which the signal is strongly correlated with itself, i.e. the life time of the largest turbulent vortex, is around two units of dimensionless time. This means that the largest turbulent structure is rather persistent in time. This is a confirmation of the fact that the regime is only weakly turbulent even if the Rayleigh number is almost two orders of magnitude greater than the critical Rayleigh number (that marks the first transition to periodicity).

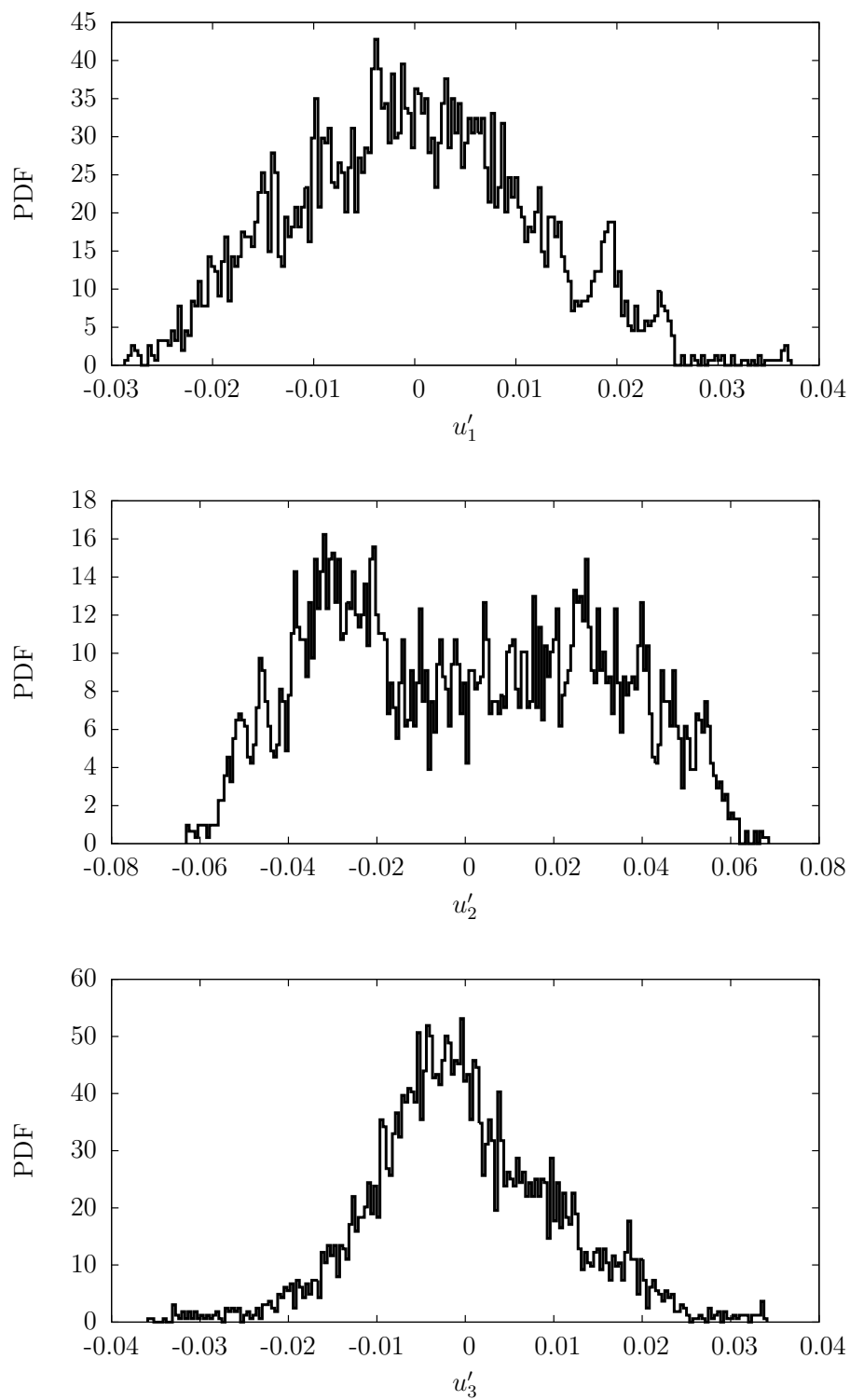


Fig. 4.33: *Probability Density Functions (PDF) of velocity component fluctuation time-histories.*

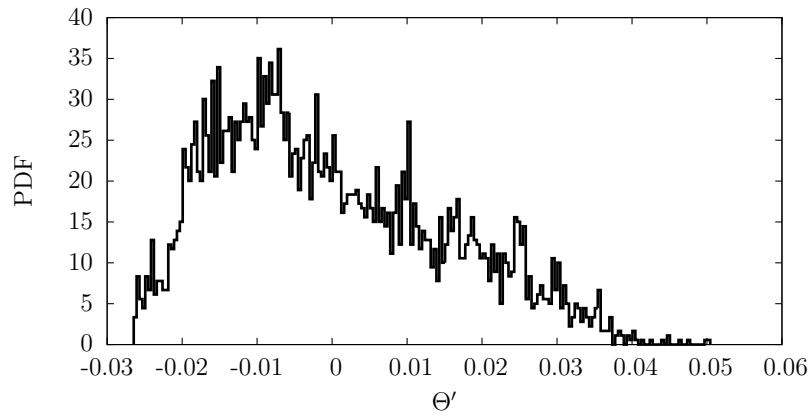


Fig. 4.34: *Probability Density Functions (PDF) of temperature fluctuation time-histories.*

	\mathcal{T}_0	\mathcal{T}_{min}
u'_1	1.96	1.75
u'_2	2.63	2.40
u'_3	1.52	1.23
Θ'	1.84	1.70

Tab. 4.8: *Integral time scales evaluated with three different criteria: integration up to the first ACF root (\mathcal{T}_0) and integration up the first ACF minimum (\mathcal{T}_{min}).*

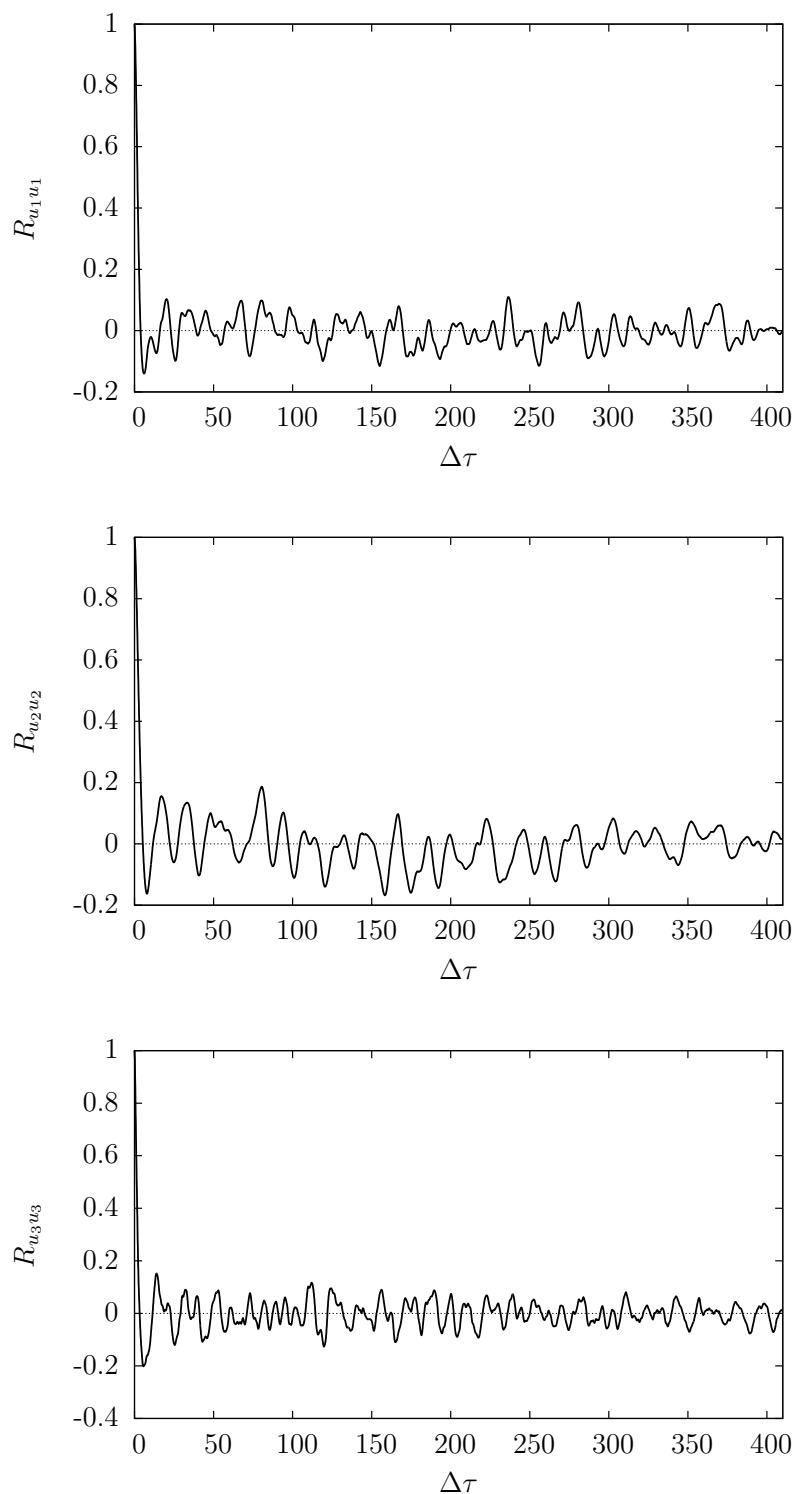


Fig. 4.35: Auto-correlation functions of the fluctuations of the three components of velocity at $p^{k_{max}} == (-0.3469, 0.3601, -0.1113)$.

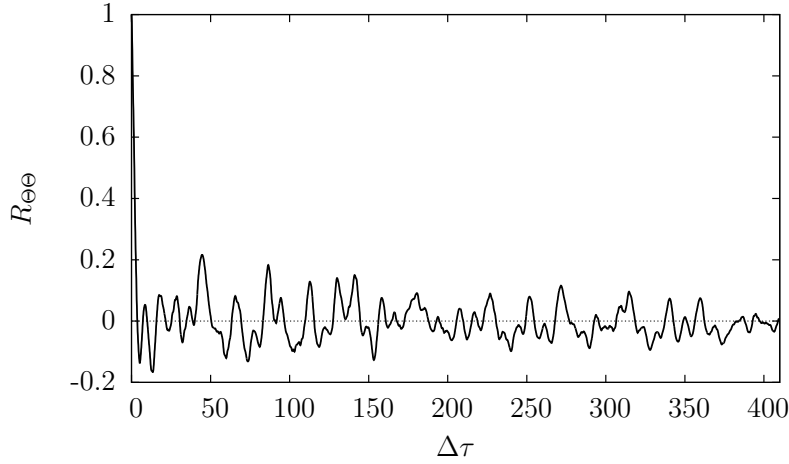


Fig. 4.36: *Auto-correlation function of temperature fluctuations at $p^{k_{max}} = (-0.3469, 0.3601, -0.1113)$.*

Finally, in natural convection at relatively low Reynolds number the energy cascade that describes the transfer of energy in the inertial subrange, i.e. the transfer of turbulent kinetic energy among the scales from the large energetic turbulent eddies, for which the viscous effects are negligible, up to the Kolmogorov microscales that are then dissipated by the molecular diffusion and their energy is converted into heat, is described by Bolgiano's theory [Bol62]. The theory states that the asymptotic form of the velocity Power Spectral Density in the inertial range is proportional to $\mathcal{K}^{-11/5}$ (where \mathcal{K} is the wave number that can be defined using Taylor's frozen field hypothesis $\mathcal{K} = 2\pi f/|\bar{\mathbf{u}}|$ with f the frequency of the time signal) whereas the Power Spectral Density of the temperature depends on $\mathcal{K}^{-7/5}$. In the present case the normalized PSD of the velocity components and the temperature fluctuations are provided in Fig.4.37-4.38. The normalization is made in the way that

$$\int_0^{\infty} S_{\phi}(f)df = 1. \quad (4.26)$$

We note that the velocity PSDs are in general agreement with Bolgiano's theory, whereas the temperature PSD shows the same scaling as the velocity instead of the theoretical result of $-7/5$ law. Two possible explanations of this discrepancy are:

1. The mean temperature profile is not completely stably stratified in the location of the sampling point (as required by Bolgiano's theory);
2. The strong anisotropy of the present flow.

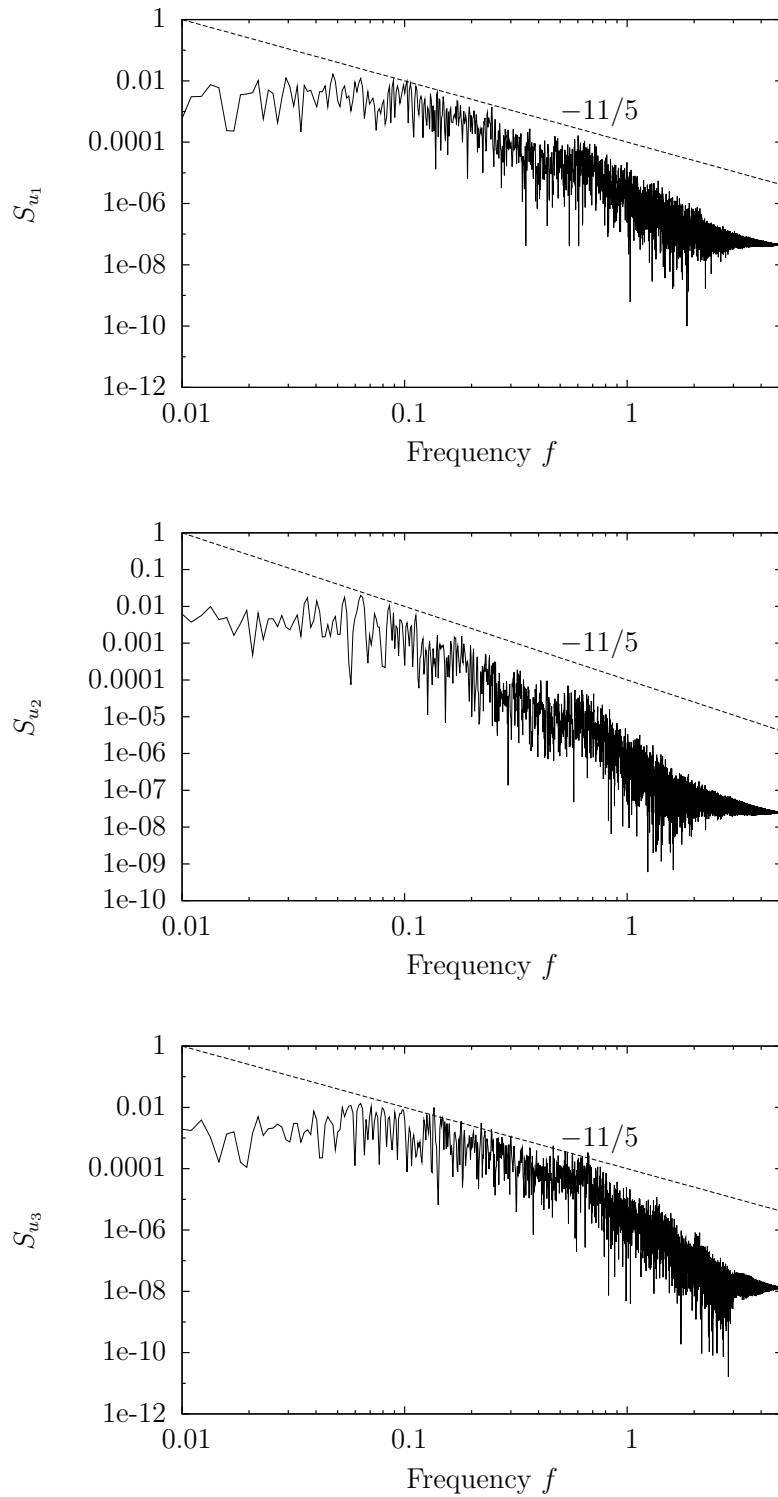


Fig. 4.37: *Normalized Power Spectral Densities of the three components of velocity.*

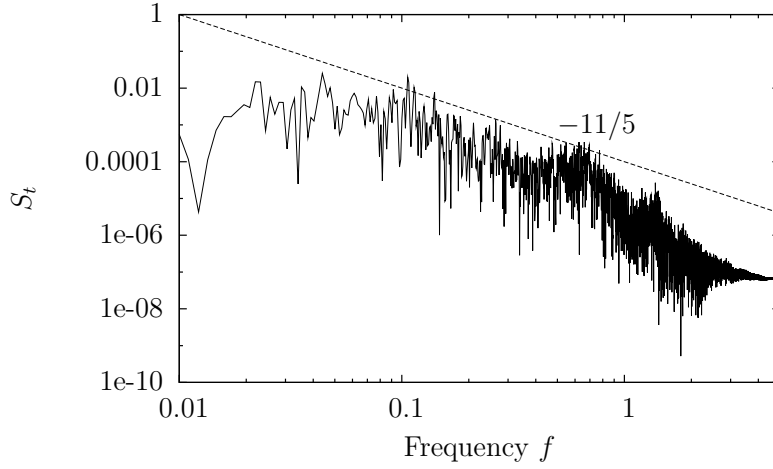


Fig. 4.38: *Normalized Power Spectral Densities of the temperature.*

Turbulent kinetic energy production

From a physical viewpoint it is interesting to understand the mechanisms of production of the turbulent kinetic energy and the associated flow structures. It has been shown for example that in a Lid Driven Cavity (LDC) flow at $Re = 12000$ (see [LG00]) the flow structure associated with the maximum of turbulent kinetic energy production is caused by the instantaneous formation of a vortex pair, located at the bottom of the cavity and characterized by a relevant up-flow velocity, that deflects and distorts the strong downward wall jet.

In the natural convective flow two terms play a role in the production of k , namely $P_k = (P_{11} + P_{22} + P_{33})/2$ and $G_k = (G_{11} + G_{22} + G_{33})/2$ but the first one is usually more important due to the high shear of the mean flow at the active walls, and as expected the grid point is located at $p_{\max P_k} \equiv p_k^{max} = (0.483, -0.373, 0.019)$. Moreover, it appears that the term

$$P_{22} = -\langle u'_2 u'_i \rangle \frac{\partial \langle u_2 \rangle}{\partial x_i} \quad (4.27)$$

provides the largest contribution to $\max P_k$ thanks to the high values of the gradient of the mean vertical velocity component across the boundary layer. Moreover, the largest contribution in P_{22} is given by $-\langle u'_2 u'_1 \rangle \partial \langle u_2 \rangle / \partial x_1$ and at p_k^{max} the term $\partial \langle u_2 \rangle / \partial x_1 < 0$ meaning that in order to have positive production the Reynolds stress component $\langle u'_2 u'_1 \rangle > 0$ (see Fig.4.21(b)). The time-series of Π_{22} is shown in Fig.4.39 together with its time-average P_{22} and the threshold value $\hat{\Pi}$ used to distinguish intense production events from weak events in order to select similar occurrences and perform a conditional sampling on the entire database. It is important to notice since now that the time signal shows peaks characterized by very high frequency superposed to low frequency signal. The low

frequency signal modulates the intensity of the peaks and the time extension of successive high intensity production events. Due to this dual nature of the production events the choice of the threshold $\hat{\Pi}$ becomes important and not trivial. Usually, the choice of the threshold is rather arbitrary and depending on that, it might lead to sensible different results. In order to avoid this problem, the author has computed a characteristic threshold of the time-signal itself by means of the Probability Density Function of the signal (PDF) and its Cumulative Distribution function (CDF) (Fig.4.40) imposing that the conditional mean over the χ fraction of the total instantaneous realizations, such that $\Pi_{22} > \hat{\Pi}$, is equal to $(1 - \chi)P_{22}$. In other words the threshold $\hat{\Pi}$ is obtained by finding a fraction χ of events Π_{22} for which $\Pi_{22} > \hat{\Pi}$, such that $(1 - \chi)$ is the relative contribution to the mean value P_{22} of the total number of realizations. The system of integral equations to solve in the two unknowns $(\chi, \hat{\Pi})$ is here provided

$$\begin{cases} \int_{\hat{\Pi}}^{\Pi_{22}^{\max}} \text{PDF}(\rho) d\rho = \chi \\ \int_{\hat{\Pi}}^{\Pi_{22}^{\max}} \text{PDF}(\rho) \rho d\rho = (1 - \chi)P_{22}. \end{cases} \quad (4.28)$$

The first equation gives the probability/frequency with which event $P_{22} > \hat{\Pi}$ occurs (PDF is null for values $\Pi_{22} < \Pi_{22}^{\min}$ and $\Pi_{22} > \Pi_{22}^{\max}$). The second equation can be obtained by the definition of expected value (i.e. mean value) of the given PDF. The reader should note that the proposed self-consistent technique allows to identify the fraction $0 < \chi \leq 0.5$ of events that amounts for $0.5 \leq (1 - \chi) < 1$ of the mean value depending on specific PDF. It identifies a small fraction of intense events that account for a large part of the mean value. In the present case $(\chi, \hat{\Pi}) = (0.290, 4.64 \times 10^{-3})$.

Performing the conditional averaging on the selected fields allows to identify the mechanisms and the structures involved in the production of the turbulent kinetic energy. In Fig.4.41 iso-surfaces of the distribution of P_{22} at the hot wall are presented together with the contour plots over the crossing horizontal plane which contains the point of maximum production P_k and the mean coherent structure identified using λ_2 method [JH95]. We note that the locations of high turbulent kinetic energy production take place close to the active walls (as expected since the high velocity gradients) downstream the detachment of buoyant fluid from the vertical boundary layers. Furthermore, the mean coherent structure identified from the conditional sampling is located exactly in the neighboring of the production maximum. The extension of the coherent structure is compatible with the region of high production P_k .

The mean coherent structure now identified is presumably responsible of the high frequency component in the time sequence of Fig.4.39 as shown in the plot of the time history of the horizontal and vertical velocity component fluctuations (see Fig.4.42). The second phenomena at lower frequency that interacts with the high frequency quasi-period signal (physically recognized as traveling waves of turbulent coherent structures ejected from the

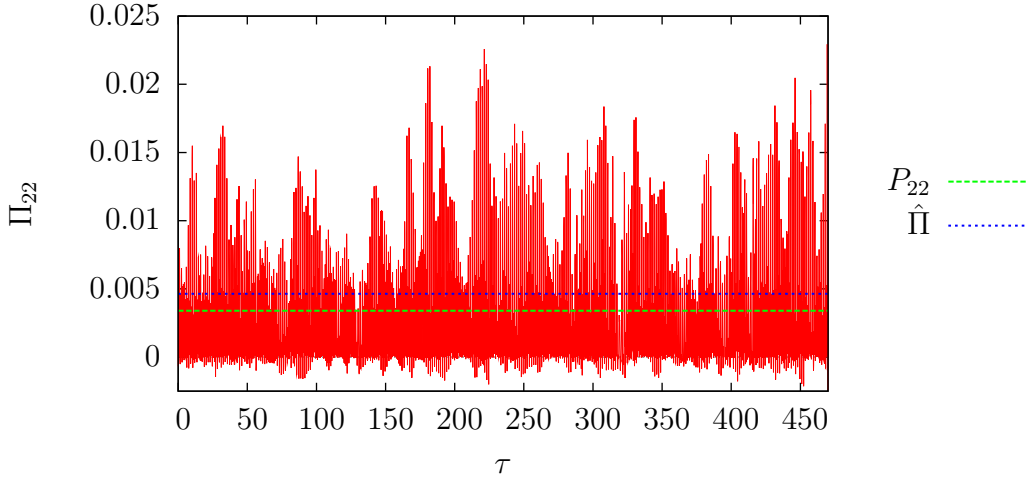


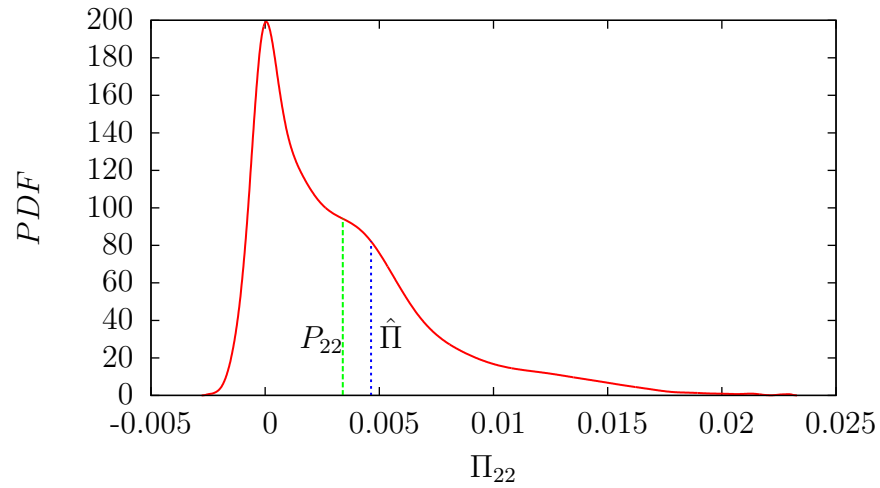
Fig. 4.39: *Time-series of the instantaneous production of turbulent kinetic energy Π_{22} and mean P_{22} and threshold values $\hat{\Pi}$ measured at the maximum of the turbulent kinetic hnergy production.*

unstable boundary layer) and produces the higher peaks of the Π_{22} cannot be identified so easily from the conditional averaged field. A closest inspection of the time-series Π_{22} shows two very high peaks for $0 \leq \tau \leq 50$ located approximately at $\tau \approx 10$ and $\tau \approx 32$ (see Fig.4.39). It should be noted that these events can be associated with the slow quasi-periodic motion of the unsteady hook-like structure reported in Fig.4.11-4.12. In fact, when peaks of production occurs the hook-like structure rolls up with its extremity in the vicinity of the vertical unsteady boundary layer shifting the position of the commencement of wavy motion. In other words the unsteady behavior of the hook-like structures besides the fact that it induces internal gravity waves that propagates in the core region (see []), it also introduces disturbances that affect the wave nature of the BL. This complicated and reciprocal interaction of the two structures might also lead to sporadic re-laminarization events.

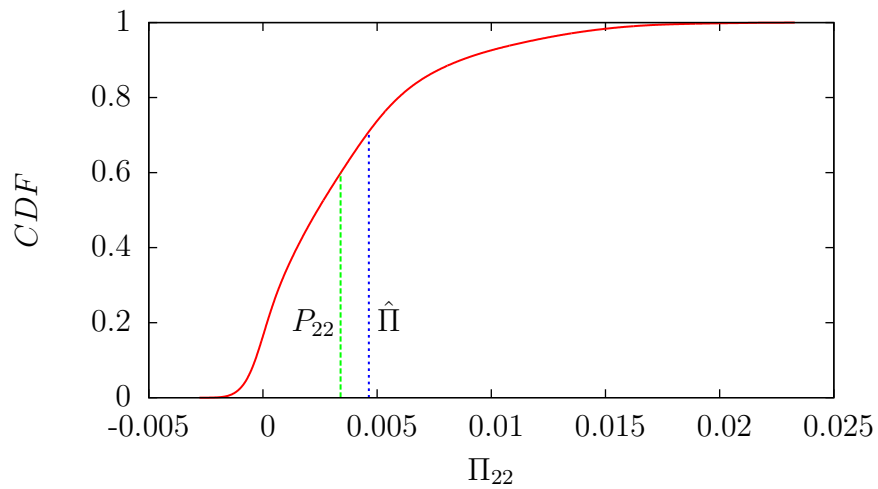
4.3 Particle deposition

The study of particle depletion inside a three-dimensional turbulent DHC flow is performed in order to clarify the main deposition mechanisms and the degree of importance of different effects like turbophoresis, thermophoresis and 3D effects (i.e. corner spiral motions) for instance.

The numerical experimental setup is realized with the injection of three swarms of inertial particle with size $d_p = 15, 25, 35 [\mu\text{m}]$ each one containing one million point-wise particles.



(a) PDF



(b) CDF

Fig. 4.40: *Probability Density Function (PDF) and Cumulative Distribution Function (CDF) of the time signal Π_{22} . Vertical lines refer to the mean value P_{22} and the threshold $\hat{\Pi}$.*

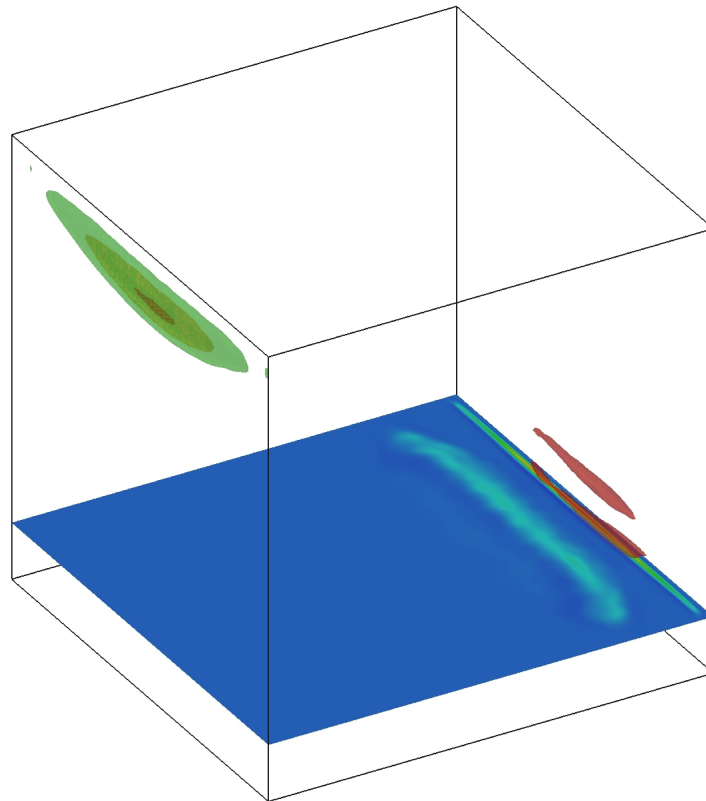
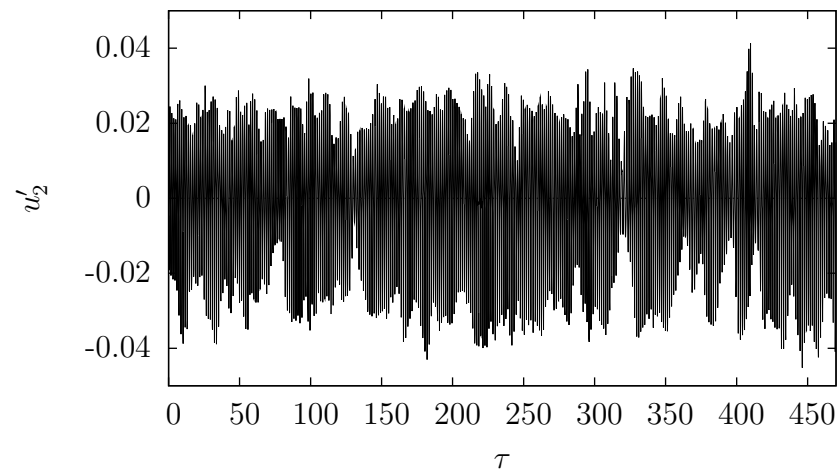
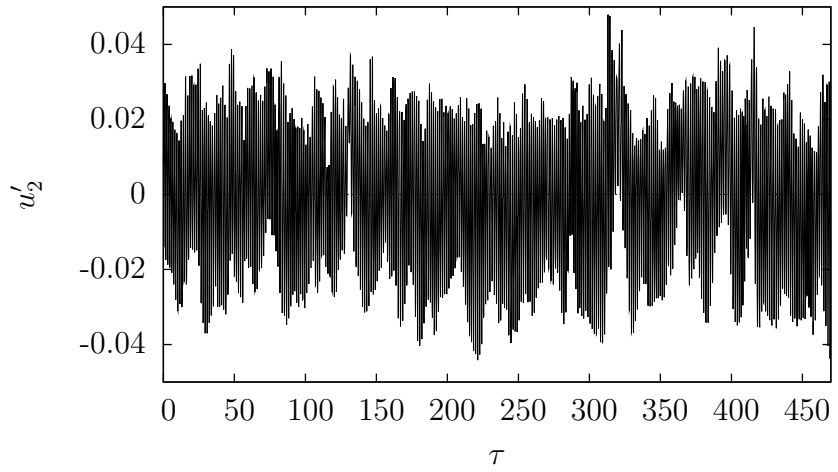


Fig. 4.41: *Top-left corner: Iso-surfaces of P_{22} . Bottom: Iso-contour map of P_{22} on the cross-plane containing P_K^{max} . In light-red two coherent structures identified by imposing $\lambda_2 = -0.5$.*



(a) u'_1



(b) u'_2

Fig. 4.42: *Time-history of horizontal and vertical velocity fluctuations measured at the maximum of the turbulent kinetic energy production.*

4.3. PARTICLE DEPOSITION

Ra_H	N_p	$d_p[\mu\text{m}]$	$\rho_p[\text{kg m}^{-3}]$	St	$\Delta\tau$	$Time$
10^9	1×10^6	15	1000	1.26×10^{-3}	5.00×10^{-4}	200
"	"	25	"	3.50×10^{-3}	1.00×10^{-3}	"
"	"	35	"	6.86×10^{-3}	1.00×10^{-3}	"

Tab. 4.9: *Particle tracking computational parameters.*

At the injection time, the flow has already reached statistically steady-state mean values. Furthermore, the particles are uniformly distributed inside the domain and their velocity at the injection time is imposed equal to the velocity of the fluid at the injection position of the particles. This technique is used in order to minimize the delay inertial particles would experience in adapting their velocity to the one of the carrier phase if injected with zero velocity (see [Elg94]). The details of the simulation are reported in Tab.4.9. The time integration of the Eulerian momentum and energy equations of the fluid and the Lagrangian particle equations of motion is performed sequentially because the alternative of tracking the particles on the whole database in a post-processing stage would require a huge storage facility for the instantaneous flow data. The three swarms of particles injected at the same time are then make evolving with different time steps in order to speed up the computation of the larger particles that allow larger time steps, hence less iterations are required to let a large number of particle deposit. Based on the two-dimensional calculations at $Ra_H = 10^9$ the integration time-step $\Delta\tau^3$ has been adapted in such a way it fulfills the Nyquist sampling theorem for each Stokes number St . The walls are considered as perfectly absorbing, i.e. when a particle hits any boundary surface it sticks to it and is immediately removed. Finally, in the particle equation of motion (Eq.(1.51)) the term dealing with the lift is dropped since its contribution to the deposition is negligible as shown by the two-dimensional calculations. On the other hand, the thermophoretic force is still retained to understand how the presence of a temperature gradient influences the deposition at the vertical walls depending on the particle diameter even if it is clear that its contribution to the depletion will be irrelevant for the present configuration.

4.3.1 Deposition velocity

The side view of the instantaneous particle positions of each set of particles is shown in Fig.4.43-4.44 at $\tau = 5, 25, 125$. As previously noted in the two dimensional results, the cavity is characterized essentially by two distinct regions: the core region from where particles basically settle by gravitational deposition; the hot wall where particles are lifted

³ In the present configuration, due to this limitation the time-step used for advancing the particles is in general smaller than the one based on the CFL condition for the carrier fluid (see Tab.4.5).

up and mixed by the hot jet and the unsteady hook-like structure. In the latter case, there are strong periodic ejections of particles away from the hot wall caused by the hook-like structure that give a wavy vertical profile at the particle swarm that remains suspended at the hot wall. As expected, small size particles settle very slowly under gravity and a large amount of them is entrained in the recirculation at the hot wall. They also shows the presence of the counterflow at the cold side. Large size particles, due to their significant inertia, deposit very quickly and are less affected by the turbulence. The time history of the airborne particles inside the cavity is depicted in Fig.4.45 for the three different particle sizes together with the corresponding profiles obtained from the two dimensional simulations at the same Rayleigh number. For all the particle diameters considered here, good agreement between the two- and three-dimensional calculations is found and can be explained by the fact that the third component of the fluid velocity has a negligible effect on the deposition process, but a slightly larger deposition rate is found at long times since the horizontal velocity component at the top (and the bottom) is not modulated in the spanwise direction as in the 3D cavity, hence leading to stronger ejections of particles from the hot wall towards the core of the cavity. Moreover, the statistics in the square cavity can be affected by the small number of particles that are recirculating for long time. The probability density function \mathcal{P} over the bottom wall is defined as

$$\mathcal{P} = \frac{1}{N_p} \frac{\Delta n_d}{\Delta x_1 \Delta x_3} \quad (4.29)$$

(its integral gives 1 only when the deposition is completed) is shown in Fig.4.46-4.47. It is possible to see that for small size diameter, the initial deposition distribution is almost uniform, whereas for large times shows a constant high value for $x_1 < 0$, while close to the cold wall ($x_1 = 0.5$) particle distribution is very low and slightly affected by the fluid spanwise velocity component of the hook-like structure that tends to drive particles from the lateral walls towards the midplane ($x_3 = 0$). Increasing in the diameter size leads to suppress the spanwise velocity influence, so that the distribution appears basically mono dimensional along x_1 , but very narrowed peaks of particle concentration appear at the corners at $x_1 = -0.5$. The latter phenomena is explained first by the fact that particles injected in the vertical edges do fall down by gravity only (fluid velocities are very low) and also by the formation of the vertical hot boundary layer which creates a suction effect that accelerates particles coming from the core and eventually, being unable to turn up, undergo settling. The presence of peaks around the midplane is explained by the work done by hook-like structure at the top of the cavity and its spanwise component of velocity.

4.3. PARTICLE DEPOSITION

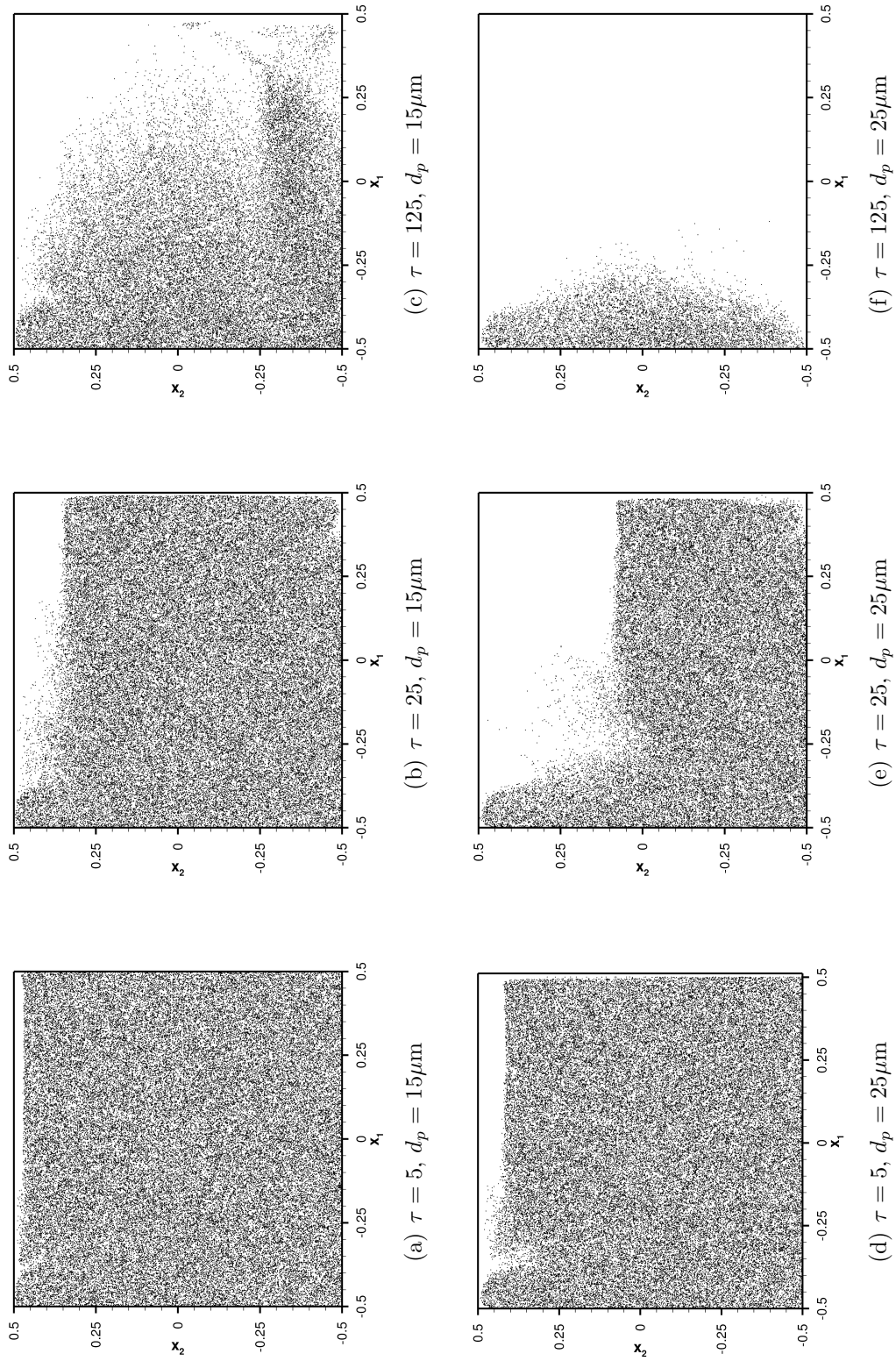


Fig. 4.43: Three instantaneous snapshots (side view) of particle distribution at time $\tau = 5, 25, 125$ for $Ra_H = 10^9$ and $d_p = 15, 25 [\mu\text{m}]$.

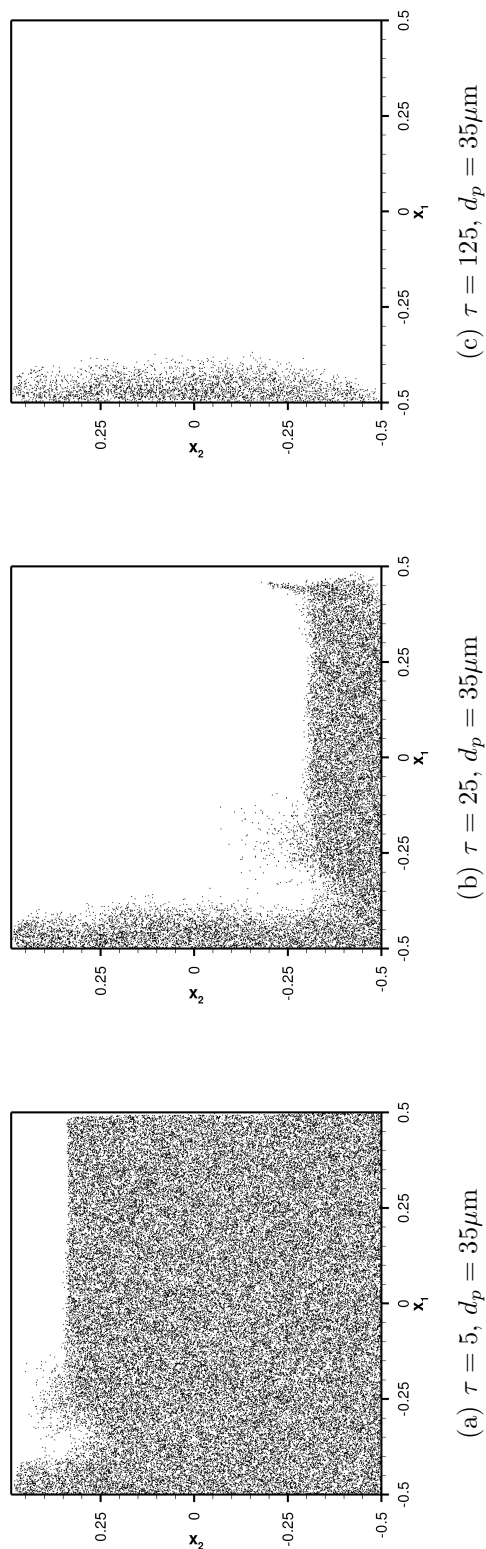


Fig. 4.44: Three instantaneous snapshots (side view) of particle distribution at time $\tau = 5, 25, 125$ for $Ra_H = 10^9$ and $d_p = 35 [\mu\text{m}]$.

4.3. PARTICLE DEPOSITION

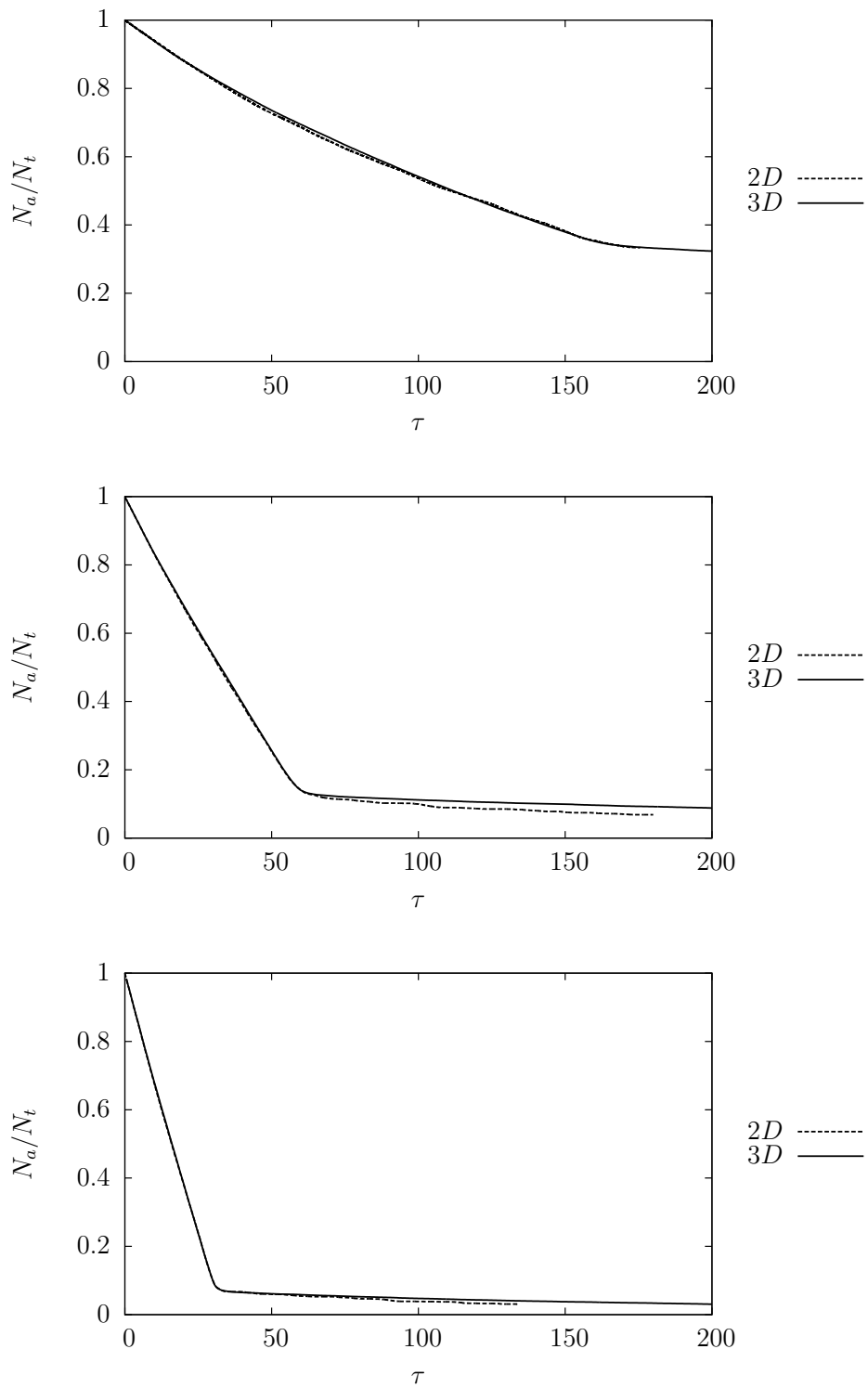


Fig. 4.45: Comparison of two and three dimensional time histories of the airborne fraction of particles in the enclosure for $d_p = 15, 25, 35 \mu\text{m}$ at $Ra_H = 10^9$.

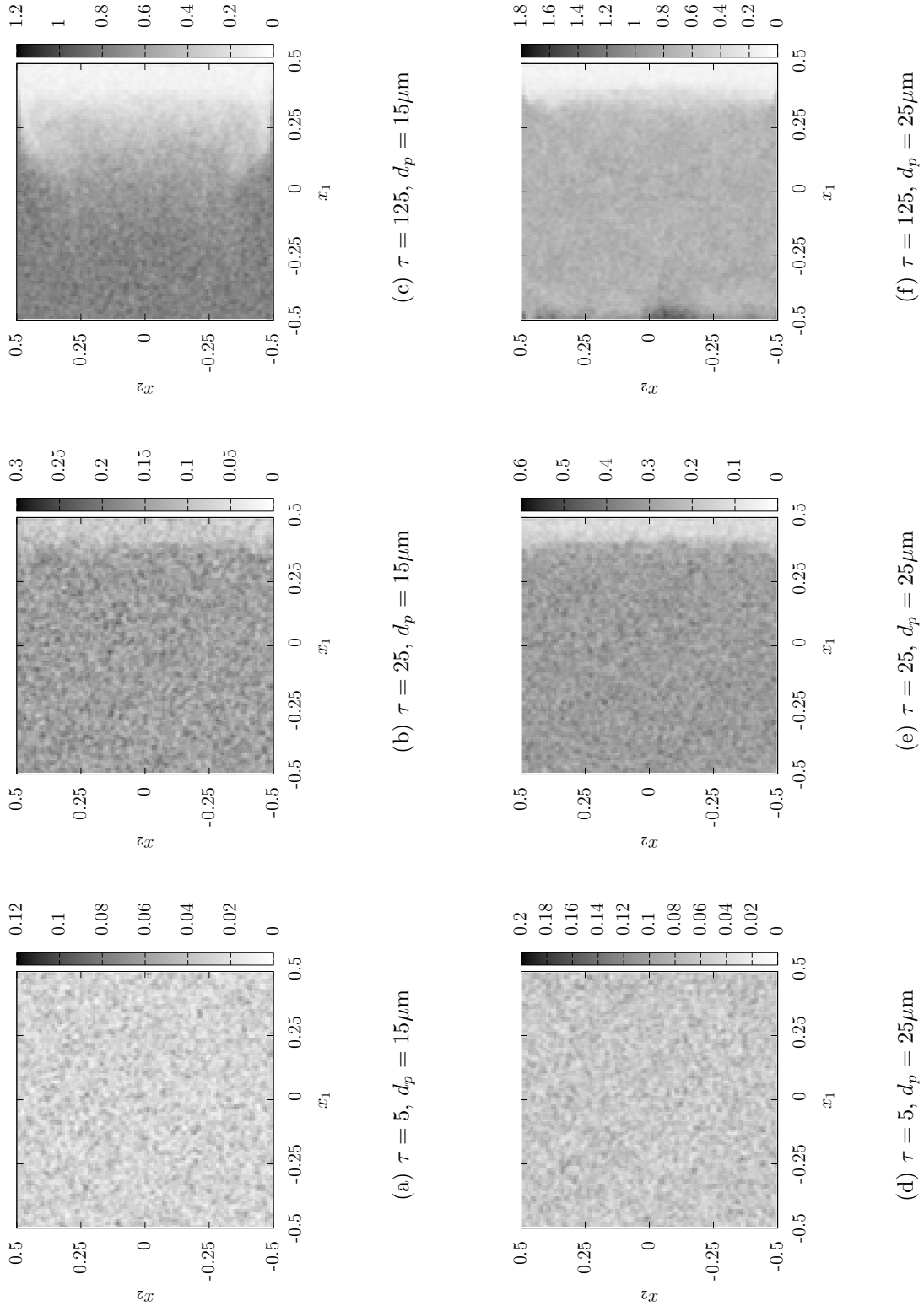
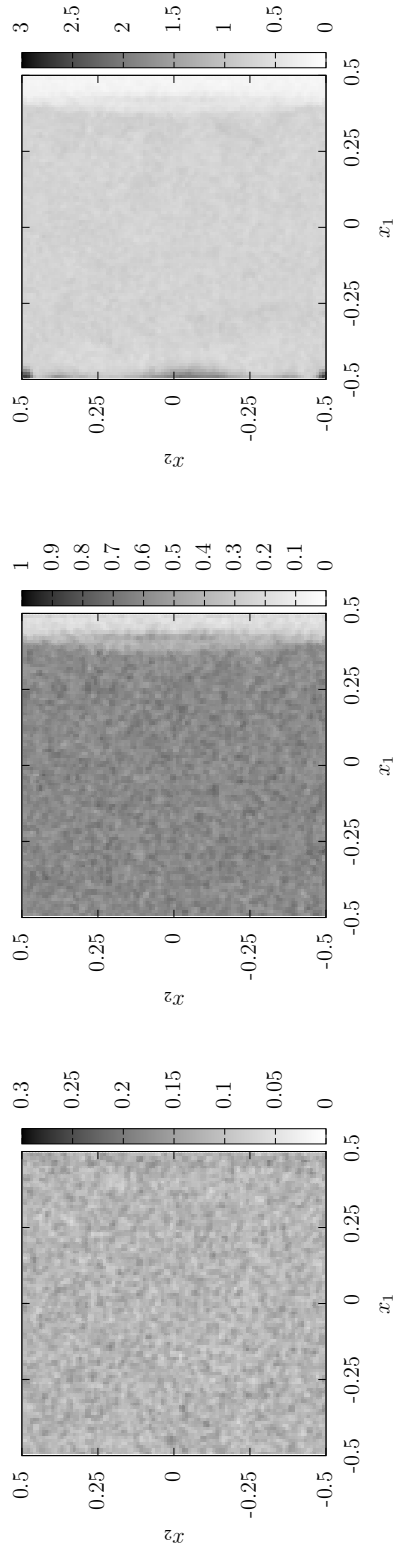


Fig. 4.46: PDF \mathcal{P} of particle distribution on the bottom wall surface at time $\tau = 5, 25, 125$ for $d_p = 15, 25 \mu\text{m}$ at $Ra_H = 10^9$.

4.3. PARTICLE DEPOSITION



(a) $\tau = 5, d_p = 35 \mu\text{m}$

(b) $\tau = 25, d_p = 35 \mu\text{m}$

(c) $\tau = 125, d_p = 35 \mu\text{m}$

Fig. 4.47: PDF \mathcal{P} of particle distribution on the bottom wall surface at time $\tau = 5, 25, 125$ for $d_p = 35 [\mu\text{m}]$ at $Ra_H = 10^9$.

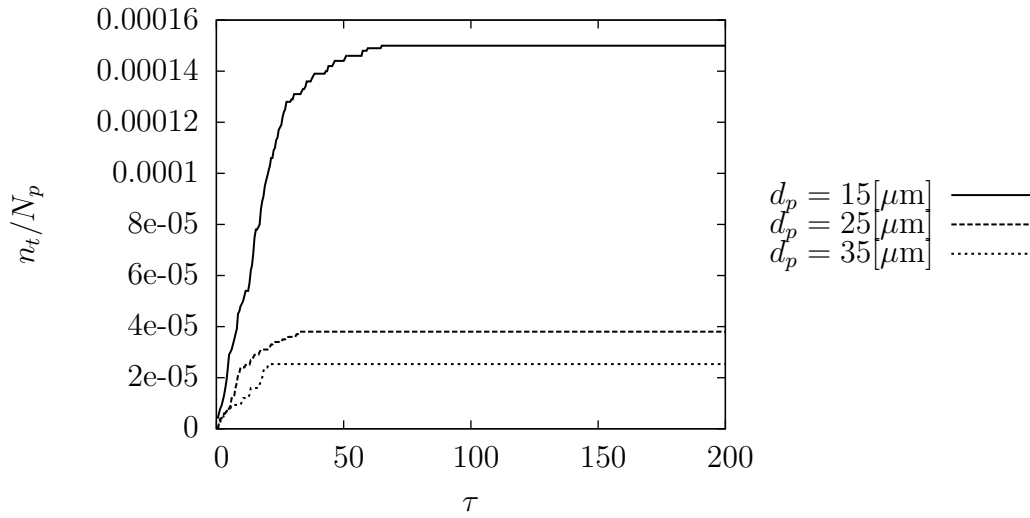


Fig. 4.48: *Time evolution of deposited particles at the cold wall for the three different particle sizes.*

Influence of thermophoretic force

Unlike the two-dimensional simulations, for the 3D case the lift force has been discarded from the Particle Equation of Motion (PEM) and only drag, gravity and thermophoretic forcing terms have been kept. This change affects the depletion of particles at the cold wall and how this effect scales with the size of the particles. In fact, as already found in the two dimensional cavity, the dilute phase deplete only at the bottom and at the active cold wall. It is worth to say that after all in the present setup this force is totally negligible for understanding the global behavior of the aerosol particles. More in details, the deposition caused by the temperature gradient takes place in the very early stages of the process (Fig.4.48) and so it is directly linked to the initial position at the injection time: particle injected inside the cold laminar boundary layer will have high probability to deposit by thermophoresis. On the other hand, due to the fluid vertical stratification and the turbulent mixing downstream the cold wall, the particles injected inside the turbulent cold boundary layer will experience a weaker temperature gradient, so the thermal drift will also decrease. Nevertheless, the importance of the thermophoretic effect increases for decreasing size particles. On the other hand, it is important to recall the fact that the lift force works better for large particles. Thus, even if in the present case the depletion due to lift is some orders of magnitude larger than the one caused by thermophoresis (as seen in the two dimensional case), for smaller particles an opposite behavior could be observed.

4.3.2 Particle residence time

The residence time of a substance is defined as the average time the substance spends inside a chosen control volume. If there is no contaminant generation, or influx in the control volume, given the time evolution of the substance concentration $G(\tau)$, then it is easy to show that the mean residence time can be computed as

$$\overline{R}_t = \frac{1}{G(0)} \int_0^{\infty} G(\tau) d\tau \quad (4.30)$$

For the discrete case here considered, Eq.(4.30) is written

$$\overline{R}_t = \frac{1}{n_v(0)} \sum_{i=0}^n n_v(\tau_i) \Delta\tau \quad (4.31)$$

where $n_v(\tau_i)$ is the number of particles in the control volume at the instant τ_i and τ_n is the last computed time (if at this time the deposition is not completed the estimation might be affected by truncation error). Another way is to fit the discrete deposition curve and successively to apply Eq.(4.30). The latter technique has been implemented in MATLAB[®] using a non-linear least squares fitting of the deposition curves that describe the time evolution of the particle number fraction that occupies a given volume. The identification of the volume is based on the center of mass of the swarm of particles still suspended at the last time step of the simulation. Each volume extends from the hot wall up to the double of the distance of the center of mass from the active hot wall. In this way it is possible to select a large number of particles that undergo large recirculation loops and do not deposit simply by gravity. The choice of shape function (or model function) is critical. For the present analysis an exponential model function of the form

$$m(\tau) = a \exp\left(-\frac{\tau}{b}\right) \quad (4.32)$$

where a and b are the unknown parameters corresponding to the initial number of particles and a time constant. It can be easily seen that the latter quantity correspond to the mean residence time itself by using the definition of mean residence time of Eq.(4.30) and substituting $G(\tau)$ with $m(\tau)$. The exponential shape function is preferred to the others because it implies that the particles that remain in suspension are well mixed (thanks to the action of the hook-like structure) and that the outgoing mass flux is proportional to the actual concentration (uniform in the volume) through a constant. It should be noted that the first part of all the curves (Fig.4.49) is rather affected by the initial conditions (meaning that some particles deposit by gravity in the first instants) and by the fact that particles in the upper part are ejected outside the control volume and then some of them

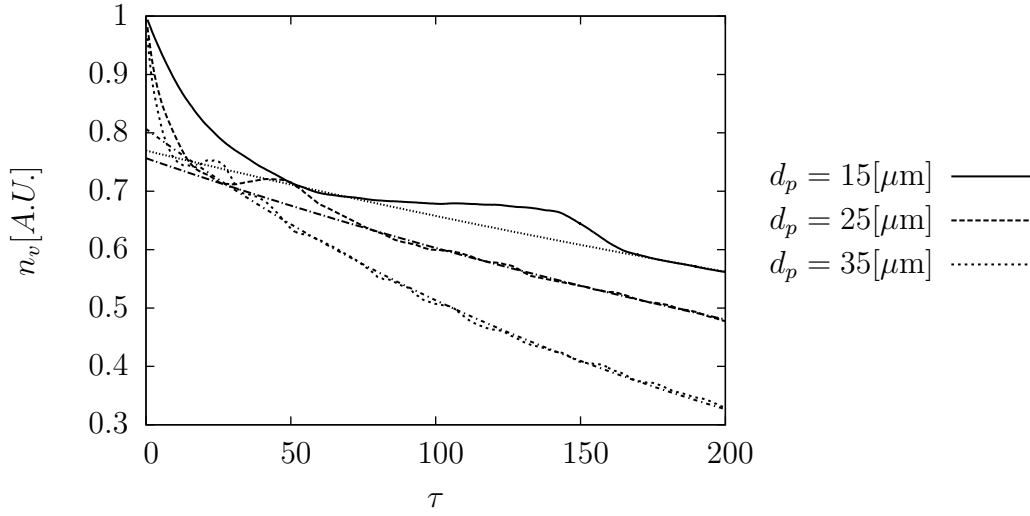


Fig. 4.49: *Time evolution of the recirculating particle fraction inside the control volume and correspondent fitting curves.*

re-enter later inducing the local minima and maxima or plateau zones. In order to exclude from the fitting those particles that initially belong to the control volume but sediment because of gravity, the time range valid for the fitting has been defined from the theoretical settling time to the end of the simulation, i.e. $\tau_s \leq \tau \leq 200$ where τ_s is the settling time that reads in dimensionless form

$$\tau_s = \frac{1}{v_t} = \frac{\beta \Delta T}{Pr St}. \quad (4.33)$$

The parameters obtained applying the model to the numerical results are reported in Tab.4.10 together with the estimator of the quality of the fitting R^2 (coefficient of determination) that for a general quantity $\phi_i = \phi(x_i)$ with n entries and the modeled function values $\phi_M^i = \phi_M(x_i)$

$$R^2 = 1 - \frac{\sum_{i=1}^n (\phi_i - \phi_M^i)^2}{\sum_{i=1}^n (\phi_i - \langle \phi_M \rangle)^2}. \quad (4.34)$$

The latter quantity simply compares the sum squared of the errors to the variance of the original data with respect to the mean value given by the model multiplied by the number of entries n .

$d_p[\mu\text{m}]$	a	$b = \overline{R_t}$	R^2
15	0.7696	636.9	0.994
25	0.7566	440.0	0.996
35	0.8067	221.2	0.997

Tab. 4.10: *Model function parameters a and b (Eq.4.32) for recirculating particle concentration number and coefficient of determination R^2 .*

4.3.3 Segregation parameter: correlation dimension

The mathematical definition of correlation dimension (also known as fractal dimension) is here recalled

$$\mathcal{D} := \frac{d \ln(\mathcal{N}(r))}{d \ln(r)}, \quad (4.35)$$

which expresses the dimensionality of the space occupied by the swarms of particles. As discussed in Sec.3.3.2 heavy inertial particles driven by an unsteady turbulent flow might select zones of the fluid where the instantaneous fluid motion presents determined characteristics as for example low vorticity. This behavior can be seen as a compressibility property of the dispersed phase. On the other hand for a fluid particle of an incompressible flow the fractal dimension remains constant and equal to the spatial dimension of the computation. In general this parameter is both used to recognize if the particles do cluster and consequently the dimensionality of the space occupied by the clusters: for particles well mixed and well distributed inside a volume $\mathcal{D} \rightarrow 3$, for particles that segregate from zones characterized by large eddies and concentrate over complicated surfaces $\mathcal{D} \rightarrow 2$, and finally if particles tends to form filaments (as in the case where particles are lighter then the fluid, bubbles for instance) $\mathcal{D} \rightarrow 1$. In Fig.4.50 the fractal dimension of the swarm of particles that are still airborne at $\tau = 200$ is plotted versus the diameter size. It should be noticed that for $d_p = 15$ and $25[\mu\text{m}]$ the correlation dimension is about $\mathcal{D} \approx 2.8$. This value is very close to the theoretical limit of 3 for incompressible fluid, meaning that the particles remain rather well distributed since the injection time. On the contrary, the largest set of particles with $d_p = 35 [\mu\text{m}]$ show a fractal dimension of 2.5. This departure is explained by the fact that ejection events caused by the motion of the hook-like structure do not affect significantly large particles coming from the hot plume. Therefore, large particles do not *diffuse* from the hot boundary layer to the core but they realize a very narrowed loop close to the wall. Eventually, these recirculating particles occupy a region of fluid which extend mainly in the two directions parallel to the hot wall (i.e. x_2 and x_3) with a very small thickness along x_1 , so that $\mathcal{D} \rightarrow 2$. This behavior should not be confused with a tendency of the particles to cluster in this layer since it has been already shown in

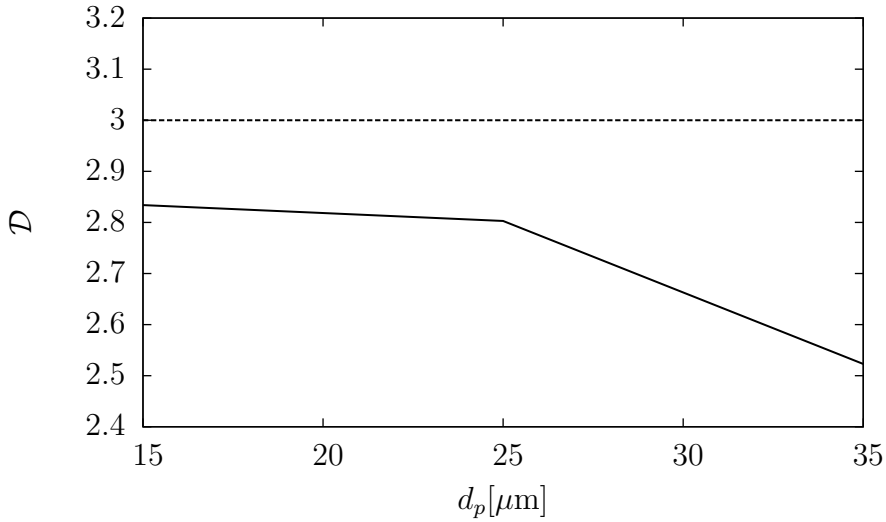


Fig. 4.50: *Correlation dimension of particle swarm as function of particle diameter at time $\tau = 200$ for $Ra_H = 10^9$.*

the previous section that the number of particles contained in the control volume decrease with time.

4.3.4 Theoretical simplified deposition model

The theoretical model is based on few important observations here synthesized:

1. Time evolution of the deposited particles at the wall shows clearly at least two regions. The time τ' at which the change of trend occurs is strongly related to the theoretical value of the settling time τ_s given by gravitational settling;
2. Local changes in particle concentration in the core region induced by the fluid motion are negligible;
3. Particles that remain suspended in the fluid due to the vertical hot jet are well mixed and deposit with a constant velocity;
4. Deposition at the cold wall caused by initial conditions and second order phenomena (i.e. lift and/or thermophoresis) is irrelevant for the particle sizes considered in the present work;
5. The domain can be schematically partitioned mainly in three regions as depicted in Fig.4.51.

4.3. PARTICLE DEPOSITION

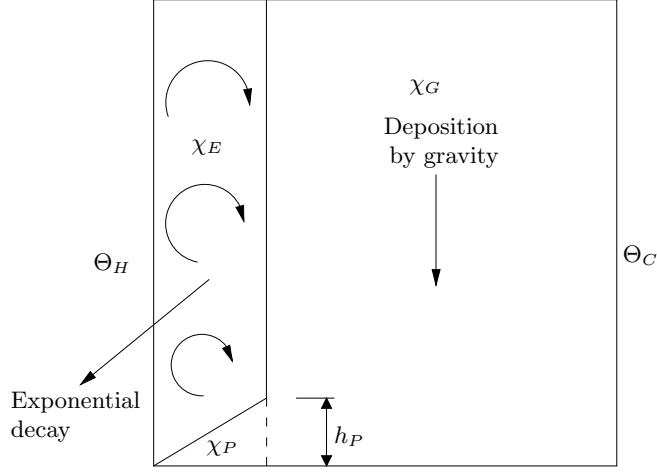


Fig. 4.51: *Schematic representation of the cavity partitions.*

The first two statements imply that a fraction of particles χ_G leaves the fluid in a time τ' , close to the settling time τ_s , with a law that reads

$$f_G(\tau) = \chi_G \left(1 - \frac{\tau}{\tau'}\right), \quad \text{for } 0 \leq \tau \leq \tau'. \quad (4.36)$$

Another fraction of particles, χ_E , deposits with the typical exponential decay law as stated by the third observation with a characteristic mean residence time \overline{R}_t

$$f_E(\tau) = \chi_E \exp\left(-\frac{\tau}{\overline{R}_t}\right), \quad \text{for } \tau \geq 0. \quad (4.37)$$

Finally, a fraction of particles χ_P settles because of gravity but does not follow the first law since their distribution along the height of the cavity differs from the constant one implied in Eq.(4.36) and occupies the triangular region shown in Fig.4.51. The deposition law for this fraction of particles is simply described by the following equation

$$f_P(\tau) = \chi_P \left(1 - \frac{\tau}{\tau''}\right)^2, \quad \text{for } \tau \leq \tau'', \quad (4.38)$$

where $\tau'' \propto h_P/v_s \leq \tau'$.

In conclusion the time evolution of the total fraction of particles inside the cavity is expressed by the six parameter model

$$\frac{N_a}{N_p} = \begin{cases} \chi_P \left(1 - \frac{\tau}{\tau''}\right)^2 + \chi_G \left(1 - \frac{\tau}{\tau'}\right) + \chi_E \exp\left(-\frac{\tau}{\overline{R}_t}\right), & \text{for } 0 \leq \tau < \tau' \\ \chi_G \left(1 - \frac{\tau}{\tau'}\right) + \chi_E \exp\left(-\frac{\tau}{\overline{R}_t}\right), & \text{for } \tau' \leq \tau < \tau_s \\ \chi_E \exp\left(-\frac{\tau}{\overline{R}_t}\right), & \text{for } \tau \geq \tau_s \end{cases} \quad (4.39)$$

where the conservation of mass for the particle imposes the additional constrain $\chi_P + \chi_G + \chi_E = 1$. Applying the model to particles of $d_p = 25, 35 \text{ } [\mu\text{m}]$ shows that the parabolic

CHAPTER 4. DIFFERENTIALLY HEATED CAVITY: THREE DIMENSIONAL
INVESTIGATIONS

d_p [μm]	τ_s	χ_P	τ''	χ_G	τ'	\overline{R}_t	χ_E	$\chi_P + \chi_G + \chi_E$	Err_τ [%]
15	163.96	0.161	116.98	0.397	163.96	636.9	0.442	1.000	0.00
25	59.03	0	–	0.861	58.57	440.0	0.139	1.000	0.78
35	30.12	0	–	0.925	30.44	221.2	0.075	1.000	0.01

Tab. 4.11: *Particle settling time, model parameters and Err_τ for particle sizes $d_p = 15, 25, 35$ [μm].*

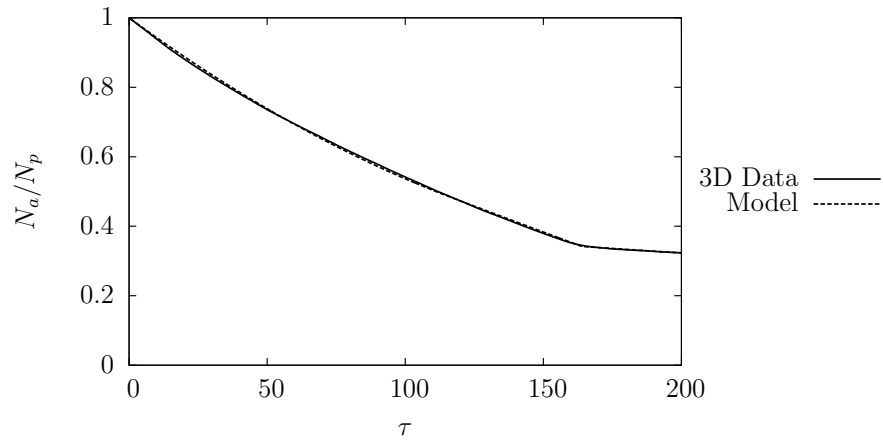
profile can be neglected in the initial times, committing an error in the settling time less than 1% as shown in Tab.4.11. The comparison of the data and the fitting is shown in Fig.4.52. Whereas for small size particles ($d_p = 15$ [μm]) the parabolic term has to be taken into account since more than 10% of the total particles are interested by such a process. Finally, in Fig.4.53-4.54 is shown the comparison of the actual instantaneous particle mass flow rate at the wall \dot{n} and the deposition velocity \mathcal{C}_d which are given respectively by

$$\dot{n} = -\frac{dN_a(\tau)}{N_p d\tau}, \quad (4.40)$$

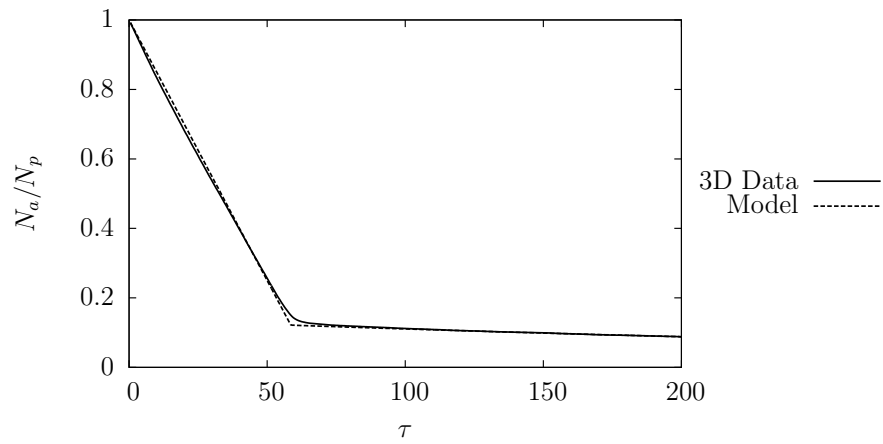
$$\mathcal{C}_d = \frac{1}{\Delta\tau} \ln \left(\frac{N_a(\tau)}{N_a(\tau + \Delta\tau)} \right) \quad (4.41)$$

It should be noticed that the deposition process presents constant mass flow rate for large and medium size particles and then abruptly changes (at the time $\tau' \approx \tau_s$) for an exponential trend. This last part is also affected by isolated deposition events of particles coming from the hot boundary layer that have been previously ejected by the action of the hook- like structure in the upper part of the cavity and are not able to restart the loop. The proposed model well captures all the main features of the process. For smaller particles it appears that the initial stages of deposition are characterized by an almost linear mass flow rate trend. It is still possible to identify a narrowed plateau region before the abrupt change to the exponential decay trend. Also in this case the model performs well. Concerning the deposition velocity \mathcal{C}_d the simplified theoretical model is generally in very good agreement with the numerical data. A slight discrepancy is visible for smallest set at the beginning of the deposition process. This issue is explained by the fact that there are only few points that describe the exponential tail yielding to a poor description of the residence time that affects also the particle mass fraction repartition.

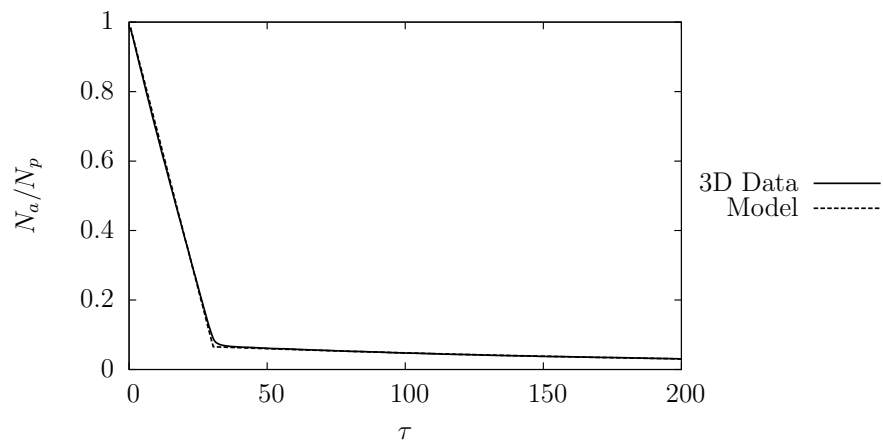
4.3. PARTICLE DEPOSITION



(a) $d_p = 15 \mu\text{m}$

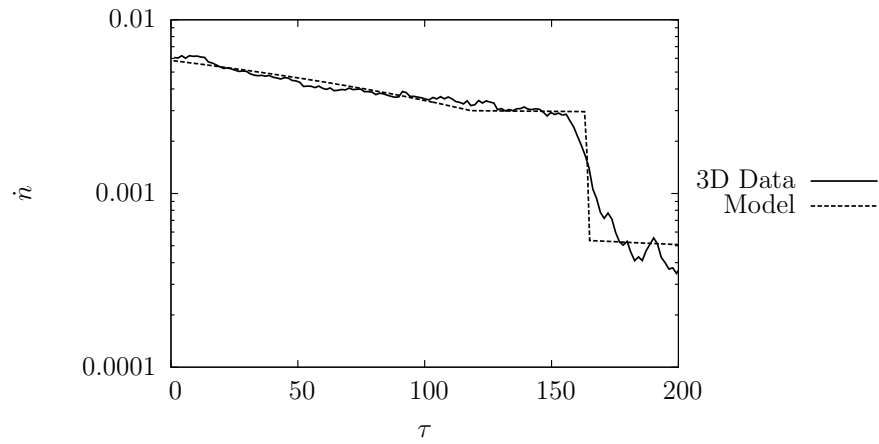


(b) $d_p = 25 \mu\text{m}$

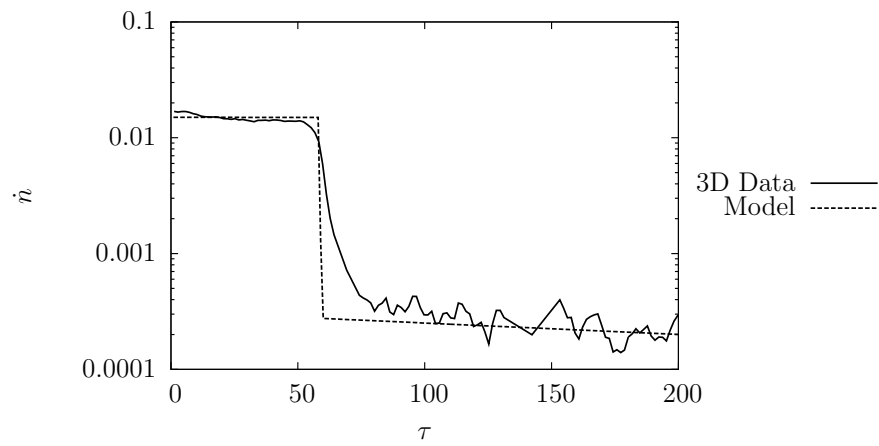


(c) $d_p = 35 \mu\text{m}$

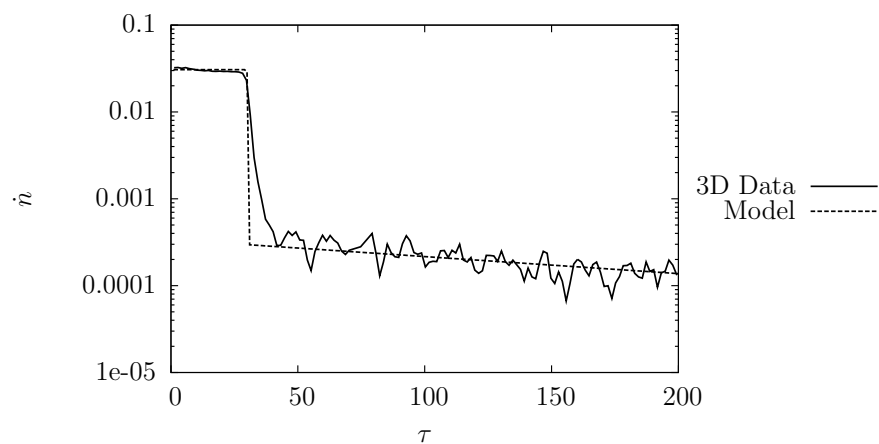
Fig. 4.52: Time evolution of particle airborne fraction inside the cavity for $d_p = 15, 25, 35 \mu\text{m}$. Three-dimensional data and theoretical model.



(a) $d_p = 15 \mu\text{m}$



(b) $d_p = 25 \mu\text{m}$



(c) $d_p = 35 \mu\text{m}$

Fig. 4.53: Time evolution of mass flow rate \dot{n} for $d_p = 15, 25, 35 [\mu\text{m}]$. Three-dimensional data and theoretical model.

4.3. PARTICLE DEPOSITION

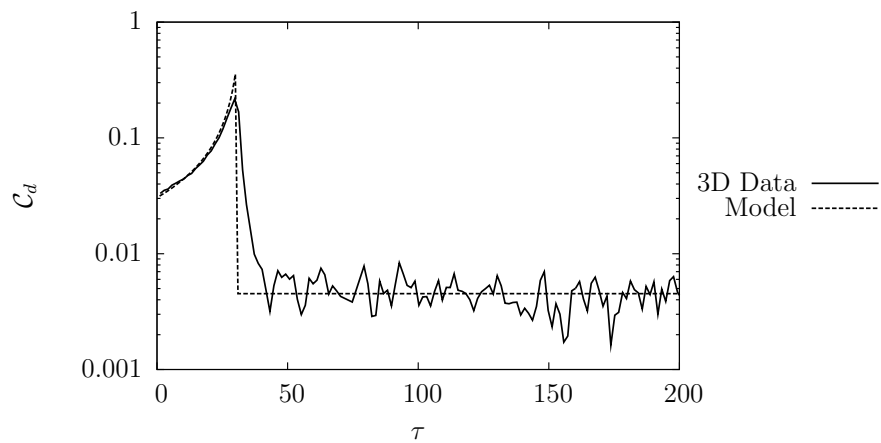
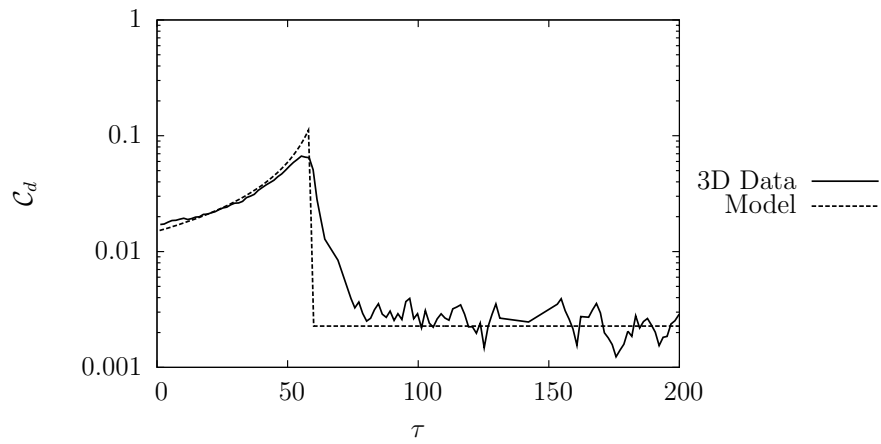
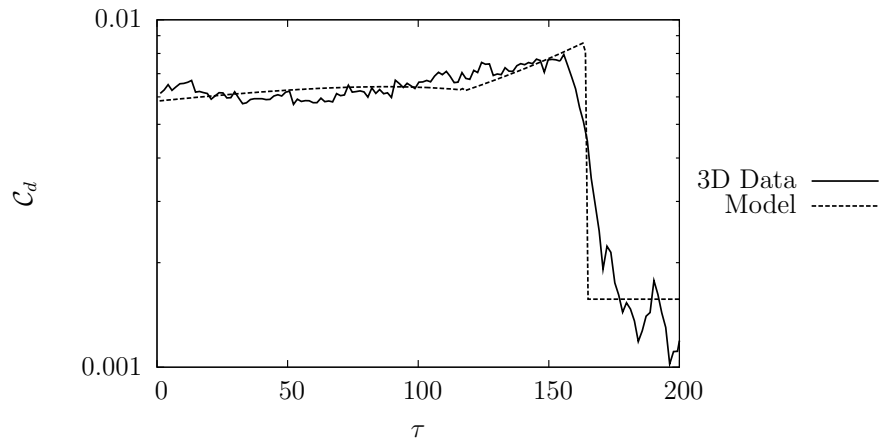


Fig. 4.54: Time evolution of deposition velocity C_d for $d_p = 15, 25, 35 [\mu\text{m}]$. Three-dimensional data and theoretical model.

CHAPTER 4. DIFFERENTIALLY HEATED CAVITY: THREE DIMENSIONAL
INVESTIGATIONS

Conclusions and perspectives

Nowadays, the increased safety requirements of the new generation nuclear power plants have led to investigate the mechanisms of deposition of radioactive aerosol inside closed containment like the heat exchanger of the steam generator or inside large containment buildings in order to be able to improve their design and to be able to control the phenomena in an active way with ad-hoc solutions, when possible, or in a passive way planning appropriate security procedures.

The present fundamental study aims at providing a first insight in natural convective turbulence at high Rayleigh numbers in simple closed domains, i.e. square and cubical Differentially Heated Cavities (DHC), as well as in the micro-size dispersed aerosol settling process by using very accurate numerical techniques. A pseudo-spectral Chebyshev code was coupled with a 6th-order Lagrangian particle tracking code and Direct Numerical Simulations of an incompressible, homogeneous, Newtonian, Boussinesq fluid were performed in two- and three-dimensional configurations and a parametric study was carried on for three different aerosol particle diameter sizes. Due to the characteristic boundary layer topology of the DHC flow along the active vertical walls, particular attention was taken in considering second order forces acting on the particles, like lift and thermophoresis.

Two and three-dimensional laminar flows were used as benchmark to validate the pseudo-spectral code providing new and more accurate values than those already published in the literature.

First and second order statistics of turbulent flows at Rayleigh $Ra_H = 10^9$ (2D/3D) and $Ra_H = 10^{10}$ (only 2D) and mean momentum and energy budgets were analyzed in order to understand the leading terms that govern the mean flows. Furthermore, informations about turbulent kinetic energy and temperature variance transport equations are provided for the first time in this configuration, focusing the attention on the production and dissipation terms. In particular, for the 3D case the interaction of boundary layer waves and the unsteady corner "hook-like" structures was identified as the main mechanism that produces turbulent kinetic energy.

Spectral analysis of the turbulent quantities in the three-dimensional case confirms Bolgiano's theory for what concerns the velocity time-signal, whereas a different scaling is

found for the temperature signals. The last result is caused by the strong anisotropy of the flow and by the local temperature distribution.

In this work the dependency of the flow structure on the cavity aspect ratios was not taken into account. Indeed, in recent works attempts to perform simulations at high Rayleigh numbers for cavities with aspect ratios four or eight were made. Secondly, an interesting development would be to consider the influence of real (or linear) temperature profiles at the top and bottom walls. A few published works have investigated such cases but only at moderate Rayleigh numbers. Furthermore, in the present work all the fluid physical properties are considered constant in the limit of the Boussinesq approximation but in thermal convection this approximation might be not always fulfilled and the influence of temperature dependent physical properties can strongly affect the turbulence.

The main results concerning particle sedimentation that confirm experimental and other numerical results are:

1. Particles have the tendency to deposit only on the bottom horizontal surface;
2. The settling process is basically two dimensional;
3. Depending on the aerosol diameter size a rather important fraction of particles is entrained in long time recirculation loops at the hot wall;
4. Turbophoresis does not significantly affect the deposition process in the present configuration.

Second order effects, like lift and thermophoresis, appears to be negligible for the particle sizes under investigation ($d_p = 15, 25, 35 [\mu\text{m}]$). Moreover, there is clear evidence that the settling velocity plays a very important role and so gravity. It is also important to stress the fact that particles do not present the tendency to cluster: no preferential fluid structures appear to be selected for accumulation.

A simplified theoretical model that describe the time evolution of aerosol total concentration has been proposed and discussed. The model contains macroscopic quantities that characterize the gravitational settling and the settling of the particles involved in the recirculation at the hot wall. The latter has been modeled with an exponential decay law. The model matches very well the numerical data and provides a tool to forecast and interpret the numerical or experimental data.

In the present work only one-way coupling was considered between the two phases. It might be interesting to study the effect of momentum and thermal coupling, even if, it is the author's opinion, this would globally decrease the thermal driving force of the carrier phase leading to a configuration for the aerosol phase that resembles more to a

CONCLUSIONS AND PERSPECTIVES

deposition process in a quiescent environment. Finally, due to the lack of literature in this field, Eulerian approach instead of Lagrangian one might give useful informations even for smaller aerosol ($d_p = 1 \div 5 [\mu\text{m}]$) and larger volume fractions including also diffusive phenomena.

CONCLUSIONS AND PERSPECTIVES

Bibliography

- [ABG95] M. Azaïez, C. Bernardi, and M. Grundmann. Spectral Method Applied to Porous Media Equations. *East-West J. Numer. Math.*, 2:91–105, 1995.
- [ABH08] C. Allery, C. Beghein, and A. Hamdouni. On investigation of particle dispersion by a POD approach. *Int. Appl. Mech.*, 44(1):110–119, 2008.
- [Bat67] G.K. Batchelor. *An Introduction to Fluid Dynamics*. Cambridge Univ. Press, Cambridge, 1967.
- [BBAHZ08] M. N. Borjini, H. Ben Aissia, K. Halouani, and B. Zeghmati. Effect of radiative heat transfer on the three-dimensional buoyancy flow in cubic enclosure heated from the side. *Int. J. Heat Fluid Flow*, 29(1):107–118, 2008.
- [Bej84] A. Bejan. *Convection Heat Transfer*. Wiley, N.Y., 1984.
- [BH06] B. A. V. Bennett and J. Hsueh. Natural convection in a cubic cavity: Implicit numerical solution of two benchmark problems. *Numer. Heat Tr. A–Appl.*, 50(2):99–123, 2006.
- [BKL94] A. Batoul, H. Khallouf, and G. Labrosse. Une Méthode de Résolution Directe (Pseudo-Spectrale) du Problème de Stokes 2D/3D Instationnaire. Application à la Cavité Entraînée Carrée. *C.R. Acad. Sci. Paris*, 319(I):1455–1461, 1994.
- [BM89] S. Balachandar and M. R. Maxey. Methods for evaluating fluid velocities in spectral simulations of turbulence. *J. Comput. Phys.*, 83(1):96–125, 1989.
- [Boi00] P.A. Bois. *Introduction à la Mécanique théorique des fluides*. Ellipses, 2000.
- [Bol62] R. Bolgiano. Structure of turbulence in stratified media. *J. Geophys. Res.*, 67(8):3015, 1962.
- [Bou03] J. Boussinesq. *Théorie Analytique de la Chaleur*, volume 2. Gauthier-Villars, Paris, 1903.

BIBLIOGRAPHY

- [But87] J.C. Butcher. *The Numerical Analysis of Ordinary Differential Equations. Runge-Kutta and General Linear Methods*. Wiley, New York, 1987.
- [CC99] G. Comini and G. Cortella. *Fondamenti di Trasmissione del Calore*. SGE, 1999.
- [CCO04] G. Colomer, M. Costa, and A. Oliva. Three-dimensional numerical simulation of convection and radiation in a differentially heated cavity using the discrete ordinates method. *Int. J Heat Mass Transfer*, 47:257–269, 2004.
- [CGS02] M. A. Christon, P.M. Gresho, and S.B. Sutton. Computational predictability of time-dependent natural convection flows in enclosures (including a benchmark solution). *Int. J. Numer. Meth. Fl.*, 40(8):953–980, 2002.
- [CHGR⁺03] B. Clément, N. Hanniet-Girault, G. Repetto, D. Jacquemain, A. V. Jones, M. P. Kissane, and P. von der Hardt. LWR severe accident simulation: synthesis of the results and interpretation of the first Phebus FP experiment FPT0. *Nucl. Eng. Des.*, 226:5–82, 2003.
- [CHQZ88] C. Canuto, M. Y. Hussaini, A. Quarteroni, and T. A. Zang. *Spectral Methods in Fluid Dynamics*. Springer Series in Computational Physics. Springer-Verlag, New-York, 1988.
- [CL01] K. S. Choi and J. L. Lumley. The return to isotropy of homogeneous turbulence. *J. Fluid Mech.*, 436:59–84, 2001.
- [Cro05] C. Crowe. *Multiphase flow handbook*. CRC Press, N.Y., 2005.
- [CST98] C. Crowe, M. Sommerfeld, and Y. Tsuji. *Multiphase flows with Droplets and Particles*. CRC, N.Y., 1998.
- [Dav79] C. N. Davies. Particle-fluid interaction. *J. Aerosol Sci.*, 10(5):477–513, 1979.
- [DFM02] M.O. Deville, P.F. Fischer, and E.H. Mund. *High-Order Method for Incompressible Fluid Flow*. Cambridge University Press, Cambridge, 2002.
- [DL82] M. Deville and G. Labrosse. An algorithm for the evaluation of multidimensional (direct and inverse) discrete Chebyshev transform. *J. Comput. Appl. Math.*, 8:293–304, 1982.
- [dVD83] G. de Vahl Davis. Natural convection of air in a square cavity : a benchmark numerical solution. *Int. J. Numer. Meth. Fl.*, 3(3):249–264, 1983.

BIBLIOGRAPHY

- [dVDJ83] G. de Vahl Davis and I. P. Jones. Natural-convection in a square cavity - a comparison exercise. *Int. J. Numer. Meth. Fl.*, 3(3):227–248, 1983.
- [dXD03] G. de Gassowski, S. Xin, and O. Daube. Bifurcations et solutions multiples en cavité 3D différentiellement chauffée. *C.R. Mécanique*, 331:705–711, 2003.
- [EF94] J. K. Eaton and J. R. Fessler. Preferential concentration of particles by turbulence. *Int. J. Multiphase Flow*, 20:169–209, 1994.
- [Elg94] S. Elghobashi. On predicting particle-laden turbulent flows. *Appl. Sci. Res.*, 52(4):309–329, 1994.
- [ET92] S. Elghobashi and G.C. Truesdell. Direct simulation of particle dispersion in a decaying isotropic turbulence. *J. Fluid Mech.*, 242:655–700, 1992.
- [FHKF91] T. Fusegi, J.M. Hyun, K. Kuwahara, and B. Farouk. A numerical study of three-dimensional natural convection in a differentially heated cubical enclosure. *Int. J. Heat Mass Transfer*, 34(6):1543–1557, 1991.
- [FKE94] J. R. Fessler, J. D. Kulick, and J. K. Eaton. Preferential concentration of heavy-particles in a turbulent channel flow. *Phys. Fluids*, 6(11):3742–3749, 1994.
- [Fus94] T. Fusegi. Laminar and transitional natural convection in an enclosure with complex and realistic conditions. *Int. J. Heat and Fluid Flow*, 15, 1994.
- [GB98] G. Gouesbet and A. Berlemont. Eulerian and Lagrangian approaches for predicting the behaviour of discrete particles in turbulent flows. *Prog. Energy Combust. Sci.*, 25(2):133–159, 1998.
- [Gel04] A. Y. Gelfgat. Stability and slightly supercritical oscillatory regimes of natural convection in a 8 : 1 cavity: solution of the benchmark problem by a global Galerkin method. *Int. J. Numer. Meth. Fl.*, 44(2):135–146, 2004.
- [GG76] D. D. Gray and A. Giorgini. The validity of the Boussinesq approximation for liquids and gases. *Int. J. Heat Mass Transfer*, 19:545–551, 1976.
- [GLS05] A. Giusti, F. Lucci, and A. Soldati. Influence of the lift force in direct numerical simulation of upward/downward turbulent channel flow laden with surfactant contaminated microbubbles. *Chem. Eng. Sci.*, 60:6176–6187, 2005.
- [GO77] D. Gottlieb and S.A. Orszag. *Numerical Analysis of Spectral Methods : Theory and Applications*. SIAM-CBMS, Philadelphia, 1977.

BIBLIOGRAPHY

- [GP83] P. Grassberger and I. Procaccia. Measuring the strangeness of strange attractors. *Physica D*, 9(1-2):189–208, 1983.
- [GSDK04] S. Guentay, D. Suckow, A. Dehbi, and R. Kapulla. ARTIST: Introduction and first results. *Nucl. Eng. Des.*, 231(1):109–120, 2004.
- [HL96] R. A. W. M. Henkes and P. Le Quéré. Three-dimensional transition of natural-convection flows. *J. Fluid Mech.*, 319(-1):281–303, 1996.
- [HLAD84] P. Haldenwang, G. Labrosse, S.A. Abboudi, and M. Deville. Chebyshev 3D Spectral and 2D Pseudospectral Solvers for the Helmholtz Equation. *J. Comput. Phys.*, 55:115–128, 1984.
- [JH95] J. Jeong and F. Hussain. On the identification of a vortex. *J. Fluid Mech.*, 285:69–94, 1995.
- [JH96] R. J. A. Janssen and R. A. W. M. Henkes. Instabilities in three-dimensional differentially-heated cavities with adiabatic horizontal walls. *Phys. Fluids*, 8:62–74, 1996.
- [KHM92] K. Kontomaris, T. J. Hanratty, and J. B. McLaughlin. An algorithm for tracking fluid particles in a spectral simulation of turbulent channel flow. *J. Comput. Phys.*, 103(2):231–242, 1992.
- [KIO91] G.E.M. Karniadakis, M. Israeli, and S. A. Orszag. High-Order Splitting Methods for the Incompressible Navier-Stokes Equations. *J. Comput. Phys.*, 97:414–443, 1991.
- [KJ83] R.J. Krane and J. Jessee. Some detailed field measurements for a natural convection flow in a vertical square enclosure. In *Proc. Ist ASME-JSME Thermal Engineering Joint Conference*, volume 1, pages 323–329, 1983.
- [KP95] G.G. Katul and M.B. Parlange. Analysis of land surface heat fluxes using the orthonormal wavelet approaches. *Water Resour. Res.*, 31:2743–2749, 1995.
- [LA74] B.Y.H. Liu and J.K. Agarwal. Experimental observation of aerosol deposition in turbulent flow. *J. Aerosol Sci.*, 5(2):145–148, IN1–IN2, 149–155, 1974.
- [Le 87] P. Le Quéré. *Étude de la Transition à l’Instationnarité des Écoulements de Convection Naturelle en Cavité Verticale Différentiellement Chauffée par Méthodes Spectrales Chebyshev*. PhD thesis, Université De Poitiers, 1987.

BIBLIOGRAPHY

- [Le 91] P. Le Quéré. Accurate solutions to the square thermally driven cavity at high Rayleigh number. *Comput. Fluids*, 20(1):29–41, 1991.
- [Ler99] E. Leriche. *Direct Numerical Simulation of a Lid-Driven Cavity Flow by a Chebyshev Spectral Method*. PhD thesis, no:1932, École Polytechnique Fédérale de Lausanne, Lausanne, 1999.
- [LG00] E. Leriche and S. Gavrilakis. Direct Numerical Simulation of the Flow in a Lid-Driven Cubical Cavity. *Phys. Fluids*, 12(6):1363–1376, 2000.
- [LHB98] W.H. Leong, K.G.T. Hollands, and A.P. Brunger. On a physically-realizable benchmark problem in internal natural convection. *Int. J. Heat Mass Transfer*, 41:3817–3828, 1998.
- [LHB99] W. H. Leong, K. G. T. Hollands, and A. P. Brunger. Experimental Nusselt number for a cubical-cavity benchmark problem in natural convection. *Int. J. Heat Mass Transfer*, 42:1979–1989, 1999.
- [LL00] E. Leriche and G. Labrosse. High-order direct Stokes solvers with or without temporal splitting : numerical investigations of their comparative properties. *SIAM J. Sci. Comput.*, 22(4):1386–1410, 2000.
- [LMP92] P. Le Quéré, R. Masson, and P. Perrot. A Chebyshev collocation algorithm for 2D non-Boussinesq convection. *J. Comp. Physics*, 103:320–334, 1992.
- [LPLD06] E. Leriche, E. Perchat, G. Labrosse, and M.O. Deville. Numerical evaluation of the accuracy and stability properties of high-order direct Stokes solvers with or without temporal splitting. *J. Sci. Comput.*, 26:25–43, 2006.
- [LQB98] P. Le Quéré and M. Behnia. From onset of unsteadiness to chaos in a differentially heated square cavity. *J. Fluid Mech.*, 359:81–107, 1998.
- [MA02] C. Marchioli and A. Soldati. Mechanisms for particle transfer and segregation in a turbulent boundary layer. *J. Fluid Mech.*, 468:283–315, 2002.
- [MdVD77] G. D. Mallinson and G. de Vahl Davis. 3-dimensional natural-convection in a box - numerical study. *J. Fluid Mech.*, 83(NOV):1–31, 1977.
- [MH03] J.C. Mason and D.C. Handscomb. *Chebyshev Polynomials*. Chapman & Hall/CRC, N.Y., 2003.
- [MJHL08] M. Mamun, D. Johnson, K. Hollands, and W. Leong. PIV measurements of the flow field inside an enclosed cubical cavity in natural convection. *Exp. Fluids*, 44(4):647–659, 2008.

BIBLIOGRAPHY

- [MLHJ03] M. A. H. Mamun, W. H. Leong, K. G. T. Hollands, and D. A. Johnson. Cubical-cavity natural-convection benchmark experiments: an extension. *Int. J. Heat Mass Transfer*, 46(19):3655–3660, 2003.
- [MP96] S. Mergui and F. Penot. Convection naturelle en cavité carrée différentiellement chauffée: investigation expérimentale à $Ra = 1.69 \times 10^9$. *Int. J. Heat Mass Transfer*, 39:563–574, 1996.
- [MP97] S. Mergui and F. Penot. Analyse des vitesses et température de l’air en convection naturelle dans une cavité carrée différentiellement chauffée à $Ra = 1.69 \times 10^9$. *Int. J. Heat Mass Transfer*, 40:3427–3441, 1997.
- [MR83] M.R. Maxey and J.J. Riley. Equation of motion for a small rigid sphere in a nonuniform flow. *Phys. Fluids*, 26:883–889, 1983.
- [MTN97] H. Mlaouah, T. Tsuji, and Y. Nagano. A study of non-Boussinesq effect on transition of thermally induced flow in a square cavity. *Int. J. Heat and Fluid Flow*, 18:100–106, 1997.
- [MY07] A.S. Monin and A.M. Yaglom. *Statistical Fluid Dynamics*, volume II. Dover Publication, 2007.
- [Nie04] J. J. Niemela. High Rayleigh number thermal convection. *J. Low Temp. Phys.*, 134(1):447–456, 2004.
- [NS06] J. Niemela and K. Sreenivasan. The use of cryogenic helium for classical turbulence: promises and hurdles. *J. Low Temp. Phys.*, 143(5):163–212, 2006.
- [Obe79] A. Oberbeck. Über die Wärmeleitung der Flüssigkeiten bei Berücksichtigung der Strömungen infolge von Temperaturdifferenzen. *Ann. Phys.*, 243(6):271–292, 1879.
- [OLVS06] P. Oresta, A. Lippolis, R. Verzicco, and A. Soldati. Dispersion and Deposition of Particles in Rayleigh-Bénard Turbulent Flows. In *FEDSM2006-98243*, 2006.
- [Pan84] R.L. Panton. *Incompressible flow*. John Wiley & Sons Ltd, 1984.
- [PC89] S. Paolucci and D. R. Chenoweth. Transition to chaos in a differentially heated vertical cavity. *J. Fluid Mech.*, 201:379–410, 1989.
- [PD01] S.H. Peng and L. Davidson. Large eddy simulation for turbulent buoyant flow in a confined cavity. *Int. J. Heat Fluid Flow*, 22(3):323–331, 2001.

BIBLIOGRAPHY

- [Pei99] J. Peiret. *Turbulent Flows: Models and Physics*. Springer, Berlin, Germany, 1999.
- [Pey02] R. Peyret. *Spectral Methods for Incompressible Viscous Flow*. Springer, N.Y., 2002.
- [PI80] J. Patterson and J. Imberger. Unsteady natural-convection in a rectangular cavity. *J. Fluid Mech.*, 100(SEP):65–86, 1980.
- [PL07] M. Pons and P. Le Quéré. Modeling natural convection with the work of pressure-forces: a thermodynamic necessity. *Int. J. Numer. Method H.*, 17(3):322–332, 2007.
- [PMB92] S. Pedinotti, G. Mariotti, and S. Banerjee. Direct numerical simulation of particle behaviour in the wall region of turbulent flows in horizontal channels. *Int. J. Multiphase Flow*, 18(6):927–941, 1992.
- [PMRS05] M. Picciotto, C. Marchioli, M.W. Reeks, and A. Soldati. Statistics of velocity and preferential accumulation of micro-particles in boundary layer turbulence. *Nucl. Eng. Des.*, 235:1239–1249, 2005.
- [PQ01] B. Podvin and P. Lé Quéré. Low-order models for the flow in a differentially heated cavity. *Phys. Fluids*, 13(11):3204–3214, 2001.
- [PSC03] Y. Peng, C. Shu, and Y.T. Chew. A 3D incompressible thermal lattice Boltzmann model and its application to simulate natural convection in a cubic cavity. *J. Comp. Physics*, 193:260–274, 2003.
- [QSS07] A. Quarteroni, R. Sacco, and F. Saleri. *Numerical mathematics*. Springer, Berlin, 2007.
- [RE01] D. W. I. Rouson and J. K. Eaton. On the preferential concentration of solid particles in turbulent channel flow. *J. Fluid Mech.*, 428:149–169, 2001.
- [Ree83] M.W. Reeks. The transport of discrete particles in inhomogeneous turbulence. *J. Aerosol Sci.*, 14:729–739, 1983.
- [RHH94] M. R. Ravi, R. A. W. M. Henkes, and C. J. Hoogendoorn. On the high-Rayleigh-number structure of steady laminar natural-convection flow in a square enclosure. *J. Fluid Mech.*, 262:325–351, 1994.
- [RS76] M.W. Reeks and G. Skyrme. The dependence of particle deposition velocity on particle inertia in turbulent pipe flow. *J. Aerosol Sci.*, 7(6):485–495, 1976.

BIBLIOGRAPHY

- [RSH06] J. Ravník, L. Skerget, and M. Hribersek. Two-dimensional velocity-vorticity based LES for the solution of natural convection in a differentially heated enclosure by wavelet transform based BEM and FEM. *Eng. Anal. Boundary Elem.*, 30(8):671–686, 2006.
- [SE91] Kyle D. Squires and John K. Eaton. Preferential concentration of particles by turbulence. *Phys. Fluids A*, 3(5):1169–1178, 1991.
- [SM09] Alfredo Soldati and Cristian Marchioli. Physics and modelling of turbulent particle deposition and entrainment: Review of a systematic study. *Int. J. Multiphase Flow*, 35(9):827–839, 2009.
- [Sol05] A. Soldati. Particles turbulence interactions in boundary layers. *Z. Angew. Math. Mech.*, 85:683–699, 2005.
- [SP95] S. A. Suslov and S. Paolucci. Stability of natural convection flow in a tall vertical enclosure under non-Boussinesq condition. *Int. J. Heat Mass Transfer*, 38:2143–2157, 1995.
- [SP97] S. A. Suslov and S. Paolucci. Nonlinear analysis of convection flow in a tall vertical enclosure under non-Boussinesq conditions. *J. Fluid Mech.*, 344:1–41, 1997.
- [SXJ⁺04] J. Salat, S. Xin, P. Joubert, A. Sergent, F. Penot, and P. Le Quéré. Experimental and numerical investigation of turbulent natural convection in a large air-filled cavity. *Int. J. Heat Fluid Flow*, 25:824–832, 2004.
- [TCL⁺08] S. J. Tsorng, H. Capart, D.C. Lo, J. S. Lai, and D. L. Young. Behaviour of macroscopic rigid spheres in lid-driven cavity flow. *Int. J. Multiphase Flow*, 34(1):76–101, 2008.
- [TCLY06] S. Tsorng, H. Capart, J. Lai, and D. Young. Three-dimensional tracking of the long time trajectories of suspended particles in a lid-driven cavity flow. *Exp. Fluids*, 40(2):314–328, 2006.
- [TK00a] Y.S. Tiang and T.G. Karayiannis. Low turbulence natural convection in an air filled square cavity Part I: the thermal and fluid flow fields. *Int. J. Heat Mass Transfer*, 43:849–866, 2000.
- [TK00b] Y.S. Tiang and T.G. Karayiannis. Low turbulence natural convection in an air filled square cavity Part II: turbulence quantities. *Int. J. Heat Mass Transfer*, 43:867–884, 2000.

BIBLIOGRAPHY

- [TLB00] E. Tric, G. Labrosse, and M. Betrouni. A first incursion into the 3D structure of natural convection of air in a differentially heated cubic cavity, from accurate numerical solutions. *Int. J. Heat Mass Transfer*, 43:4043–4056, 2000.
- [Tri88] D.J. Tritton. *Physical Fluid Dynamics*. Oxford University Press, 1988.
- [TSOPS07] F.X. Trias, M. Soria, A. Oliva, and C.D. Pérez-Segarra. Direct numerical simulation of two- and three-dimensional turbulent natural convection flows in a differentially heated cavity of aspect ratio 4. *J. Fluid Mech.*, 586:259–293, 2007.
- [UO96] W. S. J. Uijttewaal and R. V. A. Oliemans. Particle dispersion and deposition in direct numerical and large eddy simulations of vertical pipe flows. *Phys. Fluids*, 8(10):2590–2604, 1996.
- [WS04] S. Wakashima and T. S. Saitoh. Benchmark solutions for natural convection in a cubic cavity using the high-order time-space method. *Int. J. Heat Mass Transfer*, 47(4):853–864, 2004.
- [WXL06] H. Wang, S. Xin, and P. Le Quéré. Étude numérique du couplage de la convection naturelle avec le rayonnement de surfaces en cavité carrée remplie d’air. *C.R. Acad. Sci. Paris*, 334:48–57, 2006.
- [XL06] S. Xin and P. Le Quéré. Natural-convection flows in air-filled, differentially heated cavities with adiabatic horizontal walls. *Numer. Heat Tr. A–Appl.*, 50(5):437–466, 2006.
- [XLQ02] S. Xin and P. Lé Quéré. An extended Chebyshev pseudo-spectral benchmark for the 8 : 1 differentially heated cavity. *Int. J. Numer. Meth. Fl.*, 40(8):981–998, 2002.
- [YKHK96] A. L. Yarin, T. A. Kowalewski, W. J. Hiller, and S. Koch. Distribution of particles suspended in convective flow in differentially heated cavity. *Phys. Fluids*, 8(5):1130–1140, 1996.
- [YP88] P. K. Yeung and S. B. Pope. An algorithm for tracking fluid particles in numerical simulations of homogeneous turbulence. *J. Comput. Phys.*, 79(2):373–416, 1988.

BIBLIOGRAPHY

Curriculum Vitæ

Riccardo Puragliesi

Personal Information:

Date of birth: 23rd May 1981.

Place of birth: Sacile (PN), Italy.

Education:

2006-2009: PhD student at LIN (Laboratoire d'ingénierie numérique) at EPFL.

2005: MS in mechanical engineering with a specialization in design and production.

2004-2005: Student in mechanical engineering at Università degli Studi di Udine.

2004: BS in mechanical engineering.

2001-2004: Student in mechanical engineering at Università degli Studi di Udine.

Teaching Experience:

2008: Assistant for the course “Compressible Fluid Dynamics”, Prof. P. Maruzewski, SGM/EPFL.

2007: Assistant for the course “Compressible Fluid Dynamics”, Prof. M. O. Deville, LIN/EPFL.

Publications:

Direct numerical simulation of buoyancy driven turbulence inside a cubic cavity, R. Puragliesi, A. Dehbi, E. Leriche, A. Soldati, M. Deville, Proceedings of the 2nd International Conference on Turbulence and Interaction, TI2009, 31 May – 5 Jun. 2009, Martinique (FR).

Conferences:

2nd International Conference on Turbulence and Interaction, TI2009, 31 May – 5 Jun. 2009, Martinique (FR);

International Conference On Spectral and High Order Methods, ICOSAHOM07, 18 – 22 Jun. 2007, Beijing (CN);

Congresso nazionale sulla trasmissione del calore, XXV UIT 2007, 18 – 20 Jun. 2007, Trieste (IT).